INTERNATIONAL CENTER FOR NUMERICAL METHODS IN ENGINEERING

Nonlinear Analysis of Orthotropic Membrane and Shell Structures Including Fluid-Structure Interaction

J. G. Valdés
E. Oñate
J. M. Canet

Monograph CIMNE Nº-107, October 2007

Nonlinear Analysis of Orthotropic Membrane and Shell Structures including Fluid-Structure Interaction

J. G. Valdés
E. Oñate
J.M. Canet

Monograph CIMNE Nº-107, **October 2007**

International Center for Numerical Methods in Engineering
Gran Capitán s/n, 08034 Barcelona, Spain

INTERNACIONAL CENTER FOR NUMERICAL METHODS IN ENGINEERING
Edificio C1, Campus Norte UPC
Gran Capitán s/n
08034 Barcelona, sPAIN
www.cimne.upc.es

Fist edition: October 2007

NONLINEAR ANALYSIS OF ORTHOTROPIC MEMBRANE AND SHELL STRUCTURES INCLUDING FLUID-STRUCTURE INTERACTION
Monograph CIMNE M107

ISBN: 978-84-96736-37-5

Agradecimientos

Agradezco a mis directores de tesis, Eugenio Oñate y Juan Miquel Canet, por la oportunidad y buena disposición para llevar a cabo este trabajo. Gracias a ellos y especialmente a Salvador Botello he descubierto el maravilloso mundo de la mecánica computacional, destacado por la pasión, dedicación y coraje que se necesita para lograr nuevas metas.

Asimismo quiero agradecer a Carlos Arnold y Sergio Silva, profesores de la facultad de Ingeniería Civil de la Universidad de Guanajuato por haber depositado en mi su confianza y apoyarme para conseguir la beca PROMEP. También agradezco al CIMNE por la financiación prestada que me permitió concluir este trabajo.

A todas aquellas personas que han hecho que este trabajo sea posible les agradezco infinitamente su buena disposición, en especial al grupo de fluidos del CIMNE dirigido por Ramón Codina y a mis compañeros Herbert Owen y Javier Principe. También agradezco a Sergio Oller, Fernando Flores, Francisco Zárate, Michele Chiumenti, Miguel Cervera, Carlos Agelet, Juan Carlos Cante, Javier Oliver, Gabriel Bugeda y Robert L. Taylor, porque siempre me resolvieron más de una duda. Asimismo agradezco al personal del CIMNE y del departamento de resistencia de materiales y estructuras en ingeniería RMEE por su siempre buena disposición y amables atenciones, en especial a Rosa María Olea. Debo agradecer también a Mariano Vázquez y Guillaume Houzeaux por las correcciones y recomendaciones hechas a este trabajo.

Quiero agradecer profundamente a Dorian Luis Linero, Martha Liliana Carreño, Sergio Blanco, Carlos González Ferrari, Guillermo Díaz y Mabel Cristina Marulanda, mis compañeros del despacho 111, por su compañía, compresión, y gran amistad nacida durante estos años. Asimismo, quiero agradecer a Noel Hernández, Fernando Guzmán, Gelacio Juárez, Humberto Esqueda e Ivo Dias por esos grandes momentos dedicados al estudio y reir siempre a la hora de la comida. No me puedo olvidar de Roberto Clemente, Fernando Rastellini y Jeovan Faleiro con quienes compartí ideas y momentos difíciles durante el doctorado, así como a Pablo Mata, José Manuel González, Joaquín Hernández, Riccardo Rossi, Pere Andreu, Santiago Badía y Xavier Martínez.

A las personas que me enseñaron el camino a seguir en Barcelona cuando recién llegue para comenzar mis estudios les estaré por siempre agradecido, en especial a mis queridos e inolvidables amigos Quino, Ysabel y por supuesto Elizabeth, que más puedo decir, simplemente gracias por todo. También agradezco a mis amigos de la generación de salida con quienes compartí muchos agradables momentos, a

Guillaume, Ana, Eduardo y Esteban. También agradezco a las nuevas generaciones del doctorado por esos momentos que hemos podido compartir, a Pablo, Maritzabel, Christian, Juan Carlos, Flavia y María Laura.

Quiero agradecer a la gente del futbol de los viernes por la noche por los momentos inolvidables durante y después del partido, en especial a Manolo, Lucho, Antonio, Alex y Gigio.

No puedo dejar de mencionar en este trabajo a mis grandes amigos de toda la vida, Luis Eugenio, Victor, Ismael, Carlos y Julio César, asi como a mis compañeros y tambien grandes amigos de la universidad, Alberto, Heriberto, Miguel Eugenio, Julio, Lalo, Vero, Ana y en especial a Sandra, gracias por las palabras de ánimo en los momentos más difíciles cuando no veía la salida.

Y por último, quiero agradecer a toda mi familia, empezando por mi hermano Fernando y mis padres Irma y Jesús por estar siempre ahí, apoyándome y dándome palabras de aliento que me dieron la fuerza necesaria para salir adelante. Gracias a mis primos, tíos y todos mis familiares, y muy especialmente quiero agradecer a mis abuelos José, Jesús y Lolo porque de ellos proviene mi escencia y de quienes siempre me acuerdo. Sé que algunos de ellos me vieron partir pero no pudieron verme regresar, pero saben que siempre los llevaré en mi corazón y les estaré eternamente agradecido.

Jesús Gerardo Valdés Vázquez
Octubre de 2007

Abstract

Nowadays, fluid-structure interaction problems are a great challenge of different fields in engineering and applied sciences. In civil engineering applications, wind flow and structural motion may lead to aeroelastic instabilities on constructions such as long-span bridges, high-rise buildings and light-weight roof structures. On the other hand, biomechanical applications are interested in the study of hemodynamics, i.e. blood flow through large arteries, where large structural membrane deformations interact with incompressible fluids.

In the structural part of this work, a new methodology for the analysis of geometrically nonlinear orthotropic membrane and rotation-free shell elements is developed based on the principal fiber orientation of the material. A direct consequence of the fiber orientation strategy is the possibility to analyze initially out-of-plane prestressed membrane and shell structures. Additionally, since conventional membrane theory allows compression stresses, a wrinkling algorithm based on modifying the constitutive equation is presented. The structure is modeled with finite elements emerging from the governing equations of elastodynamics.

The fluid portion of this work is governed by the incompressible Navier-Stokes equations, which are modeled by stabilized equal-order interpolation finite elements. Since the monolithic solution for these equations has the disadvantage that take great computer effort to solve large algebraic system of equations, the fractional step methodology is used to take advantage of the computational efficiency given by the uncoupling of the pressure from the velocity field. In addition, the generalized-α time integration scheme for fluids is adapted to be used with the fractional step technique.

The fluid-structure interaction problem is formulated as a three-field system: the structure, the fluid and the moving fluid mesh solver. Motion of the fluid domain is accounted for with the arbitrary Lagrangian-Eulerian formulation with two different mesh update strategies. The coupling between the fluid and the structure is performed with the strong coupling block Gauss-Seidel partitioned technique. Since the fluid-structure interaction problem is highly nonlinear, a relaxation technique based on Aitken's method is implemented in the strong coupling formulation to accelerate the convergence.

Finally several example problems are presented in each field to verify the robustness and efficiency of the overall algorithm, many of them validated with reference solutions.

Table of Contents

List of Figures

Chapter 1

Introduction

1.1 Motivation

Modeling of structural elements, such as membranes and thin shells, is widely used in many engineering fields. In civil engineering applications, their elegance, effectiveness and optimal material usage make these light weight structures an ideal construction element.

The introduction of new fiber materials, such as glass, carbon or aramide fibers with orthotropic material behavior have motivated a deep study of such elements which are used to build membrane and thin shell structures.

Moreover membrane and thin shell structures are characterized by their low

Figure 1.1 *Membrane long span structure*

Figure 1.2 *Prestressed membrane structure*

flexural stiffness. Consequently these elements should not resist any compression at all. Therefore the usage of such construction materials is performed by introducing a prestressed force to the structure. Figs. 1.1 and 1.2 show different applications of membranes in civil engineering structures.

Other examples where light weight structures can be found include aircraft and spacecraft applications, parachutes, automobile airbags, sails, windmills and human tissues.

Since this kind of structures are highly flexible systems, they are susceptible to wind loads applied to them. Wind flow and structural motion may lead to aeroelastic instabilities which may cause important damage or even collapse of the structure.

Maybe one of the most important examples of aeroelastic instabilities is the disaster of the Tacoma Narrows suspension bridge that took place in the U.S.A. on November 7, 1940. The collapse of the bridge was due to wind-induced vibrations that at the beginning produced large transverse and rotational oscillations, as can be seen in Fig. 1.3.

In general many physical problems of different fields belong to multiphysic problems. In particular, numerical simulation of fluid-structure interaction problems have gained great interest from the industry community in order to reduce development time and cost in coupled systems. This kind of problems are complex because they consist of structural nonlinear boundary conditions imposed on fluid moving domains where the position is part of the solution.

Recently biomechanical applications are interested in the numerical simulation of hemodynamics, which study the blood flow through veins and arteries. In this problem, large structural deformations of the arteries interact with viscous blood

Figure 1.3 *Aeroelastic instabilities of the Tacoma Narrows suspension bridge, U.S.A.*

flow as a consequence of each heart beat. Another field where fluid-structure interaction plays an important role is the aerospace engineering which study wind flow around flexible wings of aircrafts.

1.2 Background

In this work, membrane and shell structures with large deformations are studied. A numerical solution for membranes may be constructed using the finite element method, which solution for small deformations can be found in Zienkiewicz and Taylor (1989), Cook et al. (1989) or Oñate (1992).

Theory for large deformations can proceed following the presentations of Simo and Fox (1989), Simo et al. (1990a), Bütchter et al. (1992) or Braun et al. (1994). In particular a large displacement formulation of membrane elements composed by three-node triangular finite elements based on rectangular Cartesian coordinates is proposed by Taylor (2001).

This last formulation together with the study of Lu et al. (2001) form the basis for the development of the membrane formulation given in this work, which includes orthotropic material behavior and prestressed forces.

Several studies have been carried out to study the geometrically nonlinear behavior of shells, for example the works of Simo and Fox (1989), Simo et al. (1990a), Simo and Kennedy (1992), among many others. Since shell analysis requires a lot of memory and cpu-time to compute, several authors have tried to derive plate and shell elements with displacements as the only nodal variables.

In this area, Oñate and Cervera (1993) proposed a general procedure based on finite volume concepts for deriving linear thin plate elements of triangular and quadrilateral shapes with the nodal deflections as the only degree of freedom. Brunet and Sabourin (1994) proposed a different approach to compute the con-

stant curvature field within each triangle in terms of the six-node displacement of a macro-element. This triangular element was successfully applied to nonlinear shell analysis using an explicit dynamic approach. Zárate (1996) continue with the study of rotation free elements of Oñate and Cervera (1993) developing new triangular elements. This formulation applied to large deformations with an explicit dynamic procedure was presented by Cendoya (1996). Rojek et al. (1998) proposed the same element that Cendoya (1996) but applied to metal forming processes.

As an alternative formulation for large strain plasticity, the BST shell element was introduced by Flores and Oñate (2001). This formulation constitutes the starting point for the development of the rotation-free shell formulation developed in this work, which includes orthotropic material behavior and prestressed forces.

Besides the structural developments, to perform a fluid-structure interaction study the fluid flow for incompressible problems has to be implemented. Finite element analysis of fluids present potential numerical instabilities that emerge for incompressible flow problems. To circumvent these problems, different stabilization techniques have been proposed. One of the stabilization techniques that has been extensively used is the *streamline-upwind/Petrov-Galerkin* SUPG method. Here numerical oscillations could be avoided by introducing numerical diffusion only along the streamlines as explained in the work of Hughes and Brooks (1979) for advection-diffusion equation. The use of the streamline diffusion in the context of weighted residual methods is given in Hughes and Brooks (1982). Another kind of stabilization is the *pressure-stabilizing/Petrov-Galerkin* PSPG method. In Tezduyar et al. (1990), the SUPG and PSPG stabilization methods are used together with equal-order interpolations.

With the idea to better understand the origins of stabilized methods, which can be derived from a firm theoretical foundation and a precise definition of the intrinsic time scale parameter, Hughes (1995) developed the *subgrid scale* method. In the context of these methods, the *orthogonal sub-scales* OSS method was introduced by Codina (2000). The stabilization methods described require the addition of some artificial diffusion terms. However another technique where the stabilization terms emerge from the governing equations of the problem is the *finite calculus* FIC method given by Oñate (1998). An application of the FIC for incompressible viscous flow problems can be found in Oñate (2000).

The monolithic coupled equations for incompressible fluid problems have the disadvantage that take great computer effort to solve the algebraic system for each time step in a transient analysis. Since the original works of Chorin (1967) and Temam (1969), fractional step methods for the incompressible Navier-Stokes equations have earned widespread popularity because of the computational efficiency given by the uncoupling of the pressure from the velocity field. A detailed stability analysis of fractional step methods for incompressible flows is given in Codina (2001). In this work, the FIC and OSS stabilization techniques are implemented to study the coupled problem of large structural deformations and incompressible fluids flow using pressure segregation methods.

With the structural and fluid problem introduced, the remaining task to study is the coupled problem between both of them. The implementation of a coupled problem can be done using two different global strategies, which are the *monolithic*

methods and the *partitioned* methods. In partitioned methods application of existing appropriate and sophisticated solvers for either structural or fluid subsystems will be used. Partitioned methods were introduced by Park and Felippa (1983). The key idea for these methods is clearly described in Felippa et al. (1998). Partitioned solutions with staggered coupling algorithms are developed by Farhat et al. (1997) to be used in aeroelastic wing problems.

Applications of strongly partitioned algorithms to large displacements structural problems coupled to viscous incompressible fluids are given by Wall and Ramm (1998) and Wall (1999). Other large displacements structural problems interacting with incompressible fluids are detailed in Mok (2001), Mok and Wall (2001) and Tallec and Mouro (2001). More sophisticated developments on strong partitioned method for FSI problems can be found in Steindorf (2002), Matthies and Steindorf (2004) and Tezduyar et al. (2006). A study on strong coupling partitioned methods for fluid-structure interaction problems applied to hemodynamic can be found in Nobile (2001), Causin et al. (2005), and Fernández and Moubachir (2005). In this work, strong coupling partitioned methods are used for fluid-structure interaction problems.

1.3 Objectives

Two general objectives in this work are pursued. The first of them is the improvement of prior developments made at CIMNE related to nonlinear membrane and shell analysis. The second general objective is the study of fluid-structure interaction problems using fluid flow pressure segregation methods and stabilization techniques developed at CIMNE.

The two general objectives must be implemented in one efficient, robust and accurate computational tool that use finite element technology to solve the problem in study, which also must have possibilities to analyze each subproblem, i.e. the solid or fluid part, independently as a highly developed software that exchange data for the solution of the coupled problem with other separate solvers.

The following particular objectives belong to the structural part:

- To review the state of the art for geometrically nonlinear membrane and shell finite elements.
- To improve the membrane and rotation-free shell finite elements developed at CIMNE in prior studies.
- To develop a new methodology to analyze orthotropic material behavior of membrane and shell finite elements, including the wrinkling phenomena to avoid compression stresses in membranes.
- To propose a new strategy to study prestressed membrane elements.
- To explore existing time integration schemes for structural dynamic problems and to work with the best choice for long time analysis periods.

- To implement the membrane and rotation-free shell finite elements together with their new developments in the COMET program, which is a software for coupled contact, mechanical and thermal analysis built at CIMNE.

The particular objectives belonging to the fluid-structure interaction problem part are:

- To implement in the COMET program the finite element fluid problem based on the incompressible Navier-Stokes equations and to use the stabilization techniques developed at CIMNE.
- To implement the mesh update strategy developed at CIMNE for the motion of the fluid domain.
- To explore existing time integration schemes for fluid dynamic problems and to work with the best choice for long time analysis periods.
- To review the state of the art for fluid-structure interaction problems.
- To implement a general and simple methodology to perform the study of coupled problems using the COMET program.

All these objectives are oriented to improve and to combine the developments made *in-the-house* in the solid mechanics field, i.e. membrane and thin shell finite elements, and the fluid dynamics field, i.e. stabilization techniques and mesh moving algorithms, to perform fluid-structure interaction of problems involving large structural displacements and incompressible fluid flows.

1.4 Outline

Since this work deals with different topics, a detailed review of the state-of-the-art is provided at the beginning of each theme to be developed. The work presented is organized as follows:

Chapter 2. Since the computational models emerged in this work are developed from the mechanics of a continuous medium, in this chapter the kinematics, stress and strain measures for solids and fluids, conservation equations, and the constitutive and Navier-Stokes equations used in this work are given. The remainder of this work is referred to these equations.

Chapter 3. In this chapter a review of the total Lagrangian formulation for geometrically nonlinear solid mechanics is made. From the continuum mechanics theory, the general formulation of each subject is presented which later is discretized with finite elements. Here the concept of principal fiber orientation is introduced. Next a new formulation for membrane elements is developed based on the fiber orientation, including orthotropic material behavior and initially out-of-plane prestressed conditions. Also a basic wrinkling algorithm to avoid compression stresses is studied.

Then the rotation-free shell elements are derived, using the fiber orientation to yield a new formulation to study prestressed and orthotropic material behavior of shells. Later a review of some time integration schemes for solids are addressed. The solution strategy used in this work and linearization of the semi-discrete equations of motion is explained. Finally some example problems are presented to validate the finite element implementations in the COMET code.

Chapter 4. This chapter deals with the fluid dynamic equations that solve the incompressible flow problem. Next the governing equations which yield the weak form and the finite element discretization for fluids are explained. Later a review of some time integration schemes for fluids are studied. Two different pressure segregation methods to solve the incompressible fluid equations problem are presented. Then three stabilization techniques for the incompressible fluid problem are introduced. The solution strategy used in this work to solve the nonlinear algebraic equations is shown. Finally some benchmark problems are solved and compared to validate the finite element implementation in the COMET program.

Chapter 5. In this chapter the coupling strategies for fluid-structure interaction problems are explained. The finite element formulation described in chapter 4 dealing with the incompressible flow problem is extended to account for moving fluid domains by means of the arbitrary Lagrangian-Eulerian formulation. Next the governing equations which yield the weak form of the coupled problem are obtained. Then different partitioned methods to solve the fluid-structure interaction problem are studied. Later two different mesh update techniques are presented. A detailed algorithm for the strong coupling with relaxation used in this work is given. Finally some example problems are presented to validate the finite element implementations in the COMET code.

Chapter 6. Here the conclusions and achievements of this work are presented. This monograph concludes with some suggestions for future research lines to be developed as a direct consequence of this work.

Chapter 2

Continuum Mechanics

This work deals with the study of structures with large deformations interacting with incompressible fluids. As mentioned in Batchelor (2000), the distinction between solids and fluids is not a sharp one. While a solid has a definite shape which changes are small when there is a small change in the external conditions, a fluid does not have a preferred shape and the relative positions of their elements change by an amount which is not small even tough the applied forces are small.

The macroscopic behavior of fluids, solids and structures is given by models emerged from the mechanics of a continuous medium. In this chapter a summary of the continuum mechanics *used in this work* for fluid-structure interaction problems is presented. A general and more detailed description of continuum mechanics can be found in Malvern (1969), Gurtin (1981), Holzapfel (2000), Batchelor (2000), Kundu and Cohen (2002), and Spencer (1980) among many other well known books.

This chapter begins with the kinematics that involved motion of a body. Next the concepts of stress and strain related to nonlinear solid mechanics and fluids are described. Then the conservation equations, also known as balance equations, are presented. Finally the constitutive and Navier-Stokes equations are given.

2.1 Kinematics

Kinematics is the study of motion and deformation of a body without regard to the forces responsible for such action. A body $\mathcal{B}$ can be imagined as a composition of a set of particles which are called *material points*. This body is in an initial state when time $t = 0$ as shown in Fig. 2.1. The domain of the body in this state is denoted by Ω_0 which occupies a region in space and is known as the *initial configuration*. To describe the kinematics of a body another configuration is needed where equations are referred to and is called the *reference configuration*. Most of the times the initial configuration is used as the referenced configuration, unless we specify otherwise.

Now we assume that the domain Ω_0 moves to a new region Ω which is occupied by the body $\mathcal{B}$ for any subsecuent time $t > 0$. At this time the configuration of the

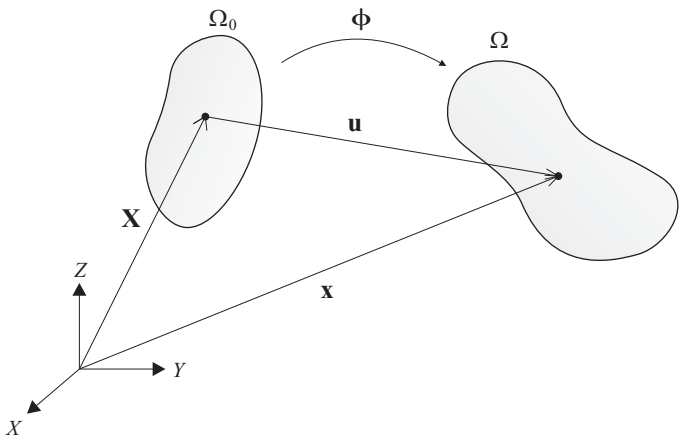

Figure 2.1 *Configurations of a body*

body is called the *current configuration*, also known as the *deformed configuration*. The boundary of the domain, in this case for the current configuration, is denoted by Γ. The dimension of any model is denoted by n_{dime} denoting the number of space dimensions of the body $\mathcal{B}$.

The position vector of a material point in the reference configuration is defined by $\mathbf{X}$, where

$$\mathbf{X} = X_i \mathbf{e}_i = \sum_{i=1}^{n_{\text{dime}}} X_i \mathbf{e}_i \tag{2.1.1}$$

where X_i are the components of $\mathbf{X}$ in the reference configuration and $\mathbf{e}_i$ are the unit base vectors for a rectangular Cartesian coordinate system. The variable vectors $\mathbf{X}$ are called *material coordinates* or *Lagrangian coordinates*. The *motion* of the body $\mathcal{B}$ is given by

$$\mathbf{x} = \boldsymbol{\phi}(\mathbf{X}, t) = \mathbf{x}(\mathbf{X}, t) \tag{2.1.2}$$

where

$$\mathbf{x} = x_i \mathbf{e}_i = \sum_{i=1}^{n_{\text{dime}}} x_i \mathbf{e}_i \tag{2.1.3}$$

is the position of the material point $\mathbf{X}$ in the current configuration. The variable vectors $\mathbf{x}$ are called *spatial coordinates* or *Eulerian coordinates*, and the function $\boldsymbol{\phi}(\mathbf{X}, t)$ is a mapping of the reference configuration onto the current configuration.

When describing the kinematics of a continuum two approaches can be used. First, if we take material coordinates X_i and time t as the independent variables, the description is called *material description* or *Lagrangian description*. On the other hand, if the independent variables are the spatial coordinates x_i and time

t, we are taking about a *spatial description* or *Eulerian description*. In general solid mechanics use Lagrangian descriptions while fluid mechanics use Eulerian descriptions.

The difference for a material point between its current and reference configuration gives the *displacement* which in material description is

$$\mathbf{u}(\mathbf{X},t) = \mathbf{x} - \mathbf{X} \tag{2.1.4}$$

Using Eq. (2.1.1) and Eq. (2.1.2) into Eq. (2.1.4) yields

$$\mathbf{u}(\mathbf{X},t) = \boldsymbol{\phi}(\mathbf{X},t) - \boldsymbol{\phi}(\mathbf{X},0) = \boldsymbol{\phi}(\mathbf{X},t) - \mathbf{X} \tag{2.1.5}$$

since for $t = 0$, $\mathbf{x} = \boldsymbol{\phi}(\mathbf{X},0) = \mathbf{X}$ which means that at reference configuration $\mathbf{x} = \mathbf{X}$. Given $(\mathbf{x},t)$ as the independent variables, the inverse mapping of the motion is defined as

$$\mathbf{X} = \boldsymbol{\phi}^{-1}(\mathbf{x},t) = \mathbf{X}(\mathbf{x},t) \tag{2.1.6}$$

meaning that the material point $\mathbf{X}$ is associated with the place $\mathbf{x}$ at time t. For a material point the *velocity* is the rate of change, or derivative, of the position vector. When $\mathbf{X}$ is held constant then the derivative is called *material time derivative* or *total time derivative*. Using Eq. (2.1.2) and Eq. (2.1.5) the material velocity is given by

$$\mathbf{v}(\mathbf{X},t) = \frac{\partial \mathbf{x}(\mathbf{X},t)}{\partial t} = \frac{\partial \mathbf{u}(\mathbf{X},t)}{\partial t} = \dot{\mathbf{u}}(\mathbf{X},t) \tag{2.1.7}$$

The material *acceleration* is the rate of change of the velocity, or the material time derivative of the velocity expressed by

$$\mathbf{a}(\mathbf{X},t) = \frac{\partial \mathbf{v}(\mathbf{X},t)}{\partial t} = \dot{\mathbf{v}}(\mathbf{X},t) = \ddot{\mathbf{u}}(\mathbf{X},t) \tag{2.1.8}$$

For expressions given in spatial description, i.e. the velocity $\mathbf{v}(\mathbf{x},t) = \mathbf{v}(\mathbf{x}(\mathbf{X},t),t)$ where we use Eq. (2.1.2), its material time derivative can be found using

$$\frac{Dv_i(\mathbf{x},t)}{Dt} = \frac{\partial v_i(\mathbf{x},t)}{\partial t} + \frac{\partial v_i(\mathbf{x},t)}{\partial x_j} \cdot \frac{\partial x_j(\mathbf{X},t)}{\partial t} = \frac{\partial v_i}{\partial t} + \frac{\partial v_i}{\partial x_j} v_j \tag{2.1.9}$$

where $\partial v_i(\mathbf{x},t)/\partial t$ is the *spatial time derivative* and the second term in the right hand side is the *convective* term, where $\partial v_i/\partial x_j$ is the *right gradient* of the velocity vector field with respect to the spatial coordinates, which in indicial form is $v_{i,j}$ or in tensor notation is $\mathbf{v}\nabla$. Using the inverse mapping of the motion, Eq. (2.1.6) to express the velocity in spatial description, Eq. (2.1.9) can be written as

$$\frac{D\mathbf{v}(\mathbf{x},t)}{Dt} = \frac{\partial \mathbf{v}(\mathbf{x},t)}{\partial t} + \mathbf{v}(\mathbf{x},t) \cdot \nabla \mathbf{v}(\mathbf{x},t) \tag{2.1.10}$$

where $\nabla\mathbf{v}$ is the *left gradient* of the velocity vector field with respect to the spatial coordinates, which in indicial form is $\partial_j v_i$. It is important to see that

$$\frac{D\mathbf{v}(\mathbf{x},t)}{Dt} = \frac{\partial \mathbf{v}(\mathbf{X},t)}{\partial t} \tag{2.1.11}$$

In general the material time derivative of any function, vector or tensor given in spatial variables $\mathbf{x}$ and time t can be obtained with

$$\frac{D(\bullet)}{Dt} = \frac{\partial(\bullet)}{\partial t} + \mathbf{v} \cdot \nabla(\bullet) \tag{2.1.12}$$

When a continuum body moves from the reference configuration Ω_0 to the current configuration Ω, it changes its size and shape giving a *deformation*. A primary measure of deformation in nonlinear mechanics is the material *deformation gradient* tensor given by

$$\mathbf{F} = \frac{\partial \mathbf{x}}{\partial \mathbf{X}} \qquad \text{or} \qquad F_{ij} = \frac{\partial \phi_i}{\partial X_j} = \frac{\partial x_i}{\partial X_j} \tag{2.1.13}$$

which relates a quantity in the reference configuration to its corresponding quantity in the current configuration. For example consider an infinitesimal line segment $d\mathbf{X}$ in the reference configuration, then using Eq. (2.1.13) the resulting line segment $d\mathbf{x}$ in the current configuration is

$$d\mathbf{x} = \mathbf{F} \cdot d\mathbf{X} \qquad \text{or} \qquad dx_i = F_{ij} dX_j \tag{2.1.14}$$

The deformation gradient $\mathbf{F}$ is also known as the *Jacobian matrix*. Another important quantity related to $\mathbf{F}$ is the *Jacobian determinant* given by

$$J = \det(\mathbf{F}) \tag{2.1.15}$$

The Jacobian determinant is useful to relate integrals in the reference configuration to its counterpart in the current configuration.

Using $\mathbf{x}$ from Eq. (2.1.4) in Eq. (2.1.13), the deformation gradient tensor can be expressed by

$$F_{ij} = \frac{\partial u_i}{\partial X_j} + \frac{\partial X_i}{\partial X_j} = \frac{\partial u_i}{\partial X_j} + \delta_{ij} \tag{2.1.16}$$

where $\partial u_i / \partial X_j$ is the material *displacement gradient* tensor and δ_{ij} is the Kronecker delta which values are

$$\delta_{ij} = \begin{cases} 1 & \text{when } i = j \\ 0 & \text{otherwise} \end{cases} \tag{2.1.17}$$

2.2 Strain Measures

In the behavior of materials, the strain measures the geometrical deformation caused by the forces applied on a continuum body $\mathcal{B}$. The strain is computed as the change between the undeformed initial configuration of the body and its

final deformed configuration. Therefore, the strain expresses itself the motion and deformation of a body.

There are many kinematic measures of strain in continuum mechanics. For Lagrangian descriptions the most essential strain is the *Green-Lagrange strain* tensor defined by

$$\mathbf{E} = \frac{1}{2}\left(\mathbf{F}^T \cdot \mathbf{F} - \mathbf{I}\right) \qquad \text{or} \qquad E_{ij} = \frac{1}{2}\left(F_{ik}^T F_{kj} - \delta_{ij}\right) \tag{2.2.1}$$

which also can be expressed as a function of the displacement gradient tensor yielding

$$E_{ij} = \frac{1}{2}\left(\frac{\partial u_i}{\partial X_j} + \frac{\partial u_j}{\partial X_i} + \frac{\partial u_k}{\partial X_i}\frac{\partial u_k}{\partial X_j}\right) \tag{2.2.2}$$

For linear strain problems, the *infinitesimal strain tensor* can be found from Eq. (2.2.2) by neglecting the nonlinear terms giving

$$\varepsilon_{ij} = \frac{1}{2}\left(\frac{\partial u_i}{\partial X_j} + \frac{\partial u_j}{\partial X_i}\right) \tag{2.2.3}$$

Now we define the spatial *velocity gradient* tensor by

$$\mathbf{l} = \frac{\partial \mathbf{v}}{\partial \mathbf{x}} \qquad \text{or} \qquad l_{ij} = \frac{\partial v_i}{\partial x_j} \tag{2.2.4}$$

which can be decomposed into its symmetric and skew-symmetric parts using

$$\mathbf{l} = \frac{1}{2}\left(\mathbf{l} + \mathbf{l}^T\right) + \frac{1}{2}\left(\mathbf{l} - \mathbf{l}^T\right) \tag{2.2.5}$$

where the spatial *rate of deformation* tensor $\mathbf{d}$, also known as the *velocity strain* tensor or *strain rate* tensor is given by the symmetric part of the velocity gradient according to

$$\mathbf{d} = \frac{1}{2}\left(\mathbf{l} + \mathbf{l}^T\right) \qquad \text{or} \qquad d_{ij} = \frac{1}{2}\left(\frac{\partial v_i}{\partial x_j} + \frac{\partial v_j}{\partial x_i}\right) \tag{2.2.6}$$

The spatial *rate of rotation* tensor $\mathbf{w}$, also known as the *spin* tensor is given by the skew-symmetric part of $\mathbf{l}$ yielding

$$\mathbf{w} = \frac{1}{2}\left(\mathbf{l} - \mathbf{l}^T\right) \qquad \text{or} \qquad w_{ij} = \frac{1}{2}\left(\frac{\partial v_i}{\partial x_j} - \frac{\partial v_j}{\partial x_i}\right) \tag{2.2.7}$$

Taking the material time derivative of the deformation gradient tensor, Eq. (2.1.13), gives

$$\dot{\mathbf{F}} = \frac{\partial \mathbf{v}}{\partial \mathbf{X}} \qquad \text{or} \qquad \dot{F}_{ij} = \frac{\partial v_i}{\partial X_j} \tag{2.2.8}$$

and now Eq. (2.2.4) can be written as

$$\mathbf{l} = \dot{\mathbf{F}} \cdot \mathbf{F}^{-1} \qquad \text{or} \qquad l_{ij} = \dot{F}_{ik} F_{kj}^{-1} \tag{2.2.9}$$

where we use the spatial *deformation gradient* tensor

$$\mathbf{F}^{-1} = \frac{\partial \mathbf{X}}{\partial \mathbf{x}} \qquad \text{or} \qquad F^{-1}_{kj} = \frac{\partial X_k}{\partial x_j} \tag{2.2.10}$$

If we take the material time derivative of the Green-Lagrange strain tensor, Eq. (2.2.1), we get

$$\dot{\mathbf{E}} = \frac{1}{2}\left(\mathbf{F}^T \cdot \dot{\mathbf{F}} + \dot{\mathbf{F}}^T \cdot \mathbf{F}\right) = \mathbf{F}^T \cdot \mathbf{d} \cdot \mathbf{F} \tag{2.2.11}$$

2.3 Stress Measures

The motion and deformation of a continuum body $\mathcal{B}$ gives rise to *forces* emerging from interactions between interior parts of the body or between the body and its environment. Physically, the stress measures a force per unit area within a body. Let P be a point on the boundary Γ of the body, $\mathbf{n}$ the outward *normal* unit vector for P and $d\Gamma$ the part of the surface on the body where P is contained. Then $d\mathbf{f}_s$ is the *surface force* acting at P that depends of $\mathbf{n}$ and $d\Gamma$. Henceforth the *surface traction* $\mathbf{t}$ at point P on the surface with normal $\mathbf{n}$ is defined by

$$\mathbf{t} = \mathbf{t}(\mathbf{n}) = \lim_{d\Gamma \to 0} \frac{d\mathbf{f}_s}{d\Gamma} \tag{2.3.1}$$

where $\mathbf{t}$ does not necessarily coincide in direction with $\mathbf{n}$. It is important to see that the surface traction has units of force per unit area. There exists a spatial tensor field $\boldsymbol{\sigma}$ called the *Cauchy stress* tensor such that for each unit vector $\mathbf{n}$

$$\mathbf{t} = \mathbf{n} \cdot \boldsymbol{\sigma} = \boldsymbol{\sigma}^T \cdot \mathbf{n} \qquad \text{or} \qquad t_i = \sigma_{ji} n_j \tag{2.3.2}$$

which is also known as the *Cauchy's theorem*. Since the Cauchy stress tensor involves the normal to the current surface and the traction on the current surface too, this tensor is also known as the *true physical* stress tensor and has the property that is symmetric, see section **2.4.2**. In the reference configuration the counterpart of Eq. (2.3.2) is

$$\mathbf{t}_0 = \mathbf{n}_0 \cdot \mathbf{P} \qquad \text{or} \qquad t^0_i = P_{ji} n^0_j \tag{2.3.3}$$

where $\mathbf{P}$ is the *nominal* stress tensor and $\mathbf{t}_0$ and $\mathbf{n}_0$ is the traction force and unit normal respectively in the reference configuration. Unlike the Cauchy stress tensor, the nominal stress tensor is not symmetric and is important to see that the normal is to the left. The transpose of the nominal stress tensor is the *first Piola-Kirchhoff* stress tensor. The *second Piola-Kirchhoff* stress tensor $\mathbf{S}$ is defined by

$$\mathbf{F}^{-1} \cdot \mathbf{t}_0 = \mathbf{n}_0 \cdot \mathbf{S} \tag{2.3.4}$$

where the transformation of the forces by $\mathbf{F}^{-1}$ makes it a symmetric tensor. The transformation between these stresses is given by

$$\boldsymbol{\sigma} = J^{-1}\mathbf{F} \cdot \mathbf{P} = J^{-1}\mathbf{F} \cdot \mathbf{S} \cdot \mathbf{F}^T \tag{2.3.5}$$

$$\mathbf{P} = J\mathbf{F}^{-1} \cdot \boldsymbol{\sigma} = \mathbf{S} \cdot \mathbf{F}^{T} \tag{2.3.6}$$

$$\mathbf{S} = J\mathbf{F}^{-1} \cdot \boldsymbol{\sigma} \cdot \mathbf{F}^{-T} = \mathbf{P} \cdot \mathbf{F}^{-T} \tag{2.3.7}$$

2.4 Conservation Equations

The *conservation equations* reflect some physical quantity for a continuum medium which always must be satisfied and that are not restricted in their application to any material. Applying the conservation equations to the domain Ω of a body $\mathcal{B}$ leads to an integral relation. Since the integral relation must hold for any subdomain of the body, then the conservation equations can be expressed as *partial differential equations*.

Before continuing with the conservation equations, the material time derivative of an integral relation for any spatial property is defined by

$$\frac{D}{Dt}\int_{\Omega}(\bullet) = \int_{\Omega}\left(\frac{D(\bullet)}{Dt} + (\bullet)\nabla\cdot\mathbf{v}\right)d\Omega \tag{2.4.1}$$

which is the Reynold's transport theorem. The *divergence* $\nabla\cdot(\bullet)$ taken respect to current coordinates can also be expressed as $\mathrm{div}(\mathbf{v})$ or in indicial form $v_{i,i}$.

2.4.1 Mass Conservation

Consider the domain Ω of a body $\mathcal{B}$ bounded by the surface Γ which is filled with a constant material *density* $\rho(\mathbf{X}, t)$. Then the *mass* of the body is given by

$$m = \int_{\Omega}\rho(\mathbf{X},t)d\Omega = \int_{\Omega_0}\rho(\mathbf{X},t)Jd\Omega_0 = \int_{\Omega_0}\rho_0(\mathbf{X})d\Omega_0 \tag{2.4.2}$$

where we use Eq. (2.1.15) to relate integrals in the reference and current configurations. *Mass conservation* requires that the mass of any material domain be constant. Consequently the material time derivative of the mass must be zero, giving

$$\frac{Dm}{Dt} = \frac{D}{Dt}\int_{\Omega}\rho d\Omega = 0 \tag{2.4.3}$$

which leads to the following integral relation using Eq. (2.4.1)

$$\frac{Dm}{Dt} = \int_{\Omega}\left(\frac{D\rho}{Dt} + \rho\nabla\cdot\mathbf{v}\right)d\Omega = 0 \tag{2.4.4}$$

where the quantities used are expressed in spatial coordinates. Since the above holds for any subdomain Ω, the mass conservation yields the following first-order partial differential equation

$$\frac{D\rho}{Dt} + \rho\nabla\cdot\mathbf{v} = 0 \qquad \text{or} \qquad \dot{\rho} + \rho v_{i,i} = 0 \tag{2.4.5}$$

The above equation is also known as the *continuity equation*. Using the definition of material time derivative Eq. (2.1.12) in first term of Eq. (2.4.5), the continuity equation can be written as

$$\frac{\partial \rho}{\partial t} + (\rho v_i)_{,i} = 0 \tag{2.4.6}$$

which is known as the *conservative form* of the mass conservation equation. When a material is said to be *incompressible*, the density keeps constant in time so that its material time derivative vanishes and the continuity equation becomes

$$\nabla \cdot \mathbf{v} = 0 \qquad \text{or} \qquad v_{i,i} = 0 \tag{2.4.7}$$

This is the continuity equation used in this work for fluid problems which always are considered as incompressible.

For Lagrangian descriptions, the mass conservation equation Eq. (2.4.3) can be integrated in time to obtain an algebraic equation for the density in the form of Eq. (2.4.2) yielding

$$\rho(\mathbf{X}, t)J = \rho_0(\mathbf{X}) \tag{2.4.8}$$

which is the Lagrangian description for the mass conservation equation.

2.4.2 Conservation of Linear and Angular Momentum

The *conservation of linear momentum* states that the rate of change of its linear momentum is equal to the total force applied to it. The conservation of linear momentum is also known as the *balance of momentum* principle or simply the *momentum conservation* principle. If we consider an arbitrary domain Ω with boundary Γ in the current configuration subjected to *body forces* $\rho\mathbf{b}$ and surface tractions $\mathbf{t}$, where $\mathbf{b}$ is a force per unit mass, then the total force $\mathbf{f}$ is given by

$$\mathbf{f}(t) = \int_\Omega \rho\mathbf{b}(\mathbf{x}, t)d\Omega + \int_\Gamma \mathbf{t}(\mathbf{x}, t)d\Gamma \tag{2.4.9}$$

The linear momentum is given by the product of the density ρ and the velocity $\mathbf{v}$ over the domain Ω in the form

$$\mathbf{p}(t) = \int_\Omega \rho\mathbf{v}(\mathbf{x}, t)d\Omega \tag{2.4.10}$$

Hence the conservation of linear momentum is expressed by

$$\frac{D}{Dt}\int_\Omega \rho\mathbf{v}(\mathbf{x}, t)d\Omega = \int_\Omega \rho\mathbf{b}(\mathbf{x}, t)d\Omega + \int_\Gamma \mathbf{t}(\mathbf{x}, t)d\Gamma \tag{2.4.11}$$

Using Eq. (2.4.1) and Eq. (2.4.5) in Eq. (2.4.11), the rate of change of the linear momentum is found to be

$$\frac{D}{Dt}\int_\Omega \rho\mathbf{v}(\mathbf{x}, t)d\Omega = \int_\Omega \rho\frac{D\mathbf{v}(\mathbf{x}, t)}{Dt}d\Omega \tag{2.4.12}$$

The boundary integral in Eq. (2.4.11) can be transformed to a domain integral using Eq. (2.3.2) and Gauss' divergence theorem yielding

$$\int_{\Gamma} \mathbf{t}(\mathbf{x},t)d\Gamma = \int_{\Omega} \nabla \cdot \boldsymbol{\sigma}(\mathbf{x},t)d\Omega \tag{2.4.13}$$

Substituting Eq. (2.4.12) and (2.4.13) into (2.4.11) gives

$$\int_{\Omega} \left(\rho \frac{D\mathbf{v}}{Dt} - \rho\mathbf{b} - \nabla \cdot \boldsymbol{\sigma} \right) d\Omega = 0 \tag{2.4.14}$$

and since it holds for any arbitrary domain we find

$$\rho \frac{D\mathbf{v}}{Dt} = \nabla \cdot \boldsymbol{\sigma} + \rho\mathbf{b} \qquad \text{or} \qquad \rho \frac{Dv_i}{Dt} = \frac{\partial \sigma_{ij}}{\partial x_j} + \rho b_i \tag{2.4.15}$$

This is called the *momentum equation*. In an Eulerian description for the momentum equation, the material time derivative of the velocity in Eq. (2.4.15) is developed using Eq. (2.1.12) yielding

$$\rho \left(\frac{\partial \mathbf{v}}{\partial t} + \mathbf{v} \cdot \nabla \mathbf{v} \right) = \nabla \cdot \boldsymbol{\sigma} + \rho\mathbf{b} \qquad \text{or} \qquad \rho \left(\frac{\partial v_i}{\partial t} + v_j \partial_j v_i \right) = \frac{\partial \sigma_{ij}}{\partial x_j} + \rho b_i \tag{2.4.16}$$

where all the quantities are given is spatial coordinates. In this work, Eq. (2.4.16) is the one to be used in the fluid mechanics problem. For fluid finite elements this equation is called *Eulerian formulation*.

The momentum equation Eq. (2.4.15) can also be written in a Lagrangian description where all the quantities are expressed in material coordinates, giving

$$\rho \frac{\partial \mathbf{v}}{\partial t} = \nabla \cdot \boldsymbol{\sigma} + \rho\mathbf{b} \qquad \text{or} \qquad \rho \frac{\partial v_i}{\partial t} = \frac{\partial \sigma_{ij}}{\partial x_j} + \rho b_i \tag{2.4.17}$$

Since Eq. (2.4.15) is in the current configuration, the divergence term is taken respect to spatial coordinates and therefore $\boldsymbol{\sigma}(\mathbf{X},t)$ is expressed by $\boldsymbol{\sigma}\left(\boldsymbol{\phi}^{-1}(\mathbf{x},t),t\right)$ so that the spatial gradient of the stress field can be evaluated. For nonlinear solid finite elements, Eq. (2.4.17) is called *updated Lagrangian formulation*.

The *conservation of angular momentum* is obtained by taking the cross product of the current vector position $\mathbf{x}$ by each term of the linear momentum equation Eq. (2.4.11), yielding

$$\frac{D}{Dt} \int_{\Omega} \mathbf{x} \times \rho\mathbf{v}(\mathbf{x},t)d\Omega = \int_{\Omega} \mathbf{x} \times \rho\mathbf{b}(\mathbf{x},t)d\Omega + \int_{\Gamma} \mathbf{x} \times \mathbf{t}(\mathbf{x},t)d\Gamma \tag{2.4.18}$$

where it can be shown that leads to the following result

$$\boldsymbol{\sigma} = \boldsymbol{\sigma}^T \tag{2.4.19}$$

The acceleration term in Eq. (2.4.15) can be neglected when the loads are applied slowly so that the inertial forces become insignificant. Then we can write

$$\nabla \cdot \boldsymbol{\sigma} + \rho \mathbf{b} = 0 \qquad \text{or} \qquad \frac{\partial \sigma_{ij}}{\partial x_j} + \rho b_i = 0 \tag{2.4.20}$$

which is known as the *equilibrium equation*. Problems that use Eq. (2.4.20) are called *static problems*.

The conservation of linear momentum can also be expressed in the reference configuration. Consider an arbitrary domain Ω_0 with boundary Γ_0 in the reference configuration subjected to body forces $\rho_0 \mathbf{b}$ and surface tractions $\mathbf{t}_0$, then the total force $\mathbf{f}$ is given by

$$\mathbf{f}(t) = \int_{\Omega_0} \rho_0 \mathbf{b}(\mathbf{X}, t) d\Omega_0 + \int_{\Gamma_0} \mathbf{t}_0(\mathbf{X}, t) d\Gamma_0 \tag{2.4.21}$$

The linear momentum is given by

$$\mathbf{p}(t) = \int_{\Omega_0} \rho_0 \mathbf{v}(\mathbf{X}, t) d\Omega_0 \tag{2.4.22}$$

Hence the conservation of linear momentum is expressed by

$$\frac{d}{dt} \int_{\Omega_0} \rho_0 \mathbf{v}(\mathbf{X}, t) d\Omega_0 = \int_{\Omega_0} \rho_0 \mathbf{b}(\mathbf{X}, t) d\Omega_0 + \int_{\Gamma_0} \mathbf{t}_0(\mathbf{X}, t) d\Gamma_0 \tag{2.4.23}$$

The boundary integral in Eq. (2.4.23) can be transformed to a domain integral using Eq. (2.3.3) and Gauss' divergence theorem yielding

$$\int_{\Gamma_0} \mathbf{t}_0(\mathbf{X}, t) d\Gamma_0 = \int_{\Omega_0} \nabla_0 \cdot \mathbf{P}(\mathbf{X}, t) d\Omega_0 \tag{2.4.24}$$

where $\nabla_0 \cdot (\bullet)$ is the divergence taken respect to material coordinates. Leaving the derivation of the conditions which follow from Eq. (2.4.23), the conservation of linear momentum in reference configuration for Lagrangian coordinates is

$$\rho_0 \frac{\partial \mathbf{v}}{\partial t} = \nabla_0 \cdot \mathbf{P} + \rho_0 \mathbf{b} \qquad \text{or} \qquad \rho_0 \frac{\partial v_i}{\partial t} = \frac{\partial P_{ji}}{\partial X_j} + \rho_0 b_i \tag{2.4.25}$$

This is called the Lagrangian form of the momentum equation. For nonlinear solid finite elements, Eq. (2.4.25) is called *total Lagrangian formulation*. The corresponding equilibrium equation for this description is

$$\nabla_0 \cdot \mathbf{P} + \rho_0 \mathbf{b} = 0 \qquad \text{or} \qquad \frac{\partial P_{ji}}{\partial X_j} + \rho_0 b_i = 0 \tag{2.4.26}$$

As a consequence of the conservation of angular momentum Eq. (2.4.18) and Eq. (2.4.19) the nominal stress tensor yields

$$\mathbf{F} \cdot \mathbf{P} = \mathbf{P}^T \cdot \mathbf{F}^T \tag{2.4.27}$$

which is in general not symmetric. The number of conditions imposed by angular momentum conservation are usually imposed directly on the constitutive equation.

Using Eq. (2.3.6) in Eq. (2.4.27) we obtain that for the second Piola-Kirchhoff stress

$$\mathbf{S} = \mathbf{S}^T \tag{2.4.28}$$

is a symmetric tensor.

2.4.3 Conservation of Energy

The *kinetic energy* of a material is given by

$$\mathcal{E}^{\text{kin}} = \int_\Omega \frac{1}{2}\rho \mathbf{v}\cdot\mathbf{v} d\Omega \tag{2.4.29}$$

which for a continuum body $\mathcal{B}$ is only part of the total energy. The remainder energy is called the *internal energy* that is expressed by w^{int} per unit mass. The internal energy per unit volume is denoted by

$$\mathcal{E}^{\text{int}} = \int_\Omega \rho w^{\text{int}} d\Omega \tag{2.4.30}$$

The total energy is then expressed by $\mathcal{E}^{\text{tot}} = \mathcal{E}^{\text{int}} + \mathcal{E}^{\text{kin}}$. Then the *conservation of energy* requires that the power of the total energy equals the power of the applied forces plus the power at which *other energy* enters in the domain. The other energy may take different forms, but the most important is the energy due to heat sources and heat flux across $\mathcal{B}$. Other energy sources arise from radiation, chemical changes, electromagnetic fields, etc. We consider thermomechanical processes only.

The power of the total energy is given by

$$\mathcal{P}^{\text{tot}} = \mathcal{P}^{\text{int}} + \mathcal{P}^{\text{kin}} = \frac{D}{Dt}\int_\Omega \rho w^{\text{int}} d\Omega + \frac{D}{Dt}\int_\Omega \frac{1}{2}\rho \mathbf{v}\cdot\mathbf{v} d\Omega \tag{2.4.31}$$

while the power of the applied forces is expressed by

$$\mathcal{P}^{\text{ext}} = \int_\Omega \mathbf{v}\cdot\rho\mathbf{b} d\Omega + \int_\Gamma \mathbf{v}\cdot\mathbf{t} d\Gamma \tag{2.4.32}$$

The power supplied by heat sources s and the heat flux $\mathbf{q}$ is

$$\mathcal{P}^{\text{heat}} = \int_\Omega \rho s d\Omega - \int_\Gamma \mathbf{n}\cdot\mathbf{q} d\Gamma \tag{2.4.33}$$

The conservation of energy states that

$$\mathcal{P}^{\text{tot}} = \mathcal{P}^{\text{ext}} + \mathcal{P}^{\text{heat}} \tag{2.4.34}$$

which is known as the *first law of thermodynamics*. Replacing Eqs. (2.4.31)-(2.4.33) into Eq. (2.4.34) yields the equation of conservation of energy

$$\frac{D}{Dt}\int_{\Omega}\rho w^{\text{int}}d\Omega+\frac{D}{Dt}\int_{\Omega}\frac{1}{2}\rho\mathbf{v}\cdot\mathbf{v}d\Omega=\int_{\Omega}\mathbf{v}\cdot\rho\mathbf{b}d\Omega+\int_{\Gamma}\mathbf{v}\cdot\mathbf{t}d\Gamma+\int_{\Omega}\rho s d\Omega-\int_{\Gamma}\mathbf{n}\cdot\mathbf{q}d\Gamma \tag{2.4.35}$$

The equation which emerges from the above integral form leads to the following Eulerian partial differential equation of energy conservation

$$\rho\frac{Dw^{\text{int}}}{Dt}=\boldsymbol{\sigma}:\mathbf{d}-\nabla\cdot\mathbf{q}+\rho s \tag{2.4.36}$$

For a purely mechanical process, the above equation becomes

$$\rho\frac{Dw^{\text{int}}}{Dt}=\boldsymbol{\sigma}:\mathbf{d} \tag{2.4.37}$$

which is no longer a partial differential equation. As a consequence of Eq. (2.4.37) we can say that the Cauchy stress tensor $\boldsymbol{\sigma}$ and the rate of deformation tensor $\mathbf{d}$ are *conjugate in power*.

The conservation of energy can also be expressed in Lagrangian coordinates and in the reference configuration, where the counterpart of Eq. (2.4.35) gives

$$\frac{d}{dt}\int_{\Omega_0}\left(\rho_0 w^{\text{int}}+\frac{1}{2}\rho_0\mathbf{v}\cdot\mathbf{v}\right)d\Omega_0=\int_{\Omega_0}\mathbf{v}\cdot\rho_0\mathbf{b}d\Omega_0+\int_{\Gamma_0}\mathbf{v}\cdot\mathbf{t}_0 d\Gamma_0+\int_{\Omega_0}\rho_0 s d\Omega_0-\int_{\Gamma_0}\mathbf{n}_0\cdot\mathbf{q}d\Gamma_0 \tag{2.4.38}$$

which gives the Lagrangian partial differential equation of energy conservation

$$\rho_0\dot{w}^{int}=\mathbf{P}:\dot{\mathbf{F}}^{T}-\nabla_0\cdot\mathbf{q}+\rho_0 s \tag{2.4.39}$$

For a purely mechanical process, the Lagrangian energy conservation is

$$\rho_0\dot{w}^{int}=\mathbf{P}:\dot{\mathbf{F}}^{T} \tag{2.4.40}$$

showing that the nominal stress tensor is conjugate in power to the material time derivative of the deformation gradient tensor. Using Eq. (2.3.6) in Eq. (2.4.40) we obtain the energy conservation equation in terms of the second Piola-Kirchhoff stress tensor

$$\rho_0\dot{w}^{int}=\mathbf{S}:\dot{\mathbf{E}} \tag{2.4.41}$$

which shows that the second Piola-Kirchhoff stress tensor is conjugate in power to the rate of the Green-Lagrange strain tensor.

2.5 Constitutive Equations

The equations given so far are still insufficient to describe the mechanical behavior of any material. Therefore we need additional equations called *constitutive equations* which complete the set of equations specifying the mechanical properties of a material. For a purely mechanical process, the constitutive equation of a material specifies the dependence of the stress tensor in terms of kinematic variables such as the strain tensor.

2.5.1 Linear Elasticity

Engineering materials such as metals or concrete usually undergo very small changes of shape when they are subjected to the forces which they are exposed. They also have an initial shape to which they will return if the forces applied are removed. Since the changes of shape are very small, there is no difference between the reference and current configuration.

The *linear elasticity* theory gives an excellent model for the behavior of such materials. The infinitesimal strain tensor $\boldsymbol{\varepsilon}$ is used to measure strains while the Cauchy stress tensor $\boldsymbol{\sigma}$ measures the stresses. For the linear elasticity theory the energy conservation equation takes the form

$$\rho_0 \dot{w}^{int} = \boldsymbol{\sigma} : \dot{\boldsymbol{\varepsilon}} = \sigma_{ij}\dot{\varepsilon}_{ij} \tag{2.5.1}$$

where $\boldsymbol{\sigma}$ and $\dot{\boldsymbol{\varepsilon}}$ are conjugate in power.

It is conventional to denote the internal energy per unit volume $\rho_0 w^{\text{int}}$ by W^{int} which is called the *strain energy function*. For a linear elastic material the strain energy function depends only of the components ε_{ij} and is a quadratic function of the form

$$W^{\text{int}} = \frac{1}{2}\mathbb{C}_{ijkl}\varepsilon_{ij}\varepsilon_{kl} \qquad \text{or} \qquad W^{\text{int}} = \frac{1}{2}\boldsymbol{\varepsilon} : \mathbb{C} : \boldsymbol{\varepsilon} \tag{2.5.2}$$

where $\mathbb{C}_{ijkl}$ are called *elastic constants*. Since the elastic constants possess symmetry of the form

$$\mathbb{C}_{ijkl} = \mathbb{C}_{jikl} = \mathbb{C}_{ijlk} = \mathbb{C}_{klij} \tag{2.5.3}$$

then for an *isotropic material*, its properties are the same in all directions.

Since W^{int} depends only on ε_{ij}, the material time derivative of Eq. (2.5.2) gives

$$\frac{\partial W^{\text{int}}}{\partial t} = \frac{\partial W^{\text{int}}}{\partial \varepsilon_{ij}}\frac{\partial \varepsilon_{ij}}{\partial t} = \frac{\partial W^{\text{int}}}{\partial \varepsilon_{ij}}\dot{\varepsilon}_{ij} \tag{2.5.4}$$

where the symmetry of the material has been used. Substituting Eq. (2.5.4) into Eq. (2.5.1) gives

$$\sigma_{ij} = \frac{\partial W^{\text{int}}}{\partial \varepsilon_{ij}} \tag{2.5.5}$$

However from Eq. (2.5.2) and Eq. (2.5.3)

$$\frac{\partial W^{\text{int}}}{\partial \varepsilon_{ij}} = \mathbb{C}_{ijkl}\varepsilon_{kl} \tag{2.5.6}$$

Substituting Eq. (2.5.6) into Eq. (2.5.5) yields

$$\sigma_{ij} = \mathbb{C}_{ijkl}\varepsilon_{kl} \qquad \text{or} \qquad \boldsymbol{\sigma} = \mathbb{C} : \boldsymbol{\varepsilon} \tag{2.5.7}$$

which is the constitutive equation that relates stresses and strains. The constitutive equation complete the equations to describe the mechanical behavior of linear elastic materials. For an isotropic material $\mathbb{C}_{ijkl}$ takes the form

$$\mathbb{C}_{ijkl} = \lambda\delta_{ij}\delta_{kl} + \mu\left(\delta_{ik}\delta_{jl} + \delta_{il}\delta_{jk}\right) \qquad \text{or} \qquad \mathbb{C} = \lambda\mathbf{I}\otimes\mathbf{I} + 2\mu\mathbb{I} \tag{2.5.8}$$

where only two constants λ and μ of the original 81 of the fourth-order tensor survived after the restrictions of material isotropy and stress symmetry. The two independent material constants λ and μ are called the *Lamé constants*, $\mathbf{I}$ is the second-order identity tensor and $\mathbb{I}$ is the fourth-order symmetric identity tensor given by $\frac{1}{2}\left(\delta_{ik}\delta_{jl} + \delta_{il}\delta_{jk}\right)$. The constitutive equation Eq. (2.5.7) becomes

$$\sigma_{ij} = \lambda\varepsilon_{kk}\delta_{ij} + 2\mu\varepsilon_{ij} \qquad \text{or} \qquad \boldsymbol{\sigma} = \lambda\text{tr}(\boldsymbol{\varepsilon})\mathbf{I} + 2\mu\boldsymbol{\varepsilon} \tag{2.5.9}$$

where $\text{tr}(\boldsymbol{\varepsilon})$ is the trace of $\boldsymbol{\varepsilon} = \varepsilon_{kk}$.

2.5.2 Nonlinear Elasticity

Engineering applications also involved small strains and large deformations, where these effects arise from large displacements and large rotations of the structure. The response of such materials may be modeled with a *Saint Venant-Kirchhoff* material which is a generalization of the linear theory to large deformations giving the *nonlinear elasticity* theory.

The strain energy function for a nonlinear elastic material is a generalization of Eq. (2.5.2) and is given by

$$W^{\text{int}} = \frac{1}{2}\mathbb{C}_{ijkl}E_{ij}E_{kl} \qquad \text{or} \qquad W^{\text{int}} = \frac{1}{2}\mathbf{E} : \mathbb{C} : \mathbf{E} \tag{2.5.10}$$

where the stress is

$$S_{ij} = \frac{\partial W^{\text{int}}}{\partial E_{ij}} \tag{2.5.11}$$

The counterpart of Eq. (2.5.7) in the nonlinear theory yields

$$S_{ij} = \mathbb{C}_{ijkl}E_{kl} \qquad \text{or} \qquad \mathbf{S} = \mathbb{C} : \mathbf{E} \tag{2.5.12}$$

where $\mathbb{C}_{ijkl}$ is given by Eq. (2.5.8). Finally, the constitutive equation for nonlinear elastic materials is

$$S_{ij} = \lambda E_{kk}\delta_{ij} + 2\mu E_{ij} \qquad \text{or} \qquad \mathbf{S} = \lambda\text{tr}(\mathbf{E})\mathbf{I} + 2\mu\mathbf{E} \tag{2.5.13}$$

The Lamé constants λ and μ can be expressed in terms of other physical measurements given by

$$\mu = \frac{E}{2(1+\upsilon)} \tag{2.5.14}$$

$$\lambda = \frac{\upsilon E}{(1+\upsilon)(1-2\upsilon)} \tag{2.5.15}$$

$$K = \lambda + \frac{2}{3}\mu \tag{2.5.16}$$

where E is the Young's modulus, υ is the Poisson's ratio and K is the bulk modulus.

2.5.3 Newtonian Fluid

An equation that linearly relates the stress tensor to the rate of strain tensor in a fluid medium is called the constitutive equation for *Newtonian fluids*.

In a static fluid there are only normal components of the stress tensor on a boundary, so the stress tensor for a fluid at rest is isotropic and takes the form

$$\sigma_{ij} = -p\delta_{ij} \tag{2.5.17}$$

where p is the *thermodynamic pressure* related to the density ρ and the temperature T. A moving fluid develops additional components of stress due to viscosity yielding

$$\sigma_{ij} = -p\delta_{ij} + \sigma_{ij}^{\text{dev}} \tag{2.5.18}$$

where the deviatoric stress tensor σ_{ij}^{dev} is linearly related to the strain rate tensor by

$$\sigma_{ij}^{\text{dev}} = \mathbb{C}_{ijkl} d_{kl} \tag{2.5.19}$$

Substituting Eq. (2.2.6) and Eq. (2.5.8) into Eq. (2.5.19) and this new equation in Eq. (2.5.18), the resulting equation is

$$\sigma_{ij} = -p\delta_{ij} + \lambda d_{kk}\delta_{ij} + 2\mu d_{ij} \tag{2.5.20}$$

where $d_{kk} = \nabla\cdot\mathbf{v}$ is the volumetric strain rate. If the Stokes assumption, $\lambda + \frac{2}{3}\mu = 0$, is used in Eq. (2.5.20) to relate λ and μ the new equation is

$$\sigma_{ij} = -\left(p + \frac{2}{3}\mu\nabla\cdot\mathbf{v}\right)\delta_{ij} + 2\mu d_{ij} \quad \text{or} \quad \boldsymbol{\sigma} = -\left(p + \frac{2}{3}\mu\nabla\cdot\mathbf{v}\right)\mathbf{I} + 2\mu\mathbf{d} \tag{2.5.21}$$

which is the constitutive equation for Newtonian fluids. For incompressible fluids the continuity equation Eq.(2.4.7) is substituted into Eq. (2.5.21) and the constitutive equation for incompressible fluids takes the simple form

$$\sigma_{ij} = -p\delta_{ij} + 2\mu d_{ij} \quad \text{or} \quad \boldsymbol{\sigma} = -p\mathbf{I} + 2\mu\mathbf{d} \tag{2.5.22}$$

where p is the pressure. For incompressible fluids, p is called mechanical pressure.

2.6 Navier-Stokes Equation

The equation of motion for a Newtonian fluid is obtained by substituting the constitutive equation for Newtonian fluids Eq. (2.5.21) into the momentum equation in Eulerian description Eq. (2.4.16) to obtain

$$\rho\left(\frac{\partial v_i}{\partial t}+v_j\partial_j v_i\right)=-\frac{\partial p}{\partial x_i}+\rho b_i+\frac{\partial}{\partial x_j}\left(2\mu d_{ij}-\frac{2}{3}\mu(\nabla\cdot\mathbf{v})\delta_{ij}\right) \tag{2.6.1}$$

Equation (2.6.1) is the general form of the *Navier-Stokes* equation. If μ is taken as a constant, the derivative in the right hand side term can be written as

$$\frac{\partial}{\partial x_j}\left(2\mu d_{ij}-\frac{2}{3}\mu(\nabla\cdot\mathbf{v})\delta_{ij}\right)=\mu\left(\nabla^2 v_i+\frac{1}{3}\frac{\partial}{\partial x_i}(\nabla\cdot\mathbf{v})\right) \tag{2.6.2}$$

where $\nabla^2 v_i$ is the *Laplacian*[1] of v_i. For incompressible fluids the continuity equation Eq.(2.4.7) is substituted into Eq. (2.6.2) and the Navier-Stokes equation reduces to

$$\rho\left(\frac{\partial v_i}{\partial t}+v_j\partial_j v_i\right)=-\frac{\partial p}{\partial x_i}+\rho b_i+\mu\nabla^2 v_i \tag{2.6.3}$$

If viscous effects are negligible, which may occur far from boundaries of the flow field,

$$\rho\left(\frac{\partial v_i}{\partial t}+v_j\partial_j v_i\right)=-\frac{\partial p}{\partial x_i}+\rho b_i \tag{2.6.4}$$

and the *Euler* equation is obtained. Now consider given a characteristic velocity scale v_c and a characteristic length scale l_c, then the Reynolds number is defined as $\mathrm{Re}=\rho v_c l_c/\mu$. When the Reynolds number for the flow is very low, the convective term can be neglected yielding

$$\rho\frac{\partial v_i}{\partial t}+\frac{\partial p}{\partial x_i}-\mu\nabla^2 v_i=\rho b_i \tag{2.6.5}$$

which is known as the Stokes flow. In the literature, it is common to express Eq. (2.6.5) without the inertial term.

[1] $\nabla^2 v_i=\frac{\partial}{\partial x_j}\frac{\partial v_i}{\partial x_j}=\frac{\partial^2 v_i}{\partial x_1^2}+\frac{\partial^2 v_i}{\partial x_2^2}+\frac{\partial^2 v_i}{\partial x_3^2}$

Chapter 3

Structural Dynamics

Structural elements such as membranes and thin shells are widely used in modern technology in many engineering fields. Their elegance, effectiveness and optimal material usage make these light weight structures an ideal construction element for structural and decorative purposes.

This chapter begins with a review of the standard total Lagrangian formulation. Then membrane elements are developed for isotropic and orthotropic material behavior and prestressed fields. Next cable elements are given as a particular case of the membrane theory. Rotation-free shell elements are developed for isotropic and orthotropic materials too. Finally time integration schemes and solution strategies for these structural elements are presented.

3.1 Preliminaries

Before developing membrane and shell elements, the *principle of virtual work* is developed for standard elements of the total Lagrangian formulation. The principle of virtual work emerges as a consequence of the *strong form* of the momentum equation.

3.1.1 Total Lagrangian Weak Form

The strong form consists of the momentum equation, the displacement boundary conditions $\bar{u}_i$ on the Dirichlet boundary Γ^D and the traction boundary conditions $\bar{t}_i$ on the Neumann boundary Γ^N. See for example Hughes (1987), Zienkiewicz and Taylor (1989) and Bathe (1996). In particular for total Lagrangian formulations, the momentum equation used is Eq. (2.4.25). A complete deduction can be found in Bonet and Wood (1997) and Belytschko et al. (2000).

To develop the *weak form*, test function $\delta u_i(\mathbf{X})$ and trial functions $u_i(\mathbf{X}, t)$ are require. The space of the test functions is defined as

$$\delta u_i(\mathbf{X}) \in \mathcal{U}_0, \quad \mathcal{U}_0 = \left\{ \delta u_i | \delta u_i \in C^0(\mathbf{X}), \;\; \delta u_i = 0 \text{ on } \Gamma^D \right\} \tag{3.1.1}$$

where C^0 describes the *continuity of the function* and the boundary Γ_0 is defined by $\Gamma_0 = \Gamma^D \cup \Gamma^N$. In general, a function is C^n if the n^{th} derivative is a continuous function. Eq. (3.1.1) means that for the weak form, the integral over the kinematic boundary is neglected and remains only the integral over the traction boundary. Since the principal of virtual work is to be developed, the space of the trial functions for the displacements is given by

$$u_i(\mathbf{X}, t) \in \mathcal{U}, \quad \mathcal{U} = \left\{ u_i | u_i \in C^0(\mathbf{X}), \;\; u_i = \bar{u}_i \text{ on } \Gamma^D \right\} \tag{3.1.2}$$

Note that the spaces of test and trial functions are similar except that the test displacements vanish wherever the trial displacement are prescribed.

The development of a Galerkin-type weak form consists of taking the product of the momentum equation Eq. (2.4.25) by the test function δu_i and integrating over the reference configuration giving

$$\int_{\Omega_0} \delta u_i \left(\underline{\frac{\partial P_{ji}}{\partial X_j}} + \rho_0 b_i - \rho_0 \ddot{u}_i \right) d\Omega_0 = 0 \tag{3.1.3}$$

This weak form is useless because the space of trial functions for the displacements needs to be C^1. To solve this problem, the underlined term of Eq. (3.1.3) is integrated by parts[1] leading to

$$\int_{\Omega_0} \left(\delta F_{ij} P_{ji} - \delta u_i \rho_0 b_i + \delta u_i \rho_0 \ddot{u}_i \right) d\Omega_0 - \int_{\Gamma_0^N} \delta u_i \bar{t}_i^0 d\Gamma_0 = 0 \tag{3.1.4}$$

which is the weak form of the momentum equation together with the traction boundary conditions $\bar{t}_i$. Note that the spaces of test and trial functions are C^0. Substituting Eq. (2.3.6) into Eq. (3.1.4), the resulting equation takes the form

$$\int_{\Omega_0} \left(\delta F_{ij} S_{jk} F_{ik} - \delta u_i \rho_0 b_i + \delta u_i \rho_0 \ddot{u}_i \right) d\Omega_0 - \int_{\Gamma_0^N} \delta u_i \bar{t}_i^0 d\Gamma_0 = 0 \tag{3.1.5}$$

where the second Piola-Kirchhoff stress tensor has been replaced by the nominal stress tensor. Eq. (3.1.4) and Eq. (3.1.5) are the principle of virtual work which can be written as

$$\delta \mathcal{W}^{\text{int}} - \delta \mathcal{W}^{\text{ext}} + \delta \mathcal{W}^{\text{kin}} = 0 \tag{3.1.6}$$

where

$$\begin{aligned} \delta \mathcal{W}^{\text{int}} &= \int_{\Omega_0} \delta F_{ij} P_{ji} d\Omega_0 = \int_{\Omega_0} \delta F_{ij} S_{jk} F_{ik} d\Omega_0 \quad \text{or} \\ \delta \mathcal{W}^{\text{int}} &= \int_{\Omega_0} \delta \mathbf{F}^T : \mathbf{P} d\Omega_0 = \int_{\Omega_0} \delta \mathbf{F}^T : \mathbf{S} \cdot \mathbf{F}^T d\Omega_0 \end{aligned} \tag{3.1.7}$$

[1] $\int d(\mathbf{uv}) = \int \mathbf{u} d\mathbf{v} + \int \mathbf{v} d\mathbf{u}, \qquad \int \mathbf{u} d\mathbf{v} = \mathbf{uv} - \int \mathbf{v} d\mathbf{u}$

$$\begin{aligned} \delta\mathcal{W}^{\text{ext}} &= \int_{\Omega_0} \delta u_i \rho_0 b_i d\Omega_0 + \int_{\Gamma_0^N} \delta u_i \bar{t}_i^0 d\Gamma_0 \quad \text{or} \\ \delta\mathcal{W}^{\text{ext}} &= \int_{\Omega_0} \rho_0 \delta\mathbf{u}\cdot\mathbf{b} d\Omega_0 + \int_{\Gamma_0^N} \delta\mathbf{u}\cdot\bar{\mathbf{t}}_0 d\Gamma_0 \end{aligned} \tag{3.1.8}$$

$$\delta\mathcal{W}^{\text{kin}} = \int_{\Omega_0} \delta u_i \rho_0 \ddot{u}_i d\Omega_0 \quad \text{or} \quad \delta\mathcal{W}^{\text{kin}} = \int_{\Omega_0} \rho_0 \delta\mathbf{u}\cdot\ddot{\mathbf{u}} d\Omega_0 \tag{3.1.9}$$

are the virtual internal work, the virtual external work and the virtual kinetic work respectively. From the virtual internal work the following identity emerges

$$\begin{aligned} \delta\mathbf{F}^T : \mathbf{P} &= \text{tr}\left(\mathbf{P}\cdot\delta\mathbf{F}\right) = \text{tr}\left(\mathbf{S}\cdot\mathbf{F}^T\cdot\delta\mathbf{F}\right) = \text{tr}\left(\mathbf{F}^T\cdot\delta\mathbf{F}\cdot\mathbf{S}\right) = \\ &= \delta\mathbf{F}^T\cdot\mathbf{F} : \mathbf{S} = \frac{1}{2}\left(\delta\mathbf{F}^T\cdot\mathbf{F} + \mathbf{F}^T\cdot\delta\mathbf{F}\right) : \mathbf{S} = \\ &= \frac{1}{2}\delta\left(\mathbf{F}^T\cdot\mathbf{F} - \mathbf{I}\right) : \mathbf{S} = \delta\mathbf{E} : \mathbf{S} \end{aligned} \tag{3.1.10}$$

and the virtual internal work becomes

$$\delta\mathcal{W}^{\text{int}} = \int_{\Omega_0} \delta E_{ij} S_{ij} d\Omega_0 \quad \text{or} \quad \delta\mathcal{W}^{\text{int}} = \int_{\Omega_0} \delta\mathbf{E} : \mathbf{S} d\Omega_0 \tag{3.1.11}$$

as it was expected from Eq. (2.4.41). Substituting Eq. (3.1.10) into Eq. (3.1.4) yields

$$\int_{\Omega_0} \left(\delta E_{ij} S_{ij} - \delta u_i \rho_0 b_i + \delta u_i \rho_0 \ddot{u}_i\right) d\Omega_0 - \int_{\Gamma_0^N} \delta u_i \bar{t}_i^0 d\Gamma_0 = 0 \tag{3.1.12}$$

which is another form to express the principle of virtual work in the reference configuration.

3.1.2 Finite Element Discretization

In this section the finite element discretization for total Lagrangian formulations is described . It is assumed that the reference domain Ω_0 is discretized by a finite number of elements that conform the finite element mesh. For each finite element of the mesh, the equation of motion is approximated by

$$x_i^h(\mathbf{X}, t) = \sum_{I=1}^{n_{\text{node}}} N_I(\mathbf{X}) x_{iI}(t) \qquad \forall i = 1,\, n_{\text{dime}} \tag{3.1.13}$$

where $N_I(\mathbf{X})$ are the *shape functions* of each node, n_{node} is the number of nodes for the finite element and $x_{iI}(t)$ are the nodal values of the motion at node I with direction i. The displacements are given by

$$u_i^h(\mathbf{X},t) = \sum_{I=1}^{n_{\text{node}}} N_I(\mathbf{X}) u_{iI}(t) \qquad \forall i = 1,\ n_{\text{dime}} \tag{3.1.14}$$

The corresponding velocity and acceleration is

$$\dot{u}_i^h(\mathbf{X},t) = \sum_{I=1}^{n_{\text{node}}} N_I(\mathbf{X}) \dot{u}_{iI}(t) \qquad \forall i = 1,\ n_{\text{dime}} \tag{3.1.15}$$

$$\ddot{u}_i^h(\mathbf{X},t) = \sum_{I=1}^{n_{\text{node}}} N_I(\mathbf{X}) \ddot{u}_{iI}(t) \qquad \forall i = 1,\ n_{\text{dime}} \tag{3.1.16}$$

Substituting Eq. (3.1.13) into Eq. (2.1.13) the material deformation gradient tensor is found to be

$$F_{ij} = x_{iI} B_{jI}^0 \quad \text{or} \quad \mathbf{F} = \mathbf{x} \cdot \mathbf{B}_0^T \tag{3.1.17}$$

where

$$B_{jI}^0 = \frac{\partial N_I}{\partial X_j} \tag{3.1.18}$$

is the *strain-displacement* tensor. The space of the test functions is time independent and its discretization yields

$$\delta u_i^h(\mathbf{X}) = \sum_{I=1}^{n_{\text{node}}} N_I(\mathbf{X}) \delta u_{iI} \qquad \forall i = 1,\ n_{\text{dime}} \tag{3.1.19}$$

Since $\mathbf{X}_I$ is a constant vector, the *variation* of $\mathbf{x}_I$ gives

$$\delta x_{iI} = \delta u_{iI} \tag{3.1.20}$$

Consequently, the variation of the material deformation gradient tensor is

$$\delta F_{ij} = \delta u_{iI} B_{jI}^0 \quad \text{or} \quad \delta \mathbf{F} = \delta \mathbf{u} \cdot \mathbf{B}_0^T \tag{3.1.21}$$

Recalling that work can be obtained by a force multiplied by a distance, the *internal forces* emerge from the virtual internal work, Eq. (3.1.7), as

$$\delta W^{\text{int}} = \delta u_{iI} f_{iI}^{\text{int}} = \int_{\Omega_0} \delta F_{ij} P_{ji} d\Omega_0 = \delta u_{iI} \int_{\Omega_0} B_{jI}^0 P_{ji} d\Omega_0 \tag{3.1.22}$$

Since the variations of the displacements δu_{iI} are arbitrary, the internal forces are expressed by

$$f_{iI}^{\text{int}} = \int_{\Omega_0} B_{jI}^0 P_{ji} d\Omega_0 \quad \text{or} \quad \mathbf{f}^{\text{int}} = \int_{\Omega_0} \mathbf{B}_0^T \cdot \mathbf{P} d\Omega_0 \tag{3.1.23}$$

where the internal forces are given in terms of the nominal stress tensor. Since the nominal stress tensor is not symmetric, it is more convenient to express the internal

forces as a function of the second Piola-Kirchhoff stress tensor $\mathbf{S}$. Substituting Eq. (2.3.6) into Eq. (3.1.23) yields

$$f_{iI}^{\text{int}} = \int_{\Omega_0} B_{jI}^0 S_{jk} F_{ik} d\Omega_0 = \int_{\Omega_0} B_{jI}^0 F_{ik} S_{jk} d\Omega_0 \tag{3.1.24}$$

where the second Piola-Kirchhoff stress tensor $\mathbf{S}$ is a symmetric tensor in (j,k) and defining the strain-displacement tensor $\mathbf{B}$ as

$$B_{ijkI} = sym_{(j,k)} \left(B_{jI}^0 F_{ik} \right) \tag{3.1.25}$$

the internal forces are expressed by

$$f_{iI}^{\text{int}} = \int_{\Omega_0} B_{ijkI} S_{jk} d\Omega_0 \tag{3.1.26}$$

At this point, it is convenient to use the Voigt notation to express Eq. (3.1.26) in the form

$$f_a^{\text{int}} = \int_{\Omega_0} B_{ab}^T S_b d\Omega_0 \quad \text{or} \quad \mathbf{f}^{\text{int}} = \int_{\Omega_0} \mathbf{B}^T \{\mathbf{S}\} d\Omega_0 \quad \text{or} \quad \mathbf{f}_I^{\text{int}} = \int_{\Omega_0} \mathbf{B}_I^T \{\mathbf{S}\} d\Omega_0 \tag{3.1.27}$$

where the internal forces $f_a^{\text{int}} = f_{iI}^{\text{int}}$ and its positions are given by

$$a = (I-1) n_{\text{dime}} + i \tag{3.1.28}$$

The second Piola-Kirchhoff stress components are transformed by the kinetic Voigt rule as shown in table 3.1.

S_{ij}		S_a
i	j	a
1	1	1
2	2	2
3	3	3
2	3	4
1	3	5
1	2	6

Table 3.1 *Voigt rule for stresses*

The strain-displacement tensor $\mathbf{B}_I$ in Voigt notation for 3D problems is

$$\mathbf{B}_I = \begin{bmatrix} \frac{\partial N_I}{\partial X_1}\frac{\partial x_1^h}{\partial X_1} & \frac{\partial N_I}{\partial X_1}\frac{\partial x_2^h}{\partial X_1} & \frac{\partial N_I}{\partial X_1}\frac{\partial x_3^h}{\partial X_1} \\ \frac{\partial N_I}{\partial X_2}\frac{\partial x_1^h}{\partial X_2} & \frac{\partial N_I}{\partial X_2}\frac{\partial x_2^h}{\partial X_2} & \frac{\partial N_I}{\partial X_2}\frac{\partial x_3^h}{\partial X_2} \\ \frac{\partial N_I}{\partial X_3}\frac{\partial x_1^h}{\partial X_3} & \frac{\partial N_I}{\partial X_3}\frac{\partial x_2^h}{\partial X_3} & \frac{\partial N_I}{\partial X_3}\frac{\partial x_3^h}{\partial X_3} \\ \frac{\partial N_I}{\partial X_2}\frac{\partial x_1^h}{\partial X_3} + \frac{\partial N_I}{\partial X_3}\frac{\partial x_1^h}{\partial X_2} & \frac{\partial N_I}{\partial X_2}\frac{\partial x_2^h}{\partial X_3} + \frac{\partial N_I}{\partial X_3}\frac{\partial x_2^h}{\partial X_2} & \frac{\partial N_I}{\partial X_2}\frac{\partial x_3^h}{\partial X_3} + \frac{\partial N_I}{\partial X_3}\frac{\partial x_3^h}{\partial X_2} \\ \frac{\partial N_I}{\partial X_1}\frac{\partial x_1^h}{\partial X_3} + \frac{\partial N_I}{\partial X_3}\frac{\partial x_1^h}{\partial X_1} & \frac{\partial N_I}{\partial X_1}\frac{\partial x_2^h}{\partial X_3} + \frac{\partial N_I}{\partial X_3}\frac{\partial x_2^h}{\partial X_1} & \frac{\partial N_I}{\partial X_1}\frac{\partial x_3^h}{\partial X_3} + \frac{\partial N_I}{\partial X_3}\frac{\partial x_3^h}{\partial X_1} \\ \frac{\partial N_I}{\partial X_1}\frac{\partial x_1^h}{\partial X_2} + \frac{\partial N_I}{\partial X_2}\frac{\partial x_1^h}{\partial X_1} & \frac{\partial N_I}{\partial X_1}\frac{\partial x_2^h}{\partial X_2} + \frac{\partial N_I}{\partial X_2}\frac{\partial x_2^h}{\partial X_1} & \frac{\partial N_I}{\partial X_1}\frac{\partial x_3^h}{\partial X_2} + \frac{\partial N_I}{\partial X_2}\frac{\partial x_3^h}{\partial X_1} \end{bmatrix} \tag{3.1.29}$$

Assuming that body forces and surface tractions are given, the *external forces* come from the virtual external work by substituting Eq. (3.1.19) into Eq. (3.1.8) yielding

$$\delta\mathcal{W}^{\text{ext}} = \delta u_{iI} f_{iI}^{\text{ext}} = \delta u_{iI} \left(\int_{\Omega_0} N_I \rho_0 b_i d\Omega_0 + \int_{\Gamma_0^N} N_I \bar{t}_i^0 d\Gamma_0 \right) \tag{3.1.30}$$

where the external forces are found to be

$$f_{iI}^{\text{ext}} = \int_{\Omega_0} N_I \rho_0 b_i d\Omega_0 + \int_{\Gamma_0^N} N_I \bar{t}_i^0 d\Gamma_0 \tag{3.1.31}$$

The *kinetic forces* are a consequence of the virtual kinetic work, which are expressed by the relation

$$\delta\mathcal{W}^{\text{kin}} = \delta u_{iI} f_{iI}^{\text{kin}} = \int_{\Omega_0} \delta u_i^h \rho_0 \ddot{u}_i^h d\Omega_0 = \delta u_{iI} \int_{\Omega_0} N_I \rho_0 N_J \ddot{u}_{iJ} d\Omega_0 \tag{3.1.32}$$

where Eq. (3.1.16) and Eq. (3.1.19) have been substituted into Eq. (3.1.32), and the kinetic forces are given by

$$f_{iI}^{\text{kin}} = \int_{\Omega_0} N_I \rho_0 N_J \ddot{u}_{iJ} d\Omega_0 = \int_{\Omega_0} N_I \rho_0 N_J d\Omega_0 \ddot{u}_{iJ} \tag{3.1.33}$$

However, it is common to express the kinetic forces as the product of the *mass matrix* and the accelerations. From Eq. (3.1.33) the mass matrix is defined by

$$M_{ijIJ} = \delta_{ij} \int_{\Omega_0} \rho_0 N_I N_J d\Omega_0 \tag{3.1.34}$$

and the kinetic forces become

$$f_{iI}^{\text{kin}} = M_{ijIJ}\ddot{u}_{jJ} = M_{ijIJ}a_{jJ} \tag{3.1.35}$$

The kinetic forces are also known as the *inertial forces*.

All the above equations have not been discretized in time, so instead of finite element discretization, sometimes these equations are called *finite element semidiscretization*. Finally the *equations of motion* are given by

$$f_{iI}^{\text{int}} + M_{ijIJ}a_{jJ} = f_{iI}^{\text{ext}} \quad \text{or} \quad \mathbf{f}^{\text{int}} + \mathbf{Ma} = \mathbf{f}^{\text{ext}} \tag{3.1.36}$$

3.2 Membrane Elements

3.2.1 Introduction

Membrane structures are used for many purposes because they are built with very light materials which are optimally used since the structures are subjected to membrane tension stresses. Examples include aircraft and spacecraft applications, parachutes, automobile airbags, sails, windmills, human tissues and long span structures.

A membrane is essentially a thin shell with no flexural stiffness, consequently a membrane should not resist any compression at all. In such a theory only the in-plane stress resultants are included. The position of points on the two-dimensional surface in the Euclidean space gives the deformation state for a membrane. A numerical solution for membranes may be constructed using the finite element method, which solution for small deformations can be found in Zienkiewicz and Taylor (1989), Cook et al. (1989) or Oñate (1992). Theory for large deformations can proceed following the presentations of Simo and Fox (1989), Simo et al. (1990a), Bütchter et al. (1992) or Braun et al. (1994). A general formulation for membranes based on curvilinear coordinates is given by Bonet et al. (2000) and Lu et al. (2001). Taylor (2001) proposed a large displacement formulation of a membrane composed of three-node triangular elements based on rectangular Cartesian coordinates, where details of the various terms involved are given in Valdés (2002). This work has been generalized for different finite elements by Rossi (2005).

Some membrane structures have a very low flexural stiffness that can support a small amount of compressive stress before buckling appears. In order to avoid compression stresses, membranes are prestressed. Levy and Spillers (1995), Raible (2003) and Gil (2003) use a prestressed method to analyze membranes which are initially flat in the Euclidean space. An approach that include curved pre-stressed membranes using a projection scheme can be found in Bletzinger and Wüchner (2001).

In the present work, analysis of initially curved pre-stressed membranes is performed using the fiber orientation strategy, which is an extension of the work of Valdés et al. (2004). Also the fiber orientation allow to analyze orthotropic membranes, where other possibilities are studied in Raible (2003) and Wüchner and Bletzinger (2005).

When a membrane is subjected to compression in one principal direction and tension in the other principal direction, it will buckle and many narrow wrinkles will form with crests and troughs roughly parallel to the tensile direction. As the flexural stiffness decreases, so do the critical buckling stress and the distance between the crests. When a flexural stiffness vanishes, so does the critical buckling stress and there would be an infinite number of wrinkles exactly parallel to the tensile direction, as mentioned by Libai and Simmonds (1998). However conventional membrane theory can resist compression without wrinkling although its flexural stiffness vanishes. Therefore one difficulty in modelling membranes is to account for wrinkling phenomena that are not predicted by normal membrane theory. A membrane theory which accounts for wrinkling does not allow any negative stress to appear. When a negative stress is about to appear the membrane will wrinkle.

The modelling of wrinkled membranes was started by Wagner (1929). He tried to explain the behavior of thin metal webs and spars carrying a shear load in excess of the initial buckling value. Many authors contributed to the linear analysis of wrinkles like Reissner (1938), Kondo et al. (1955), Mansfiled (1970) or Mansfiled (1977). Since then, many significant contributions to analyze wrinkling models of membranes have been studied extensively with different approaches. In one approach, the constitutive relation of the membrane is modified to simulate wrinkling. For example, Contri and Schrefler (1988) use a no-compression material model that was carried out in a two step procedure that allows the folds and the mean deformed position of the wrinkled surface to be obtained. Liu et al. (2001) propose a penalty parameter modified material model with a constant parameter, which rotates the constitutive equation to the direction of principal strains. Then the values of the constitutive equation related to the direction of the second principal strains are penalize almost to zero and then the constitutive equation is rotated back to its original position. Rossi et al. (2003) and Rossi et al. (2005) use the same procedure that Liu et al. (2001) but with one extra parameters that keeps the convergence properties of the element. Inspired in the work of Liu et al. (2001) and Rossi et al. (2003), Jetteur (2005) proposed a material model with small resistance in compression in order to have a good convergence in a static scheme.

In the present work, following Valdés et al. (2005) a modified material model for orthotropic materials is presented. An advantage of this kind of procedure is that since commercial finite element codes do not usually support tension field models, the method can be input to the code through the user-defined material model port.

A second approach is based on modifying the deformation gradient tensor without changing the constitutive relation. Wu and Canfield (1981) presented a model describing the wrinkling of membranes in finite plane-stress theory. They modified the deformation gradient tensor by introducing an extra parameter. The value of this parameter was determined by the condition that the stress in wrinkling direction is zero. The modification of the deformation gradient tensor was chosen in a way that the principal Cauchy directions did not change because of the wrinkling, which is only true when the material is isotropic. Another model capable of dealing with anisotropy was introduced by Roddeman et al. (1987a) and Roddeman et al. (1987b). They also introduced the correct criterion to judge the state of the membrane at a point. Due to the complexity of the formulation, explicit expressions for

the nodal forces and stiffness matrix lead to lengthy derivations. Later Roddeman (1991) presented a much more simple element derivation and instead of deriving explicit expression for the nodal forces and the stiffness matrix, the equivalent nodal forces are obtained numerically. The tangent stiffness matrix follows from numerical differentiation of the nodal forces. Muttin (1996) has generalized the wrinkling theory of Roddeman (1991) for curved membranes using curvilinear coordinates, which also uses numerical differentiation to calculate the internal forces and the tangent stiffness matrix. Based on the wrinkling condition of Roddeman et al. (1987a), Ziegler (2001) and Ziegler et al. (2003) develop an algorithm in analogy to the small strain elasto-plasticity model to calculate the wrinkling strains, which was applied to isotropic materials only. The wrinkling theory of Roddeman et al. (1987a) is formulated by Lu et al. (2001) using curvilinear coordinates, and a robust scheme to find the wrinkling direction is derived with concise explicit formulas for the internal forces and the tangent stiffness matrix. An alternative formulation of Roddeman et al. (1987a) is given by Schoop et al. (2002) where a reference configuration methodology results in a simpler formulation.

Another approach similar to the second one, decompose the strain tensor in its principal directions and then using a new variable, the second principal direction is modified until the compression stresses disappear. In the works of Raible (2003) and Löhnert et al. (2003) this approach is used, where explicit formulas for the internal forces are derived.

3.2.2 Membrane Formulation

Until now a rectangular Cartesian coordinate system have been employed as the basis for the representation of vectors and tensors. However for the membrane theory, a *curvilinear coordinate system* based on differential geometry of surfaces will be used, as can be found in Farrashkhalvat and Miles (2003), Lu et al. (2001) and Wüchner and Bletzinger (2005). Here Greek indices on membrane mid-surface take on values of 1 and 2 in a plane stress state in Euclidean space.

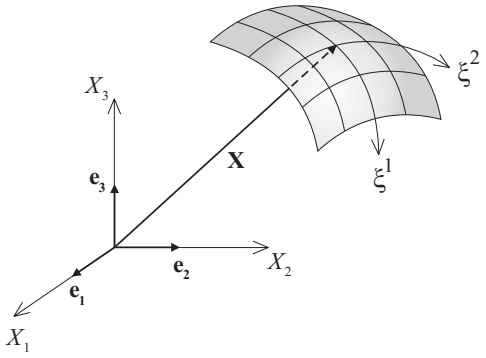

Figure 3.1 *Curvilinear coordinates for a surface*

The position vector $\mathbf{X}$ on the surface in the reference configuration Ω_0 is defined

by two independent curvilinear coordinates ξ^1 and ξ^2, shown in Fig. 3.1, as

$$\mathbf{X} = \mathbf{X}(\xi^1, \xi^2) \tag{3.2.1}$$

It is assumed that there is an invertible relationship between Eq. (2.1.1) and Eq. (3.2.1). The position vector $\mathbf{x}$ on the surface in the current configuration Ω is given by

$$\mathbf{x} = \mathbf{x}(\xi^1, \xi^2, t) \tag{3.2.2}$$

An invertible relationship between Eq. (2.1.2) and Eq. (3.2.2) is assumed.

The convected *covariant base vectors* of the curvilinear coordinate system on Ω_0 and Ω are defined respectively as

$$\mathbf{G}_\alpha = \frac{\partial \mathbf{X}}{\partial \xi^\alpha}, \qquad \mathbf{g}_\alpha = \frac{\partial \mathbf{x}}{\partial \xi^\alpha} \tag{3.2.3}$$

Note that the covariant base vectors $\mathbf{G}_\alpha$ and $\mathbf{g}_\alpha$ form the tangent space $\mathrm{T}_X\mathcal{B}$ to the membrane surface and in general they are neither unit vector nor orthogonal to each other, as can be seen in Fig. 3.2.

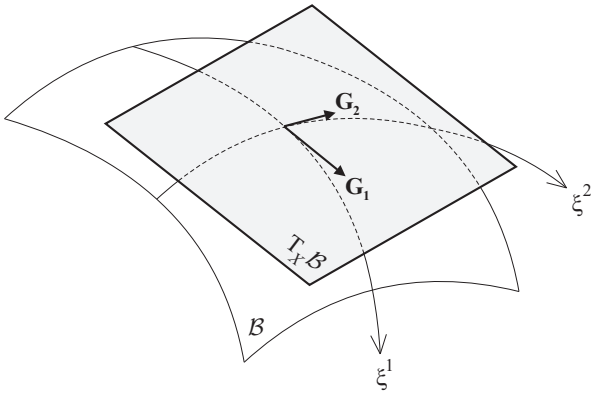

Figure 3.2 *Covariant base vectors forming a tangent plane*

Therefore the surface normals are determined by

$$\mathbf{G}_3 = \mathbf{G}_1 \times \mathbf{G}_2, \qquad \mathbf{N} = \frac{\mathbf{G}_3}{\|\mathbf{G}_3\|}, \qquad \mathbf{g}_3 = \mathbf{g}_1 \times \mathbf{g}_2, \qquad \mathbf{n} = \frac{\mathbf{g}_3}{\|\mathbf{g}_3\|} \tag{3.2.4}$$

in reference and current configuration respectively. The normals are normalized given a unit vector. The covariant components of the metric tensors are defined by

$$G_{\alpha\beta} = \mathbf{G}_\alpha \cdot \mathbf{G}_\beta, \qquad g_{\alpha\beta} = \mathbf{g}_\alpha \cdot \mathbf{g}_\beta \tag{3.2.5}$$

for the reference and current configurations respectively. The convected *contravariant base vectors* are given for Ω_0 and Ω respectively by

$$\mathbf{G}^{\alpha} = G^{\alpha\beta} \cdot \mathbf{G}_{\beta}, \qquad \mathbf{g}^{\alpha} = g^{\alpha\beta} \cdot \mathbf{g}_{\beta} \tag{3.2.6}$$

where the contravariant components of the metric tensors are obtained from

$$\left[G^{\alpha\beta}\right] = \left[G_{\alpha\beta}\right]^{-1}, \qquad \left[g^{\alpha\beta}\right] = \left[g_{\alpha\beta}\right]^{-1} \tag{3.2.7}$$

for the corresponding configurations. For the case when the contravariant base vectors are given, the covariant base vector can be obtained from

$$\mathbf{G}_{\alpha} = G_{\alpha\beta} \cdot \mathbf{G}^{\beta}, \qquad \mathbf{g}_{\alpha} = g_{\alpha\beta} \cdot \mathbf{g}^{\beta} \tag{3.2.8}$$

for reference and current configurations respectively. The covariant and contravariant base vectors define the scalar product identities

$$\mathbf{G}^{\alpha} \cdot \mathbf{G}_{\beta} = \delta^{\alpha}_{\beta}, \qquad \mathbf{g}^{\alpha} \cdot \mathbf{g}_{\beta} = \delta^{\alpha}_{\beta} \tag{3.2.9}$$

where the Kronecker delta is given by

$$\delta^{\alpha}_{\beta} = \begin{cases} 1 & \text{when } \alpha = \beta \\ 0 & \text{otherwise} \end{cases} \tag{3.2.10}$$

The deformation gradient tensor $\mathbf{F}$ in curvilinear coordinates is given by

$$\mathbf{F} = \mathbf{g}_{\alpha} \otimes \mathbf{G}^{\alpha}, \quad \mathbf{F}^{T} = \mathbf{G}^{\alpha} \otimes \mathbf{g}_{\alpha}, \quad \mathbf{F}^{-1} = \mathbf{G}_{\alpha} \otimes \mathbf{g}^{\alpha}, \quad \mathbf{F}^{-T} = \mathbf{g}^{\alpha} \otimes \mathbf{G}_{\alpha} \tag{3.2.11}$$

and substituting Eq. (3.2.11) into the Green-Lagrange strain tensor, Eq. (2.2.1), yields

$$\mathbf{E} = \frac{1}{2}\left(\mathbf{F}^{T} \cdot \mathbf{F} - \mathbf{I}\right) = \frac{1}{2}\left(\mathbf{G}^{\alpha} \otimes \mathbf{g}_{\alpha} \cdot \mathbf{g}_{\beta} \otimes \mathbf{G}^{\beta} - G_{\alpha\beta}\mathbf{G}^{\alpha} \otimes \mathbf{G}^{\beta}\right) \tag{3.2.12}$$

which components for the membrane surface in a plane stress state are given by

$$\mathbf{E} = E_{\alpha\beta}\mathbf{G}^{\alpha} \otimes \mathbf{G}^{\beta}, \qquad E_{\alpha\beta} = \frac{1}{2}\left(g_{\alpha\beta} - G_{\alpha\beta}\right) \tag{3.2.13}$$

In Eq. (3.2.12) the identity tensor $\mathbf{I}$ was written as the product of $\mathbf{F}^{-1} \cdot \mathbf{F}$ and Eq. (3.2.8) was used to expressed $\mathbf{I} = G_{\alpha\beta}\mathbf{G}^{\alpha} \otimes \mathbf{G}^{\beta}$.

Using the appropriate constitutive equation to relate the second Piola-Kirchhoff stress tensor and the Green-Lagrange strain tensor in curvilinear coordinates, the components of the stress tensor are defined as

$$\mathbf{S} = S^{\alpha\beta}\mathbf{G}_{\alpha} \otimes \mathbf{G}_{\beta} \tag{3.2.14}$$

Finally the virtual internal work, Eq. (3.1.11), can be expressed in curvilinear coordinates as

$$\delta\mathcal{W}^{\text{int}} = \int_{\Omega_0} \delta E_{\alpha\beta} S^{\alpha\beta} d\Omega_0 \tag{3.2.15}$$

3.2.2.1 Pressure Follower Forces

Although the most common example of a body force is gravity loading and a wide variety of surface traction forces exists, the most important case for geometrically nonlinear membrane elements is the case of uniform normal pressure follower forces, that change their direction each time the normal to the surface changes in the current configuration.

Consider a membrane element with an applied uniform pressure p acting on the current configuration having a pointwise normal $\mathbf{n}$. Then the traction force vector $\mathbf{t}$ is expressed as $p\mathbf{n}$, and the corresponding virtual external work in the current configuration is

$$\delta \mathcal{W}^{\text{ext}} = \int_{\Gamma} \delta \mathbf{u} \cdot p\mathbf{n} d\Gamma \tag{3.2.16}$$

3.2.3 Fiber Orientation

The idea for the *fiber orientation* comes from the manufacturing process of membrane structures, which can be built with orthotropic or composite materials and a reference principal fiber direction is needed to perform correctly an analysis with finite elements. Even for isotropic materials, the reference principal fiber direction is needed if the membrane has an initial *pre-stressed* field. With the methodology proposed, a pre-stressed field for orthotropic materials is also possible.

Another important aspect of the fiber orientation comes from postprocessing the strain and stress field in-plane on the membrane surface. Other possibilities for postprocessing these values are given in Oñate (1992).

To build the fiber orientation for a membrane structure, first a finite element mesh is needed and for each element the following methodology is applied. A local Cartesian base system is obtained from the covariant base vectors as

$$\mathbf{e}_1^{loc} = \frac{\mathbf{G}_1}{\|\mathbf{G}_1\|}, \qquad \mathbf{e}_3^{loc} = \mathbf{N} = \frac{\mathbf{G}_1 \otimes \mathbf{G}_2}{\|\mathbf{G}_1 \otimes \mathbf{G}_2\|}, \qquad \mathbf{e}_2^{loc} = \mathbf{e}_3^{loc} \otimes \mathbf{e}_1^{loc} \tag{3.2.17}$$

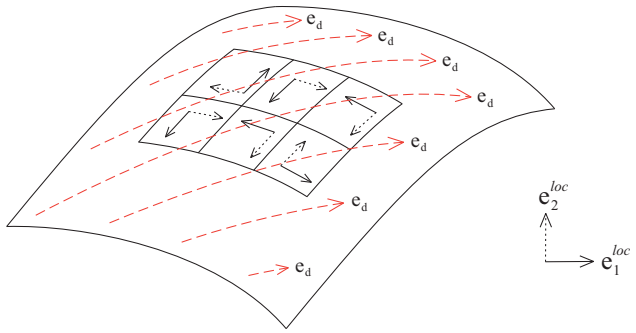

Figure 3.3 *Principal fiber direction and local base system*

If a curved membrane structure is meshed with finite elements, the local Cartesian axes of each element generally have different orientations, even for structured meshes as can be seen in Fig. 3.3.

If dashed-lines are the reference principal fibers direction or the orthotropy direction for the material, then an angle θ is needed to rotate each local Cartesian base system $\mathbf{e}_i^{loc}$ in order to apply the material orthotropy correctly (or the prestress field). Suppose that $\mathbf{e}_\mathrm{d}$ is a given vector that defines the principal fiber direction for a finite element and lies in the tangent space of the element, as shown in Fig. 3.4. This principal fiber direction is always known at least for one finite element and is given by the manufacture process of the structure.

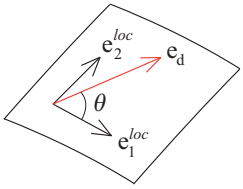

Figure 3.4 *Principal fiber direction for a finite element*

To assign correctly the principal fiber direction from a known element (or source element) to the whole mesh, first the adjacent elements of the source element must be identified, see Fig. 3.5(a). Next build the tangent space $\mathrm{T}_X\mathcal{B}^S$ for the source element together with its normal that will be called $\mathbf{N}_S$. For one adjacent element its tangent space $\mathrm{T}_X\mathcal{B}^N$ is also built and its normal will be called $\mathbf{N}_N$. The intersection line to both tangent spaces will be a common vector between both of them.

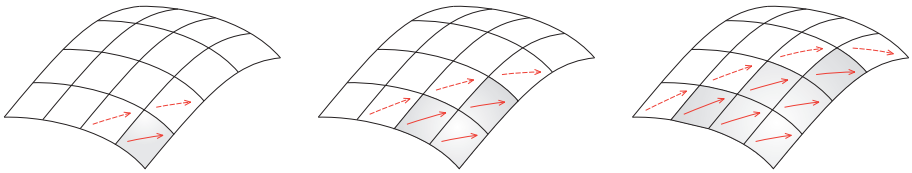

Figure 3.5 *Assignment of principal fiber direction to adjacent elements*

A new Cartesian base system for $\mathrm{T}_X\mathcal{B}^S$ is constructed. The Cross product between the normal $\mathbf{N}_S$ and the vector $\mathbf{X}_S$, given by the intersection line between both tangent spaces, yields $\mathbf{Y}_S$. This new vector $\mathbf{Y}_S$ must have a direction pointing inside of the source element, as can be seen in Fig. 3.6.

In a similar way, a new Cartesian base system for the adjacent element will be built. The Cross product between the normal $\mathbf{N}_N$ and the vector given by the intersection line $\mathbf{X}_N$ yields $\mathbf{Y}_N$, where $\mathbf{X}_N = -\mathbf{X}_S$. This new vector $\mathbf{Y}_N$ must point inside the adjacent element. Remark that vectors $\mathbf{X}_S$ and $\mathbf{Y}_S$ belong to

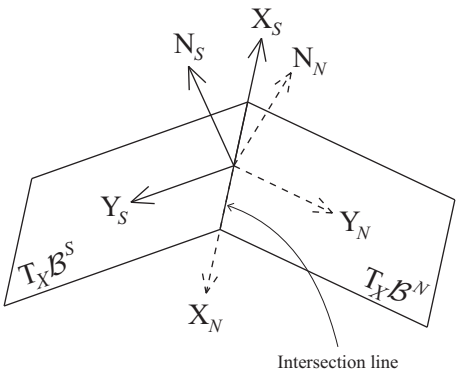

Figure 3.6 *Local Cartesian base systems for tangent spaces*

the tangent space of the source element while vectors $\mathbf{X}_N$ and $\mathbf{Y}_N$ belong to the tangent space of the adjacent element.

Once both local Cartesian base systems are defined, the next step is to choose an arbitrary point a on axis $\mathbf{X}_S$. Now over point a the principal fiber direction vector $\mathbf{e}_\mathrm{d}$ is passed and its intersection over axis $\mathbf{Y}_S$ will be the point b, as shown in Fig. 3.7.

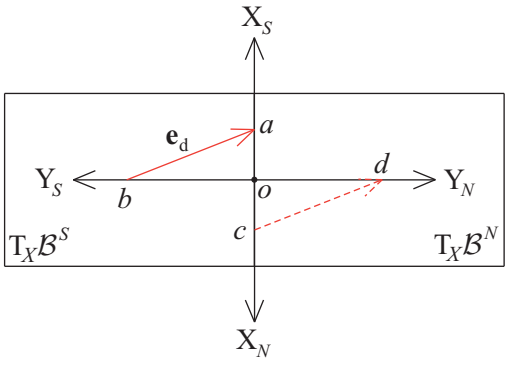

Figure 3.7 *Transferring reference principal fiber direction*

Finally to transfer the principal fiber direction to the adjacent element, the distance from the origin o to the point a must be the same that the distance from the origin o to the point c located on axis $\mathbf{X}_N$. Also the distance from the origin o to the point b must be the same that from the origin o to the point d over axis $\mathbf{Y}_N$. Then build the vector from point c to point d which will be the reference principal fiber direction of the neighbor element, as can be seen in Fig. 3.7.

This procedure of transferring the principal fiber direction from a source element to one of its adjacent elements is repeated for all adjacent elements of the source element, as in Fig. 3.5. Once each adjacent element has a principal fiber direction transferred, the procedure is repeated for the whole finite element mesh until every

element has a known principal fiber direction $\mathbf{e}_\mathrm{d}$. A finite element mesh with all its elements with a principal fiber direction assigned is shown in Fig. 3.8.

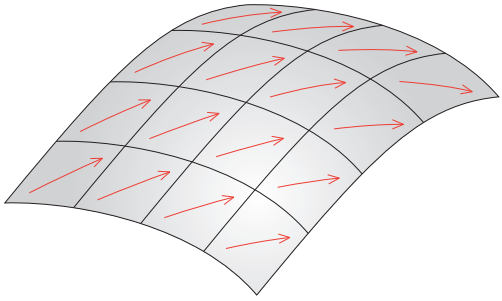

Figure 3.8 *Principal fibers direction of a mesh*

With every finite element of the mesh with a principal fiber direction vector $\mathbf{e}_\mathrm{d}$ known, the angle θ for every element that is needed to rotate each local Cartesian base system, as shown in Fig. 3.4, is given by

$$sin\,\theta = -\mathbf{e}_\mathrm{d} \cdot \mathbf{e}_2^{loc}, \qquad cos\,\theta = \mathbf{e}_\mathrm{d} \cdot \mathbf{e}_1^{loc} \tag{3.2.18}$$

and

$$\theta = tan^{-1}\left(\frac{sin\,\theta}{cos\,\theta}\right) \tag{3.2.19}$$

The local Cartesian base system with the fiber orientation is denominated local fiber Cartesian base system, and is found with the equation

$$\mathbf{e}_i^{fiber} = \mathbf{R}(\theta, \mathbf{N}) \cdot \mathbf{e}_i^{loc} \tag{3.2.20}$$

where $\mathbf{R}(\theta, \mathbf{N})$ is the Rodrigues' rotation formula that rotates an angle θ about a fixed axis specified by a unit vector, in this case the unit normal vector to the surface element $\mathbf{N}$, and is given by

$$\mathbf{R}(\theta, \mathbf{N}) = \begin{bmatrix} cos\theta + N_1^2(1-cos\theta) & N_1N_2(1-cos\theta) - N_3 sin\theta & N_2 sin\theta + N_1N_3(1-cos\theta) \\ N_3 sin\theta + N_1N_2(1-cos\theta) & cos\theta + N_2^2(1-cos\theta) & N_2N_3(1-cos\theta) - N_1 sin\theta \\ N_1N_3(1-cos\theta) - N_2 sin\theta & N_1 sin\theta + N_2N_3(1-cos\theta) & cos\theta + N_3^2(1-cos\theta) \end{bmatrix} \tag{3.2.21}$$

The finite element mesh for the analysis with the fiber orientation is shown in Fig. 3.9.

A fast algorithm to find the adjacent elements in a finite element mesh is given in Löhner (2001), which is an important step to be applied in this methodology.

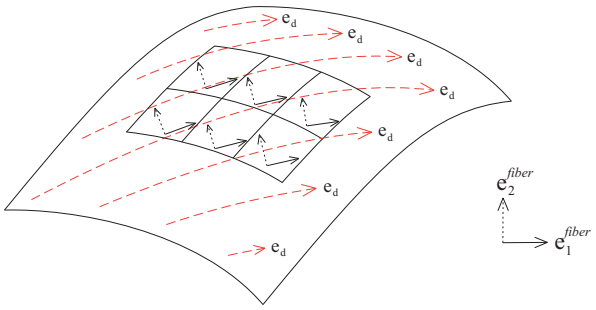

Figure 3.9 *Local fiber base system*

3.2.4 Finite Element Discretization for Membranes

This section contains different subsections that begins with the general discretization for membrane elements expressed in curvilinear coordinates. Next this discretization is transformed to local Cartesian coordinates that simplify the implementation and allow the analysis of isotropic membranes without any pre-stressed fields. To be able to add a pre-stress field or an orthotropic material to the internal forces, the discretization with fiber orientation is presented. Finally the implementation of a triangular three-node finite element is particularized.

3.2.4.1 Discretization in Curvilinear Coordinates

The discretization is established for the total Lagrangian formulation. The finite element discretization is developed with shape functions expressed in terms of the so called *parent element coordinates* or *master element coordinates*. The most common parent element coordinates are the *isoparametric coordinates*. The parent element coordinates are denoted by ξ^α for each element with a parent domain $\Omega_\square$. The shape of the parent domain depends on the type of element and the problem dimension.

In Fig. 3.10 it is shown that the ξ^1 and ξ^2 surface coordinates of the parent element can be mapped to curvilinear coordinates when plotted in local rectangular Cartesian coordinates for a given finite element. Therefore these coordinates are used to develop membrane elements. Consider a membrane element with parent element coordinates ξ^1 and ξ^2 as the curvilinear coordinate system. Then Eq. (3.2.1) can be approximated by

$$\mathbf{X}^h(\boldsymbol{\xi}) = \sum_{I=1}^{n_{\text{node}}} N_I(\boldsymbol{\xi})\mathbf{X}_I \quad \text{or} \quad X_i^h(\boldsymbol{\xi}) = \sum_{I=1}^{n_{\text{node}}} N_I(\boldsymbol{\xi})X_{iI} \qquad \forall i = 1,\, n_{\text{dime}} \tag{3.2.22}$$

where $N_I(\boldsymbol{\xi})$ are the parent element shape functions. The equation of motion Eq. (3.2.2) is given by

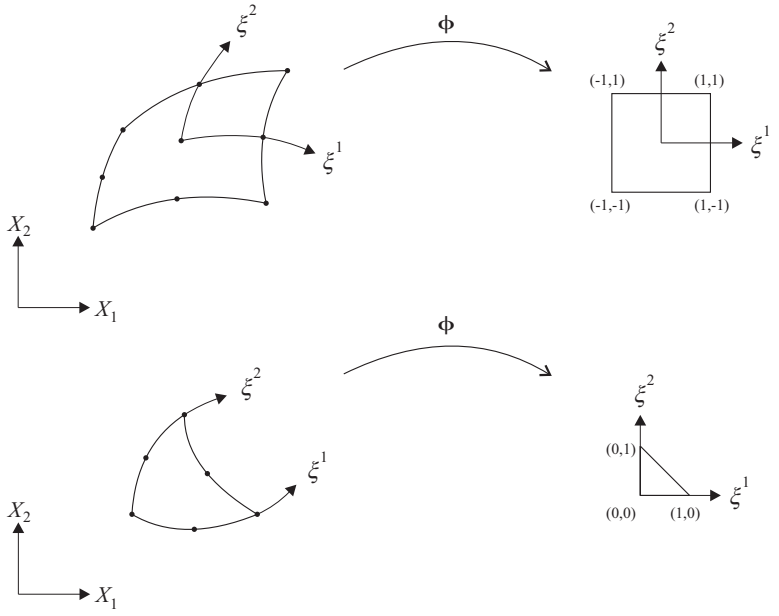

Figure 3.10 *Mapping of surface elements*

$$x_i^h(\boldsymbol{\xi},t) = \sum_{I=1}^{n_{\text{node}}} N_I(\boldsymbol{\xi}) x_{iI}(t) \qquad \forall i = 1,\ n_{\text{dime}}$$
$$\text{or} \quad \mathbf{x}^h(\boldsymbol{\xi},t) = \sum_{I=1}^{n_{\text{node}}} N_I(\boldsymbol{\xi}) \mathbf{x}_I(t) \tag{3.2.23}$$

and the displacements are

$$u_i^h(\boldsymbol{\xi},t) = \sum_{I=1}^{n_{\text{node}}} N_I(\boldsymbol{\xi}) u_{iI}(t) \qquad \forall i = 1,\ n_{\text{dime}}$$
$$\text{or} \quad \mathbf{u}^h(\boldsymbol{\xi},t) = \sum_{I=1}^{n_{\text{node}}} N_I(\boldsymbol{\xi}) \mathbf{u}_I(t) \tag{3.2.24}$$

Substituting Eq. (3.2.22) into the covariant base vectors of the curvilinear coordinates in the reference configuration Ω_0 of Eq. (3.2.3) yields

$$\mathbf{G}_\alpha = \frac{\partial}{\partial \xi^\alpha} \left(\sum_{I=1}^{n_{\text{node}}} N_I(\boldsymbol{\xi}) \mathbf{X}_I \right) = \sum_{I=1}^{n_{\text{node}}} N_{I,\alpha} \mathbf{X}_I \tag{3.2.25}$$

where

$$N_{I,\alpha} = \frac{\partial N_I(\boldsymbol{\xi})}{\partial \xi^\alpha} \tag{3.2.26}$$

Following the same procedure, Eq. (3.2.23) is substituted into the covariant base vectors of the curvilinear coordinates in the current configuration Ω, Eq. (3.2.3), to express

$$\mathbf{g}_\alpha = \sum_{I=1}^{n_{\text{node}}} N_{I,\alpha} \mathbf{x}_I(t) \tag{3.2.27}$$

With these quantities known, the covariant components of the metric tensor $G_{\alpha\beta}$ and $g_{\alpha\beta}$ given in Eq. (3.2.5) are found. Then components of the Green-Lagrange strain tensor are computed with

$$E_{\alpha\beta} = \frac{1}{2}\left(g_{\alpha\beta} - G_{\alpha\beta}\right) \tag{3.2.28}$$

The variation $\delta E_{\alpha\beta}$ becomes

$$\delta E_{\alpha\beta} = \frac{1}{2}\delta(g_{\alpha\beta} - G_{\alpha\beta}) = \frac{1}{2}\delta g_{\alpha\beta} \tag{3.2.29}$$

and

$$\delta g_{\alpha\beta} = \delta\mathbf{g}_\alpha \cdot \mathbf{g}_\beta + \mathbf{g}_\alpha \cdot \delta\mathbf{g}_\beta \tag{3.2.30}$$

where Eq. (3.2.5) has been used. The variation of the covariant base vectors in current configuration results from Eq. (3.2.27) yielding

$$\delta\mathbf{g}_\alpha = \sum_{I=1}^{n_{\text{node}}} N_{I,\alpha}\delta\mathbf{x}_I = \sum_{I=1}^{n_{\text{node}}} N_{I,\alpha}\delta\mathbf{u}_I \tag{3.2.31}$$

Substituting Eq. (3.2.27) and Eq. (3.2.31) into Eq. (3.2.30), the resulting equation is

$$\delta g_{\alpha\beta} = \sum_{I=1}^{n_{\text{node}}} N_{I,\alpha}\delta u_{iI} \cdot \sum_{J=1}^{n_{\text{node}}} N_{J,\beta} x_{iJ} + \sum_{J=1}^{n_{\text{node}}} N_{J,\alpha} x_{iJ} \cdot \sum_{I=1}^{n_{\text{node}}} N_{I,\beta}\delta u_{iI} \tag{3.2.32}$$

Substituting Eq. (3.2.32) into Eq. (3.2.29), the variation of the Green-Lagrange strain tensor becomes

$$2\,\delta E_{\alpha\beta} = \sum_{I=1}^{n_{\text{node}}} N_{I,\alpha}\delta u_{iI} \cdot \sum_{J=1}^{n_{\text{node}}} N_{J,\beta} x_{iJ} + \sum_{J=1}^{n_{\text{node}}} N_{J,\alpha} x_{iJ} \cdot \sum_{I=1}^{n_{\text{node}}} N_{I,\beta}\delta u_{iI} \tag{3.2.33}$$

and the virtual internal work, Eq. (3.2.15), yields

$$2\,\delta\mathcal{W}^{\text{int}} = \int_{\Omega_0} \sum_{I=1}^{n_{\text{node}}} N_{I,\alpha}\delta u_{iI} \cdot \sum_{J=1}^{n_{\text{node}}} N_{J,\beta} x_{iJ} S^{\alpha\beta} \; + \sum_{J=1}^{n_{\text{node}}} N_{J,\alpha} x_{iJ} \cdot \sum_{I=1}^{n_{\text{node}}} N_{I,\beta}\delta u_{iI} S^{\alpha\beta} d\Omega_0 \tag{3.2.34}$$

From Eq. (3.1.22), the virtual internal work was expressed as

$$\delta\mathcal{W}^{int} = \sum_{I=1}^{n_{\text{node}}} \delta u_{iI} f_{iI}^{\text{int}} \qquad \forall i = 1,\ n_{\text{dime}} \tag{3.2.35}$$

Substituting Eq. (3.2.34) into Eq. (3.2.35), the internal forces for a particular direction i and node I can be expressed as

$$f_{iI}^{\text{int}} = \int_{\Omega_0} \frac{1}{2} \sum_{J=1}^{n_{\text{node}}} \left(N_{I,\alpha}N_{J,\beta} + N_{J,\alpha}N_{I,\beta}\right) x_{iJ} S^{\alpha\beta} d\Omega_0 \tag{3.2.36}$$

where the strain-displacement tensor in curvilinear coordinates is given by

$$B_{\alpha\beta iI}^{cur} = \frac{1}{2} \sum_{J=1}^{n_{\text{node}}} \left(N_{I,\alpha}N_{J,\beta} + N_{J,\alpha}N_{I,\beta}\right) x_{iJ} \tag{3.2.37}$$

and the internal forces, Eq. (3.1.26), for membrane elements in curvilinear coordinates can be written as

$$f_{iI}^{\text{int}} = \int_{\Omega_0} B_{\alpha\beta iI}^{cur} S^{\alpha\beta} d\Omega_0 \tag{3.2.38}$$

Eq. (3.2.37) can be expressed in the simple form

$$B_{\alpha\beta iI}^{cur} = \frac{1}{2}\left(N_{I,\alpha}x_{i,\beta}^{h} + N_{I,\beta}x_{i,\alpha}^{h}\right) \tag{3.2.39}$$

where the equation

$$x_{i,\alpha}^{h} = \sum_{J=1}^{n_{\text{node}}} N_{J,\alpha} x_{iJ} \tag{3.2.40}$$

has been used.

Using the Voigt notation to express the internal forces in curvilinear coordinates, Eq. (3.2.38), yields

$$f_{a}^{\text{int}} = \int_{\Omega_0} [B_{ab}^{T}]^{cur} \{S^{b}\}^{cur} d\Omega_0 \quad \text{or} \quad \mathbf{f}_{I}^{\text{int}} = \int_{\Omega_0} [\mathbf{B}_{I}^{T}]^{cur} \{\mathbf{S}\}^{cur} d\Omega_0 \tag{3.2.41}$$

where the strain-displacement matrix $\mathbf{B}_{I}^{cur}$ is given by

$$\mathbf{B}_I^{cur} = \begin{bmatrix} \frac{\partial N_I}{\partial \xi^1}\frac{\partial x_1^h}{\partial \xi^1} & \frac{\partial N_I}{\partial \xi^1}\frac{\partial x_2^h}{\partial \xi^1} & \frac{\partial N_I}{\partial \xi^1}\frac{\partial x_3^h}{\partial \xi^1} \\ \frac{\partial N_I}{\partial \xi^2}\frac{\partial x_1^h}{\partial \xi^2} & \frac{\partial N_I}{\partial \xi^2}\frac{\partial x_2^h}{\partial \xi^2} & \frac{\partial N_I}{\partial \xi^2}\frac{\partial x_3^h}{\partial \xi^2} \\ \frac{\partial N_I}{\partial \xi^1}\frac{\partial x_1^h}{\partial \xi^2} + \frac{\partial N_I}{\partial \xi^2}\frac{\partial x_1^h}{\partial \xi^1} & \frac{\partial N_I}{\partial \xi^1}\frac{\partial x_2^h}{\partial \xi^2} + \frac{\partial N_I}{\partial \xi^2}\frac{\partial x_2^h}{\partial \xi^1} & \frac{\partial N_I}{\partial \xi^1}\frac{\partial x_3^h}{\partial \xi^2} + \frac{\partial N_I}{\partial \xi^2}\frac{\partial x_3^h}{\partial \xi^1} \end{bmatrix} \tag{3.2.42}$$

In Voigt notation, the virtual internal work Eq. (3.1.22) is written as

$$\delta \mathcal{W}^{int} = \{\delta E_b^T\}^{cur}\{S^b\}^{cur} = \{\delta u^a\}^T [B_{ab}^T]^{cur}\{S^b\}^{cur} \tag{3.2.43}$$

where the variation of the Green-Lagrange strain tensor in curvilinear coordinates and Voigt notation is given by

$$\delta E_b^{cur} = B_{ba}^{cur}\delta u^a \tag{3.2.44}$$

3.2.4.2 Discretization in Cartesian Coordinates

The Green-Lagrange strain tensor $\mathbf{E}$ expressed in local Cartesian coordinates can be found using the following transformation equation, see i.e. Crisfield (1991),

$$\mathbf{E}^{cur} = \bar{\mathbf{J}}_\xi^T \mathbf{E}^{loc} \bar{\mathbf{J}}_\xi \tag{3.2.45}$$

where the Jacobian transformation tensor $\bar{\mathbf{J}}_\xi$ in the reference configuration is defined as

$$\bar{\mathbf{J}}_\xi = \begin{bmatrix} \mathbf{G}_1 \cdot \mathbf{e}_1^{loc} & \mathbf{G}_2 \cdot \mathbf{e}_1^{loc} \\ \mathbf{G}_1 \cdot \mathbf{e}_2^{loc} & \mathbf{G}_2 \cdot \mathbf{e}_2^{loc} \end{bmatrix} = \begin{bmatrix} J_{11} & J_{12} \\ 0 & J_{22} \end{bmatrix} \tag{3.2.46}$$

Note that the product $\mathbf{G}_1 \cdot \mathbf{e}_2^{loc} = 0$ because they are orthogonal vectors. From Eq. (3.2.45) the Green-Lagrange strain tensor $\mathbf{E}^{loc}$ is found by

$$\mathbf{E}^{loc} = \mathbf{T}_\xi^T \mathbf{E}^{cur} \mathbf{T}_\xi \tag{3.2.47}$$

where $\mathbf{T}_\xi$ is used to denote the inverse of $\bar{\mathbf{J}}_\xi$ by

$$\mathbf{T}_\xi = \bar{\mathbf{J}}_\xi^{-1} = \begin{bmatrix} T_{11} & T_{12} \\ 0 & T_{22} \end{bmatrix} \tag{3.2.48}$$

where

$$T_{11} = \frac{1}{J_{11}}, \qquad T_{12} = \frac{-J_{12}}{J_{11}J_{22}}, \qquad T_{22} = \frac{1}{J_{22}} \tag{3.2.49}$$

Eq. (3.2.47) can be written in Voigt notation yielding

$$\{\mathbf{E}\}^{loc} = [\mathbf{Q}]\{\mathbf{E}\}^{cur} \quad \text{or} \quad E_c^{loc} = Q_{cb}\, E_b^{cur} \tag{3.2.50}$$

From Eq. (3.2.47), the variation of the Green-Lagrange strain tensor is

$$\delta \mathbf{E}^{loc} = \mathbf{T}_{\xi}^{T} \delta \mathbf{E}^{cur} \mathbf{T}_{\xi} \tag{3.2.51}$$

which in Voigt notation can be written as

$$\{\delta \mathbf{E}\}^{loc} = [\mathbf{Q}]\{\delta \mathbf{E}\}^{cur} \quad \text{or} \quad \delta E_c^{loc} = Q_{cb}\, \delta E_b^{cur} \tag{3.2.52}$$

where the transformation matrix $\mathbf{Q} = \mathbf{Q}(\mathbf{T}_{\xi})$ gives the transformation from curvilinear coordinates to local Cartesian coordinates and is defined by

$$\mathbf{Q} = \begin{bmatrix} T_{11}^2 & 0 & 0 \\ T_{12}^2 & T_{22}^2 & T_{22}T_{12} \\ 2T_{11}T_{12} & 0 & T_{11}T_{22} \end{bmatrix} \tag{3.2.53}$$

The virtual internal work, Eq. (3.2.43), written in local Cartesian coordinates yields

$$\delta \mathcal{W}^{int} = \{\delta E_c^T\}^{loc} S_c^{loc} = \{\delta u_a\}^T [B_{ac}^T]^{loc} S_c^{loc} = \{\delta u_a\}^T [B_{ab}^T]^{cur} Q_{bc}^T S_c^{loc} \tag{3.2.54}$$

where the strain-displacement tensor in local Cartesian coordinates and in Voigt notation is defined by

$$B_{ca}^{loc} = Q_{cb} B_{ba}^{cur} \quad \text{or} \quad \mathbf{B}^{loc} = \mathbf{Q}\mathbf{B}^{cur} \tag{3.2.55}$$

The internal forces in Voigt notation and local Cartesian coordinates are given by

$$f_a^{\text{int}} = \int_{\Omega_0} [B_{ab}^T]^{cur} Q_{bc}^T S_c^{loc} d\Omega_0 \quad \text{or} \quad \mathbf{f}_I^{\text{int}} = \int_{\Omega_0} [\mathbf{B}_I^T]^{cur} [\mathbf{Q}^T]\{\mathbf{S}\}^{loc} d\Omega_0 \tag{3.2.56}$$

This equation is defined only for isotropic materials without any pre-stressed field. To add a pre-stressed field or an orthotropic material to the internal forces, the fiber orientation has to be used.

3.2.4.3 Discretization with Fiber Orientation

The following relations to rotate the stress $\mathbf{S}$ and strain $\mathbf{E}$ tensor in Voigt notation are needed, see i.e. Decolon (2000),

$$\{\mathbf{S}\}^{loc} = [\mathbf{T}_{\sigma}]\{\mathbf{S}\}^{fib} \tag{3.2.57}$$

and

$$\{\mathbf{E}\}^{loc} = [\mathbf{T}_{\varepsilon}]\{\mathbf{E}\}^{fib} \tag{3.2.58}$$

where the rotation matrix for the stresses $\mathbf{T}_{\sigma}$ and the strains $\mathbf{T}_{\varepsilon}$ are given respectively by

$$\mathbf{T}_\sigma = \begin{bmatrix} cos^2\theta & sin^2\theta & -2sin\theta cos\theta \\ sin^2\theta & cos^2\theta & 2sin\theta cos\theta \\ sin\theta cos\theta & -sin\theta cos\theta & cos^2\theta - sin^2\theta \end{bmatrix} \tag{3.2.59}$$

and

$$\mathbf{T}_\varepsilon = \begin{bmatrix} cos^2\theta & sin^2\theta & -sin\theta cos\theta \\ sin^2\theta & cos^2\theta & sin\theta cos\theta \\ 2sin\theta cos\theta & -2sin\theta cos\theta & cos^2\theta - sin^2\theta \end{bmatrix} \tag{3.2.60}$$

where θ is given by Eq. (3.2.19). The inverse relationship of Eq. (3.2.57) and Eq. (3.2.58) is given respectively by

$$\{\mathbf{S}\}^{fib} = [\mathbf{T}_\varepsilon^T]\{\mathbf{S}\}^{loc} \tag{3.2.61}$$

and

$$\{\mathbf{E}\}^{fib} = [\mathbf{T}_\sigma^T]\{\mathbf{E}\}^{loc} \tag{3.2.62}$$

The variation of the Green-Lagrange strain tensor in Voigt notation with the fiber orientation yields

$$\{\delta\mathbf{E}\}^{fib} = [\mathbf{T}_\sigma^T]\{\delta\mathbf{E}\}^{loc} = [\mathbf{T}_\sigma^T][\mathbf{Q}]\{\delta\mathbf{E}\}^{cur} = [\mathbf{T}_\sigma^T][\mathbf{Q}][\mathbf{B}]^{cur}\{\delta\mathbf{u}\} \tag{3.2.63}$$

where the strain-displacement matrix with the fiber orientation is given by the following equation

$$B_{ea}^{fib} = [T_{ec}^T]_\sigma \, Q_{cb} B_{ba}^{cur} \quad \text{or} \quad \mathbf{B}^{fib} = \mathbf{T}_\sigma^T \mathbf{Q}\mathbf{B}^{cur} \tag{3.2.64}$$

Finally the internal forces with the fiber orientation and in Cartesian coordinates are given by

$$\mathbf{f}_I^{\text{int}} = \int_{\Omega_0} [\mathbf{B}_I^T]^{cur}[\mathbf{Q}^T][\mathbf{T}_\sigma]\{\mathbf{S}\}^{fib} d\Omega_0 = \int_{\Omega_0} [\mathbf{B}_I^T]^{fib}\{\mathbf{S}\}^{fib} d\Omega_0 \tag{3.2.65}$$

or in indicial notation

$$f_a^{\text{int}} = \int_{\Omega_0} [B_{ab}^T]^{cur}[Q_{bc}^T][T_{ce}]_\sigma \, \{S_e\}^{fib} d\Omega_0 = \int_{\Omega_0} [B_{ae}^T]^{fib}\{S_e\}^{fib} d\Omega_0 \tag{3.2.66}$$

Note that if the angle $\theta = 0$ when no fiber orientation is performed, the rotation matrix $\mathbf{T}_\sigma = \mathbf{I}_{3\times 3}$ and the classical membrane element is recovered.

To add a prestressed field to the membrane structure once the fiber orientation is performed, simple add the desire prestressed value, yielding

$$\mathbf{f}_I^{\text{int}} = \int_{\Omega_0} [\mathbf{B}_I^T]^{fib}\Big(\{\mathbf{S}\}^{fib} + \{\mathbf{S}\}^{prestressed}\Big) d\Omega_0 \tag{3.2.67}$$

or in indicial notation

$$f_a^{\text{int}} = \int_{\Omega_0} [B_{ae}^T]^{fib} \Big(\{S_e\}^{fib} + \{S_e\}^{prestressed} \Big) d\Omega_0 \tag{3.2.68}$$

Also an orthotropic analysis can be performed once the fiber orientation is done, as shown next.

3.2.4.4 Plane Stress Constitutive Equation

The constitutive equation used in this work is a Saint Venant-Kirchhoff material model that express the stresses $\{\mathbf{S}\}^{fib}$ from the strains $\{\mathbf{E}\}^{fib}$ as

$$\{\mathbf{S}\}^{fib} = [\mathbf{C}]\{\mathbf{E}\}^{fib} \tag{3.2.69}$$

where the constitutive matrix $[\mathbf{C}]$ for plane stress isotropic materials is given by

$$\mathbf{C} = \frac{E}{1-\upsilon^2} \begin{bmatrix} 1 & \upsilon & 0 \\ \upsilon & 1 & 0 \\ 0 & 0 & (1-\upsilon)/2 \end{bmatrix} \tag{3.2.70}$$

where E is the elastic or Young's modulus, and υ is the Poisson's ratio. For orthotropic materials the constitutive matrix is

$$\mathbf{C} = \frac{1}{1-\upsilon_{xy}\upsilon_{yx}} \begin{bmatrix} E_x & \upsilon_{yx}E_x & 0 \\ \upsilon_{xy}E_y & E_y & 0 \\ 0 & 0 & (1-\upsilon_{xy}\upsilon_{yx})G_{xy} \end{bmatrix} \tag{3.2.71}$$

with $E_x\upsilon_{yx} = E_y\upsilon_{xy}$ and G_{xy} being the shear modulus. The Green-Lagrange strain tensor in Voigt notation $\{\mathbf{E}\}^{fib}$ is found substituting Eq. (3.2.50) into Eq. (3.2.62) yielding

$$\{\mathbf{E}\}^{fib} = [\mathbf{T}_\sigma^T][\mathbf{Q}]\{\mathbf{E}\}^{cur} \tag{3.2.72}$$

3.2.4.5 Implementation of Triangular Three-Node Finite Elements

Rotation-free thin shells give excellent solutions to many structural problems when the finite element used for the discretization is a *three-node triangle*. Since any shell element is composed of a bending part and a membrane part, a membrane element for three-node triangles is developed next, which will be used as the membrane part of the rotation-free shell element described in section **3.4**.

Consider the triangular element of Fig. 3.11. To clarify the notation, components of the vector (x_1, x_2, x_3) are change to (x, y, z), while the components of (ξ^1, ξ^2) are now (ξ, η). The shape functions for this elements are given by

$$N_1 = 1 - \xi - \eta, \qquad N_2 = \xi, \qquad N_3 = \eta \tag{3.2.73}$$

Derivatives of the shape functions are

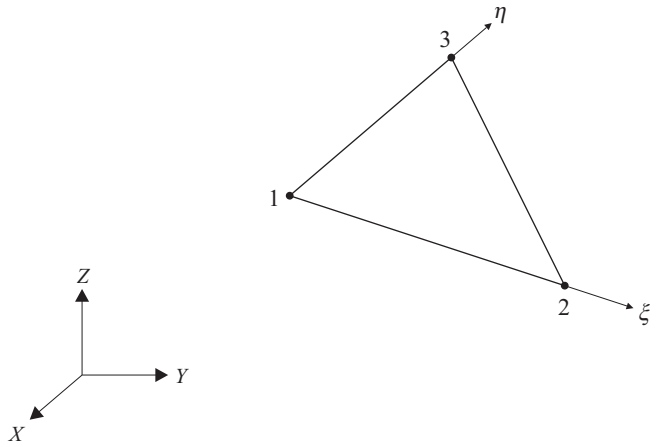

Figure 3.11 *Triangular three-node finite element*

$$\begin{aligned} \frac{\partial N_1}{\partial \xi} &= -1, \qquad \frac{\partial N_1}{\partial \eta} = -1 \\ \frac{\partial N_2}{\partial \xi} &= 1, \qquad \frac{\partial N_2}{\partial \eta} = 0 \\ \frac{\partial N_3}{\partial \xi} &= 0, \qquad \frac{\partial N_3}{\partial \eta} = 1 \end{aligned} \tag{3.2.74}$$

From Eq. (3.2.42) the following equation is derived

$$\frac{\partial x_1^h}{\partial \xi^1} = \frac{\partial x^h}{\partial \xi} = \sum_{J=1}^{n_{\text{node}}=3} \frac{\partial N_J}{\partial \xi} x_J = \frac{\partial N_1}{\partial \xi} x_{J=1} + \frac{\partial N_2}{\partial \xi} x_{J=2} + \frac{\partial N_3}{\partial \xi} x_{J=3} \tag{3.2.75}$$

where Eq. (3.2.40) has been used, and the subindexes naming the element nodes $J = 1, J = 2$ and $J = 3$ are used to clarify the notation. Substituting the corresponding values from Eq. (3.2.74) into Eq. (3.2.75) yields

$$\frac{\partial x^h}{\partial \xi} = (-1)x_{J=1} + (1)x_{J=2} + (0)x_{J=3} = x_{J=2} - x_{J=1} \tag{3.2.76}$$

Similarly for the other derivatives of Eq. (3.2.42) respect to ξ

$$\frac{\partial x_2^h}{\partial \xi^1} = \frac{\partial y^h}{\partial \xi} = \sum_{J=1}^{3} \frac{\partial N_J}{\partial \xi} y_J = y_{J=2} - y_{J=1} \tag{3.2.77}$$

$$\frac{\partial x_3^h}{\partial \xi^1} = \frac{\partial z^h}{\partial \xi} = \sum_{J=1}^{3} \frac{\partial N_J}{\partial \xi} z_J = z_{J=2} - z_{J=1} \tag{3.2.78}$$

Derivatives of Eq. (3.2.42) respect to η yield

$$\frac{\partial x_1^h}{\partial \xi^2} = \frac{\partial x^h}{\partial \eta} = \sum_{J=1}^{3} \frac{\partial N_J}{\partial \eta} x_J = \frac{\partial N_1}{\partial \eta} x_{J=1} + \frac{\partial N_2}{\partial \eta} x_{J=2} + \frac{\partial N_3}{\partial \eta} x_{J=3} \tag{3.2.79}$$

$$\frac{\partial x^h}{\partial \eta} = (-1) x_{J=1} + (0) x_{J=2} + (1) x_{J=3} = x_{J=3} - x_{J=1} \tag{3.2.80}$$

and

$$\frac{\partial x_2^h}{\partial \xi^2} = \frac{\partial y^h}{\partial \eta} = \sum_{J=1}^{3} \frac{\partial N_J}{\partial \eta} y_J = y_{J=3} - y_{J=1} \tag{3.2.81}$$

$$\frac{\partial x_3^h}{\partial \xi^2} = \frac{\partial z^h}{\partial \eta} = \sum_{J=1}^{3} \frac{\partial N_J}{\partial \eta} z_J = z_{J=3} - z_{J=1} \tag{3.2.82}$$

The strain-displacement matrix for this element is composed of

$$\mathbf{B}^{cur} = [\mathbf{B}_1^{cur}, \mathbf{B}_2^{cur}, \mathbf{B}_3^{cur}] \tag{3.2.83}$$

where each submatrix is found substituting Eqs. (3.2.74)-(3.2.82) into Eq. (3.2.42) to yield

$$\mathbf{B}_1^{cur} = \begin{bmatrix} x_{J=1} - x_{J=2} & y_{J=1} - y_{J=2} & z_{J=1} - z_{J=2} \\ x_{J=1} - x_{J=3} & y_{J=1} - y_{J=3} & z_{J=1} - z_{J=3} \\ 2x_{J=1} - x_{J=2} - x_{J=3} & 2y_{J=1} - y_{J=2} - y_{J=3} & 2z_{J=1} - z_{J=2} - z_{J=3} \end{bmatrix} \tag{3.2.84}$$

or

$$\mathbf{B}_1^{cur} = \begin{bmatrix} -(\mathbf{x}_2 - \mathbf{x}_1)^T \\ -(\mathbf{x}_3 - \mathbf{x}_1)^T \\ -(\mathbf{x}_2 - \mathbf{x}_1)^T - (\mathbf{x}_3 - \mathbf{x}_1)^T \end{bmatrix} \tag{3.2.85}$$

Similarly

$$\mathbf{B}_2^{cur} = \begin{bmatrix} x_{J=2} - x_{J=1} & y_{J=2} - y_{J=1} & z_{J=2} - z_{J=1} \\ 0 & 0 & 0 \\ x_{J=3} - x_{J=1} & y_{J=3} - y_{J=1} & z_{J=3} - z_{J=1} \end{bmatrix} = \begin{bmatrix} (\mathbf{x}_2 - \mathbf{x}_1)^T \\ \mathbf{0} \\ (\mathbf{x}_3 - \mathbf{x}_1)^T \end{bmatrix} \tag{3.2.86}$$

and

$$\mathbf{B}_3^{cur} = \begin{bmatrix} 0 & 0 & 0 \\ x_{J=3} - x_{J=1} & y_{J=3} - y_{J=1} & z_{J=3} - z_{J=1} \\ x_{J=2} - x_{J=1} & y_{J=2} - y_{J=1} & z_{J=2} - z_{J=1} \end{bmatrix} = \begin{bmatrix} \mathbf{0} \\ (\mathbf{x}_3 - \mathbf{x}_1)^T \\ (\mathbf{x}_2 - \mathbf{x}_1)^T \end{bmatrix} \tag{3.2.87}$$

The complete strain-displacement matrix for the three-node triangular finite element is given by

$$\mathbf{B}^{cur} = \begin{bmatrix} -(\mathbf{x}_2 - \mathbf{x}_1)^T & (\mathbf{x}_2 - \mathbf{x}_1)^T & \mathbf{0} \\ -(\mathbf{x}_3 - \mathbf{x}_1)^T & \mathbf{0} & (\mathbf{x}_3 - \mathbf{x}_1)^T \\ -(\mathbf{x}_2 - \mathbf{x}_1)^T - (\mathbf{x}_3 - \mathbf{x}_1)^T & (\mathbf{x}_3 - \mathbf{x}_1)^T & (\mathbf{x}_2 - \mathbf{x}_1)^T \end{bmatrix} \tag{3.2.88}$$

The internal forces for this element in Cartesian coordinates are given by

$$\mathbf{f}^{\text{int}}_{(9\times1)} = \int_{\Omega_0} [\mathbf{B}^T]^{cur}_{(9\times3)} [\mathbf{Q}^T]_{(3\times3)} [\mathbf{T}_\sigma]_{(3\times3)} \{\mathbf{S}\}^{fib}_{(3\times1)} d\Omega_0 \tag{3.2.89}$$

Usually at this point numerical integration is performed. However, for this element exact integration can be found using the Cross product

$$A_0 = \frac{1}{2} \|(\mathbf{X}_2 - \mathbf{X}_1) \times (\mathbf{X}_3 - \mathbf{X}_1)\| \tag{3.2.90}$$

giving the area A_0 of the triangular membrane element. Therefore reference domain integral for the internal forces can be written as

$$\mathbf{f}^{\text{int}} = A_0 h [\mathbf{B}^T]^{cur} [\mathbf{Q}^T] [\mathbf{T}_\sigma] \{\mathbf{S}\}^{fib} \tag{3.2.91}$$

or in indicial notation

$$f_a^{\text{int}} = A_0 h [B_{ab}^T]^{cur} [Q_{bc}^T] [T_{ce}]_\sigma \{S_e\}^{fib} \tag{3.2.92}$$

where h is the membrane thickness in the reference configuration.

To find the components of the strain tensor, discretization of the covariant base vectors for this element in the reference configuration, Eq. (3.2.25), yields

$$\mathbf{G}_1 = \sum_{I=1}^{n_{\text{node}}=3} \frac{\partial N_I}{\partial \xi} \mathbf{X}_I = \mathbf{X}_2 - \mathbf{X}_1 \tag{3.2.93}$$

and

$$\mathbf{G}_2 = \sum_{I=1}^{n_{\text{node}}=3} \frac{\partial N_I}{\partial \eta} \mathbf{X}_I = \mathbf{X}_3 - \mathbf{X}_1 \tag{3.2.94}$$

The corresponding discretization in the current configuration for this element is given by Eq. (3.2.27) yielding

$$\mathbf{g}_1 = \sum_{I=1}^{n_{\text{node}}=3} \frac{\partial N_I}{\partial \xi} \mathbf{x}_I = \mathbf{x}_2 - \mathbf{x}_1 \tag{3.2.95}$$

and

$$\mathbf{g}_2 = \sum_{I=1}^{n_{\text{node}}=3} \frac{\partial N_I}{\partial \eta} \mathbf{x}_I = \mathbf{x}_3 - \mathbf{x}_1 \tag{3.2.96}$$

Substituting Eqs. (3.2.93)-(3.2.96) into Eq. (3.2.5) gives the covariant components of the metric tensor $G_{\alpha\beta}$ and $g_{\alpha\beta}$, which substituted into Eq. (3.2.13) yields the components of the strain tensor $\mathbf{E}^{cur}$.

The transformation matrix $\mathbf{Q}$ is a function of the components of the tensor $\mathbf{J}_\xi$ given by Eq. (3.2.46) where

$$\mathbf{G}_1 \cdot \mathbf{e}_1^{loc} = \mathbf{G}_1 \cdot \frac{\mathbf{G}_1}{\|\mathbf{G}_1\|} \tag{3.2.97}$$

Here Eq. (3.2.17) has been substituted. Using the identity

$$\|\mathbf{G}_1\| = (\mathbf{G}_1 \cdot \mathbf{G}_1)^{1/2} \tag{3.2.98}$$

and the covariant base vector $\mathbf{G}_1$ of Eq. (3.2.93), Eq. (3.2.97) can be written as

$$\mathbf{G}_1 \cdot \mathbf{e}_1^{loc} = \|\mathbf{X}_2 - \mathbf{X}_1\| \tag{3.2.99}$$

The remaining components of the Jacobian tensor $\bar{\mathbf{J}}_\xi$ are found using the same methodology yielding

$$\bar{\mathbf{J}}_\xi = \begin{bmatrix} \|\mathbf{X}_2 - \mathbf{X}_1\| & \frac{(\mathbf{X}_2 - \mathbf{X}_1)\cdot(\mathbf{X}_3 - \mathbf{X}_1)}{\|\mathbf{X}_2 - \mathbf{X}_1\|} \\ 0 & \frac{\|(\mathbf{X}_2 - \mathbf{X}_1)\times(\mathbf{X}_3 - \mathbf{X}_1)\|}{\|\mathbf{X}_2 - \mathbf{X}_1\|} \end{bmatrix} \tag{3.2.100}$$

Components of Eq. (3.2.100) are used to build the transformation matrix $\mathbf{Q}$ giving by Eq. (3.2.53) and Eq. (3.2.49). Note that this matrix is always evaluated in the reference configuration.

An important advantage of this element is that all the expression can be obtained with the vectors $\mathbf{X}_2 - \mathbf{X}_1$ and $\mathbf{X}_3 - \mathbf{X}_1$ of the reference configuration which are evaluated just once, and the vectors $\mathbf{x}_2 - \mathbf{x}_1$ and $\mathbf{x}_3 - \mathbf{x}_1$ of the current configuration.

3.2.4.6 Pressure Follower Forces Discretization

From the virtual external work for pressure follower forces given by Eq. (3.2.16), the external forces emerge for the three-node triangular element with constant pressure as

$$\mathbf{f}^{\text{ext}} = \frac{1}{3} A p \mathbf{n} \tag{3.2.101}$$

where A is the area of the triangular membrane element in current configuration given by

$$A = \frac{1}{2} \|(\mathbf{x}_2 - \mathbf{x}_1) \times (\mathbf{x}_3 - \mathbf{x}_1)\| \tag{3.2.102}$$

and $\mathbf{n}$ is the normal to the current surface, which for the three-node triangle is given by

$$\mathbf{n} = \frac{(\mathbf{x}_2 - \mathbf{x}_1) \times (\mathbf{x}_3 - \mathbf{x}_1)}{\|(\mathbf{x}_2 - \mathbf{x}_1) \times (\mathbf{x}_3 - \mathbf{x}_1)\|} \tag{3.2.103}$$

Substituting Eqs. (3.2.102)-(3.2.103) into Eq. (3.2.101), the external forces can be written as

$$\mathbf{f}^{\text{ext}} = \frac{p}{6} (\mathbf{x}_2 - \mathbf{x}_1) \times (\mathbf{x}_3 - \mathbf{x}_1) \tag{3.2.104}$$

3.2.5 Wrinkling

Here a wrinkling algorithm based on a modified material model is developed. The idea of this algorithm is to present a simple algorithm that allow to solve the wrinkling phenomena that are not predicted by normal membrane theory even its flexural stiffness vanishes. This algorithm is not intended for time-history analysis, consequently only the final solution is accurate.

At any point on its surface, a membrane must be in one of three states. In a *slack* state, the membrane is not stretched in any direction. In a *taut* state, the membrane is in tension in all directions. If the membrane is neither taut not slack, it is in a *wrinkle* state corresponding to uniaxial tension. In a slack or wrinkled criterion the real configuration of the membrane is undefined. To avoid this, the slack or wrinkled region can be replaced with an average smoothed pseudo-surface where material points on the real wrinkled surface are projected onto the pseudo-surface.

To predict the real configuration of a wrinkled membrane, a very dense finite element mesh is needed to perform the analysis, which sometimes needs an initial perturbation, see Tessler et al. (2003). However from an engineering point of view, the shape of the wrinkles are not as important as the membrane stresses. Therefore different wrinkling algorithms are developed.

In this work, the wrinkling criterion based on principal stresses and principal strains introduced by Roddeman et al. (1987a) is used. Its main objective is the differentiation of a membrane state for isotropic and orthotropic materials. Table 3.2 shows this classification.

First the membrane state is determined. If the membrane is taut, the constitutive matrix $[\mathbf{C}]$ does not need to be modified. Then $[\mathbf{C}_{CON}] = [\mathbf{C}]$ and the state stress is computed as

$$\{\mathbf{S}\}^{fib} = [\mathbf{C}_{CON}]\{\mathbf{E}\}^{fib} \tag{3.2.105}$$

Stress and strain	Wrinkling	Membrane
$S_{II} > 0$	No	Taut
$E_I > 0$ and $S_{II} \leq 0$	One axial	Wrinkled
$E_I \leq 0$	Two axial	Slack

Table 3.2 *Wrinkling criterion*

If the membrane is slack, components of the constitutive matrix $[\mathbf{C}]$ are modified yielding $[\mathbf{C}_{CON}] = \mathbf{0}$ and the stress field is simply

$$\{\mathbf{S}\}^{fib} = \mathbf{0} \tag{3.2.106}$$

Finally if the membrane is wrinkled, the angle θ_σ of principal stresses is found. With this angle the rotation matrix for stresses given by Eq. (3.2.59) and the rotation matrix for strains given by Eq. (3.2.60) are built, where the angle θ is replaced by the angle θ_σ. Then the constitutive matrix is rotated with the following equation

$$[\widetilde{\mathbf{C}}] = [\mathbf{T}_\varepsilon^T][\mathbf{C}][\mathbf{T}_\varepsilon] \tag{3.2.107}$$

This new rotated constitutive matrix is modified as shown next yielding

$$[\mathbf{C}_{MOD}] = \begin{bmatrix} \widetilde{C}_{1,1} & 0 & \widetilde{C}_{1,3} \\ 0 & 0 & 0 \\ \widetilde{C}_{3,1} & 0 & \widetilde{C}_{3,3} \end{bmatrix} \tag{3.2.108}$$

Finally this modified constitutive matrix is rotated back to its original position with the following equation giving

$$[\mathbf{C}_{CON}] = [\mathbf{T}_\sigma][\mathbf{C}_{MOD}][\mathbf{T}_\sigma^T] \tag{3.2.109}$$

Now the stress field for the wrinkled state is computed using

$$\{\mathbf{S}\}^{fib} = [\mathbf{C}_{CON}]\{\mathbf{E}\}^{fib} \tag{3.2.110}$$

Since a geometrically non-linear problem is being solved, it is common to use a Newton-Raphson scheme with an appropriate linearization. Usually each time step t_i is solved within 3 to 5 Newton-Raphson iterations. If the wrinkling algorithm presented is applied at each iteration, then the number of iterations may be increased significantly.

To avoid this problem, the wrinkling algorithm is applied only for the first two iterations of the time step. After the second iteration the constitutive matrix $[\mathbf{C}_{CON}]$ is kept constant until convergence for the time step is reached. Therefore the model perform 4 to 6 Newton-Raphson iterations per time step.

An important aspect to be accounted for orthotropic materials is to find the correct wrinkling direction, as given in Jarasjarungkiat et al. (2007).

A limitation of this work is that the principal stress direction is taken as the wrinkling direction, which is not true for orthotropic materials. However for the studied cases, the solution is quite similar to the reported by other investigations.

3.3 Cable Elements

Cable elements are modeled as geometrically non-linear unidimensional truss elements in Euclidean space. Here a cable element is developed as a particular case of the membrane theory.

3.3.1 Cable Formulation

The position vector $\mathbf{X}$ for the cable element in the reference configuration Ω_0 is defined by one independent curvilinear coordinate ξ, shown in Fig. 3.12, as

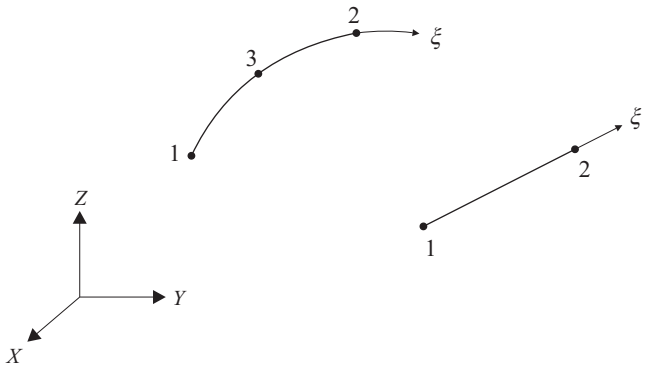

Figure 3.12 *Cable two-node and three-node finite elements*

$$\mathbf{X} = \mathbf{X}(\xi) \tag{3.3.1}$$

The position vector $\mathbf{x}$ of the current configuration Ω is given by

$$\mathbf{x} = \mathbf{x}(\xi, t) \tag{3.3.2}$$

The covariant base vector of the curvilinear coordinate system for this element on Ω_0 and Ω are defined respectively by

$$\mathbf{G}_1 = \frac{\partial \mathbf{X}}{\partial \xi}, \qquad \mathbf{g}_1 = \frac{\partial \mathbf{x}}{\partial \xi} \tag{3.3.3}$$

The covariant components of the metric tensors are given by

$$G_{11} = \mathbf{G}_1 \cdot \mathbf{G}_1 \qquad g_{11} = \mathbf{g}_1 \cdot \mathbf{g}_1 \tag{3.3.4}$$

for the reference and current configurations respectively. The contravariant base vectors are given for Ω_0 and Ω respectively by

$$\mathbf{G}^1 = G^{11} \cdot \mathbf{G}_1 \qquad \mathbf{g}^1 = g^{11} \cdot \mathbf{g}_1 \tag{3.3.5}$$

where the contravariant components of the metric tensors are

$$G^{11} = \frac{1}{G_{11}} \qquad g^{11} = \frac{1}{g_{11}} \tag{3.3.6}$$

for the corresponding configurations. The Green-Lagrange strain tensor for the cable element is given by

$$E_{11}^{cur} = \frac{1}{2}\left(g_{11} - G_{11}\right) \tag{3.3.7}$$

Using the appropriate constitutive equation to relate the second Piola-Kirchhoff stress tensor and the Green-Lagrange strain tensor in curvilinear coordinates, the stress tensor S_{cur}^{11} is found.

From Eq. (3.3.4) and Eq. (3.3.7), the variation δE_{11}^{cur} yields

$$\delta E_{11}^{cur} = \frac{1}{2}\delta g_{11} = \mathbf{g}_1 \cdot \delta \mathbf{g}_1 \tag{3.3.8}$$

Finally the virtual internal work, Eq. (3.1.11), can be expressed in curvilinear coordinates for the cable element as

$$\delta \mathcal{W}^{\text{int}} = \int_{\Omega_0} \delta E_{11}^{cur} S_{cur}^{11} d\Omega_0 \tag{3.3.9}$$

3.3.2 Finite Element Discretization for Cables

The discretization is established for the total Lagrangian formulation. Here a two-node cable element is developed. Consequently Eq. (3.3.1) is approximated by

$$\mathbf{X}^h(\xi) = \sum_{I=1}^{n_{\text{node}}} N_I(\xi)\mathbf{X}_I \quad \text{or} \quad X_i^h(\xi) = \sum_{I=1}^{n_{\text{node}}} N_I(\xi) X_{iI} \qquad \forall i = 1,\, n_{\text{dime}} \tag{3.3.10}$$

where the shape functions $N_I(\xi)$ are given by

$$N_1 = \frac{1}{2}\left(1 - \xi\right), \qquad N_2 = \frac{1}{2}\left(1 + \xi\right) \tag{3.3.11}$$

Derivatives of the shape functions yield

$$\frac{\partial N_1}{\partial \xi} = -\frac{1}{2}\,\xi, \qquad \frac{\partial N_2}{\partial \xi} = \frac{1}{2}\,\xi \tag{3.3.12}$$

The equation of motion, Eq. (3.3.2), is given by

$$x_i^h(\xi,t) = \sum_{I=1}^{n_{\text{node}}} N_I(\xi) x_{iI}(t) \qquad \forall i = 1,\ n_{\text{dime}}$$
$$\text{or} \qquad \mathbf{x}^h(\xi,t) = \sum_{I=1}^{n_{\text{node}}} N_I(\xi)\mathbf{x}_I(t) \tag{3.3.13}$$

The covariant base vector in the reference configuration Ω_0 is expressed by

$$\mathbf{G}_1 = \sum_{I=1}^{n_{\text{node}}} \frac{\partial N_I}{\partial \xi}\mathbf{X}_I = \frac{1}{2}(\mathbf{X}_2 - \mathbf{X}_1) \tag{3.3.14}$$

In the current configuration Ω the covariant base vector is

$$\mathbf{g}_1 = \sum_{I=1}^{n_{\text{node}}} \frac{\partial N_I}{\partial \xi}\mathbf{x}_I = \frac{1}{2}(\mathbf{x}_2 - \mathbf{x}_1) \tag{3.3.15}$$

which variation $\delta\mathbf{g}_1$ is expressed as

$$\delta\mathbf{g}_1 = \frac{1}{2}(\delta\mathbf{u}_2 - \delta\mathbf{u}_1) \tag{3.3.16}$$

Covariant components of the metric tensor, Eq. (3.3.4), yield

$$G_{11} = \frac{1}{4}(\mathbf{X}_2 - \mathbf{X}_1)\cdot(\mathbf{X}_2 - \mathbf{X}_1) = \frac{1}{4}L^2, \qquad g_{11} = \frac{1}{4}(\mathbf{x}_2 - \mathbf{x}_1)\cdot(\mathbf{x}_2 - \mathbf{x}_1) = \frac{1}{4}l^2 \tag{3.3.17}$$

where L is the length of the element in the reference configuration and l is the length of the current configuration. Substituting Eq. (3.3.17) into Eq. (3.3.7) the Green-Lagrange strain tensor yields

$$E_{11}^{cur} = \frac{1}{8}\left(l^2 - L^2\right) \tag{3.3.18}$$

Transformation from curvilinear coordinates to Cartesian coordinates requires

$$J_{11} = \mathbf{G}_1 \cdot \mathbf{e}_1^{loc} = \frac{1}{2}L \tag{3.3.19}$$

and

$$E_{11}^{cur} = J_{11}E_{11}^{loc}J_{11} = J_{11}^2 E_x^{loc} \tag{3.3.20}$$

From Eq. (3.3.20)

$$E_x^{loc} = \frac{1}{J_{11}^2}E_{11}^{cur} \tag{3.3.21}$$

and

$$E_x^{loc} = \frac{l^2 - L^2}{2L^2} \tag{3.3.22}$$

The discretization of δE_{11}^{cur}, given by Eq. (3.3.8) yields

$$\delta E_{11}^{cur} = \frac{1}{4}\left(\mathbf{x}_2 - \mathbf{x}_1\right) \cdot \left(\delta\mathbf{u}_2 - \delta\mathbf{u}_1\right) \tag{3.3.23}$$

which can be written in matrix notation as

$$\delta E_{11}^{cur} = \frac{1}{4}\begin{bmatrix} -\left(\mathbf{x}_2 - \mathbf{x}_1\right)^T & \left(\mathbf{x}_2 - \mathbf{x}_1\right)^T \end{bmatrix} \begin{bmatrix} \delta\mathbf{u}_1 \\ \delta\mathbf{u}_2 \end{bmatrix} \tag{3.3.24}$$

where the strain-displacement matrix for the cable element is given by

$$\mathbf{B}_{(1\times 6)}^{cur} = \frac{1}{4}\begin{bmatrix} -\left(\mathbf{x}_2 - \mathbf{x}_1\right)^T & \left(\mathbf{x}_2 - \mathbf{x}_1\right)^T \end{bmatrix} \tag{3.3.25}$$

From Eq. (3.3.21), transformation of $\mathbf{B}^{cur}$ from curvilinear coordinates to Cartesian coordinates yields

$$\mathbf{B}_{(1\times 6)}^{loc} = \frac{1}{L^2}\begin{bmatrix} -\left(\mathbf{x}_2 - \mathbf{x}_1\right)^T & \left(\mathbf{x}_2 - \mathbf{x}_1\right)^T \end{bmatrix} \tag{3.3.26}$$

Finally, the internal forces for a two-node cable element are

$$\mathbf{f}_{(6\times 1)}^{\text{int}} = A_0\, L\, [\mathbf{B}^T]_{(6\times 1)}^{loc} \{S_x\}_{(1\times 1)}^{loc} \tag{3.3.27}$$

where A_0 is the cross-sectional area of the element, L is the length in the reference configuration and $S_x^{loc} = E\, E_x^{loc}$ with E being the Young's modulus.

3.4 Shell Elements

3.4.1 Introduction

Shells are used in wide structural fields such as civil, mechanical, naval and airspace engineering. A formulation based on thin-shell theory can be used to analyze several applications of shell structures. Since shell analysis demand a lot of computer memory and cpu time to be computed, a formulation using displacements as the only degrees of freedom is developed.

The basic idea of the shell theory is to take into account the particular three-dimension model and by *integration over the thickness* get a two-dimensional model in the Euclidean space formulated on the middle surface of the shell. The pioneers of this kind of derivation were Kirchhoff (1876) and Love (1934). The main assumption of this theory of shells (plates) is to preserve the orthogonality of the normal to the middle-surface. The well-known problems to derive conforming C^1 continuous thin shell elements motivated a number of authors to explore the possibilities of Reissner (1945) and Mindlin (1951) theory. This theory relaxes the normal orthogonality condition, introducing the shear deformation stress that is important for thick shell

simulations. Unfortunately Reissner-Mindlin plate and shell elements suffer the so-called *shear locking* in the thin limit. This difficulty wrecked the full success of Reissner-Mindlin plate and shell elements for practical engineering analysis.

The first developments of plate and shell elements using Kirchhoff-Love theory were made by Melosh (1961), Zienkiewics and Cheung (1964), Clough and Tocher (1965) among many others. On the other hand, Hughes et al. (1977), Oñate et al. (1979), Bathe and Dvorkin (1985) and Zienkiewics et al. (1990) proposed the first plate and shell elements based on Reissner-Mindlin theory. A complete state of the art for linear plate elements can be found in Oñate (1992).

Nonlinear behavior of shell elements is continuously increasing because of its important aspects in which large rotations and large deformations are involved as well as nonlinear material properties. Several studies have been carried out for example by Simo and Fox (1989), Simo et al. (1990a), Simo and Kennedy (1992), among many others. Since shell analysis requires a lot of memory and cpu-time to compute, several authors have tried to derive plate and shell elements with displacements as the only nodal variables.

The idea of using the deflection as the only nodal variables, i.e. rotation-free, is not new and many different procedures are based on this approach, i.e. Ugural (1981). The well-known difficulties of finite difference analysis with boundary conditions and the problems for dealing with non-orthogonal or unstructured grids limited their progress. One of the first attempts to use finite elements was due to Nay and Utku (1972) who derived a rotation free thin plate triangle using a least-square quadratic approximation to describe the deflection field within the patch surrounding a node in terms of the deflections of the patch nodes. Later, Barnes (1977) proposed a method for deriving a three-node triangle with the nodal deflections as the only degrees of freedom based on the computation of the curvatures in terms of the nodal rotations at the middle-side points from the nodal deflections of adjacent elements. This method was exploited by Hampshire et al. (1992) assuming that the elements are hinged together at their common boundaries and the bending stiffness is represented by torsional springs resisting rotations about the hinge line. Oñate and Cervera (1993) proposed a general procedure based on finite volume concepts for deriving thin plate elements of triangular and quadrilateral shapes with the nodal deflections as the only degree of freedom. Brunet and Sabourin (1994) proposed a different approach to compute the constant curvature field within each triangle in terms of the six-node displacement of a macro-element. This triangular element was successfully applied to nonlinear shell analysis using an explicit dynamic approach. Zárate (1996) continue with the study of rotation free elements of Oñate and Cervera (1993) developing new triangular elements. This formulation applied to large deformations with an explicit dynamic procedure was presented by Cendoya (1996). Rojek et al. (1998) proposed the same element that Cendoya (1996) but applied to metal forming processes. As an alternative formulation for large strain plasticity, the BST shell element was introduced by Flores and Oñate (2001). A new perspective using a subdivision of surfaces for thin-shell analysis was introduced by Cirak et al. (2000) for small strains, and Cirak and Ortiz (2001) for large deformations. An improvement of the BST shell element using an assumed strain approach is given by Flores and Oñate (2005).

3.4.2 Shell Formulation

A finite deformation shell formulation is presented. Here Greek indices take on values of 1 and 2 while lower latin indices take on values of 1, 2 and 3. The position vector $\widetilde{\mathbf{R}}$ on the middle surface in the reference configuration is defined by the indepent curvilinear coordinates ξ^1, ξ^2 and ζ as

$$\widetilde{\mathbf{R}}\left(\xi^1,\xi^2,\zeta\right) = \mathbf{X}\left(\xi^1,\xi^2\right) + \zeta\mathbf{N}\left(\xi^1,\xi^2\right) \tag{3.4.1}$$

where $\mathbf{N}$ is the normal to the middle surface on Ω_0 and $-\frac{h_0}{2} \leq \zeta \leq \frac{h_0}{2}$ with h_0 being the shell thickness in the reference configuration, see Fig. 3.13.

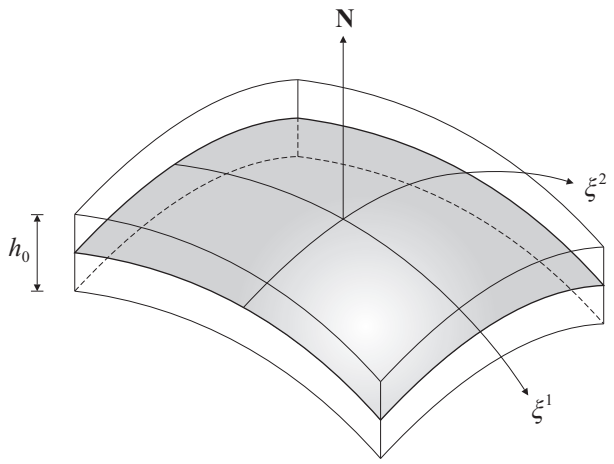

Figure 3.13 *Shell middle surface*

The position vector $\widetilde{\mathbf{r}}$ on the current configuration is given by

$$\widetilde{\mathbf{r}}\left(\xi^1,\xi^2,\zeta,t\right) = \mathbf{x}\left(\xi^1,\xi^2,t\right) + \zeta\lambda\left(\xi^1,\xi^2,t\right)\mathbf{n}\left(\xi^1,\xi^2,t\right) \tag{3.4.2}$$

where $\mathbf{n}$ is the normal to the middle surface on Ω and λ is the thickness stretch that relates the thickness h of the deformed shell to the thickness h_0 of the undeformed shell. Finite thickness stretch measured by λ play an important role in problems involving finite membrane strains or contact, as given in Simo et al. (1990b). However, in this work a Saint Venant-Kirchhoff material model is used and therefore only small strains are assumed. Consequently, the λ term is not considered.

The convected covariant base vectors of the curvilinear coordinates system on Ω_0 are defined by

$$\begin{aligned}
\widetilde{\mathbf{G}}_\alpha &= \frac{\partial\widetilde{\mathbf{R}}}{\partial\xi^\alpha} = \frac{\partial\mathbf{X}}{\partial\xi^\alpha} + \zeta\frac{\partial\mathbf{N}}{\partial\xi^\alpha} = \mathbf{G}_\alpha + \zeta\mathbf{N}_{,\alpha} \\
\widetilde{\mathbf{G}}_3 &= \frac{\partial\widetilde{\mathbf{R}}}{\partial\zeta} = \mathbf{N}
\end{aligned} \tag{3.4.3}$$

Here $\mathbf{G}_\alpha$ are the middle surface basis vectors in the reference configuration. The convected covariant base vectors on the current configuration Ω are given by

$$\begin{aligned}\widetilde{\mathbf{g}}_\alpha &= \frac{\partial \widetilde{\mathbf{r}}}{\partial \xi^\alpha} = \frac{\partial \mathbf{x}}{\partial \xi^\alpha} + \zeta \frac{\partial \mathbf{n}}{\partial \xi^\alpha} = \mathbf{g}_\alpha + \zeta \mathbf{n}_{,\alpha} \\ \widetilde{\mathbf{g}}_3 &= \frac{\partial \widetilde{\mathbf{r}}}{\partial \zeta} = \mathbf{n}\end{aligned} \tag{3.4.4}$$

where $\mathbf{g}_\alpha$ are the middle surface basis vectors in the current configuration. The convected contravariant base vectors follow from the relations

$$\widetilde{\mathbf{G}}^{\,i} \cdot \widetilde{\mathbf{G}}_j = \delta^i_j, \qquad \widetilde{\mathbf{g}}^{\,i} \cdot \widetilde{\mathbf{g}}_j = \delta^i_j \tag{3.4.5}$$

where δ^i_j is the Kronecker delta. The covariant metric tensors in both configurations follow as

$$\widetilde{G}_{ij} = \widetilde{\mathbf{G}}_i \cdot \widetilde{\mathbf{G}}_j, \qquad \widetilde{g}_{ij} = \widetilde{\mathbf{g}}_i \cdot \widetilde{\mathbf{g}}_j \tag{3.4.6}$$

Components of the Green-Lagrange strain tensor are given as the difference between the covariant metric tensors on the current and reference configurations of the shell yielding

$$E_{ij} = \frac{1}{2}\left(\widetilde{g}_{ij} - \widetilde{G}_{ij}\right) \tag{3.4.7}$$

The Green-Lagrange strain tensor can be extended to be written in the form of

$$E_{ij} = \epsilon_{ij} + \zeta \kappa_{ij} + \zeta^2 \gamma_{ij} \tag{3.4.8}$$

where the non-zero components of the above expression are given by

$$\begin{aligned}\epsilon_{\alpha\beta} &= \frac{1}{2}\left(\mathbf{g}_\alpha \cdot \mathbf{g}_\beta - \mathbf{G}_\alpha \cdot \mathbf{G}_\beta\right), \qquad \epsilon_{\alpha 3} = \frac{1}{2}\left(\mathbf{g}_\alpha \cdot \mathbf{n} - \mathbf{G}_\alpha \cdot \mathbf{N}\right) \\ \epsilon_{33} &= \frac{1}{2}\left(\mathbf{n} \cdot \mathbf{n} - \mathbf{N} \cdot \mathbf{N}\right)\end{aligned} \tag{3.4.9}$$

$$\kappa_{\alpha\beta} = \mathbf{g}_\alpha \cdot \mathbf{n}_{,\beta} - \mathbf{G}_\alpha \cdot \mathbf{N}_{,\beta} \tag{3.4.10}$$

$$\gamma_{\alpha\beta} = \frac{1}{2}\left(\mathbf{n}_{,\alpha} \cdot \mathbf{n}_{,\beta} - \mathbf{N}_{,\alpha} \cdot \mathbf{N}_{,\beta}\right) \tag{3.4.11}$$

This work is intended for the Kirchhoff-Love theory of thin shells, consequently the deformed director $\mathbf{n}$ coincides with the unit normal to the current middle surface. Therefore the values $\epsilon_{\alpha 3}$ and ϵ_{33} vanish identically and values for thin shells of ζ^2 can be neglected. This constraint yields the components of the Green-Lagrange strain tensor to be deduced from the deformation of the middle surface of the shell as

$$E_{\alpha\beta} = \epsilon_{\alpha\beta} + \zeta\kappa_{\alpha\beta} = E^{\text{memb}}_{\alpha\beta} + \zeta E^{\text{bend}}_{\alpha\beta} \tag{3.4.12}$$

where

$$\epsilon_{\alpha\beta} = \frac{1}{2}\left(g_{\alpha\beta} - G_{\alpha\beta}\right) \tag{3.4.13}$$

is identical to Eq. (3.2.13) and measure membrane strains. For convenience of the discretization given in section **3.4.3**, the bending strains are written as[2]

$$\kappa_{\alpha\beta} = \mathbf{G}_{\alpha,\beta} \cdot \mathbf{N} - \mathbf{g}_{\alpha,\beta} \cdot \mathbf{n} = K_{\alpha\beta} - k_{\alpha\beta} \tag{3.4.14}$$

The variation of the Green-Lagrange strain tensor is given by the variation of Eq. (3.4.12) yielding

$$\delta E_{\alpha\beta} = \delta E^{\text{memb}}_{\alpha\beta} + \zeta \delta E^{\text{bend}}_{\alpha\beta} \tag{3.4.15}$$

With an appropriate constitutive equation to relate stresses and strains, the virtual internal work is expressed as

$$\delta \mathcal{W}^{\text{int}} = \int_{\overline{\Omega}_0} \int_{-\frac{h}{2}}^{+\frac{h}{2}} \delta E_{\alpha\beta} S^{\alpha\beta} d\zeta d\overline{\Omega}_0 \tag{3.4.16}$$

where $\overline{\Omega}_0$ is the middle surface domain.

3.4.3 Finite Element Discretization for Shells

The discretization used for the thin shell element is given for the total Lagrangian formulation. Discretization only for bending strains is presented since membrane strains given in Eq. (3.4.13) are developed in section **3.2.4**.

In this work the rotation free triangle element presented by Flores and Oñate (2001) is extended to account for the principal fiber direction and perform the analysis with initially pre-stressed fields or orthotropic materials.

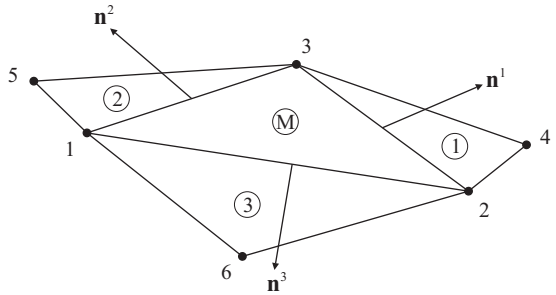

Figure 3.14 *Shell patch*

[2] $(\mathbf{g}_\alpha \cdot \mathbf{n})_{,\beta} = \mathbf{g}_\alpha \cdot \mathbf{n}_{,\beta} + \mathbf{g}_{\alpha,\beta} \cdot \mathbf{n} = 0$ and $(\mathbf{G}_\alpha \cdot \mathbf{N})_{,\beta} = \mathbf{G}_\alpha \cdot \mathbf{N}_{,\beta} + \mathbf{G}_{\alpha,\beta} \cdot \mathbf{N} = 0$

Bending effect for this rotation-free triangle element is given by the displacement field of one element and all nodes of immediately adjacent elements, as shown in Fig. 3.14.

The path description is as follows:

- Element number is inside a circle.
- Nodes of the main element (M) are numbered locally as 1, 2 and 3.
- Sides of the main element are defined by its local node opposite to the side.
- Adjacent elements are numbered with the number associated to the common side 1, 2 and 3.
- The remaining nodes of the patch are numbered locally as 4, 5, and 6 corresponding to nodes on adjacent elements (1), (2) and (3) respectively.

Conectivities for the path element are defined in table 3.3.

	Conectivities		
Element	Node 1	Node 2	Node 3
(M)	1	2	3
(1)	4	3	2
(2)	5	1	3
(3)	6	2	1

Table 3.3 *Patch conectivities*

A local coordinate system must be defined for the patch. In the original work of Flores and Oñate (2001), the following definition was proposed: the unit vector $\mathbf{e}_1^{loc}$ was directed from node 1 to node 2. Unit vector $\mathbf{e}_3^{loc}$ was given by the normal of the main element (M). The last unit vector was obtained by $\mathbf{e}_2^{loc} = \mathbf{e}_3^{loc} \times \mathbf{e}_1^{loc}$.

In this work, the local coordinate system is given by the local fiber Cartesian base system, defined in section **3.2.3**. Then the base system for each finite element is given by the unit vectors $\mathbf{e}_1^{fib}$, $\mathbf{e}_2^{fib}$ and the normal $\mathbf{e}_3^{fib}$. The choice for this local system allow us to compute shells with a prestressed field as well as orthotropic material definitions.

The bending part of Eq. (3.4.16) is given by,

$$\delta \mathcal{W}^{\text{int}} = \int_{-\frac{h}{2}}^{+\frac{h}{2}} \int_{\overline{\Omega}_0} \delta E_{\alpha\beta}^{\text{bend}} \, S_{\text{bend}}^{\alpha\beta} \, d\overline{\Omega}_0 d\zeta \tag{3.4.17}$$

and the values of $E_{\alpha\beta}^{\text{bend}}$ and $\delta E_{\alpha\beta}^{\text{bend}}$ are needed to evaluate the internal forces. The bending strains for the current configuration are expressed by

$$k_{\alpha\beta} = \mathbf{g}_{\alpha,\beta} \cdot \mathbf{n} \tag{3.4.18}$$

which can be written in the form

$$k_{\alpha\beta} = \frac{1}{A_0} \int_{\overline{\Omega}_0} \mathbf{g}_{\alpha,\beta} d\overline{\Omega}_0 \cdot \mathbf{n} \tag{3.4.19}$$

and then applying the divergence theorem[3] yields

$$k_{\alpha\beta} = \frac{1}{A_0} \int_{\overline{\Gamma}_0} \bar{n}_\beta \, \mathbf{g}_\alpha d\overline{\Gamma}_0 \cdot \mathbf{n} \tag{3.4.20}$$

where $\bar{n}_\beta$ are the components of the normal to the boundary, in-plane with the unit base vectors $\mathbf{e}_1^{fib}$ and $\mathbf{e}_2^{fib}$, of the main element (M), as shown in Fig. 3.14. Since the boundary integral of the three-node triangular main element can be computed explicitly, then Eq. (3.4.20) is expressed as

$$k_{\alpha\beta} = \frac{1}{A_0} \sum_{J=1}^{n_{\text{sides}}} l^J \bar{n}_\beta^J \, \mathbf{g}_\alpha \cdot \mathbf{n} \tag{3.4.21}$$

where $n_{\text{sides}} = 3$, J is the number of the side in the main element, l^J is the length of side J and $\bar{n}_\beta^J$ are the components of the normal to the boundary of side J of the main element.

At this point it is convenient to change from curvilinear coordinates to the local fiber Cartesian base system, so the whole patch is with the same local coordinate system.

Discretization of $\mathbf{g}_\alpha$ is expressed in Eq. (3.2.27), which can be written explicitly as

$$\begin{bmatrix} \mathbf{g}_1 \\ \mathbf{g}_2 \end{bmatrix} = \sum_{I=1}^{n_{\text{node}}} \begin{bmatrix} \frac{\partial N_I}{\partial \xi} \\ \\ \frac{\partial N_I}{\partial \eta} \end{bmatrix} \mathbf{x}_I(t) \tag{3.4.22}$$

Since the formulation is to be carried out in the local fiber system, the derivatives of the shape functions need to be transformed. The Jacobian transformation tensor $\mathbf{J}_\xi$ in the current configuration is defined as

$$\mathbf{J}_\xi = \begin{bmatrix} \mathbf{g}_1 \cdot \mathbf{e}_1^{fib} & \mathbf{g}_2 \cdot \mathbf{e}_1^{fib} \\ \mathbf{g}_1 \cdot \mathbf{e}_2^{fib} & \mathbf{g}_2 \cdot \mathbf{e}_2^{fib} \end{bmatrix} \tag{3.4.23}$$

and the Cartesian derivatives become

$$\begin{bmatrix} \frac{\partial N_I}{\partial x} \\ \\ \frac{\partial N_I}{\partial y} \end{bmatrix} = \mathbf{J}_\xi^{-T} \begin{bmatrix} \frac{\partial N_I}{\partial \xi} \\ \\ \frac{\partial N_I}{\partial \eta} \end{bmatrix} \tag{3.4.24}$$

Then Eq. (3.4.22) can be written in Cartesian coordinates as

$$\begin{bmatrix} \mathbf{x}_{,1}^h \\ \mathbf{x}_{,2}^h \end{bmatrix} = \sum_{I=1}^{n_{\text{node}}} \begin{bmatrix} \frac{\partial N_I}{\partial x} \\ \\ \frac{\partial N_I}{\partial y} \end{bmatrix} \mathbf{x}_I(t) \tag{3.4.25}$$

Using Voigt notation, Eq. (3.4.21) can be written in local fiber Cartesian coordinates as

[3] $\int_\Omega \frac{\partial \mathbf{u}}{\partial x_i} d\Omega = \int_\Gamma \bar{n}_i \mathbf{u} d\Gamma$

$$\begin{bmatrix} k_{11} \\ k_{22} \\ k_{12} \end{bmatrix} = \frac{1}{A_0} \sum_{J=1}^{n_{\text{sides}}} l^J \begin{bmatrix} \bar{n}_1^J & 0 \\ 0 & \bar{n}_2^J \\ \bar{n}_2^J & \bar{n}_1^J \end{bmatrix} \begin{bmatrix} \mathbf{x}_{,1}^h \cdot \mathbf{n} \\ \mathbf{x}_{,2}^h \cdot \mathbf{n} \end{bmatrix} \tag{3.4.26}$$

The constraints imposed by the Kirchhoff-Love theory of thin shells make the product $\mathbf{x}_{,\alpha}^h \cdot \mathbf{n} = 0$. This problem is solved taking for $\mathbf{x}_{,\alpha}^h$ the average value between the main triangle and each one of the adjacent elements yielding

$$\begin{bmatrix} k_{11} \\ k_{22} \\ k_{12} \end{bmatrix} = \frac{1}{A_0} \sum_{J=1}^{n_{\text{sides}}} l^J \begin{bmatrix} \bar{n}_1^J & 0 \\ 0 & \bar{n}_2^J \\ \bar{n}_2^J & \bar{n}_1^J \end{bmatrix} \begin{bmatrix} \frac{1}{2}\left(\mathbf{x}_{,1}^{\text{M}} + \mathbf{x}_{,1}^J\right) \cdot \mathbf{n} \\ \\ \frac{1}{2}\left(\mathbf{x}_{,2}^{\text{M}} + \mathbf{x}_{,2}^J\right) \cdot \mathbf{n} \end{bmatrix} \tag{3.4.27}$$

which can be simplified to

$$\begin{bmatrix} k_{11} \\ k_{22} \\ k_{12} \end{bmatrix} = \frac{1}{2A_0} \sum_{J=1}^{n_{\text{sides}}} l^J \begin{bmatrix} \bar{n}_1^J & 0 \\ 0 & \bar{n}_2^J \\ \bar{n}_2^J & \bar{n}_1^J \end{bmatrix} \begin{bmatrix} \mathbf{x}_{,1}^J \cdot \mathbf{n} \\ \\ \mathbf{x}_{,2}^J \cdot \mathbf{n} \end{bmatrix} \tag{3.4.28}$$

since $\mathbf{x}_{,\alpha}^{\text{M}} \cdot \mathbf{n} = 0$ and where $\mathbf{x}_{,\alpha}^J$ is given by

$$\begin{bmatrix} \mathbf{x}_{,1}^J \\ \\ \mathbf{x}_{,2}^J \end{bmatrix} = \sum_{I=1}^{n_{\text{node}}} \begin{bmatrix} \frac{\partial N_I^J}{\partial x} \\ \\ \frac{\partial N_I^J}{\partial y} \end{bmatrix} \mathbf{x}_I^J \tag{3.4.29}$$

The same methodology is used to obtain the bending strains for the reference configuration yielding

$$\begin{bmatrix} K_{11} \\ K_{22} \\ K_{12} \end{bmatrix} = \frac{1}{2A_0} \sum_{J=1}^{n_{\text{sides}}} L^J \begin{bmatrix} \bar{n}_1^J & 0 \\ 0 & \bar{n}_2^J \\ \bar{n}_2^J & \bar{n}_1^J \end{bmatrix} \begin{bmatrix} \mathbf{X}_{,1}^J \cdot \mathbf{N} \\ \\ \mathbf{X}_{,2}^J \cdot \mathbf{N} \end{bmatrix} \tag{3.4.30}$$

The bending strain tensor in Voigt notation is then given by

$$\{\mathbf{E}\}^{\text{bend}} = \begin{bmatrix} \kappa_{11} \\ \kappa_{22} \\ \kappa_{12} \end{bmatrix} = \begin{bmatrix} K_{11} \\ K_{22} \\ K_{12} \end{bmatrix} - \begin{bmatrix} k_{11} \\ k_{22} \\ k_{12} \end{bmatrix} \tag{3.4.31}$$

The variation of the bending strain tensor in Voigt notation yields

$$\delta\{\mathbf{E}\}^{\text{bend}} = \begin{bmatrix} \delta\kappa_{11} \\ \delta\kappa_{22} \\ \delta\kappa_{12} \end{bmatrix} = - \begin{bmatrix} \delta k_{11} \\ \delta k_{22} \\ \delta k_{12} \end{bmatrix} \tag{3.4.32}$$

where

$$\begin{bmatrix} \delta k_{11} \\ \delta k_{22} \\ \delta k_{12} \end{bmatrix} = \frac{1}{2A_0} \sum_{J=1}^{n_{\text{sides}}} l^J \begin{bmatrix} \bar{n}_1^J & 0 \\ 0 & \bar{n}_2^J \\ \bar{n}_2^J & \bar{n}_1^J \end{bmatrix} \begin{bmatrix} \delta\left(\mathbf{x}_{,1}^J \cdot \mathbf{n}\right) \\ \\ \delta\left(\mathbf{x}_{,2}^J \cdot \mathbf{n}\right) \end{bmatrix} \tag{3.4.33}$$

The last term of the right hand side of Eq. (3.4.33) can be expanded to become

$$\delta\left(\mathbf{x}^J_{,\alpha}\cdot\mathbf{n}\right)=\delta\mathbf{x}^J_{,\alpha}\cdot\mathbf{n}+\mathbf{x}^J_{,\alpha}\cdot\delta\mathbf{n} \tag{3.4.34}$$

The variation $\delta\mathbf{x}^J_{,\alpha}$ yields

$$\begin{bmatrix}\delta\mathbf{x}^J_{,1}\\ \\ \delta\mathbf{x}^J_{,2}\end{bmatrix}=\sum_{I=1}^{n_{\text{node}}}\begin{bmatrix}\frac{\partial N^J_I}{\partial x}\\ \\ \frac{\partial N^J_I}{\partial y}\end{bmatrix}\delta\mathbf{u}^J_I \tag{3.4.35}$$

From Eq. (3.2.4), the normal $\mathbf{n}$ is given as a function of $\mathbf{g}_3$ which can be written as

$$\mathbf{n}=\frac{\mathbf{g}_3}{\|\mathbf{g}_3\|}=\frac{\mathbf{g}_1\times\mathbf{g}_2}{\|\mathbf{g}_1\times\mathbf{g}_2\|}=\frac{\mathbf{x}^h_{,1}\times\mathbf{x}^h_{,2}}{\left\|\mathbf{x}^h_{,1}\times\mathbf{x}^h_{,2}\right\|} \tag{3.4.36}$$

Therefore the normal variation yields

$$\delta\mathbf{n}=\delta\left(\frac{\mathbf{g}_3}{\|\mathbf{g}_3\|}\right)=\delta\mathbf{g}_3\frac{1}{\|\mathbf{g}_3\|}-\mathbf{g}_3\frac{\delta\mathbf{g}_3\cdot\mathbf{g}_3}{\|\mathbf{g}_3\|^3} \tag{3.4.37}$$

which components of the convective covariant base vectors $\mathbf{x}^h_{,\alpha}$ give

$$\begin{aligned}\delta n_1&=\mathbf{x}^h_{,1}\cdot\delta\mathbf{n}=\mathbf{x}^h_{,1}\cdot\delta\mathbf{g}_3\frac{1}{\|\mathbf{g}_3\|}-\mathbf{x}^h_{,1}\cdot\mathbf{g}_3\frac{\delta\mathbf{g}_3\cdot\mathbf{g}_3}{\|\mathbf{g}_3\|^3}\\ \delta n_2&=\mathbf{x}^h_{,2}\cdot\delta\mathbf{n}=\mathbf{x}^h_{,2}\cdot\delta\mathbf{g}_3\frac{1}{\|\mathbf{g}_3\|}-\mathbf{x}^h_{,2}\cdot\mathbf{g}_3\frac{\delta\mathbf{g}_3\cdot\mathbf{g}_3}{\|\mathbf{g}_3\|^3}\end{aligned} \tag{3.4.38}$$

where $\mathbf{x}^h_{,\alpha}\cdot\mathbf{g}_3=0$. The variation of $\mathbf{g}_3$ is

$$\delta\mathbf{g}_3=\delta\left(\mathbf{x}^h_{,1}\times\mathbf{x}^h_{,2}\right)=\delta\mathbf{x}^h_{,1}\times\mathbf{x}^h_{,2}+\mathbf{x}^h_{,1}\times\delta\mathbf{x}^h_{,2} \tag{3.4.39}$$

Instead of the Cross product, it is convenient to express Eq. (3.4.39) in a matrix form yielding

$$\delta\mathbf{g}_3=-\hat{\mathbf{x}}^h_{,2}\delta\mathbf{x}^h_{,1}+\hat{\mathbf{x}}^h_{,1}\delta\mathbf{x}^h_{,2} \tag{3.4.40}$$

where

$$\hat{\mathbf{x}}^h_{,\alpha}=\begin{bmatrix}0 & -x_{3,\alpha} & x_{2,\alpha}\\ x_{3,\alpha} & 0 & -x_{1,\alpha}\\ -x_{2,\alpha} & x_{1,\alpha} & 0\end{bmatrix} \tag{3.4.41}$$

Substituting Eq. (3.4.40) into Eq. (3.4.38) leads to

$$\begin{aligned}\delta n_1&=\frac{1}{\|\mathbf{g}_3\|}\left(-\mathbf{x}^h_{,1}\cdot\hat{\mathbf{x}}^h_{,2}\delta\mathbf{x}^h_{,1}+\mathbf{x}^h_{,1}\cdot\hat{\mathbf{x}}^h_{,1}\delta\mathbf{x}^h_{,2}\right)\\ \delta n_2&=\frac{1}{\|\mathbf{g}_3\|}\left(-\mathbf{x}^h_{,2}\cdot\hat{\mathbf{x}}^h_{,2}\delta\mathbf{x}^h_{,1}+\mathbf{x}^h_{,2}\cdot\hat{\mathbf{x}}^h_{,1}\delta\mathbf{x}^h_{,2}\right)\end{aligned} \tag{3.4.42}$$

However $\mathbf{x}^h_{,1} \cdot \hat{\mathbf{x}}^h_{,1} \delta\mathbf{x}^h_{,2} = \mathbf{x}^h_{,2} \cdot \hat{\mathbf{x}}^h_{,2} \delta\mathbf{x}^h_{,1} = 0$, yielding

$$\begin{aligned} \delta n_1 &= \frac{1}{\|\mathbf{g}_3\|} \left(-\mathbf{x}^h_{,1} \times \mathbf{x}^h_{,2} \cdot \delta\mathbf{x}^h_{,1} \right) = -\mathbf{n} \cdot \delta\mathbf{x}^h_{,1} \\ \delta n_2 &= \frac{1}{\|\mathbf{g}_3\|} \left(\mathbf{x}^h_{,2} \times \mathbf{x}^h_{,1} \cdot \delta\mathbf{x}^h_{,2} \right) = -\mathbf{n} \cdot \delta\mathbf{x}^h_{,2} \end{aligned} \tag{3.4.43}$$

and Eq. (3.4.37) can be written as

$$\delta\mathbf{n} = \delta n_1 \tilde{\mathbf{x}}^h_{,1} + \delta n_2 \tilde{\mathbf{x}}^h_{,2} \tag{3.4.44}$$

where $\tilde{\mathbf{x}}^h_{,\alpha}$ are the convective contravariant base vectors given by Eq. (3.2.6) or simply by

$$\tilde{\mathbf{x}}^h_{,1} = \frac{1}{\|\mathbf{g}_3\|} \mathbf{x}^h_{,2} \times \mathbf{n} \,, \qquad \tilde{\mathbf{x}}^h_{,2} = -\frac{1}{\|\mathbf{g}_3\|} \mathbf{x}^h_{,1} \times \mathbf{n} \tag{3.4.45}$$

From Eq. (3.4.25) the variation $\delta\mathbf{x}^h_{,\alpha}$ is

$$\begin{bmatrix} \delta\mathbf{x}^h_{,1} \\ \delta\mathbf{x}^h_{,2} \end{bmatrix} = \sum_{I=1}^{n_{\text{node}}} \begin{bmatrix} \frac{\partial N_I}{\partial x} \\ \\ \frac{\partial N_I}{\partial y} \end{bmatrix} \delta\mathbf{u}_I \tag{3.4.46}$$

Substituting Eq. (3.4.46) into Eq. (3.4.43), and the resulting equation into Eq. (3.4.44) yields

$$\delta\mathbf{n} = -\sum_{I=1}^{n_{\text{node}}} \left(\frac{\partial N_I}{\partial x} \tilde{\mathbf{x}}^h_{,1} + \frac{\partial N_I}{\partial y} \tilde{\mathbf{x}}^h_{,2} \right) \mathbf{n} \cdot \delta\mathbf{u}_I \tag{3.4.47}$$

Substituting Eq. (3.4.35) and Eq. (3.4.47) into Eq. (3.4.34) leads to

$$\begin{bmatrix} \delta \left(\mathbf{x}^J_{,1} \cdot \mathbf{n} \right) \\ \\ \delta \left(\mathbf{x}^J_{,2} \cdot \mathbf{n} \right) \end{bmatrix} = \sum_{I=1}^{n_{\text{node}}} \begin{bmatrix} \frac{\partial N^J_I}{\partial x} \\ \\ \frac{\partial N^J_I}{\partial y} \end{bmatrix} \mathbf{n} \cdot \delta\mathbf{u}^J_I - \sum_{I=1}^{n_{\text{node}}} \begin{bmatrix} \frac{\partial N_I}{\partial x} \mathbf{x}^J_{,1} \cdot \tilde{\mathbf{x}}^h_{,1} + \frac{\partial N_I}{\partial y} \mathbf{x}^J_{,1} \cdot \tilde{\mathbf{x}}^h_{,2} \\ \\ \frac{\partial N_I}{\partial x} \mathbf{x}^J_{,2} \cdot \tilde{\mathbf{x}}^h_{,1} + \frac{\partial N_I}{\partial y} \mathbf{x}^J_{,2} \cdot \tilde{\mathbf{x}}^h_{,2} \end{bmatrix} \mathbf{n} \cdot \delta\mathbf{u}_I \tag{3.4.48}$$

Now substituting Eq. (3.4.48) into Eq. (3.4.33) yields

$$\begin{aligned} \begin{bmatrix} \delta k_{11} \\ \delta k_{22} \\ \delta k_{12} \end{bmatrix} = {} & \frac{1}{2A_0} \sum_{J=1}^{n_{\text{sides}}} l^J \begin{bmatrix} \bar{n}^J_1 & 0 \\ 0 & \bar{n}^J_2 \\ \bar{n}^J_2 & \bar{n}^J_1 \end{bmatrix} \sum_{I=1}^{n_{\text{node}}} \begin{bmatrix} \frac{\partial N^J_I}{\partial x} \\ \\ \frac{\partial N^J_I}{\partial y} \end{bmatrix} \mathbf{n} \cdot \delta\mathbf{u}^J_I \quad + \\ & - \frac{1}{2A_0} \sum_{J=1}^{n_{\text{sides}}} l^J \begin{bmatrix} \bar{n}^J_1 & 0 \\ 0 & \bar{n}^J_2 \\ \bar{n}^J_2 & \bar{n}^J_1 \end{bmatrix} \sum_{I=1}^{n_{\text{node}}} \begin{bmatrix} \frac{\partial N_I}{\partial x} \mathbf{x}^J_{,1} \cdot \tilde{\mathbf{x}}^h_{,1} + \frac{\partial N_I}{\partial y} \mathbf{x}^J_{,1} \cdot \tilde{\mathbf{x}}^h_{,2} \\ \\ \frac{\partial N_I}{\partial x} \mathbf{x}^J_{,2} \cdot \tilde{\mathbf{x}}^h_{,1} + \frac{\partial N_I}{\partial y} \mathbf{x}^J_{,2} \cdot \tilde{\mathbf{x}}^h_{,2} \end{bmatrix} \mathbf{n} \cdot \delta\mathbf{u}_I \end{aligned} \tag{3.4.49}$$

Finally substituting Eq. (3.4.49) into Eq. (3.4.32), the variation of the bending strain tensor in Voigt notation can be written explicitly as

$$\begin{aligned}\delta\{\mathbf{E}\}^{\text{bend}} = \frac{1}{2A_0}\sum_{J=1}^{n_{\text{sides}}} l^J \begin{bmatrix} \bar{n}_1^J & 0 \\ 0 & \bar{n}_2^J \\ \bar{n}_2^J & \bar{n}_1^J \end{bmatrix} \sum_{I=1}^{n_{\text{node}}} \begin{bmatrix} \frac{\partial N_I}{\partial x}\mathbf{x}_{,1}^J \cdot \tilde{\mathbf{x}}_{,1}^h + \frac{\partial N_I}{\partial y}\mathbf{x}_{,1}^J \cdot \tilde{\mathbf{x}}_{,2}^h \\ \frac{\partial N_I}{\partial x}\mathbf{x}_{,2}^J \cdot \tilde{\mathbf{x}}_{,1}^h + \frac{\partial N_I}{\partial y}\mathbf{x}_{,2}^J \cdot \tilde{\mathbf{x}}_{,2}^h \end{bmatrix} \mathbf{n}\cdot\delta\mathbf{u}_I \quad + \\ - \frac{1}{2A_0}\sum_{J=1}^{n_{\text{sides}}} l^J \begin{bmatrix} \bar{n}_1^J & 0 \\ 0 & \bar{n}_2^J \\ \bar{n}_2^J & \bar{n}_1^J \end{bmatrix} \sum_{I=1}^{n_{\text{node}}} \begin{bmatrix} \frac{\partial N_I^J}{\partial x} \\ \frac{\partial N_I^J}{\partial y} \end{bmatrix} \mathbf{n}\cdot\delta\mathbf{u}_I^J \end{aligned} \tag{3.4.50}$$

The variation of the bending strain tensor can be expressed in compact form as

$$\delta\{\mathbf{E}\}^{\text{bend}} = [\mathbf{B}]^{\text{main}}\,\delta\mathbf{u}_I + [\mathbf{B}]^{\text{adj}}\,\delta\mathbf{u}_I^J \tag{3.4.51}$$

where the expression of the strain-displacement matrix $[\mathbf{B}]^{\text{main}}$ for the main element and $[\mathbf{B}]^{\text{adj}}$ for the adjacent element is taken from Eq. (3.4.50). The complete strain-displacement matrix for bending is given by

$$[\mathbf{B}]^{\text{bend}} = [\mathbf{B}]^{\text{main}} + [\mathbf{B}]^{\text{adj}} \tag{3.4.52}$$

3.4.3.1 Stress resultants and internal forces

The membrane and bending stress tensors may be given in a direct mechanistic interpretation as force and moment resultants .

The constitutive equation given by Eq. (3.2.69) can be written for shell elements as

$$\{\mathbf{S}\} = [\mathbf{C}]\cdot\{\mathbf{E}\} = [\mathbf{C}]\cdot\left(\{\mathbf{E}\}^{\text{memb}} + \zeta\{\mathbf{E}\}^{\text{bend}}\right) \tag{3.4.53}$$

and the virtual internal work given by Eq. (3.4.16) for shells is expressed by

$$\delta\mathcal{W}^{\text{int}} = \int_{\overline{\Omega}_0}\int_{-\frac{h}{2}}^{\frac{h}{2}} \left(\delta\{\mathbf{E}\}^{\text{memb}} + \zeta\delta\{\mathbf{E}\}^{\text{bend}}\right)\cdot[\mathbf{C}]\left(\{\mathbf{E}\}^{\text{memb}} + \zeta\{\mathbf{E}\}^{\text{bend}}\right) d\zeta d\overline{\Omega}_0 \tag{3.4.54}$$

which can be split to yield

$$\begin{aligned}\delta\mathcal{W}^{\text{int}} = &\int_{\overline{\Omega}_0}\int_{-\frac{h}{2}}^{\frac{h}{2}} \delta\{\mathbf{E}\}^{\text{memb}}\cdot[\mathbf{C}]\{\mathbf{E}\}^{\text{memb}}\, d\zeta d\overline{\Omega}_0 \quad + \\ &\int_{\overline{\Omega}_0}\int_{-\frac{h}{2}}^{\frac{h}{2}} \zeta^2\delta\{\mathbf{E}\}^{\text{bend}}\cdot[\mathbf{C}]\{\mathbf{E}\}^{\text{bend}}\, d\zeta d\overline{\Omega}_0\end{aligned} \tag{3.4.55}$$

In this work a linear material model is used and integration of the virtual internal work becomes

$$\begin{aligned}\delta \mathcal{W}^{\text{int}} =& A_0 h \delta \{\mathbf{E}\}^{\text{memb}} \cdot [\mathbf{C}] \{\mathbf{E}\}^{\text{memb}} \quad + \\ & A_0 \frac{h^3}{12} \delta \{\mathbf{E}\}^{\text{bend}} \cdot [\mathbf{C}] \{\mathbf{E}\}^{\text{bend}}\end{aligned} \tag{3.4.56}$$

where the forces resultant $\{\mathbf{N}\}^{\text{res}}$ and the moments resultant $\{\mathbf{M}\}^{\text{res}}$ are obtained as

$$\begin{aligned}\{\mathbf{N}\}^{\text{res}} &= h [\mathbf{C}] \{\mathbf{E}\}^{\text{memb}} \\ \{\mathbf{M}\}^{\text{res}} &= \frac{h^3}{12} [\mathbf{C}] \{\mathbf{E}\}^{\text{bend}}\end{aligned} \tag{3.4.57}$$

Finally the internal forces for the rotation-free shell element are expressed by

$$\mathbf{f}^{\text{int}} = A_0 \left[\mathbf{B}^T\right]^{\text{memb}} \{\mathbf{N}\}^{\text{res}} + A_0 \left[\mathbf{B}^T\right]^{\text{bend}} \{\mathbf{M}\}^{\text{res}} \tag{3.4.58}$$

where all expressions related to the membrane part are given directly in section **3.2.4**.

3.4.3.2 Boundary conditions

The main difference between classical formulations for shells and rotation-free formulations for shells is that the boundary conditions for rotation-free elements become a part of the formulation that also needs to be implemented into the finite element code.

It is important to give special considerations to the boundaries where there might be one or two missing adjacent elements. In this work, the boundary conditions are treated as given by Flores and Oñate (2001).

3.5 Time Integration Schemes

Time integration schemes can be classified as *explicit* solution and *implicit* solution. In an explicit scheme the lumped mass is commonly used and consists in finding the position vector $\mathbf{x}$ at time t_{n+1} using the known value of $\mathbf{x}$ at time t_n. However $\mathbf{x}$ is defined as $\mathbf{x} = \mathbf{X} + \mathbf{u}$, and the only variable to find reduces to the displacement vector $\mathbf{u}$ at time t_{n+1}. Therefore in an explicit method, the time integration of the discrete momentum equations does not require the solution of any equations. An explicit solution is conditionally stable and requires that the time step size Δt be less or equal than a critical time step size Δt_{crit} for all time steps. The critical time step depends on element size and the maximum wave speed for the element material. The resulting time increment is often too small for practical considerations in computer effort and for the response necessary to model slowly varying loads.

Implicit schemes are based on finding the position vector $\mathbf{x}$ at time t_{n+1} using not only the known value of $\mathbf{x}$ at time t_n but also the values at t_{n+1}. Therefore in an implicit method, the time integration of the discrete momentum equations requires the solution of algebraic equations. An implicit solution is generally unconditionally stable, i.e. see Hughes (1987), and can be one or two orders of magnitude larger than the time step used in an explicit scheme. However the accuracy of the implicit schemes deteriorates as the time step size increases relative to the period of response of the system.

In this work only implicit schemes are solved for structural dynamic problems. The semi-discrete equations of motion to be solved are given by

$$\mathbf{f}^{\text{int}}(\mathbf{u}_{n+1}) + \mathbf{M}\ddot{\mathbf{u}}_{n+1} = \mathbf{f}^{\text{ext}}(\mathbf{u}_{n+1}) \tag{3.5.1}$$

where the acceleration vector $\ddot{\mathbf{u}}_{n+1}$ has to be integrated in time to solve the algebraic equations for $\mathbf{u}_{n+1}$ from the second-order differential equations.

Among the several numerical integration methods available to integrate second order equations, the most popular used in structural dynamics is the method developed by Newmark (1959). A major drawback of the Newmark integrator is the tendency for high frequency noise to persist in the solution. On the other hand, when linear damping or artificial viscosity is added, the accuracy is markedly degraded. Therefore other integration schemes are utilized with minor modifications as the ones given by Hilber et al. (1977), Wood et al. (1980) and Chung and Hulbert (1993). These methods improve numerical dissipation for high frequencies without degrading the accuracy as much. Details of these methods can also be found in Adams and Wood (1983) and Barbat and Canet (1994).

3.5.1 Newmark Method

In the Newmark method it is supposed that the solution at time step t_n is known for the displacements $\mathbf{u}_n$ and its time derivatives $\dot{\mathbf{u}}_n$ and $\ddot{\mathbf{u}}_n$. The semi-discrete equations of motion to be solved at time t_{n+1} are given by

$$\mathbf{f}^{\text{int}}(\mathbf{u}_{n+1}) + \mathbf{M}\ddot{\mathbf{u}}_{n+1} = \mathbf{f}^{\text{ext}}(\mathbf{u}_{n+1}) \tag{3.5.2}$$

and the displacements $\mathbf{u}_{n+1}$ and its time derivative are approximated according to

$$\dot{\mathbf{u}}_{n+1} = \dot{\mathbf{u}}_n + \Delta t\,(1-\gamma)\,\ddot{\mathbf{u}}_n + \Delta t\gamma\ddot{\mathbf{u}}_{n+1} \tag{3.5.3}$$

$$\mathbf{u}_{n+1} = \mathbf{u}_n + \Delta t\dot{\mathbf{u}}_n + \Delta t^2\left(\frac{1}{2}-\beta\right)\ddot{\mathbf{u}}_n + \Delta t^2\beta\ddot{\mathbf{u}}_{n+1} \tag{3.5.4}$$

where Δt is the time step size, and γ, β are the parameters that determine the stability and accuracy of the scheme. The different values for the parameters γ and β originate the Newmark family methods. Stability conditions for the Newmark method are given for implicit schemes by

$$\text{Unconditional} \qquad 2\beta \geq \gamma \geq \frac{1}{2} \tag{3.5.5}$$

$$\begin{aligned} &\text{Conditional} && \gamma \geq \frac{1}{2}, \qquad \beta < \frac{\gamma}{2} \\ &\text{with} && \omega \Delta t \leq \Omega_{crit} \end{aligned} \tag{3.5.6}$$

where Ω_{crit} is the stability condition and ω is the natural frequency and must be satisfied for each mode in the system. Second-order accuracy is achieved if and only if $\gamma = \frac{1}{2}$, and viscous damping has no effect on stability. When $\gamma > \frac{1}{2}$ the effect of viscous damping is to increase the critical time step of conditionally stable Newmark methods. Two of the methods from the Newmark family for implicit schemes with second-order of accuracy are given in table 3.4. Other methods can be found, i.e. Hughes (1987).

Method	γ parameter	β parameter	Stability condition
Trapezoidal rule	1/2	1/4	Unconditional
Linear acceleration	1/2	1/6	$\Omega_{crit} = 2\sqrt{3}$

Table 3.4 *Most commons members of the implicit Newmark family*

To solve the semi-discrete equations of motion with algebraic equations, the value of $\ddot{\mathbf{u}}_{n+1}$ is obtained from Eq. (3.5.4) yielding

$$\ddot{\mathbf{u}}_{n+1} = \frac{1}{\beta \Delta t^2} \left(\mathbf{u}_{n+1} - \mathbf{u}_n \right) - \frac{1}{\beta \Delta t} \dot{\mathbf{u}}_n - \left(\frac{1}{2\beta} - 1 \right) \ddot{\mathbf{u}}_n \tag{3.5.7}$$

The value of $\dot{\mathbf{u}}_{n+1}$ is obtained from the resulting equation of substituting Eq. (3.5.7) into Eq. (3.5.3) yielding

$$\dot{\mathbf{u}}_{n+1} = \frac{\gamma}{\beta \Delta t} \left(\mathbf{u}_{n+1} - \mathbf{u}_n \right) - \left(\frac{\gamma}{\beta} - 1 \right) \dot{\mathbf{u}}_n - \Delta t \left(\frac{\gamma}{2\beta} - 1 \right) \ddot{\mathbf{u}}_n \tag{3.5.8}$$

When the system has some kind of damping, i.e. viscous damping as described in section **3.5.5**, the internal forces are function not only of $\mathbf{u}_{n+1}$ but also of $\dot{\mathbf{u}}_{n+1}$ and are written as $\mathbf{f}^{\text{int}}(\mathbf{u}_{n+1}, \dot{\mathbf{u}}_{n+1})$. Now substituting Eq. (3.5.7), and Eq. (3.5.8) when necessary, into Eq. (3.5.2) yields

$$\begin{aligned} \mathbf{f}^{\text{int}}(\mathbf{u}_{n+1}) + \frac{1}{\beta \Delta t^2} \mathbf{M}\, \mathbf{u}_{n+1} - \mathbf{f}^{\text{ext}}(\mathbf{u}_{n+1}) = \\ \mathbf{M} \left[\frac{1}{\beta \Delta t^2} \mathbf{u}_n + \frac{1}{\beta \Delta t} \dot{\mathbf{u}}_n + \left(\frac{1}{2\beta} - 1 \right) \ddot{\mathbf{u}}_n \right] \end{aligned} \tag{3.5.9}$$

and the algebraic equations can be solved for $\mathbf{u}_{n+1}$ since all values at time t_n are known. With $\mathbf{u}_{n+1}$ solved, the values for $\dot{\mathbf{u}}_{n+1}$ and $\ddot{\mathbf{u}}_{n+1}$ are updated with Eqs. (3.5.8) and (3.5.7) respectevely. The solution strategy used in this work to solve Eq. (3.5.9) is given ahead in section **3.6**.

3.5.2 Hilber-Hughes-Taylor Method

Hilber, Hughes and Taylor introduced the α-method as given in Hilber et al. (1977). This method introduces numerical dissipation for high frequencies without degrading the order of accuracy. In the α-method, the Newmark formulas given by Eqs. (3.5.3) and (3.5.4) are retained, whereas the semi-discrete equations of motion are modified as follows

$$\mathbf{f}^{\text{int}}(\mathbf{u}_{n+1+\alpha_H}) + \mathbf{M}\ddot{\mathbf{u}}_{n+1} = \mathbf{f}^{\text{ext}}(\mathbf{u}_{n+1+\alpha_H}) \tag{3.5.10}$$

where the only change is given by

$$\mathbf{u}_{n+1+\alpha_H} = (1+\alpha_H)\,\mathbf{u}_{n+1} - \alpha_H\,\mathbf{u}_n \tag{3.5.11}$$

If $\alpha_H = 0$ this method reduces to the Newmark method. The method is unconditionally stable for linear systems when the parameters are selected such that

$$\alpha_H \in \left[-\frac{1}{3}, 0\right], \qquad \gamma = \frac{1-2\alpha_H}{2}, \qquad \beta = \frac{(1-\alpha_H)^2}{4} \tag{3.5.12}$$

Any value given here for α_H results in a second-order accurate scheme. If $\alpha_H = 0$, the method correspond to the Newmark trapezoidal rule method. There are no general stability results for this method for nonlinear problems. Now substituting Eq. (3.5.7), and Eq. (3.5.8) when necessary, into Eq. (3.5.10) yields

$$\begin{aligned}\mathbf{f}^{\text{int}}(\mathbf{u}_{n+1+\alpha_H}) + \frac{1}{\beta\Delta t^2}\mathbf{M}\,\mathbf{u}_{n+1} - \mathbf{f}^{\text{ext}}(\mathbf{u}_{n+1+\alpha_H}) = \\ \mathbf{M}\left[\frac{1}{\beta\Delta t^2}\mathbf{u}_n + \frac{1}{\beta\Delta t}\dot{\mathbf{u}}_n + \left(\frac{1}{2\beta} - 1\right)\ddot{\mathbf{u}}_n\right]\end{aligned} \tag{3.5.13}$$

and the algebraic equations can be solved for $\mathbf{u}_{n+1}$. Note that the expression $\mathbf{f}^{\text{int}}(\mathbf{u}_{n+1+\alpha_H})$ is not equal to $(1-\alpha_H)\,\mathbf{f}^{\text{int}}(\mathbf{u}_{n+1}) - \alpha_H\mathbf{f}^{\text{int}}(\mathbf{u}_n)$ since the problem is nonlinear. The solution strategy used in this work to solve Eq. (3.5.13) is given ahead in section **3.6**.

3.5.3 Bossak Method

An extension of the Newmark method was proposed by Bossak as given in Wood et al. (1980). This method defined by the Newmark formulas given by Eqs. (3.5.3) and (3.5.4), and the semi-discrete equations of motion modified as follows

$$\mathbf{f}^{\text{int}}(\mathbf{u}_{n+1}) + \mathbf{M}\,\ddot{\mathbf{u}}_{n+1-\alpha_B} = \mathbf{f}^{\text{ext}}(\mathbf{u}_{n+1}) \tag{3.5.14}$$

where the only change is given by

$$\ddot{\mathbf{u}}_{n+1-\alpha_B} = (1-\alpha_B)\,\ddot{\mathbf{u}}_{n+1} + \alpha_B\,\ddot{\mathbf{u}}_n \tag{3.5.15}$$

The method is unconditionally stable for linear systems when the parameters are selected such that

$$\alpha_B \in \left[-\frac{1}{3}, 0\right], \qquad \gamma = \frac{1-2\alpha_B}{2}, \qquad \beta = \frac{(1-\alpha_B)^2}{4} \tag{3.5.16}$$

Again, any value given here for α_B results in a second-order accurate scheme. If $\alpha_B = 0$, the method correspond to the Newmark trapezoidal rule method. A comparison of Bossak's method and the Hilber-Hughes-Taylor α-method is presented in Adams and Wood (1983). Both methods posses the same high-frequency dissipation properties. Howerver it is easier to implement in a finite element code the Bossak's method. Now substituting Eq. (3.5.7), Eq. (3.5.15) , and Eq. (3.5.8) when necessary, into Eq. (3.5.14) yields

$$\begin{aligned} \mathbf{f}^{\text{int}}(\mathbf{u}_{n+1}) + \frac{1-\alpha_B}{\beta\Delta t^2}\mathbf{M}\,\mathbf{u}_{n+1} - \mathbf{f}^{\text{ext}}(\mathbf{u}_{n+1}) = \\ \mathbf{M}\left[\frac{1-\alpha_B}{\beta\Delta t^2}\mathbf{u}_n + \frac{1-\alpha_B}{\beta\Delta t}\dot{\mathbf{u}}_n + \left(\frac{1-\alpha_B}{2\beta} - 1\right)\ddot{\mathbf{u}}_n\right] \end{aligned} \tag{3.5.17}$$

and the algebraic equations can be solved for $\mathbf{u}_{n+1}$. The solution strategy used in this work to solve Eq. (3.5.17) is given ahead in section **3.6**.

3.5.4 Generalized-α Method

The generalized-α method was introduced by Chung and Hulbert (1993), which achieves high-frequency dissipation while minimizing unwanted low-frequency dissipation. This method is a combination of all the above methods presented. In the generalized-α method, the Newmark formulas given by Eqs. (3.5.3) and (3.5.4) are retained, whereas the semi-discrete equations of motion are modified as follows

$$\mathbf{f}^{\text{int}}\Big(\mathbf{u}_{n+\alpha_f^{\text{s}}}\Big) + \mathbf{M}\ddot{\mathbf{u}}_{n+\alpha_m^{\text{s}}} = \mathbf{f}^{\text{ext}}\Big(\mathbf{u}_{n+\alpha_f^{\text{s}}}\Big) \tag{3.5.18}$$

where the changes are given by

$$\mathbf{u}_{n+\alpha_f^{\text{s}}} = \left(1-\alpha_f^{\text{s}}\right)\mathbf{u}_n + \alpha_f^{\text{s}}\,\mathbf{u}_{n+1} \tag{3.5.19}$$

$$\ddot{\mathbf{u}}_{n+\alpha_m^{\text{s}}} = (1-\alpha_m^{\text{s}})\,\ddot{\mathbf{u}}_n + \alpha_m^{\text{s}}\,\ddot{\mathbf{u}}_{n+1} \tag{3.5.20}$$

Low frequency dissipation is optimal with

$$\rho_\infty^{\text{s}} \in [0,1], \qquad \alpha_f^{\text{s}} = \frac{1}{1+\rho_\infty^{\text{s}}}, \qquad \alpha_m^{\text{s}} = \frac{2-\rho_\infty^{\text{s}}}{1+\rho_\infty^{\text{s}}} \tag{3.5.21}$$

and the method is second-order accurate and posses high frequency dissipation when

$$\gamma = \frac{1}{2} + \alpha_m^{\text{s}} - \alpha_f^{\text{s}}, \qquad \beta = \frac{1}{4}\left(1+\alpha_m^{\text{s}} - \alpha_f^{\text{s}}\right)^2 \tag{3.5.22}$$

Other possibilities for α_f^{s} and α_m^{s}, as given in Chung and Hulbert (1993), result in the methods of Newmark, Bossak or α-method. For example if $\alpha_f^{\text{s}} = 1$ and $\alpha_m^{\text{s}} = 1$,

the method correspond to the Newmark trapezoidal rule method. The algebraic equations to be solved for $\mathbf{u}_{n+1}$ are given by

$$\begin{aligned}\mathbf{f}^{\text{int}}\Big(\mathbf{u}_{n+\alpha_f^{\text{s}}}\Big) + \frac{\alpha_m^{\text{s}}}{\beta\Delta t^2}\mathbf{M}\,\mathbf{u}_{n+1} - \mathbf{f}^{\text{ext}}\Big(\mathbf{u}_{n+\alpha_f^{\text{s}}}\Big) = \\ \mathbf{M}\left[\frac{\alpha_m^{\text{s}}}{\beta\Delta t^2}\mathbf{u}_n + \frac{\alpha_m^{\text{s}}}{\beta\Delta t}\dot{\mathbf{u}}_n + \left(\frac{\alpha_m^{\text{s}}}{2\beta} - 1\right)\ddot{\mathbf{u}}_n\right]\end{aligned} \tag{3.5.23}$$

The solution strategy used in this work to solve Eq. (3.5.23) is given ahead in section **3.6**.

3.5.5 Structural Damping

The purpose of structural damping is to dissipate strain energy in a structure that is stored due to deformation processes. The energy dissipation within a structure due to material and structural damping depends on many factors such as the structural material or the magnitude of deformations experienced. In a dynamic analysis, this energy dissipation usually is accounted for by specifying an amount of viscoelastic damping that would result in energy dissipation in the analytical model equivalent to that expected to occur as a result of material and structural damping in the real structure.

In this work, a viscoelastic damping is taken in account for geometrically nonlinear structures and consists of an extension of the viscoelastic damping given in Oller (2001) for geometrically linear structures with Kelvin's model.

In this model, the viscoelastic strain tensor is given as a function of the Green-Lagrange strain tensor by

$$\mathbf{E}^{vis} = \mathbf{E} + \tau\dot{\mathbf{E}} \tag{3.5.24}$$

where τ is the retardation time. For linear problems this model yields a damping term which is a function of the stiffness matrix $\mathbf{K}$ in the form of

$$\mathbf{D} = \tau\mathbf{K} \tag{3.5.25}$$

where $\mathbf{D}$ is the damping matrix. A very popular damping scheme in structural dynamics is given by the Rayleigh damping, which is a linear combination of the stiffness and mass matrices as

$$\mathbf{D} = \alpha\mathbf{M} + \beta\mathbf{K} \tag{3.5.26}$$

where α and β are the mass and stiffness damping constants respectively. As demonstrated in Oller (2001), when $\alpha = 0$, the Rayleigh and viscoelastic damping are equivalent, that is

$$\mathbf{D} = \beta\mathbf{K} = \tau\mathbf{K} \tag{3.5.27}$$

and the constant $\tau = \beta$. Note that the damping matrix is only proportional to the stiffness matrix. For nonlinear analysis, the damping is introduced directly only in the internal forces, which are written as

$$\mathbf{f}^{\text{int}} = \mathbf{f}^{\text{int}}(\mathbf{u}_{n+1}, \dot{\mathbf{u}}_{n+1}) \tag{3.5.28}$$

This way of introducing the viscoelastic strain yields in a natural form to add the damping, and not like a trick as in the Rayleigh case.

The only difference in the solution between both damping schemes is given by the stress field. While in the Rayleigh damping the stresses are given by $\mathbf{S} = \mathbf{CE}$, the stresses for the viscoelastic model are given by $\mathbf{S} = \mathbf{C}\left(\mathbf{E} + \tau\dot{\mathbf{E}}\right)$.

3.5.6 Quasi-static Solution

The methods described before are used to analyze dynamic problems since the inertial forces are computed. However if a static analysis is required, problems may be encountered when the membrane or shell problem has coplanar nodes yielding a singular matrix. To solve this inconvenient, a quasi-static solution can be employed. The quasi-static problem is expressed as a dynamic problem, only that the inertial terms are neglected and a damping matrix is added explicitly. This damping matrix is taken equal to the mass matrix. The problems solved in this work with the quasi-static analysis give a good solution with this methodology.

3.6 Solution Strategies

The numerical procedures used to solve nonlinear algebraic equations, given i.e. by Eq. (3.5.9) for the Newmark method, are iterative. Among the many different procedures available to solve nonlinear problems, in this work only the *Newton-Raphson* method, see i.e. Reddy (2004), is outlined for structural dynamic problems.

3.6.1 Newton-Raphson Iterative Method

In the Newton-Raphson method, Eq. (3.5.9) is written in a residual form given by

$$\begin{aligned}\mathbf{R}_{n+1} = \mathbf{f}^{\text{ext}}(\mathbf{u}_{n+1}) - \frac{1}{\beta\Delta t^2}\mathbf{M}\,\mathbf{u}_{n+1} - \mathbf{f}^{\text{int}}(\mathbf{u}_{n+1}) + \\ \mathbf{M}\left[\frac{1}{\beta\Delta t^2}\mathbf{u}_n + \frac{1}{\beta\Delta t}\dot{\mathbf{u}}_n + \left(\frac{1}{2\beta} - 1\right)\ddot{\mathbf{u}}_n\right]\end{aligned} \tag{3.6.1}$$

where it is supposed that the solution for iteration $i-1$ is known and the solution for iteration i is been searched. If the residual is expanded about the known solution $\mathbf{u}_{n+1}^{i-1}$ in Taylor's series yields

$$\mathbf{R}_{n+1}^{i} \approx \mathbf{R}_{n+1}^{i-1} + \left.\frac{\partial \mathbf{R}_{n+1}}{\partial \mathbf{u}_{n+1}}\right|^{i-1} \cdot \Delta\mathbf{u}_{n+1}^{i} = \mathbf{0} \tag{3.6.2}$$

where higher-order terms have been neglected. If the tangent stiffness matrix is defined as

$$\mathbf{K}^{\mathrm{T}} = \frac{\partial \mathbf{R}}{\partial \mathbf{u}} \tag{3.6.3}$$

then Eq. (3.6.2) can be written in the form

$$\left(\mathbf{K}^{\mathrm{T}}\right)_{n+1}^{i-1} \cdot \Delta \mathbf{u}_{n+1}^{i} = -\mathbf{R}_{n+1}^{i-1} \tag{3.6.4}$$

which is an algebraic system for $\Delta \mathbf{u}_{n+1}^{i}$. If the procedure converges, the residual is gradually reduced to zero and the solution at the i^{th} iteration is given by

$$\mathbf{u}_{n+1}^{i} = \mathbf{u}_{n+1}^{i-1} + \Delta \mathbf{u}_{n+1}^{i} \tag{3.6.5}$$

The iteration procedure is continued until a certain convergence criterion is satisfied for the system. Then the value for the current position vector is given by $\mathbf{x}_{n+1} = \mathbf{X} + \mathbf{u}_{n+1}$.

For the first iteration $i = 1$ of the time step $n + 1$, the predictor for $\mathbf{u}_{n+1}^{i-1}$ is taken from the previous converged solution at time step n, that is

$$\mathbf{u}_{n+1}^{0} = \mathbf{u}_{n} \tag{3.6.6}$$

From the residual equation given by Eq. (3.6.1), the tangent stiffness matrix is evaluated yielding

$$\mathbf{K}^{\mathrm{T}} = \mathbf{K}_{\mathrm{ext}}^{\mathrm{T}} - \mathbf{K}_{\mathrm{kin}}^{\mathrm{T}} - \mathbf{K}_{\mathrm{int}}^{\mathrm{T}} \tag{3.6.7}$$

where the internal tangent matrix $\mathbf{K}_{\mathrm{int}}^{\mathrm{T}}$ comes from the internal forces, the kinetic tangent matrix $\mathbf{K}_{\mathrm{kin}}^{\mathrm{T}}$ is associated to the mass matrix and and the external tangent matrix $\mathbf{K}_{\mathrm{ext}}^{\mathrm{T}}$ comes from the external forces. Here the external tangent matrix is different from zero only when pressure follower forces exist or in the presence of any other non-conservative load types.

3.6.2 Linearization

A difficult task in the solution of implicit systems for the semi-discrete equations of motion is the linearization of the governing equations. Here the expressions for the tangent stiffness matrix are derived. This is done with the continuum tangent moduli which does not account for the actual constitutive update algorithm and is the one used in this work because it is intended only for linear materials. Other constitutive equations may need an algorithmic tangent moduli, which gives rise to the consistent tangent stiffness matrix.

The linearization depends on the type of formulation for the different elements studied. Here only membrane, cable and shell linearization is taken into account.

3.6.2.1 Membrane Linearization

The internal tangent stiffness matrix for a membrane element is computed by taking the derivative of the internal forces in the displacements direction. The general expression for the internal membrane forces is given in Eq. (3.2.38) yielding the following derivative

$$(K_{ijIJ})^{\mathrm{T}}_{\mathrm{int}} = \frac{\partial f^{\mathrm{int}}_{iI}}{\partial u_{jJ}} = \int_{\Omega_0} \left(B^{cur}_{\alpha\beta iI} \frac{\partial S^{\alpha\beta}}{\partial u_{jJ}} + \frac{\partial B^{cur}_{\alpha\beta iI}}{\partial u_{jJ}} S^{\alpha\beta} \right) d\Omega_0 \tag{3.6.8}$$

Expressing the second Piola-Kirchhoff stress tensor as a function of the Green-Lagrange strain tensor, then $S^{\alpha\beta} = C^{\alpha\beta\gamma\epsilon} E_{\gamma\epsilon}$ and since in this work the components of the constitutive tensor are constant, the first term in the integral is expressed by

$$B^{cur}_{\alpha\beta iI} \frac{\partial S^{\alpha\beta}}{\partial u_{jJ}} = B^{cur}_{\alpha\beta iI} C^{\alpha\beta\gamma\epsilon} \frac{\partial E_{\gamma\epsilon}}{\partial u_{jJ}} \tag{3.6.9}$$

Now substituting Eq. (3.2.5) in the derivative term yields

$$\frac{\partial E_{\gamma\epsilon}}{\partial u_{jJ}} = \frac{1}{2} \frac{\partial g_{\gamma\epsilon}}{\partial u_{jJ}} \tag{3.6.10}$$

which can be expanded leading to

$$\frac{\partial g_{\gamma\epsilon}}{\partial u_{jJ}} = \frac{\partial \mathbf{g}_\gamma}{\partial u_{jJ}} \cdot \mathbf{g}_\epsilon + \mathbf{g}_\gamma \cdot \frac{\partial \mathbf{g}_\epsilon}{\partial u_{jJ}} \tag{3.6.11}$$

and

$$\frac{\partial \mathbf{g}_\gamma}{\partial u_{jJ}} = \sum_{I=1}^{n_{\mathrm{node}}} \frac{\partial N_I}{\partial \xi^\gamma} \frac{\partial \mathbf{x}_I}{\partial u_{jJ}} \tag{3.6.12}$$

However, the last term can be expressed as

$$\frac{\partial \mathbf{x}_I}{\partial u_{jJ}} = \frac{\partial u_{iI}}{\partial u_{jJ}} \mathbf{e}_i = \delta_{ij} \delta_{IJ} \mathbf{e}_i = \delta_{IJ} \mathbf{e}_j \tag{3.6.13}$$

Substituting Eq. (3.6.13) into Eq. (3.6.12) the following expression is obtained

$$\frac{\partial \mathbf{g}_\gamma}{\partial u_{jJ}} = \frac{\partial N_J}{\partial \xi^\gamma} \mathbf{e}_j \tag{3.6.14}$$

If the covariant base vector is discretized by

$$\mathbf{g}_\epsilon = \sum_{I=1}^{n_{\mathrm{node}}} \frac{\partial N_I}{\partial \xi^\epsilon} x_{iI} \mathbf{e}_i \tag{3.6.15}$$

then the first product of Eq. (3.6.11) yields

$$\frac{\partial \mathbf{g}_\gamma}{\partial u_{jJ}} \cdot \mathbf{g}_\epsilon = \sum_{I=1}^{n_{\mathrm{node}}} \frac{\partial N_J}{\partial \xi^\gamma} \frac{\partial N_I}{\partial \xi^\epsilon} x_{jI} \tag{3.6.16}$$

This last equation allow us to expressed Eq. (3.6.10) in the form of

$$\frac{\partial E_{\gamma\epsilon}}{\partial u_{jJ}} = \frac{1}{2}\sum_{I=1}^{n_{\text{node}}} \left(N_{J,\gamma}N_{I,\epsilon} + N_{I,\gamma}N_{J,\epsilon}\right) x_{jI} \tag{3.6.17}$$

which is equal to the expression for the strain-displacement tensor given in Eq. (3.2.37) and then

$$B^{cur}_{\gamma\epsilon jJ} = \frac{\partial E_{\gamma\epsilon}}{\partial u_{jJ}} \tag{3.6.18}$$

Then the tangent material stiffness is defined as

$$K^{\text{mat}}_{ijIJ} = \int_{\Omega_0} B^{cur}_{\alpha\beta iI} C^{\alpha\beta\gamma\epsilon} B^{cur}_{\gamma\epsilon jJ} d\Omega_0 \tag{3.6.19}$$

or in Voigt notation

$$\mathbf{K}^{\text{mat}}_{IJ} = \int_{\Omega_0} [\mathbf{B}^T_I]^{fib}\, [\mathbf{C}]\, [\mathbf{B}_J]^{fib}\, d\Omega_0 \tag{3.6.20}$$

With Eq. (3.6.18), the internal forces can be written in a more useful equation instead of Eq. (3.2.38) yielding

$$f^{\text{int}}_{iI} = \int_{\Omega_0} \frac{\partial E_{\alpha\beta}}{\partial u_{iI}} S^{\alpha\beta} d\Omega_0 \tag{3.6.21}$$

which derivative is given by

$$(K_{ijIJ})^{\text{T}}_{\text{int}} = \frac{\partial f^{\text{int}}_{iI}}{\partial u_{jJ}} = \int_{\Omega_0} \left(\frac{\partial E_{\alpha\beta}}{\partial u_{iI}} \frac{\partial S^{\alpha\beta}}{\partial u_{jJ}} + \frac{\partial^2 E_{\alpha\beta}}{\partial u_{iI}\partial u_{jJ}} S^{\alpha\beta} \right) d\Omega_0 \tag{3.6.22}$$

This is another way to express Eq. (3.6.8). To compute the second derivative on the right hand side of Eq. (3.6.22), the term

$$\frac{\partial^2 E_{\alpha\beta}}{\partial u_{iI}\partial u_{jJ}} = \frac{1}{2}\frac{\partial^2 g_{\alpha\beta}}{\partial u_{iI}\partial u_{jJ}} \tag{3.6.23}$$

where

$$\frac{\partial^2 g_{\alpha\beta}}{\partial u_{iI}\partial u_{jJ}} = \frac{\partial^2 \mathbf{g}_\alpha}{\partial u_{iI}\partial u_{jJ}} \cdot \mathbf{g}_\beta + \frac{\partial \mathbf{g}_\alpha}{\partial u_{iI}} \cdot \frac{\partial \mathbf{g}_\beta}{\partial u_{jJ}} + \frac{\partial \mathbf{g}_\alpha}{\partial u_{jJ}} \cdot \frac{\partial \mathbf{g}_\beta}{\partial u_{iI}} + \mathbf{g}_\alpha \cdot \frac{\partial^2 \mathbf{g}_\beta}{\partial u_{iI}\partial u_{jJ}} \tag{3.6.24}$$

From Eq. (3.6.14), the second derivative term in Eq. (3.6.24) yields

$$\frac{\partial^2 \mathbf{g}_\gamma}{\partial u_{iI}\partial u_{jJ}} = \frac{\partial N_J}{\partial \xi^\gamma}\frac{\partial \mathbf{e}_j}{\partial u_{iI}} = 0 \tag{3.6.25}$$

Now substituting Eq. (3.6.14) into Eq. (3.6.24), we find that

$$\frac{\partial^2 E_{\alpha\beta}}{\partial u_{iI}\partial u_{jJ}} = \frac{1}{2}\left(N_{I,\alpha}N_{J,\beta} + N_{I,\beta}N_{J,\alpha}\right)\delta_{ij} \tag{3.6.26}$$

This equation and the second Piola-Kirchhoff stress tensor give rise to the tangent geometrical stiffness tensor, which is given by

$$K^{\text{geo}}_{ijIJ} = \int_{\Omega_0} \frac{\partial^2 E_{\alpha\beta}}{\partial u_{iI}\partial u_{jJ}} S^{\alpha\beta} d\Omega_0 \tag{3.6.27}$$

or in Cartesian tensor notation as

$$\mathbf{K}^{\text{geo}}_{IJ} = \mathbf{I}_{(3\times 3)} \int_{\Omega_0} \mathbf{B}^T_{0I}\ \mathbf{S}\ \mathbf{B}_{0J}\ d\Omega_0 \tag{3.6.28}$$

where the components of $\mathbf{B}_{0I_{(2\times 1)}}$ are given by B^0_{jI} in Eq. (3.1.18) for $j = 1, 2$ and $\mathbf{S}$ is expressed in tensorial notation for the membrane element. Finally, the internal tangent matrix is defined by

$$\mathbf{K}^{\text{T}}_{\text{int}} = \mathbf{K}_{\text{mat}} + \mathbf{K}_{\text{geo}} \tag{3.6.29}$$

Another expression that is needed to compute the tangent stiffness matrix is the kinetic tangent matrix that is obtained directly from Eq. (3.6.1) by taking the derivative of the mass term respect to the displacements, which yields

$$\mathbf{K}^{\text{T}}_{\text{kin}} = \frac{1}{\beta\Delta t^2}\mathbf{M} \tag{3.6.30}$$

The last term in the tangent stiffness matrix comes from the derivative of the external forces respect to the displacements. Only when the external forces are functions of the displacements, an external tangent matrix different from zero is found. Since in this work pressure follower forces depend of the current displacements at each time step, this value can be computed from Eq. (3.2.104) giving

$$\mathbf{K}^{\text{T}}_{\text{ext}} = \frac{\partial\, \mathbf{f}^{\text{ext}}}{\partial \mathbf{u}} = \frac{p}{6}\frac{\partial}{\partial \mathbf{u}}\Big((\mathbf{x}_2 - \mathbf{x}_1)\times(\mathbf{x}_3 - \mathbf{x}_1)\Big) \tag{3.6.31}$$

The resulting equation is given in an explicit form of

$$\mathbf{K}^{\text{T}}_{\text{ext}} = \frac{p}{6}\begin{bmatrix} 0 & z_2 - z_3 & y_3 - y_2 & 0 & z_3 - z_1 & y_1 - y_3 & 0 & z_1 - z_2 & y_2 - y_1 \\ z_3 - z_2 & 0 & x_2 - x_3 & z_1 - z_3 & 0 & x_3 - x_1 & z_2 - z_1 & 0 & x_1 - x_2 \\ y_2 - y_3 & x_3 - x_2 & 0 & y_3 - y_1 & x_1 - x_3 & 0 & y_1 - y_2 & x_2 - x_1 & 0 \end{bmatrix} \tag{3.6.32}$$

A general expression for the external tangent matrix for pressure follower forces can be found in Bonet and Wood (1997) or Belytschko et al. (2000). With all these expressions the tangent stiffness matrix is built with

$$\mathbf{K}^{\text{T}} = \mathbf{K}^{\text{T}}_{\text{ext}} - \mathbf{K}^{\text{T}}_{\text{mat}} - \mathbf{K}^{\text{T}}_{\text{geo}} - \mathbf{K}^{\text{T}}_{\text{kin}} \tag{3.6.33}$$

and the algebraic equations given by Eq. (3.6.4) can be solve iteratively.

3.6.2.2 Cable Linearization

Following the same methodology given for the tangent stiffness matrices for membranes, the tangent stiffness matrices for cables are found. From Eq. (3.6.20) we can conclude that the material tangent stiffness matrix is

$$\mathbf{K}_{\text{mat}} = A_0 L [\mathbf{B}^T]^{loc} \, [\mathbf{C}] \, [\mathbf{B}]^{loc} \tag{3.6.34}$$

where $[\mathbf{B}]^{loc}$ is given by Eq. (3.3.26). The geometrical tangent stiffness matrix is found with the same procedure that for membrane elements, yielding

$$\mathbf{K}_{\text{geo}} = \frac{A_0 \{S_x\}^{loc}}{L} \begin{bmatrix} \mathbf{I}_{(3\times3)} & \mathbf{I}_{(3\times3)} \\ \mathbf{I}_{(3\times3)} & \mathbf{I}_{(3\times3)} \end{bmatrix} \tag{3.6.35}$$

The kinetic tangent stiffness matrix gives the same expression that Eq. (3.6.30), but with the corresponding mass matrix for two-node cable elements.

3.6.2.3 Shell Linearization

As explained in section **3.4.2**, a shell has a membrane and a bending part. Consequently its linearization is formed by a membrane tangent stiffness matrix and a bending tangent stiffness matrix.

The membrane tangent stiffness matrix is detailed in section **3.6.2.1** and is exactly the same to be used in shell elements. However the missing part corresponds to the bending tangent stiffness matrix. For the rotatinal-free shell element used in this work, this matrix is very complicated to derive, as can be found in Flores and Oñate (2001), and has no practical advantages if it is incorporated in a finite element program. Therefore as explained in Flores and Oñate (2005), the bending stiffness tangent matrix can be avoided and only the membrane tangent stiffness matrix is used in this work.

3.7 Code Development

In this work the membrane, cable and shell formulation have been implemented in the finite element program COMET (2007). The dynamic analysis with Bossak method, Hilber-Hughes-Taylor method and Generalized-α method have also been added to the code. This software is developed at the International Center for Numerical Methods in Engineering (CIMNE) and is used for coupled contact, mechanical and thermal analysis using the finite element method.

The finite element meshes and input data used in this work where generated using the program GiD (2007). This software is also developed at the International Center for Numerical Methods in Engineering (CIMNE) which is a preprocessor and postprocessor for finite element programs.

3.8 Example Problems

3.8.1 Inflation of a Square Airbag

A square membrane is inflated by internal pressure to simulate an airbag, as given by Contri and Schrefler (1988) and Lu et al. (2001). The internal pressure is 0.5 lb/ft^2. The side length of the airbag is 1 ft with a membrane thickness of 0.0001 ft. The Young's modulus is $E = 4.32 \times 10^6$ lb/ft^2 and the Poisson ratio is $\upsilon = 0.3$. The density used for the quasi-static analysis is $\rho = 100$ lb/ft^3, with 200 steps and a pseudo-time step $\Delta t = 0.0001$. The wrinkling algorithm is used for the analysis to avoid unwanted compression stresses. Because of the symmetry, only one-eighth of the airbag is modelled. A structured mesh of 200 three-node triangular membrane elements is used. The origin O is placed at the center of the airbag. Symmetry boundary conditions with fixed y-displacements are applied on side OA, fixed x-displacements are applied on side OC and fixed z-displacements are applied on side AB and BC.

The inflated airbag analyzed with the wrinkling algorithm is shown in Fig. 3.15 without amplification factor. The maximum transverse displacement is presented at the origin O in the z-direction with 0.249 ft, while the references give a value of 0.252 ft with nine-node quadrilateral elements. The maximum in-plane displacement is 0.142 ft symmetric for x- and y-direction, while the references give a value of 0.144 ft.

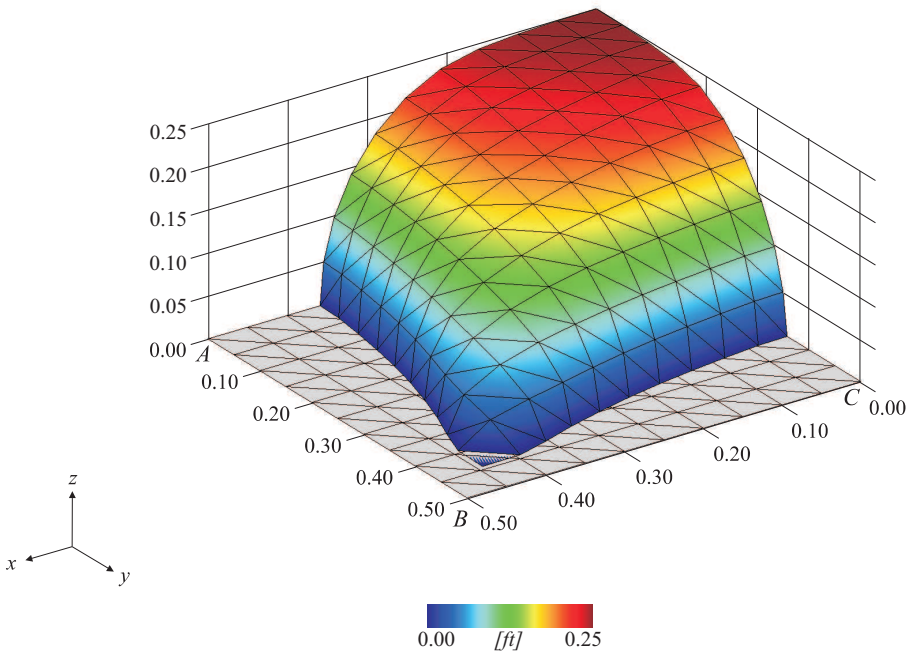

Figure 3.15 *z-displacements of inflated airbag*

The maximum principal stress is at the origin O with 4105 lb/ft^2, and no compression stresses appear in the solution since the wrinkling algorithm is used, see Fig. 3.16. The maximum principal stress given by the references is about 4000 lb/ft^2.

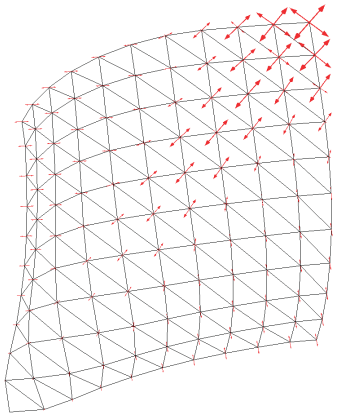

Figure 3.16 *Principal stresses with wrinkling*

A completely different solution is found with a conventional membrane analysis (no wrinkling algorithm is used), where high compression stresses appear in the solution, see blue vectors in Fig. 3.17. These negative stresses do not allow to inflate the airbag with such finite element discretization. In this analysis, the maximum transverse displacement is presented at the origin O in the z-direction with 0.097 ft, while the references give a value of 0.100 ft with nine-node quadrilateral elements. The maximum in-plane displacement is 0.066 ft symmetric for x- and y-direction, while the references give a value of 0.077 ft.

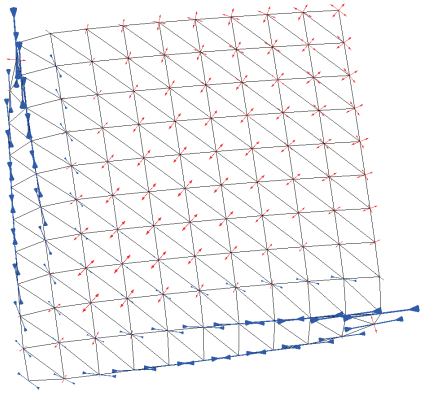

Figure 3.17 *Principal stresses without wrinkling*

The maximum principal tension stress is about 13000 lb/ft^2, and the maxi-

mum principal compression stress is $-35000\ lb/ft^2$. This example demonstrates the importance in membrane analysis of using an effective wrinkling algorithm to eliminate compression stresses. When no wrinkling algorithm is available for the membrane analysis, then a very fine mesh is needed in order to obtain a reasonable good solution.

3.8.2 Prestressed Membrane

An initially prestressed membrane is loaded by a transversal point load in its middle domain, as given by Levy and Spillers (1995) and Gil (2003). The point load is $-10000\ lb$ and the membrane side length is 240 in with a thickness of 0.004167 in. The Young's modulus is $E = 30.0 \times 10^6\ psi$ and the Poisson ratio is $\upsilon = 0.3$. The density used for the quasi-static analysis is $\rho = 0.06\ lb/in^3$, with 40 steps and a pseudo-time step $\Delta t = 0.5$. The prestressing effect is considered to be $\sigma_{xx} = 80000$ psi and $\sigma_{yy} = 80000\ psi$ in the whole domain. The sides of the membrane are fixed for the analysis. In Fig. 3.18 the mesh used in the analysis is shown, together with control nodes and control elements surrounded by a circle. The mesh has 32 three-node triangular membrane elements and 25 nodes.

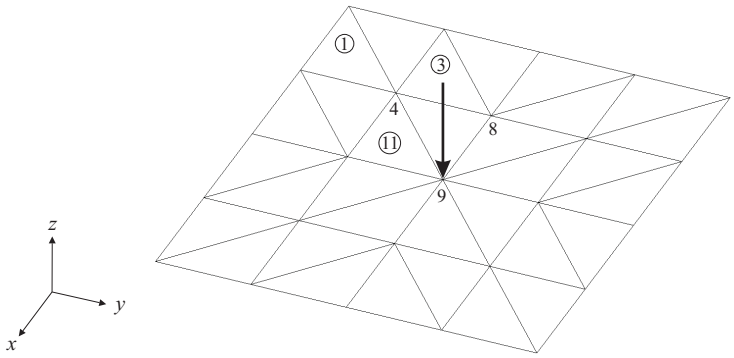

Figure 3.18 *Prestressed membrane geometry*

A comparison of the displacements at control nodes is shown in Table 3.5.

	Levy and Spillers			Gil			Present work		
Node	x-disp	y-disp	z-disp	x-disp	y-disp	z-disp	x-disp	y-disp	z-disp
4	0.015	-0.015	-1.431	0.014	-0.014	-1.423	0.014	-0.014	-1.429
8	0.000	-0.017	-2.605	0.000	-0.017	-2.600	0.000	-0.017	-2.600
9	0.000	0.000	-6.642	0.000	0.000	-6.626	0.000	0.000	-6.626

Table 3.5 *Membrane displacements [in]*

It can be seen that the displacements agree well with both referenced analysis using the same mesh. The major difference is at node 9 in the z-displacement, where Levy and Spillers (1995) give a greater value.

	Levy and Spillers			Gil			Present work		
Elem	σ_{xx}	σ_{yy}	σ_{xy}	σ_{xx}	σ_{yy}	σ_{xy}	σ_{xx}	σ_{yy}	σ_{xy}
1	97377	85212	-2801	97300	85164	-2797	97328	85139	-2794
3	83510	96859	-8657	83502	96830	-8631	83503	96839	-8677
11	144691	97831	-15616	144471	97849	-15582	144812	97649	-15711

Table 3.6 *Membrane Cauchy stresses [psi]*

A comparison of the Cauchy stresses at control elements is shown in Table 3.6, where it can be seen that the stresses are very similar between the referenced analysis.
In this example the fiber orientation is performed in order to give the elements the same orientation and then assign the correct prestressed values to the mesh. However in this special case where an initially flat membrane is analyzed, a simpler method can be used.

Just to compare the maximum z-displacement, the membrane is analyzed without the prestressed force which results in a displacement of -9.242 in compared to -6.626 in with the prestressed load. This show us how important can be the prestressed force in membrane elements.

3.8.3 Nonlinear Plate

A plate with uniform load is analyzed. The analysis is assumed to be geometrically nonlinear, as presented by Zienkiewicz and Taylor (1989) and Clemente (2007). The same geometry and material properties of Clemente are used in this analysis to simplify the comparison of the different solutions. The only difference is that Clemente used 8-node three-dimensional brick elements while in this work the 3-node rotation-free shell elements are employed. The side length of the plate is $L = 2a = 20\ m$ with a thickness of 1 m. The Young's modulus is taken as $E = 12$ Pa and the Poisson ratio is $\upsilon = 0.0$. The density used for the quasi-static analysis is $\rho = 1.0\ kg/m^3$, with 10 steps and a pseudo-time step $\Delta t = 0.1$. Because of the symmetry, only a quarter of the plate is analyzed.

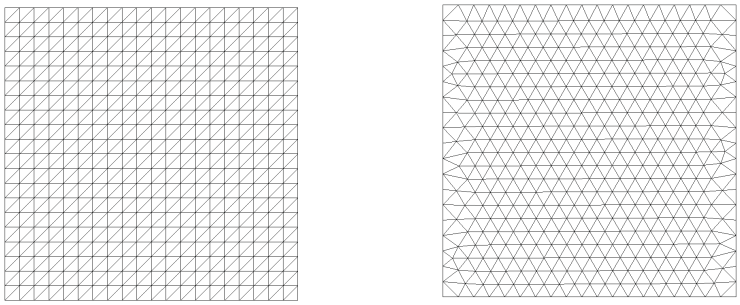

Figure 3.19 *Finite element meshes used for the analysis*

Two meshes are used for the analysis as shown in Fig. 3.19. The structured mesh has 800 elements and 441 nodes, while the unstructured mesh has 816 elements with 447 nodes. A variable uniform load q is applied to the plate, with values from 0.00 to $-0.04\ Pa$. The adimensional solution of the problem is plotted in Fig. 3.20. The transversal displacement at the central point of the plate w is normalized by the thickness t in the horizontal axis, while the load q is normalized by Dt/a^4 in the vertical axis, where the value $D = Et^3/12$.

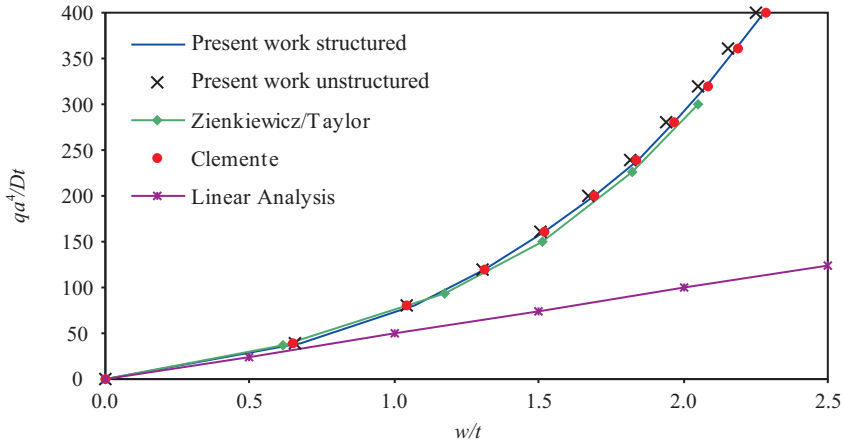

Figure 3.20 *Central plate displacement by uniform load*

The deformed without amplification factor is shown in Fig. 3.21 and Fig. 3.22 for two different views, where the reference mesh is drawn in gray color.

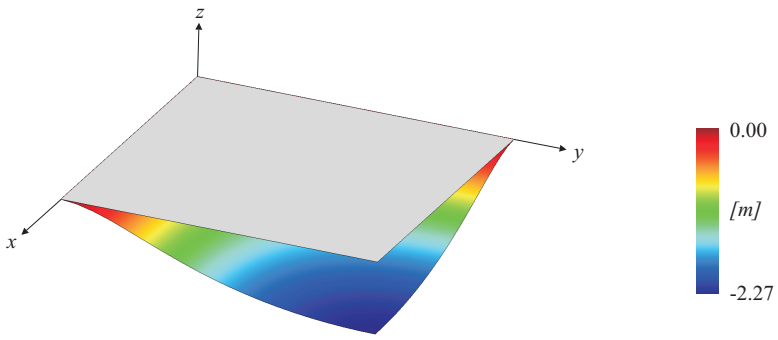

Figure 3.21 *z-displacements of nonlinear plate*

We can conclude that our shell analysis gives the same solution that using three-dimensional brick elements. Less computational effort is required in our analysis since the degrees of freedom are drastically reduced to those used by Clemente, where his analysis needed 1600 elements and 2205 nodes with four layers over the

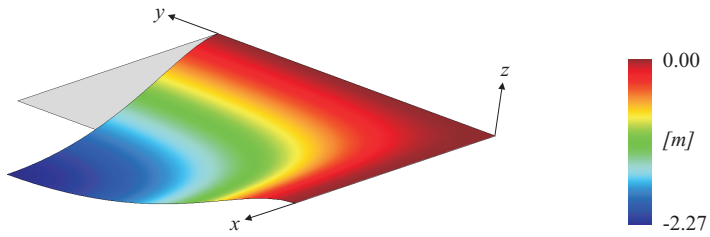

Figure 3.22 *z-displacements of nonlinear plate*

thickness. From Fig. 3.20 we can also see that the solution of the linear analysis becomes an important aspect to take care of when the load is incremented and the behavior of the linear and nonlinear analysis give great differences.

3.8.4 Hemispherical Shell with 18° Hole

A popular benchmark problem for linear shell analysis is the pinched hemisphere which is concerned with the nearly inextensional deformation of a hemispherical shell with an 18° hole at the top under the action of two inward and two outward forces 90° apart. Symmetry conditions are used in this problem and only one-quarter needs to be modelled, as shown in Fig. 3.23.

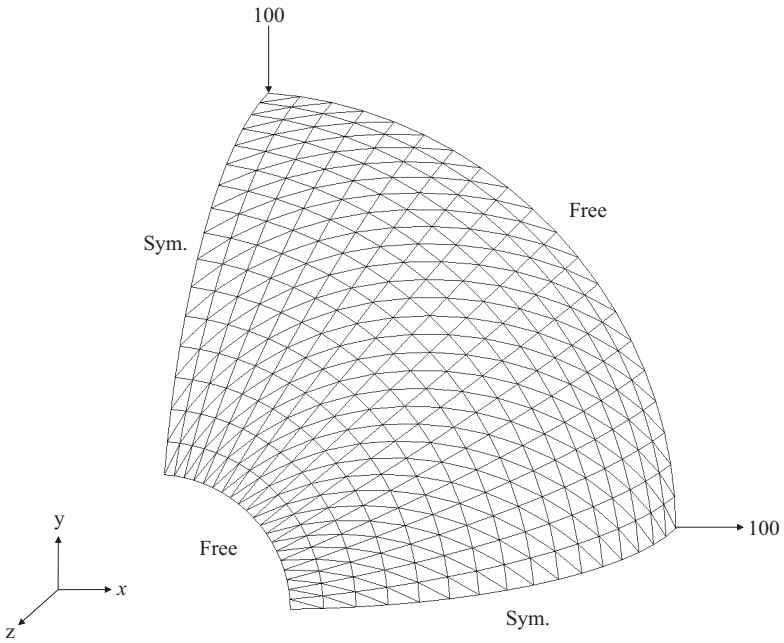

Figure 3.23 *Structured hemispherical shell geometry*

To illustrate the large deformation capabilities of the rotation-free formulation, the forces of the linear problem are incremented 100 times to obtain deflections of nearly 60% of the initial radius. This problem is compared with the solution obtained by Simo et al. (1990a) and Flores and Oñate (2001). The problem geometry consists of a sphere of radius $R = 10$ with an 18° hole and thickness of 0.04. The material properties are $E = 6.825 \times 10^7$ and $\upsilon = 0.30$. The forces and boundary conditions are shown in Fig. 3.23.

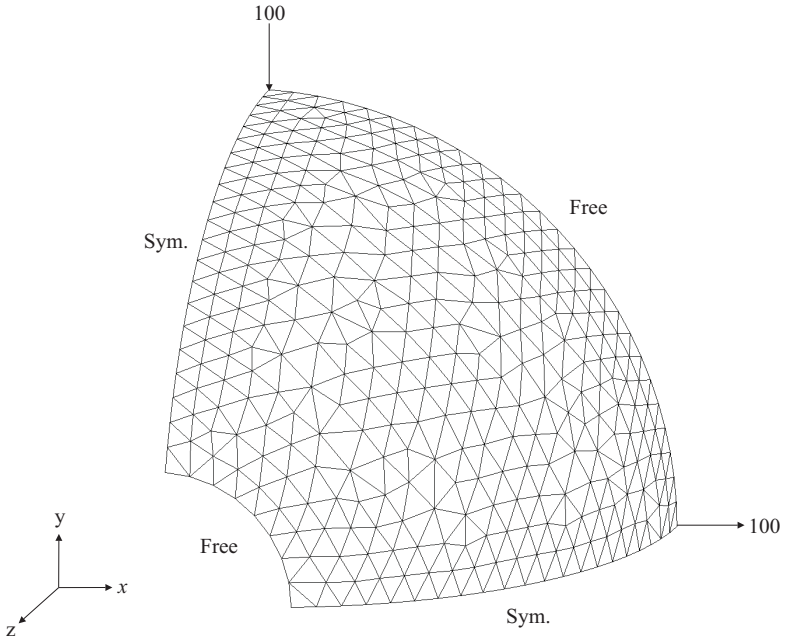

Figure 3.24 *Unstructured hemispherical shell geometry*

This problem was solved by Simo et al. (1990a) using a structured mesh of 256 quadrilateral elements with 1632 d.o.f. To compare the benchmark, in this work two meshes are studied, a structured mesh of 640 elements with 1036 d.o.f., as shown in Fig. 3.23, and an unstructured mesh of 640 elements with 1032 d.o.f. as shown in Fig. 3.24. A summary of the maximum displacements in x- and y-direction is given in Table 3.7.

Author	Elements	d.o.f.	Mesh	u disp	v disp
Simó	256	1632	structured	3.380	-5.875
Present work	640	1036	structured	3.319	-5.878
Present work	640	1032	unstructured	3.324	-5.929

Table 3.7 *Maximum displacements*

A plot different of load-displacement values is given in Fig. 3.25.

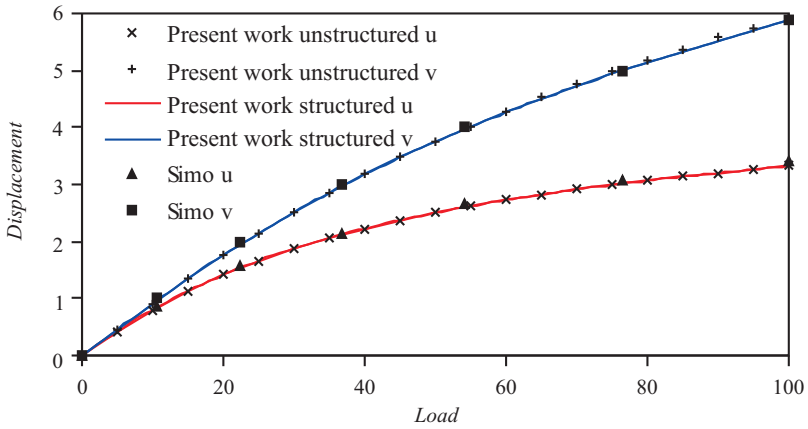

Figure 3.25 *Load-displacement comparison*

The complete deformed structured mesh without magnification factor is given in Fig. 3.26, where the norm of displacements is shown.

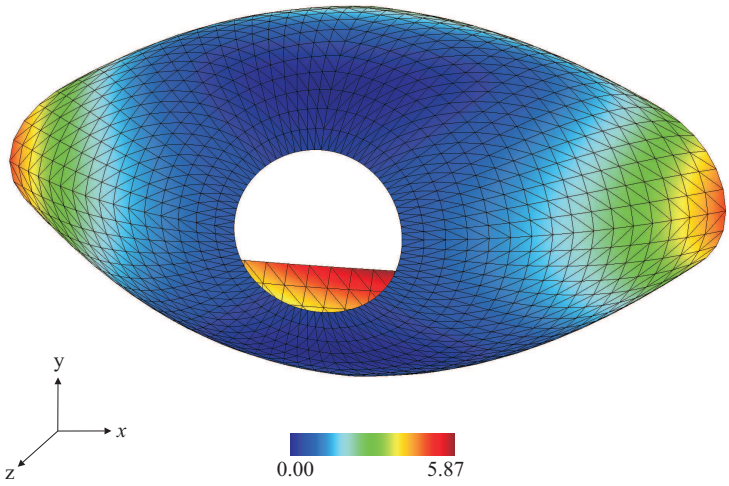

Figure 3.26 *Deformed without magnification factor*

We can conclude that the rotation-free shell formulation has an excellent behavior for problems involving large deformations with both structured and unstructured meshes, the former with uniform element size distribution.

3.8.5 Free Vibration Pendulum

The objective of the free vibration pendulum problem is to show the importance of the time integration scheme used in structural problems since sometimes high

frequency noise persists in the solution for large deformations analysis. The pendulum problem is also analyzed by Rossi (2005) using quadrilateral elements for the whole problem, and showing a graph of instability given by the modulus of reaction. The mesh used in this analysis is shown in Fig. 3.27.

Figure 3.27 *Pendulum mesh*

The cable length is 1.5 m with a cross sectional area of 0.0005 m^2. The circular end mass has a radio of 0.15 m with a thickness of 1.0 m. The Young's modulus for both the cable and mass is taken as $E = 2.1 \times 10^{11}$ Pa and the Poisson ratio is $\upsilon = 0.3$. The density used for the dynamic analysis is $\rho = 7800$ kg/m^3 for the whole problem. The mesh used in the analysis has 20 two-node cable elements and 184 three-node triangular plane stress elements with a total of 131 nodes. The time step size is $\Delta t = 0.01$ s. Gravity forces are applied to the structure.

Fig. 3.28 show the time vs. y-displacement graph, where the Generalized-α method is stable for the time studied. However the Newmark algorithm is stable only at the beginning of the analysis.

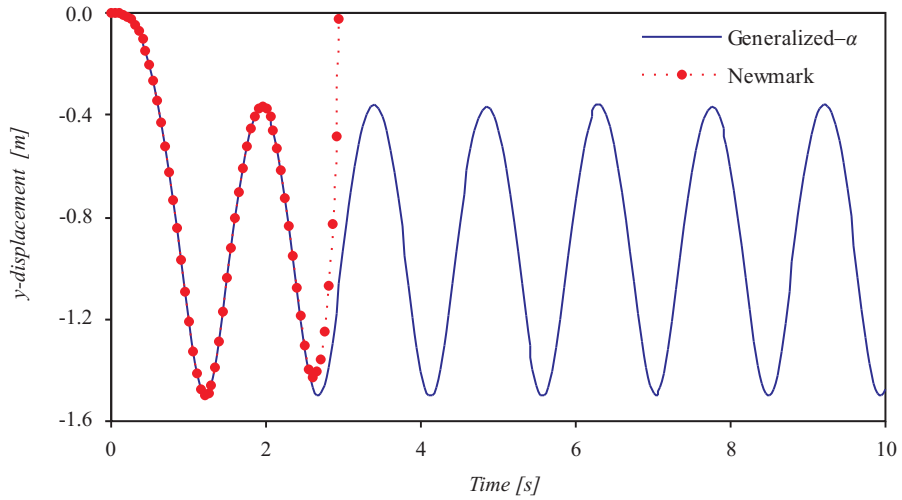

Figure 3.28 *Time-displacement graph*

In Figs. 3.29-3.33 various time instants are plotted comparing the deformed shape of the pendulum between the Generalized-α method and the Newmark algorithm. Fig. 3.31 shows that at time instant 2.18 s the high frequencies begin to appear in

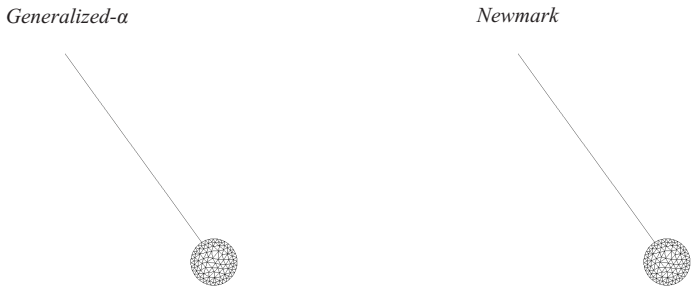

Figure 3.29 *Deformed cable at time 1.00 s.*

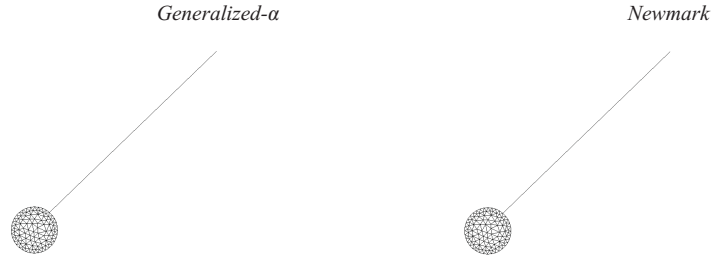

Figure 3.30 *Deformed cable at time 1.50 s.*

Figure 3.31 *Deformed cable at time 2.18 s.*

Figure 3.32 *Deformed cable at time 2.54 s.*

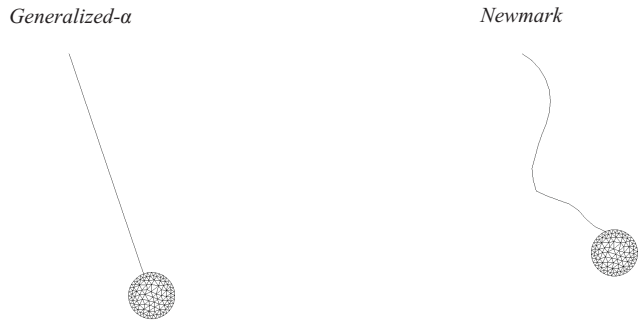

Figure 3.33 *Deformed cable at time 2.78 s.*

the Newmark analysis. Later in Fig. 3.32 the high frequencies become more evident until that in Fig. 3.33 the high frequencies spoil the solution for the Newmark algorithm. However the Generalized-α method keeps its convergence properties for the time interval studied. Also the Hilber-Hughes-Taylor and Bossak's methods show the same accuracy and stability that the Generalized-α method. The Newmark method give the same solution that the former methods with a time step size of $\Delta t = 0.001\ s$.

3.8.6 Inflation of a Parachute

In this example an initially highly folded parachute is inflated. Since high compression stresses are presented in the solution, the wrinkling algorithm is used in order to avoid an inappropriate deformed configuration. The initial configuration of the parachute is shown in Fig. 3.34. Different inflation processes of parachutes are studied by Lu et al. (2001) and Tezduyar et al. (2006).

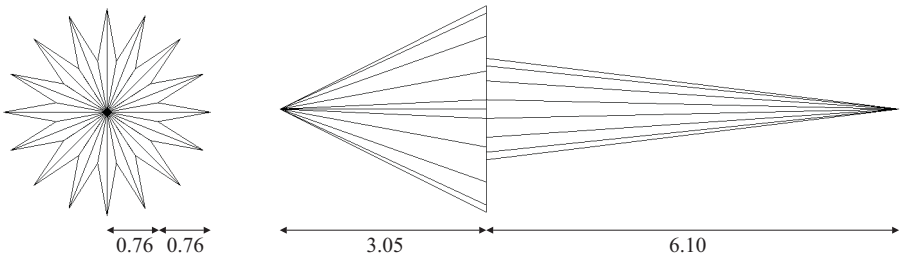

Figure 3.34 *Initial configuration of the parachute, top and side views [m]*

The mesh used for the example has 1664 membrane elements and 16 cable elements, with a total of 882 nodes. The internal pressure is taken as 5 Pa. Parachute material properties are used with the Young's modulus as $E = 2.07 \times 10^8\ Pa$, the Poisson ratio 0.3 and the material density $\rho = 9.61\ kg/m^3$. The thickness is taken as 0.00003 m. The cable properties are Young's modulus $E = 2.07 \times 10^9\ Pa$ and

the cross-sectional area of 0.00013 m^2. The initial configuration of the problem is shown in Fig. 3.35 together with an intermediate deformation step.

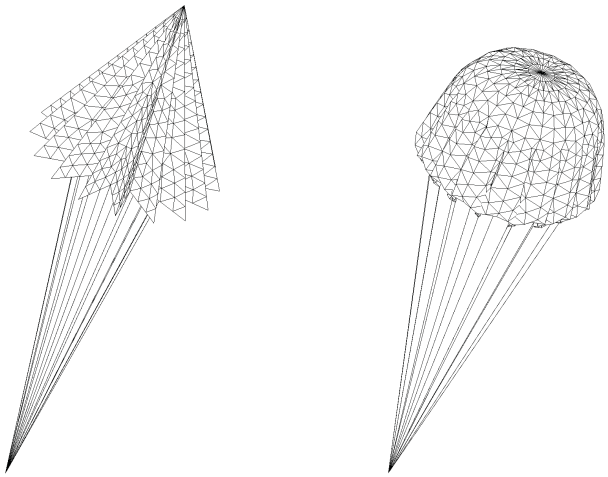

Figure 3.35 *Inflation process of the parachute from reference configuration*

The problem uses the wrinkling algorithm with a quasi-static analysis which stabilizes the solution. The number of steps are 3000 with a pseudo-time of 0.0001. Fig. 3.36 shows different instants of the inflation process of the parachute.

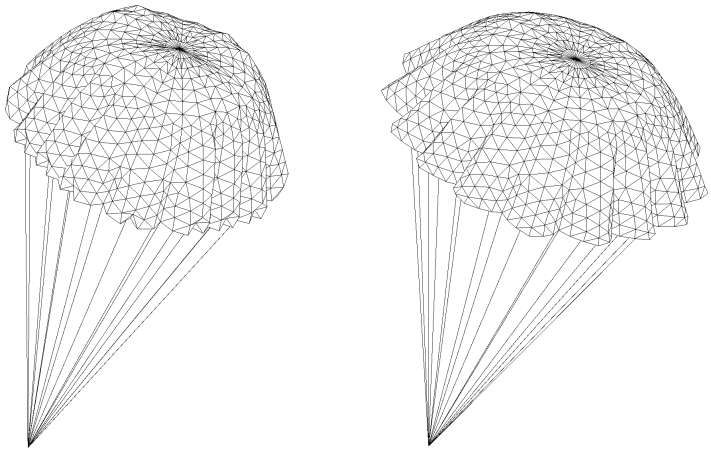

Figure 3.36 *Inflation process of the parachute until final configuration*

The same parachute is analyzed dynamically with the wrinkling algorithm using 3000 steps and a time step size $\Delta t = 0.0001\ s$. In this case stiffness proportional damping was applied to stabilized the solution of the problem. Both analysis, quasi-static and dynamic lead to the same solution.

Fig. 3.37 shows the vertical displacements while Fig. 3.38 shows the horizontal displacements where it can be seen that the problem leads to a symmetric solution.

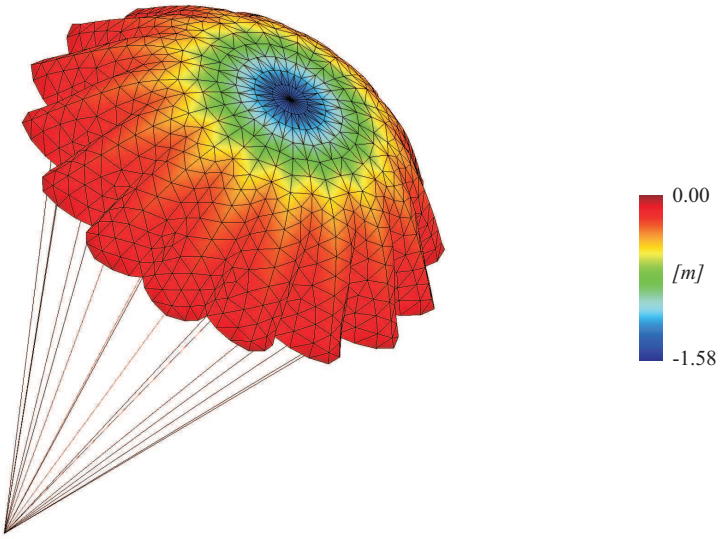

Figure 3.37 *Vertical displacements at final configuration*

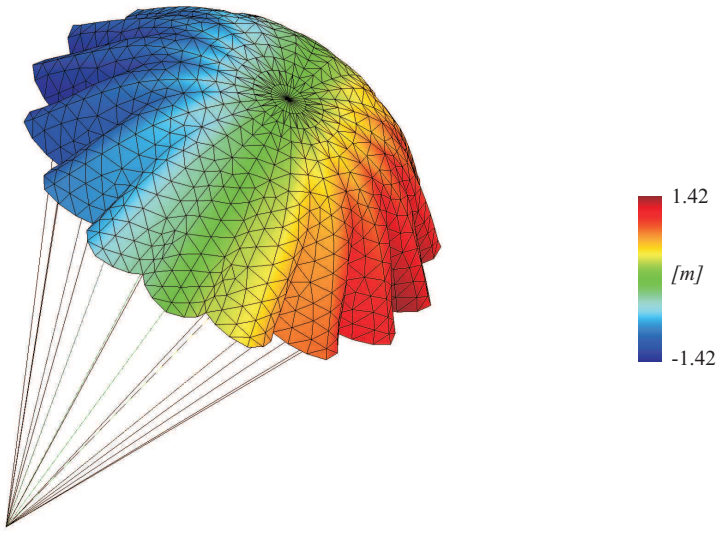

Figure 3.38 *Horizontal displacements at final configuration*

Fig. 3.39 shows the maximum principal stresses while Fig. 3.40 shows the minimum principal stresses. In both figures it can be seen that there are no compression stresses due to the use of the wrinkling algorithm.

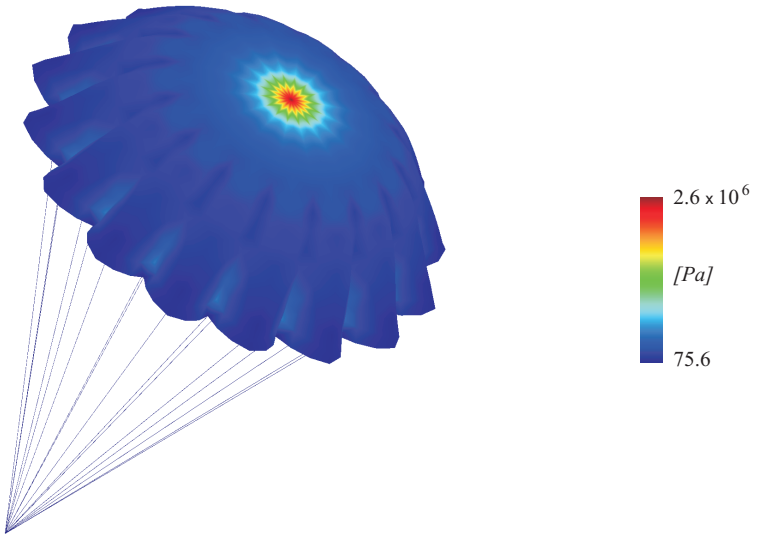

Figure 3.39 *Maximum principal stresses*

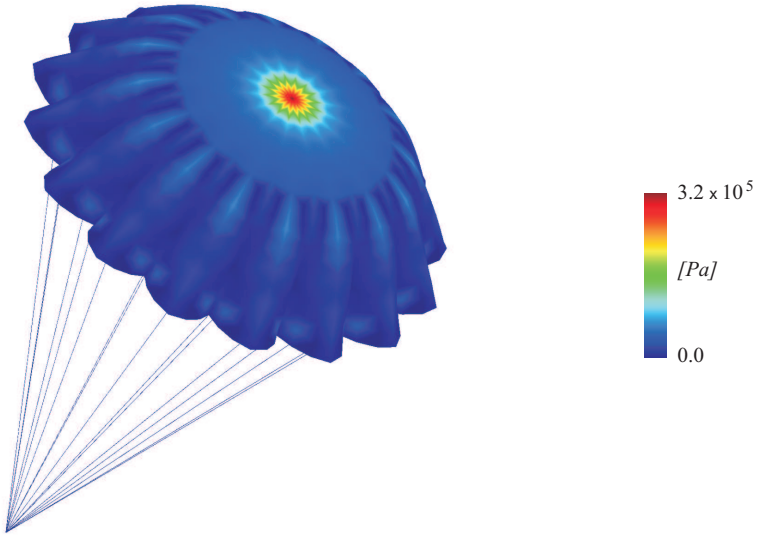

Figure 3.40 *Minimum principal stresses*

The same parachute is analyzed dynamically without the wrinkling algorithm. Fig. 3.41 shows the vertical displacements while Fig. 3.42 shows the horizontal displacements.

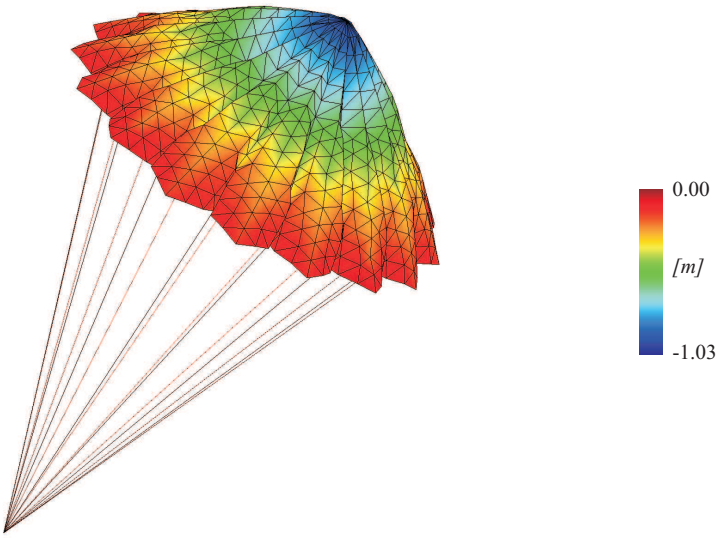

Figure 3.41 *Vertical displacements at final configuration*

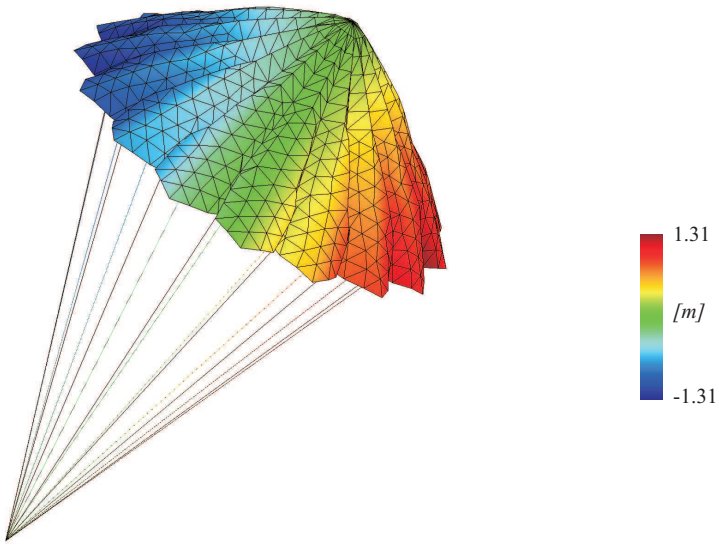

Figure 3.42 *Horizontal displacements at final configuration*

Fig. 3.43 shows the maximum principal stresses while Fig. 3.44 shows the minimum principal stresses. In both figures it can be seen that there are compression stresses due to the use of conventional membrane theory that do not include any wrinkling algorithm.

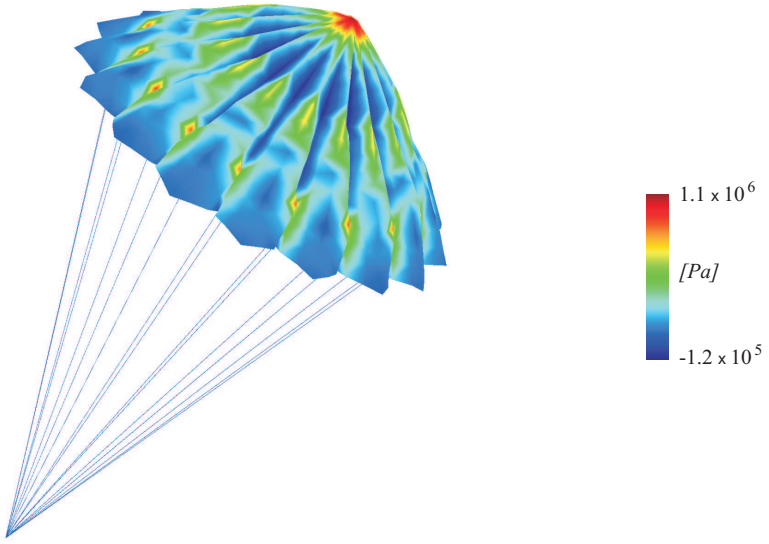

Figure 3.43 *Maximum principal stresses*

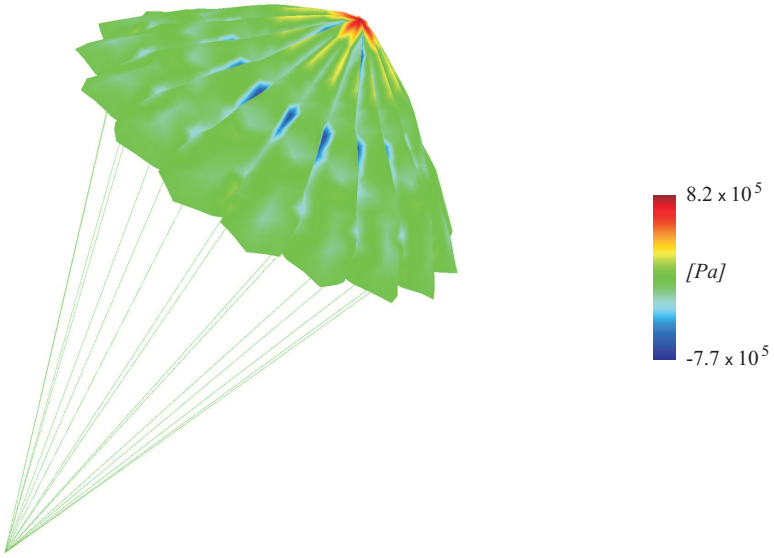

Figure 3.44 *Minimum principal stresses*

Fig. 3.45 shows two final configurations of the parachute. One includes the wrinkling algorithm while the other one does not include it.

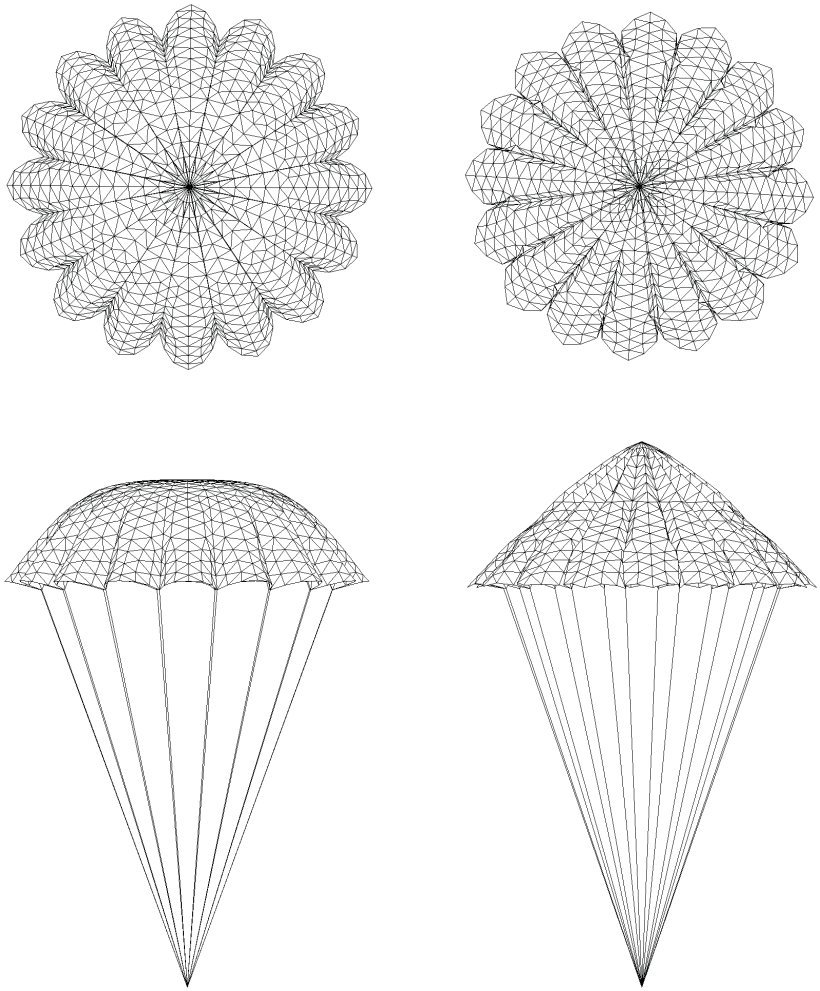

Figure 3.45 *Final configuration: left with wrinkling, right without wrinkling*

It can be seen that the shape of the inflated parachute is completely different if the wrinkling algorithm is used or not. Also the maximum principal stresses are very different. In the analysis with the wrinkling algorithm there are no compression stresses, just as it really happens. However conventional membrane analysis that do not include any wrinkling algorithm lead to an unreal final configuration due to the presence of compression stresses.

3.8.7 Hyperbolic Paraboloid

Ziegler (2001) and Raible (2003) have studied hyperbolic paraboloids under vertical loading. Geometry parameters are given in Fig. 3.46, where $a = 12\sqrt{2}\ m$, $b = 2.88$ m with a membrane thickness of 0.3 mm. Membrane boundary is fixed. The Young's modulus is $E = 21000\ kN/cm^2$ and the Poisson ratio is $\upsilon = 0.3$. A vertical load of 10 kN/m^2 is applied in various steps.

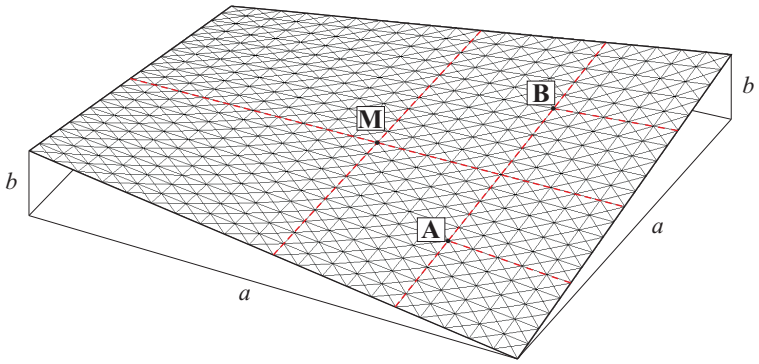

Figure 3.46 *Geometry and mesh for hyperbolic parabolid*

Also in Fig. 3.46 control points M, A and B are given for comparison purposes. A quasi-static analysis is performed using the wrinkling algorithm to avoid unwanted compression stresses. A structured three-node membrane triangular mesh of 1600 elements and 841 nodes is used for the analysis.

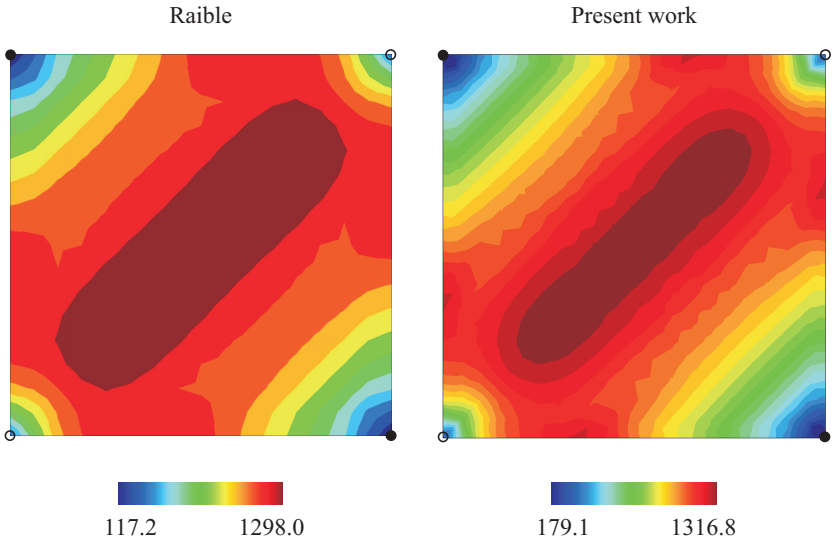

Figure 3.47 *Comparison of* 1^{st} *principal stress* S_i $[MN/m^2]$

In Fig. 3.47 the 1st principal stress S_i is compared with the one obtained by Raible (2003). The tendency of both works is the same, where little differences are found. Also maximum and minimum values for S_i are very similar in both cases. In this figure, the geometry of the hyperbolic paraboloid is indicated as follows: black circles denote the lower corner nodes while white circles mean upper ones. At point A, Ziegler (2001) seems to indicate a slack membrane state, while Raible (2003) indicate a wrinkled membrane state. In this work, at point A the slack membrane state is found.

Finally a plot of the vertical displacements at the control points is given in Fig. 3.48, where solutions of Ziegler (2001) and Raible (2003) are also included. In the work of Raible (2003) two wrinkling algorithms are studied, and here only the *corrected approach* solution is included since it delivers the most reliable results. In these three works, vertical displacement of control point M is very similar and in this work a value of 36.4 *cm* is found. A closer vertical displacement between these three works is found for control point B with a value of 26.3 *cm*. However, control point A delivers some differences between the vertical displacements of the compared cases. The solution presented in this work lies between the works of Ziegler (2001) and Raible (2003), but it can be seen that the present solution is closer to the former one, which in this work correspond to 24.6 *cm*.

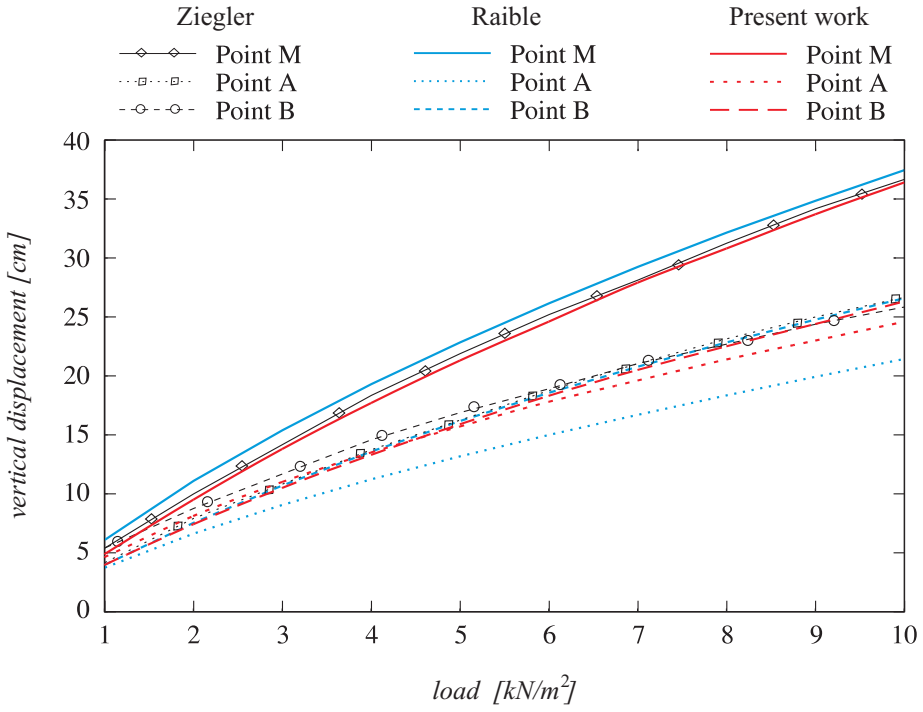

Figure 3.48 *Comparison of selected nodes*

3.8.8 Orthotropic Spinnaker

Usually sails are built with composite materials, which sometimes are modeled with isotropic or orthotropic materials. Fig. 3.49 shows different materials for sails, where the material on the left picture can be modeled as an isotropic material while the material on the right picture can be modeled as an orthotropic material.

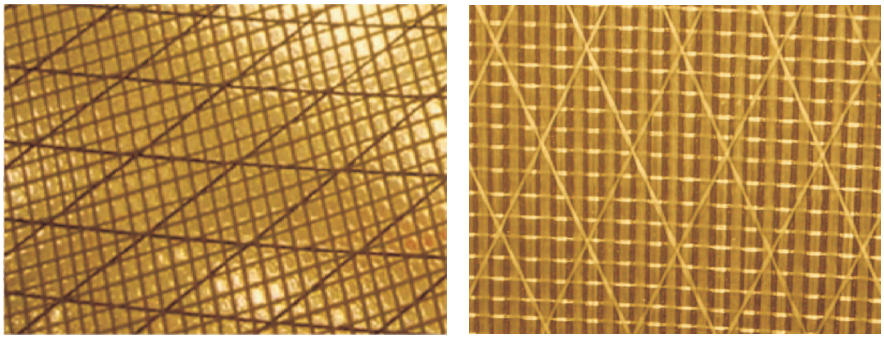

Figure 3.49 *Materials to build sails*

A sail is built as an assembling process of single parts of the cutting pattern which are sewed and glued together. Each one of the parts has fibers of principal reinforcement direction that for optimization of the sail take different forms. In the case of a spinnaker, their orientations are shown in Fig. 3.50.

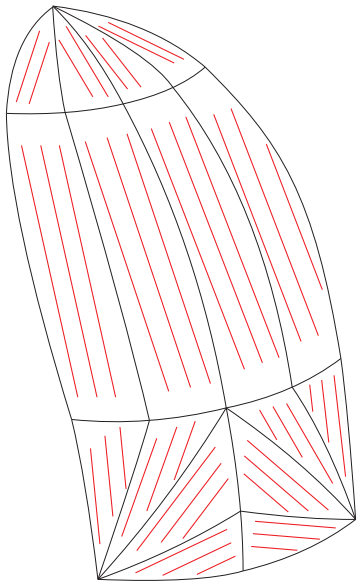

Figure 3.50 *Principal fiber orientation for a spinnaker*

The objective of this example is to show how a membrane structure build with an orthotropic material can be analyzed, including different local orientations for the material. Fig. 3.51 shows the manufacturing process for a spinnaker.

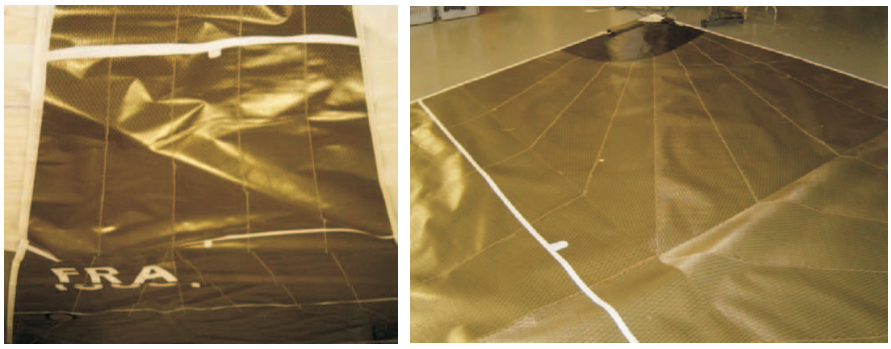

Figure 3.51 *Spinnaker manufacturing process*

Following the methodology given in this work for the fiber orientation, Figs. 3.52 - 3.53 show vectors of local x-direction for two configurations.

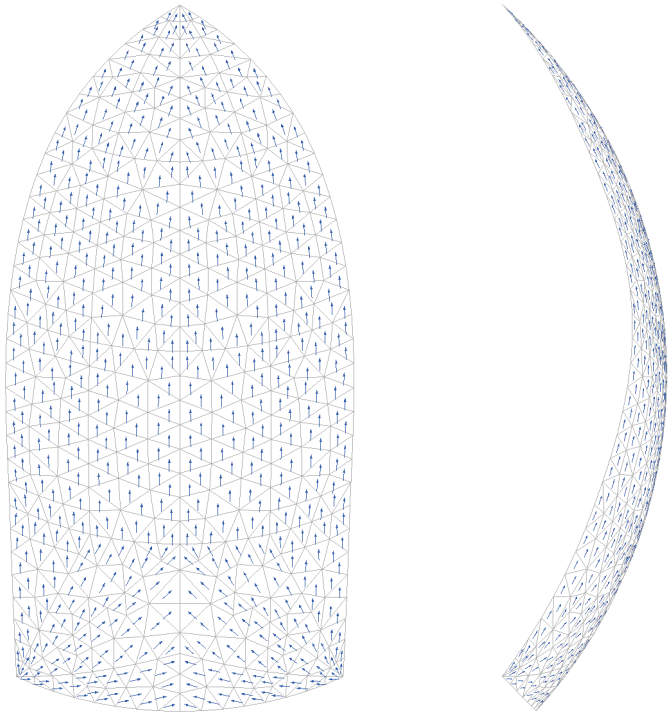

Figure 3.52 *Principal fiber direction: optimal*

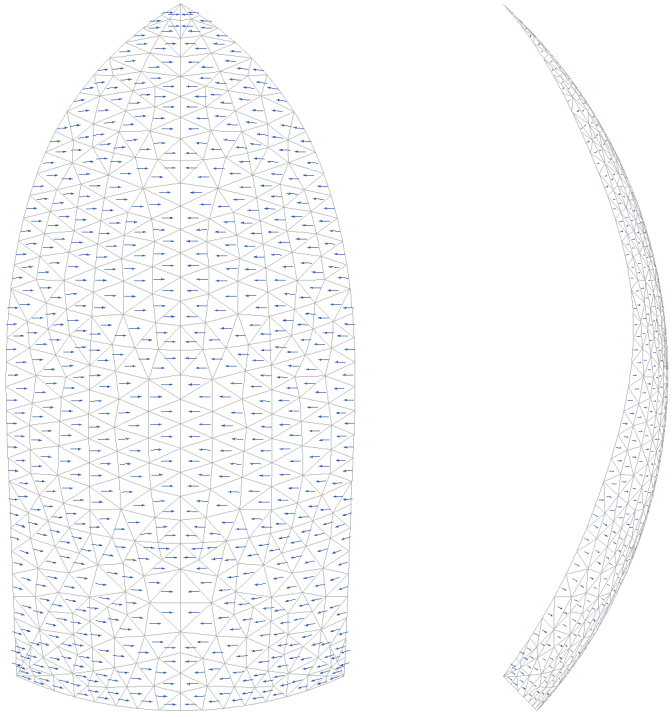

Figure 3.53 *Principal fiber direction: horizontal*

Fig. 3.52 shows the optimal fiber orientation for a spinnaker, while Fig. 3.53 shows an horizontal orientation.

Material orthotropic properties are taken with a Young modulus $E_x = 1100$ N/mm^2, $E_y = 385$ N/mm^2, Poisson ratio $\upsilon_{xy} = 035$, $\upsilon_{yx} = 0.1225$ and shear modulus $G_{xy} = 220$ N/mm^2. A uniform pressure follower load of 20 N/m^2 is applied for the analysis. The bottom dimension is 6.5 m, with a high of 14.0 m and thickness of 0.1 mm. The structure is discretized with 686 three-node triangular membrane elements and 384 nodes.

Fig. 3.54 shows values of the second Piola-Kircchoff stress tensor $\mathbf{S}$. On the left part of the figure, values for S_{xx} are plotted, where the local direction for xx is given by the optimal orientation of the fibers, as illustrated in Fig. 3.52. The corresponding local values for S_{xx} are maximum with 25.87 MPa and minimum with 0.64 Mpa. The right part of Fig. 3.54 shows values for the 1st principal component S_i of the second Piola-Kircchoff stress tensor, corresponding to a maximum of 25.92 Mpa and minimum with 0.68 Mpa. In this case, both solutions are almost identical because the orientation for the principal fiber of the material follows the vectors of the 1st principal component of the stress tensor, as shown in Fig. 3.55.

On the contrary, Fig. 3.56 gives values of the second Piola-Kircchoff stress tensor $\mathbf{S}$. On the left part of the figure, values for S_{xx} are plotted, where the local

direction for xx is given by the horizontal orientation of the fibers, as illustrated in Fig. 3.53. The corresponding local values for S_{xx} are maximum with 8.22 MPa and minimum with -0.57 Mpa. The right part of Fig. 3.56 shows values for the 1st principal component S_i of the second Piola-Kircchoff stress tensor, corresponding to a maximum of 24.46 Mpa and minimum with 0.72 Mpa. In this case, both solutions are very different because the orientation for the principal fiber of the material is horizontal, which is completely different from the vectors of the 1st principal component of the stress tensor that give an optimal material usage.

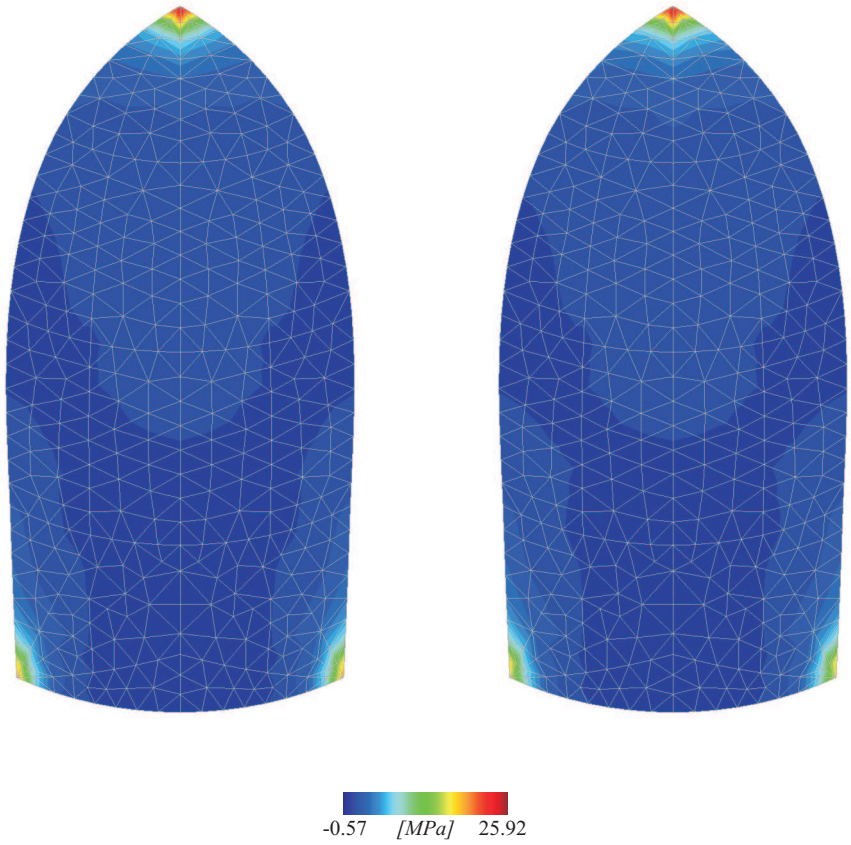

Figure 3.54 *Second Piola Kircchoff stresses: optimal fiber orientation*

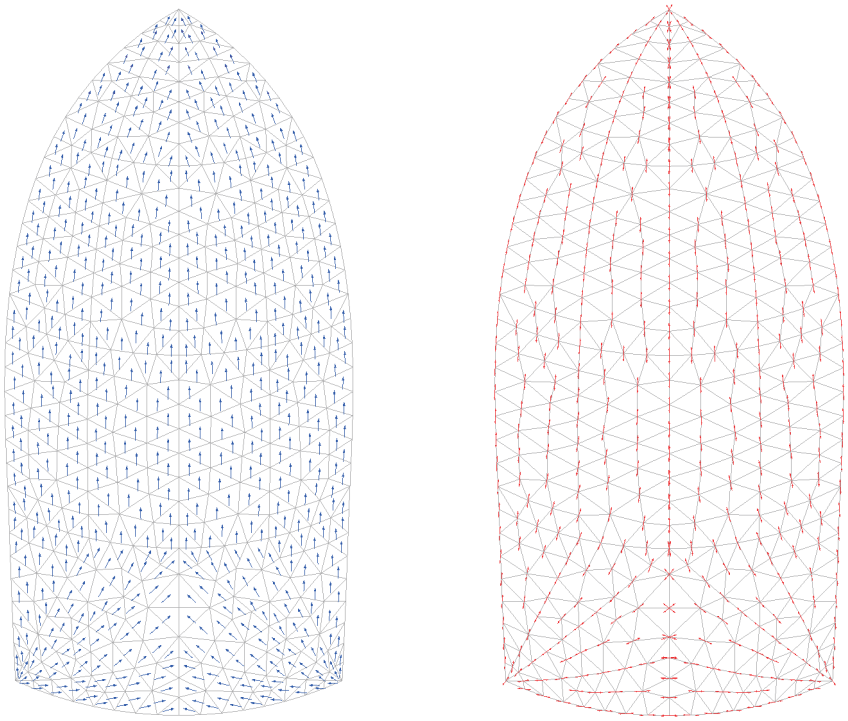

Figure 3.55 *Optimal fiber orientation and 1st principal stress direction*

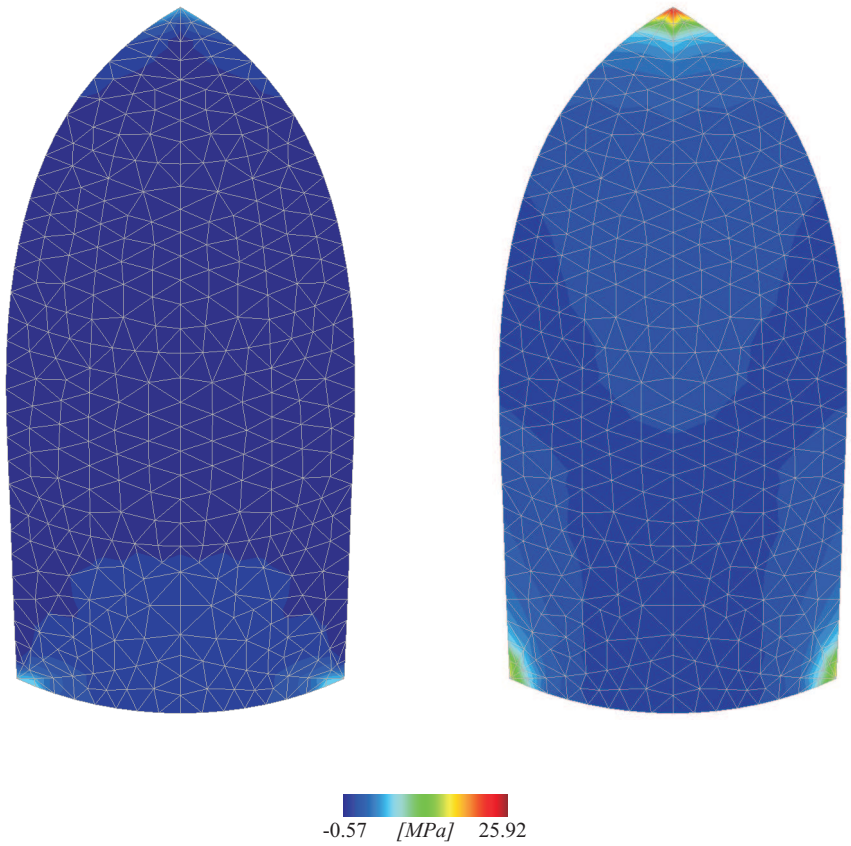

Figure 3.56 *Second Piola Kircchoff stresses: horizontal fiber orientation*

Chapter 4

Fluid Dynamics

In this chapter, the fluid dynamics equations used in this work to solve incompressible flow problems are presented. The objective here is only to explain the tools implemented to solve the fluid equations that later will be used as an application in the fluid-structure interaction problem.

4.1 Introduction

Fluid mechanics deals with the flow of fluids. The main difference between a fluid and a solid is that while solids have very strong intermolecular attractive forces, fluids are characterized by the relative mobility of its molecules. It is common that the stress in a solid is proportional to the strain, while the stress in a fluid is proportional to the rate of strain. This proportional parameter in fluids is known as the *viscosity*.

Fluid mechanics is usually divided into smaller areas based on characteristics of the fluid properties. An *inviscid fluid* is one where the viscosity is assumed to be zero. An *incompressible fluid* is one which density variations compared to a reference density are negligible.

The motion of a fluid is governed by the laws of conservation of mass, momentum (resulting in the Navier-Stokes equation) and energy, all of them described in chapter **2**. When temperature effects are not important, as assumed in this work, the energy equation is uncoupled and only the Navier-Stokes equation and the continuity equation are solved. With the help of computers, predictions of fluid flow based on the governing equations can be done, and the science responsible for this is called *computational fluid dynamics* (CFD).

4.2 Governing Equations

In fluid mechanics problems, Lagrangian methods are totally inappropriate. Lagrangian elements become severely distorted when the material is similar deformed since they follow the material. On the other hand, in fluid mechanics problems the

interest is focused on a particular spatial subdomain, therefore this type of problem is more suited to Eulerian elements. This kind of elements are fixed in space, thus undergo no distortion. However other kind of problems emerge as a consequence of the convection of the material through the elements.

4.2.1 Weak Form

The strong for consists of the Navier-Stokes and continuity equation, the velocity boundary conditions $\bar{v}_i$ on the Dirichlet boundary Γ^D and the traction boundary conditions $\bar{t}_i$ on the Neumann boundary Γ^N, where the boundary Γ_0 is defined by $\Gamma_0 = \Gamma^D \cup \Gamma^N$. To develop the weak form of the Navier-Stokes equation, the space of the test functions for the Eulerian description is defined as

$$\delta v_i(\mathbf{x}) \in \mathcal{V}_0, \quad \mathcal{V}_0 = \left\{\delta v_i | \delta v_i \in H^1(\Omega), \;\; \delta v_i = 0 \;\text{ on }\; \Gamma^D\right\} \tag{4.2.1}$$

where $H^1(\Omega)$ consists of vector functions whose components and their derivatives of order 1 are square-integrable. The space of the trial functions for the velocities is given by

$$v_i(\mathbf{x}, t) \in \mathcal{V} \quad \mathcal{V} = \left\{v_i | v_i \in H^1(\Omega), \;\; v_i = \bar{v}_i \;\text{ on }\; \Gamma^D\right\} \tag{4.2.2}$$

The development of a Galerkin-type weak form consists in taking the product of the general form of the Navier-Stokes equation, Eq. (2.6.1), by the test function δv_i, integrating over the current domain and using appropriate boundary conditions, yielding

$$\int_\Omega \delta v_i \left(\rho \left(\frac{\partial v_i}{\partial t} + v_j \partial_j v_i \right) + \underline{\frac{\partial p}{\partial x_i}} - \rho b_i - \underline{\mu \left(\nabla^2 v_i + \frac{1}{3} \frac{\partial}{\partial x_i} (\nabla \cdot \mathbf{v}) \right)} \right) d\Omega = 0 \tag{4.2.3}$$

where Eq. (2.6.2) has been substituted into Eq. (2.6.1) and μ is the *dynamic viscosity* . Integrating by parts[1] the underlined terms of Eq. (4.2.3), leads to

$$\begin{aligned} &\int_\Omega \delta v_i \left(\rho \frac{\partial v_i}{\partial t} + \rho v_j \frac{\partial v_i}{\partial x_j} - \rho b_i \right) d\Omega - \int_\Omega p \frac{\partial \delta v_i}{\partial x_i} d\Omega \; + \\ &\int_\Omega \mu \frac{\partial v_i}{\partial x_j} \frac{\partial \delta v_i}{\partial x_j} d\Omega + \int_\Omega \frac{1}{3} \mu \left(\nabla \cdot \mathbf{v} \right) \frac{\partial \delta v_i}{\partial x_i} d\Omega \; = \\ &\int_{\Gamma^N} \mu \delta v_i n_j \frac{\partial v_i}{\partial x_j} d\Gamma + \int_{\Gamma^N} \frac{1}{3} \mu \delta v_i n_j \left(\nabla \cdot \mathbf{v} \right) \delta_{ij} d\Gamma - \int_{\Gamma^N} \delta v_i n_j p \delta_{ij} d\Gamma \end{aligned} \tag{4.2.4}$$

The boundary integrals of this equation can be developed as detailed next

[1] $\int d(\mathbf{uv}) = \int \mathbf{u} d\mathbf{v} + \int \mathbf{v} d\mathbf{u}, \qquad \int \mathbf{u} d\mathbf{v} = \mathbf{uv} - \int \mathbf{v} d\mathbf{u}$

$$\begin{aligned}
&\int_{\Gamma^N} \delta v_i n_j \left(-p\delta_{ij} + \mu \frac{\partial v_i}{\partial x_j} + \frac{1}{3}\mu \frac{\partial v_j}{\partial x_j}\delta_{ij} \right) d\Gamma = \\
&\int_{\Gamma^N} \delta v_i n_j \left(-p\delta_{ij} + \mu \frac{\partial v_i}{\partial x_j} + \mu \frac{\partial v_j}{\partial x_i} - \frac{2}{3}\mu \frac{\partial v_j}{\partial x_i} \right) d\Gamma = \\
&\int_{\Gamma^N} \delta v_i n_j \left(-p\delta_{ij} + 2\mu d_{ij} - \frac{2}{3}\mu \left(\nabla \cdot \mathbf{v}\right) \delta_{ij} \right) d\Gamma
\end{aligned} \tag{4.2.5}$$

From Eq. (2.5.21), we can see that the term inside the parenthesis of Eq. (4.2.5) is equal to the stress tensor for Newtonian fluids. This allow us to express the boundary integral as

$$\int_{\Gamma^N} \delta v_i n_j \sigma_{ij} d\Gamma = \int_{\Gamma^N} \delta v_i t_i d\Gamma \tag{4.2.6}$$

For simplicity, in this work the homogeneous no-slip Dirichlet boundary condition is taken, therefore the Neumann boundary, Eq. (4.2.6), vanishes. Moreover, if the incompressibility condition given by Eq. (2.4.7) is used, i.e. $\nabla \cdot \mathbf{v} = 0$, which is widely acceptable in the application range of civil engineering and other areas[2], then Eq. (4.2.4) yields

$$\int_\Omega \delta v_i \left(\rho \frac{\partial v_i}{\partial t} + \rho v_j \frac{\partial v_i}{\partial x_j} \right) d\Omega - \int_\Omega p \frac{\partial \delta v_i}{\partial x_i} d\Omega + \int_\Omega \mu \frac{\partial v_i}{\partial x_j} \frac{\partial \delta v_i}{\partial x_j} d\Omega = \int_\Omega \delta v_i \rho b_i d\Omega \tag{4.2.7}$$

These equations are known as the weak form for the incompressible Navier-Stokes equations. To develop the weak form of the continuity equation, their space of test function is defined as

$$\delta p(\mathbf{x}) \in \mathcal{Q}, \quad \mathcal{Q} = \left\{ \delta p | \delta p \in L^2(\Omega), \quad \int_\Omega \delta p d\Omega = 0 \right\} \tag{4.2.8}$$

where $L^2(\Omega)$ consists of square-integrable functions. The space of the trial function for the pressure is given by

$$p(\mathbf{x}, t) \in \mathcal{Q} \tag{4.2.9}$$

The development of a Galerkin-type weak form consists in taking the product of the continuity equation, Eq. (2.4.7), by the test function δp, integrating over the current domain and using appropriate boundary conditions, yielding

$$\int_\Omega \delta p \frac{\partial v_j}{\partial x_j} d\Omega = 0 \tag{4.2.10}$$

which is known as the weak form of the continuity equation for incompressible materials. These weak forms can be written in a simple form, first dividing Eq.

[2]For Mach number < 0.3, air can be considered incompressible

(4.2.7) by the density and next using the following mathematical definitions. The standard L^2 inner product for functions belonging to $L^2(\Omega)$ is given by

$$(\boldsymbol{u}, \boldsymbol{v}) = \int_{\Omega} \boldsymbol{u} \cdot \boldsymbol{v} d\Omega \tag{4.2.11}$$

Also the following bilinear forms are defined

$$a(\boldsymbol{u}, \boldsymbol{v}) = \nu \int_{\Omega} \nabla \boldsymbol{u} : \nabla \boldsymbol{v} d\Omega \qquad \forall \boldsymbol{u}, \boldsymbol{v} \in H^1(\Omega) \tag{4.2.12}$$

$$b(q, \boldsymbol{v}) = \int_{\Omega} q \, \nabla \cdot \boldsymbol{v} d\Omega \qquad \forall \boldsymbol{v} \in H^1(\Omega) \quad \text{and} \quad \forall q \in L^2(\Omega) \tag{4.2.13}$$

and the trilinear form

$$c(\boldsymbol{u}, \boldsymbol{v}, \boldsymbol{w}) = \int_{\Omega} \boldsymbol{u} \cdot \nabla \boldsymbol{v} \cdot \boldsymbol{w} d\Omega \qquad \forall \boldsymbol{u}, \boldsymbol{v}, \boldsymbol{w} \in H^1(\Omega) \tag{4.2.14}$$

With these definitions, the incompressible flow equations given by Eq. (4.2.7) and Eq. (4.2.10) can be simplify to yield respectively

$$(\partial_t \mathbf{v}, \delta \mathbf{v}) + c(\mathbf{v}, \mathbf{v}, \delta \mathbf{v}) - b(p, \delta \mathbf{v}) + a(\mathbf{v}, \delta \mathbf{v}) = (\mathbf{b}, \delta \mathbf{v}) \tag{4.2.15}$$

$$b(\delta p, \mathbf{v}) = 0 \tag{4.2.16}$$

In this work, these equations are going to be called the *compact form* for the incompressible Navier-Stokes equations. More details of this mathematical formulation can be found in Gunzburger (1989).

In Eq. (4.2.12), the term ν is the *kinematic viscosity* which is defined by $\nu = \mu/\rho$. In Eq. (4.2.15), the density has been absorbed into the pressure yielding a *kinematic pressure*.

4.2.2 Finite Element Discretization

Finite elements discretization of the incompressible flow equations is presented in this section for the Galekin-type weak form. The velocities are approximated by

$$v_i^h(\mathbf{x}, t) = \sum_{I=1}^{n_{\text{node}}} N_I(\mathbf{x}) v_{iI}(t) \qquad \forall i = 1, \, n_{\text{dime}} \tag{4.2.17}$$

where $N_I(\mathbf{x})$ are the shape functions in Eulerian coordinates and $v_{iI}(t)$ are the nodal values of the velocity field. The space of the test functions for the momentum equations is time independent and its discretization yields

$$\delta v_i^h(\mathbf{x}) = \sum_{I=1}^{n_{\text{node}}} N_I(\mathbf{x}) \delta v_{iI} \qquad \forall i = 1, \, n_{\text{dime}} \tag{4.2.18}$$

The material time derivative of the velocity gives the acceleration, which is approximated by

$$\frac{\partial v_i^h(\mathbf{x},t)}{\partial t} = \sum_{I=1}^{n_{\text{node}}} N_I(\mathbf{x})\dot{v}_{iI}(t) \qquad \forall i = 1,\, n_{\text{dime}} \tag{4.2.19}$$

Gradients of the velocity and gradients of the test functions of the momentum equations yield the following Cartesian derivatives

$$\frac{\partial v_i^h(\mathbf{x},t)}{\partial x_j} = \sum_{I=1}^{n_{\text{node}}} \frac{\partial N_I(\mathbf{x})}{\partial x_j} v_{iI}(t) \qquad \forall i,j = 1,\, n_{\text{dime}} \tag{4.2.20}$$

$$\frac{\partial \delta v_i^h(\mathbf{x})}{\partial x_j} = \sum_{I=1}^{n_{\text{node}}} \frac{\partial N_I(\mathbf{x})}{\partial x_j} \delta v_{iI} \qquad \forall i,j = 1,\, n_{\text{dime}} \tag{4.2.21}$$

The divergence of the test and trial functions are given by

$$\frac{\partial \delta v_i^h(\mathbf{x})}{\partial x_i} = \sum_{I=1}^{n_{\text{node}}} \sum_{i=1}^{n_{\text{dime}}} \frac{\partial N_I(\mathbf{x})}{\partial x_i} \delta v_{iI} \tag{4.2.22}$$

$$\frac{\partial v_i^h(\mathbf{x},t)}{\partial x_i} = \sum_{I=1}^{n_{\text{node}}} \sum_{i=1}^{n_{\text{dime}}} \frac{\partial N_I(\mathbf{x},t)}{\partial x_i} v_{iI}(t) \tag{4.2.23}$$

The pressure is approximated by

$$p(\mathbf{x},t) = \sum_{I=1}^{n_{\text{node}}} N_I(\mathbf{x}) p_I(t) \tag{4.2.24}$$

and the test function for the continuity condition gives

$$\delta p(\mathbf{x}) = \sum_{I=1}^{n_{\text{node}}} N_I(\mathbf{x}) \delta p_I \tag{4.2.25}$$

These equations allow to express the incompressible Navier-Stokes equations, Eq. (4.2.7), in the form given ahead. The kinetic term can be discretized as

$$\begin{aligned} \int_\Omega \delta v_i^h \rho \frac{\partial v_i^h}{\partial t} d\Omega &= \delta v_{iI} \int_\Omega N_I \rho N_J \dot{v}_{iJ} d\Omega \\ &= \delta v_{iI} \int_\Omega N_I \rho N_J \delta_{ij} d\Omega\; \dot{v}_{jJ} \\ &= \delta v_{iI} M_{ijIJ} \dot{v}_{jJ} \end{aligned} \tag{4.2.26}$$

where the mass matrix for the eulerian description is given by

$$M_{ijIJ} = \delta_{ij} \int_\Omega \rho N_I N_J d\Omega \tag{4.2.27}$$

Discretization of the convective term yields

$$\begin{aligned}\int_\Omega \delta v_i^h \rho v_j^h \frac{\partial v_i^h}{\partial x_j} d\Omega &= \delta v_{iI} \int_\Omega N_I \rho \, \boldsymbol{v}_h \, \frac{\partial N_J}{\partial x_j} v_{iJ} d\Omega \\ &= \delta v_{iI} \int_\Omega N_I \rho \, \boldsymbol{v}_h \, \frac{\partial N_J}{\partial x_j} \delta_{ij} d\Omega \, v_{jJ} \\ &= \delta v_{iI} K^c_{ijIJ} v_{jJ}\end{aligned} \tag{4.2.28}$$

where $\boldsymbol{v}_h$ is the discretized velocity vector given by Eq. (4.2.17) and the convective stiffness matrix is defined by

$$K^c_{ijIJ} = \delta_{ij} \int_\Omega \rho N_I \, \boldsymbol{v}_h \, \frac{\partial N_J}{\partial x_j} d\Omega \tag{4.2.29}$$

The pressure term can be discretized in the form of

$$\begin{aligned}\int_\Omega p \frac{\partial \delta v_i^h}{\delta x_i} d\Omega &= \delta v_{iI} \int_\Omega \frac{\partial N_I}{\partial x_i} N_J p_J d\Omega \\ &= \delta v_{iI} G_{iIJ} p_J\end{aligned} \tag{4.2.30}$$

where the pressure matrix is expressed as

$$G_{iIJ} = \int_\Omega \frac{\partial N_I}{\partial x_i} N_J d\Omega \tag{4.2.31}$$

The viscous term can be discretized following the same procedure to obtain

$$\begin{aligned}\int_\Omega \mu \frac{\partial v_i^h}{\partial x_j} \frac{\partial \delta v_i^h}{\partial x_j} d\Omega &= \delta v_{iI} \int_\Omega \frac{\partial N_I}{\partial x_j} \mu \frac{\partial N_J}{\partial x_j} v_{iJ} d\Omega \\ &= \delta v_{iI} \int_\Omega \frac{\partial N_I}{\partial x_j} \mu \frac{\partial N_J}{\partial x_j} \delta_{ij} d\Omega \, v_{jJ} \\ &= \delta v_{iI} K^v_{ijIJ} v_{jJ}\end{aligned} \tag{4.2.32}$$

where the viscous stiffness matrix is given by

$$K^v_{ijIJ} = \delta_{ij} \, \mu \int_\Omega \frac{\partial N_I}{\partial x_j} \frac{\partial N_J}{\partial x_j} d\Omega \tag{4.2.33}$$

Since the variation δv_{iI} is arbitrary, then the forces yielding from the Navier-Stokes equations can be written in the following discretized matrix form

$$\mathbf{M}\dot{\mathbf{v}} + \mathbf{K}(\mathbf{v})\mathbf{v} - \mathbf{G}\mathbf{p} = \mathbf{f}^{\text{ext}} \tag{4.2.34}$$

where the stiffness matrix is given by $\mathbf{K}(\mathbf{v}) = \mathbf{K}^c(\mathbf{v}) + \mathbf{K}^v$. The compact form for these equations can be written as

$$(\partial_t \boldsymbol{v}_h, \boldsymbol{w}_h) + c(\boldsymbol{v}_h, \boldsymbol{v}_h, \boldsymbol{w}_h) - b(p_h, \boldsymbol{w}_h) + a(\boldsymbol{v}_h, \boldsymbol{w}_h) = (\boldsymbol{b}_h, \boldsymbol{w}_h) \tag{4.2.35}$$

where the discretized test functions for the velocity are given by

$$\boldsymbol{w}_h(\mathbf{x}) = \sum_{I=1}^{n_{\text{node}}} N_I(\mathbf{x}) \tag{4.2.36}$$

The incompressibility condition given by Eq. (4.2.10) can be discretized and the divergence term leads to

$$\begin{aligned} \int_\Omega \delta p \frac{\partial v_j^h}{\partial x_j} d\Omega &= \delta p_I \int_\Omega N_I \frac{\partial N_J}{\partial x_j} v_{jJ} d\Omega \\ &= \delta p_I G_{jIJ}^T v_{jJ} \end{aligned} \tag{4.2.37}$$

where divergence matrix is expressed by

$$G_{jIJ}^T = \int_\Omega N_I \frac{\partial N_J}{\partial x_j} d\Omega \tag{4.2.38}$$

Since the variation δp_I is arbitrary, then the continuity equation can be written in the following discretized matrix form

$$\mathbf{G}^T \mathbf{v} = 0 \tag{4.2.39}$$

which can be written in compact form as

$$b(q_h, \boldsymbol{v}_h) = 0 \tag{4.2.40}$$

where the discretized test function for the pressure is given by

$$q_h(\mathbf{x}) = \sum_{I=1}^{n_{\text{node}}} N_I(\mathbf{x}) \tag{4.2.41}$$

Note that the discretized incompressible flow equations are coupled, and the problem is expressed by

$$\begin{aligned} \mathbf{M}\dot{\mathbf{v}} + \mathbf{K}(\mathbf{v})\mathbf{v} - \mathbf{G}\mathbf{p} &= \mathbf{f}^{\text{ext}} \\ \mathbf{G}^T \mathbf{v} &= 0 \end{aligned} \tag{4.2.42}$$

which are used to find the velocity field and pressure of the problem monolithically. These equations can also be expressed by

$$\begin{aligned} (\dot{\boldsymbol{v}}_h, \boldsymbol{w}_h) + c(\boldsymbol{v}_h, \boldsymbol{v}_h, \boldsymbol{w}_h) - b(p_h, \boldsymbol{w}_h) + a(\boldsymbol{v}_h, \boldsymbol{w}_h) &= (\boldsymbol{b}_h, \boldsymbol{w}_h) \\ b(q_h, \boldsymbol{v}_h) &= 0 \end{aligned} \tag{4.2.43}$$

which is the compact form to express the coupled discretized incompressible flow equations. Eq. (4.2.43) has the advantage that no matrices need to be built to later be multiplied by a vector, which results in a more optimal code.

4.3 Time Integration Schemes

In this part, the same ideas of section **3.5** for time integration schemes of solids are followed. Therefore only implicit schemes are solved for incompressible flow problems. The semi-discrete equations to be solved are given by

$$\begin{aligned} \mathbf{M}\dot{\mathbf{v}}_{n+1} + \mathbf{K}(\mathbf{v}_{n+1})\mathbf{v}_{n+1} - \mathbf{G}\mathbf{p}_{n+1} &= \mathbf{f}^{\text{ext}}_{n+1} \\ \mathbf{G}^T\mathbf{v}_{n+1} &= 0 \end{aligned} \tag{4.3.1}$$

where the acceleration vector $\dot{\mathbf{v}}_{n+1}$ has to be integrated in time to solve the algebraic equations for $\mathbf{v}_{n+1}, \mathbf{p}_{n+1}$ from the first-order differential equations. The compact form of the above equations yields

$$\begin{aligned} (\dot{\boldsymbol{v}}_h^{n+1}, \boldsymbol{w}_h) + c(\boldsymbol{v}_h^{n+1}, \boldsymbol{v}_h^{n+1}, \boldsymbol{w}_h) - b(p_h^{n+1}, \boldsymbol{w}_h) + a(\boldsymbol{v}_h^{n+1}, \boldsymbol{w}_h) &= (\boldsymbol{b}_h^{n+1}, \boldsymbol{w}_h) \\ b(q_h, \boldsymbol{v}_h^{n+1}) &= 0 \end{aligned} \tag{4.3.2}$$

Among the different numerical integration methods available to integrate first-order equations, the simplest choice in fluid dynamics problems is the θ^{f}-family of approximation. Multistep schemes of the type of backward differentiation are also used in fluid dynamics problems. Both of these methods are better described in Gunzburger (1989). The tendency of these methods for high frequency noise to persist in the solution for long time periods can lead to non-physical instabilities. To avoid this problem, Jansen et al. (2000) have developed the generalized-α method for fluid dynamics, with the same dissipation properties that the generalized-α method for structural dynamics problems. An analysis of time integration algorithms for incompressible fluids flow is detailed in Dettmer and Peric (2003).

4.3.1 θ-Family Method

In this section, the θ^{f}-family method for implicit schemes is presented. The solution at time step t_n is assumed to be known for $\mathbf{v}_n, p_n$. In this method, the time derivative of the velocity is approximated for two consecutive time steps by linear interpolation, yielding

$$\dot{\mathbf{v}}_{n+\theta^{\text{f}}} = (1-\theta^{\text{f}})\dot{\mathbf{v}}_n + \theta^{\text{f}}\dot{\mathbf{v}}_{n+1} \cong \frac{\mathbf{v}_{n+1} - \mathbf{v}_n}{\Delta t} \tag{4.3.3}$$

with $\frac{1}{2} \leq \theta^{\text{f}} \leq 1$ for unconditionally stable implicit schemes and $\Delta t = t_{n+1} - t_n$. The velocity field is approximated according to

$$\mathbf{v}_{n+1} = \frac{1}{\theta^{\text{f}}}\left(\mathbf{v}_{n+\theta^{\text{f}}} - (1-\theta^{\text{f}})\mathbf{v}_n\right) \tag{4.3.4}$$

which is usually written as

$$\mathbf{v}_{n+\theta^{\text{f}}} = (1-\theta^{\text{f}})\mathbf{v}_n + \theta^{\text{f}}\mathbf{v}_{n+1} \tag{4.3.5}$$

For $\theta^{\mathrm{f}} = 1$, the method is first-order accurate and is known as the backward Euler method. For $\theta^{\mathrm{f}} = \frac{1}{2}$, the method is known as the Crank-Nicolson method. Only when $\theta^{\mathrm{f}} = \frac{1}{2}$ the method is second-order accurate. The semi-discrete equations to be solved for the θ^{f}-family method are then given by

$$\begin{aligned} \mathbf{M}\frac{1}{\Delta t}(\mathbf{v}_{n+1} - \mathbf{v}_n) + \mathbf{K}(\mathbf{v}_{n+\theta^{\mathrm{f}}})\mathbf{v}_{n+\theta^{\mathrm{f}}} - \mathbf{G}\mathbf{p}_{n+1} &= \mathbf{f}^{\mathrm{ext}}_{n+\theta^{\mathrm{f}}} \\ \mathbf{G}^T\mathbf{v}_{n+\theta^{\mathrm{f}}} &= 0 \end{aligned} \tag{4.3.6}$$

and the unknowns for the algebraic equations to be solved are $\mathbf{v}_{n+1}, p_{n+1}$ since all values at time t_n are known. Also we can write

$$\begin{aligned} (\dot{\boldsymbol{v}}_h^{n+\theta^{\mathrm{f}}}, \boldsymbol{w}_h) + c(\boldsymbol{v}_h^{n+\theta^{\mathrm{f}}}, \boldsymbol{v}_h^{n+\theta^{\mathrm{f}}}, \boldsymbol{w}_h) - b(p_h^{n+1}, \boldsymbol{w}_h) + a(\boldsymbol{v}_h^{n+\theta^{\mathrm{f}}}, \boldsymbol{w}_h) &= (\boldsymbol{b}_h^{n+\theta^{\mathrm{f}}}, \boldsymbol{w}_h) \\ b(q_h, \boldsymbol{v}_h^{n+\theta^{\mathrm{f}}}) &= 0 \end{aligned} \tag{4.3.7}$$

which is the compact form for incompressible fluids.

4.3.2 Backward Differentiation Method

Backward differentiation methods are also known as Gear schemes. The backward differentiation method used in this work are of first and second-order of accuracy. The simplest prototype of backward differentiation is the backward Euler, which coincides with the θ^{f}-family method when $\theta^{\mathrm{f}} = 1$. Then the time derivative for the velocity can be approximated by

$$\dot{\mathbf{v}}_{n+1} = \frac{\mathbf{v}_{n+1} - \mathbf{v}_n}{\Delta t} \tag{4.3.8}$$

and the semi-discrete equations to be solved for the BDF1 (Backward DiFferentiation method order 1) method are then given by

$$\begin{aligned} \mathbf{M}\frac{1}{\Delta t}(\mathbf{v}_{n+1} - \mathbf{v}_n) + \mathbf{K}(\mathbf{v}_{n+1})\mathbf{v}_{n+1} - \mathbf{G}\mathbf{p}_{n+1} &= \mathbf{f}^{\mathrm{ext}}_{n+1} \\ \mathbf{G}^T\mathbf{v}_{n+1} &= 0 \end{aligned} \tag{4.3.9}$$

and the unknowns for the algebraic equations to be solved are $\mathbf{v}_{n+1}, p_{n+1}$ since all values at time t_n are known. For second-order accuracy, the method is known as BDF2 and the velocity is expressed as

$$\dot{\mathbf{v}}_{n+1} = \frac{3\mathbf{v}_{n+1} - 4\mathbf{v}_n + \mathbf{v}_{n-1}}{2\Delta t} \tag{4.3.10}$$

and the semi-discrete equations to be solved are then given by

$$\begin{aligned} \mathbf{M}\frac{1}{2\Delta t}(3\mathbf{v}_{n+1} - 4\mathbf{v}_n + \mathbf{v}_{n-1}) + \mathbf{K}(\mathbf{v}_{n+1})\mathbf{v}_{n+1} - \mathbf{G}\mathbf{p}_{n+1} &= \mathbf{f}_{n+1}^{\text{ext}} \\ \mathbf{G}^T\mathbf{v}_{n+1} &= 0 \end{aligned} \tag{4.3.11}$$

and the unknowns for the algebraic equations to be solved are $\mathbf{v}_{n+1}, p_{n+1}$. One advantage of these methods is that they do not require an initial guess for the pressure, as reported in Gunzburger (1989). One disadvantage for the BDF2 is that it requires more starting values that just $\mathbf{v}_0$. But this problem can be avoided if always the first iteration is perform with the BDF1 method and then for the second iteration change to the BDF2 method.

4.3.3 Generalized-α Method

The generalized-α method for first-order systems was introduced by Jansen et al. (2000). The idea is to achieve high-frequency dissipation while minimizing unwanted low-frequency dissipation for analysis with long time periods. This method was motivated from the excellent results of the same method for second-order systems given by Chung and Hulbert (1993). In the generalized-α method, the semi-discrete equations for incompressible fluids flow are given by

$$\begin{aligned} \mathbf{M}\dot{\mathbf{v}}_{n+\alpha_m^{\text{f}}} + \mathbf{K}(\mathbf{v}_{n+\alpha_f^{\text{f}}})\mathbf{v}_{n+\alpha_f^{\text{f}}} - \mathbf{G}\mathbf{p}_{n+1} &= \mathbf{f}_{n+1}^{\text{ext}} \\ \mathbf{G}^T\mathbf{v}_{n+1} &= 0 \end{aligned} \tag{4.3.12}$$

where the changes are given by

$$\mathbf{v}_{n+1} = \mathbf{v}_n + \Delta t\left(1-\gamma^{\text{f}}\right)\dot{\mathbf{v}}_n + \Delta t\,\gamma^{\text{f}}\,\dot{\mathbf{v}}_{n+1} \tag{4.3.13}$$

$$\mathbf{v}_{n+\alpha_f^{\text{f}}} = \left(1-\alpha_f^{\text{f}}\right)\mathbf{v}_n + \alpha_f^{\text{f}}\,\mathbf{v}_{n+1} \tag{4.3.14}$$

$$\dot{\mathbf{v}}_{n+\alpha_m^{\text{f}}} = \left(1-\alpha_m^{\text{f}}\right)\dot{\mathbf{v}}_n + \alpha_m^{\text{f}}\dot{\mathbf{v}}_{n+1} \tag{4.3.15}$$

where α_f^{f}, α_m^{f} and γ^{f} are integration parameters defined ahead. From Eq. (4.3.13) we can obtain

$$\dot{\mathbf{v}}_{n+1} = \frac{1}{\Delta t\gamma^{\text{f}}}\left(\mathbf{v}_{n+1} - \mathbf{v}_n\right) - \left(\frac{1}{\gamma^{\text{f}}} - 1\right)\dot{\mathbf{v}}_n \tag{4.3.16}$$

which will allow us to update the acceleration at time t_{n+1} when the velocities $\mathbf{v}_{n+1}$ are found. Substituting Eq. (4.3.16) into Eq. (4.3.15) yields

$$\dot{\mathbf{v}}_{n+\alpha_m^{\text{f}}} = \frac{\alpha_m^{\text{f}}}{\Delta t\,\gamma^{\text{f}}}(\mathbf{v}_{n+1} - \mathbf{v}_n) + \left(1 - \frac{\alpha_m^{\text{f}}}{\gamma^{\text{f}}}\right)\dot{\mathbf{v}}_n \tag{4.3.17}$$

This last equation together with Eq. (4.3.14) are the ones that are substituted into Eq. (4.3.12) and allow us to find the unknowns $\mathbf{v}_{n+1}, p_{n+1}$ for the algebraic equations since all values at time t_n are known.

The method is second-order accurate and posses high frequency dissipation when the integration parameter γ^{f} is selected such that

$$\gamma^{\mathrm{f}} = \frac{1}{2} + \alpha_m^{\mathrm{f}} - \alpha_f^{\mathrm{f}} \tag{4.3.18}$$

Low frequency dissipation is optimal when

$$\rho_\infty^{\mathrm{f}} \in [0,1], \qquad \alpha_f^{\mathrm{f}} = \frac{1}{1+\rho_\infty^{\mathrm{f}}}, \qquad \alpha_m^{\mathrm{f}} = \frac{1}{2}\,\frac{3-\rho_\infty^{\mathrm{f}}}{1+\rho_\infty^{\mathrm{f}}} \tag{4.3.19}$$

For $\rho_\infty^{\mathrm{f}} = 1$ the method is identical to the Crank-Nicolson method given by in the θ^{f}-family. Numerical damping of the method increases with smaller values of ρ_∞^{f}.

4.4 Pressure Segregation Methods

The monolithic coupled equations for incompressible fluid problems have the disadvantage that take great computer effort to solve the algebraic system for each time step in a transient analysis.

Since the original works of Chorin (1967) and Temam (1969), fractional step methods for the incompressible Navier-Stokes equations have earned widespread popularity because of the computational efficiency given by the uncoupling of the pressure from the velocity field. A detailed stability analysis of fractional step methods for incompressible flows is given in Codina (2001).

Another proposal in the context of fractional step methods is the predictor-multicorrector algorithm born from the ideas of Brooks and Hughes (1982). Development of this method can be found in Blasco et al. (1998), and Codina and Soto (2004). Stability analysis for these methods are given by Codina and Badia (2006).

4.4.1 Fractional Step Method

The easiest form to understand the development of the fractional step method is to part from the incompressible Navier-Stokes equations given by

$$\mathbf{M}\frac{1}{\Delta t}(\mathbf{v}_{n+1} - \mathbf{v}_n) + \mathbf{K}(\mathbf{v}_{n+1})\mathbf{v}_{n+1} - \mathbf{G}\mathbf{p}_{n+1} = \mathbf{f}_{n+1}^{\mathrm{ext}} \tag{4.4.1}$$

$$\mathbf{G}^T\mathbf{v}_{n+1} = 0 \tag{4.4.2}$$

where Eq. (4.4.1) can be split and yield the equivalent incompressible flow equations

$$\mathbf{M}\frac{1}{\Delta t}(\tilde{\mathbf{v}}_{n+1} - \mathbf{v}_n) + \mathbf{K}(\tilde{\mathbf{v}}_{n+1})\tilde{\mathbf{v}}_{n+1} - \mathbf{G}\mathbf{p}_n = \mathbf{f}_{n+1}^{\mathrm{ext}} \tag{4.4.3}$$

$$\mathbf{M}\frac{1}{\Delta t}(\mathbf{v}_{n+1} - \tilde{\mathbf{v}}_{n+1}) - \mathbf{G}(\mathbf{p}_{n+1} - \mathbf{p}_n) = \mathbf{0} \tag{4.4.4}$$

$$\mathbf{G}^T\mathbf{v}_{n+1} = 0 \tag{4.4.5}$$

where $\tilde{\mathbf{v}}_{n+1}$ is an auxiliary velocity variable and the essential approximation

$$\mathbf{K}(\mathbf{v}_{n+1})\mathbf{v}_{n+1} \approx \mathbf{K}(\tilde{\mathbf{v}}_{n+1})\tilde{\mathbf{v}}_{n+1} \tag{4.4.6}$$

has been taken. From Eq. (4.4.4), $\mathbf{v}_{n+1}$ can be expressed in terms of $\tilde{\mathbf{v}}_{n+1}$ yielding

$$\mathbf{v}_{n+1} = \tilde{\mathbf{v}}_{n+1} + \Delta t\, \mathbf{M}^{-1}\mathbf{G}(\mathbf{p}_{n+1} - \mathbf{p}_n) \tag{4.4.7}$$

Substituting this last equation into Eq. (4.4.5) yields

$$-\Delta t\, \mathbf{G}^T\mathbf{M}^{-1}\mathbf{G}(\mathbf{p}_{n+1} - \mathbf{p}_n) = \mathbf{G}^T\tilde{\mathbf{v}}_{n+1} \tag{4.4.8}$$

Now observe that $\mathbf{G}^T\mathbf{M}^{-1}\mathbf{G}$ represent an approximation to the Laplacian operator, as mentioned in Codina (2001), given by $L_{IJ} = \rho\,(\nabla N_I, \nabla N_J)$.

Finally the incompressible fluid flow equations Eq. (4.4.3)-(4.4.5) to be solved using the θ^{f}-family integration scheme are expressed as

$$\mathbf{M}\frac{1}{\Delta t}(\tilde{\mathbf{v}}_{n+1} - \mathbf{v}_n) + \mathbf{K}(\tilde{\mathbf{v}}_{n+\theta^{\mathrm{f}}})\tilde{\mathbf{v}}_{n+\theta^{\mathrm{f}}} - \mathbf{G}\mathbf{p}_n = \mathbf{f}^{\mathrm{ext}}_{n+1} \tag{4.4.9}$$

$$-\Delta t\, \mathbf{L}(\mathbf{p}_{n+1} - \mathbf{p}_n) = \mathbf{G}^T\tilde{\mathbf{v}}_{n+1} \tag{4.4.10}$$

$$\mathbf{M}\frac{1}{\Delta t}(\mathbf{v}_{n+1} - \tilde{\mathbf{v}}_{n+1}) - \mathbf{G}(\mathbf{p}_{n+1} - \mathbf{p}_n) = \mathbf{0} \tag{4.4.11}$$

with $\frac{1}{2} \leq \theta^{\mathrm{f}} \leq 1$ for unconditionally stable implicit schemes. Remember that for $\theta^{\mathrm{f}} = 1$, the method coincides with the backward differentiation BDF1 method. These equation are expressed in a different form when the integration scheme used is the BDF2, yielding

$$\mathbf{M}\frac{1}{2\Delta t}(3\tilde{\mathbf{v}}_{n+1} - 4\mathbf{v}_n + \mathbf{v}_{n-1}) + \mathbf{K}(\tilde{\mathbf{v}}_{n+1})\tilde{\mathbf{v}}_{n+1} - \mathbf{G}\mathbf{p}_n = \mathbf{f}^{\mathrm{ext}}_{n+1} \tag{4.4.12}$$

$$-\frac{2}{3}\Delta t\, \mathbf{L}(\mathbf{p}_{n+1} - \mathbf{p}_n) = \mathbf{G}^T\tilde{\mathbf{v}}_{n+1} \tag{4.4.13}$$

$$\mathbf{M}\frac{1}{2\Delta t}(3\mathbf{v}_{n+1} - 3\tilde{\mathbf{v}}_{n+1}) - \mathbf{G}(\mathbf{p}_{n+1} - \mathbf{p}_n) = \mathbf{0} \tag{4.4.14}$$

In this work we use a different time integration scheme that those find in the literature for the fractional step method. This scheme is the generalized-α method, used in the monolithic problem, that for fractional steps take the form of

$$\mathbf{M}\frac{\alpha^{\mathrm{f}}_m}{\Delta t\,\gamma^{\mathrm{f}}}(\tilde{\mathbf{v}}_{n+1} - \mathbf{v}_n) + \mathbf{K}(\tilde{\mathbf{v}}_{n+\alpha^{\mathrm{f}}_f})\tilde{\mathbf{v}}_{n+\alpha^{\mathrm{f}}_f} - \mathbf{G}\mathbf{p}_n = \mathbf{f}^{\mathrm{ext}}_{n+1} - \mathbf{M}\left(1 - \frac{\alpha^{\mathrm{f}}_m}{\gamma^{\mathrm{f}}}\right)\dot{\mathbf{v}}_n \tag{4.4.15}$$

$$-\frac{\Delta t\,\gamma^{\mathrm{f}}}{\alpha^{\mathrm{f}}_m}\,\mathbf{L}(\mathbf{p}_{n+1} - \mathbf{p}_n) = \mathbf{G}^T\tilde{\mathbf{v}}_{n+1} \tag{4.4.16}$$

$$\mathbf{M}\frac{\alpha^{\mathrm{f}}_m}{\Delta t\,\gamma^{\mathrm{f}}}(\mathbf{v}_{n+1} - \tilde{\mathbf{v}}_{n+1}) - \mathbf{G}(\mathbf{p}_{n+1} - \mathbf{p}_n) = \mathbf{0} \tag{4.4.17}$$

The compact form for these equations is given by

$$\frac{\alpha_m^{\mathrm{f}}}{\Delta t\,\gamma^{\mathrm{f}}}(\tilde{\boldsymbol{v}}_h^{n+1}-\boldsymbol{v}_h^n,\boldsymbol{w}_h)+c(\tilde{\boldsymbol{v}}_h^{n+\alpha_f^{\mathrm{f}}},\tilde{\boldsymbol{v}}_h^{n+\alpha_f^{\mathrm{f}}},\boldsymbol{w}_h)-b(p_h^n,\boldsymbol{w}_h)+ a(\tilde{\boldsymbol{v}}_h^{n+\alpha_f^{\mathrm{f}}},\boldsymbol{w}_h)=(\boldsymbol{b}_h^{n+1},\boldsymbol{w}_h)-\left(1-\frac{\alpha_m^{\mathrm{f}}}{\gamma^{\mathrm{f}}}\right)(\dot{\boldsymbol{v}}_h^n,\boldsymbol{w}_h) \tag{4.4.18}$$

$$-\frac{\Delta t\,\gamma^{\mathrm{f}}}{\alpha_m^{\mathrm{f}}}(\nabla(p_h^{n+1}-p_h^n),\nabla q_h)=b(q_h,\tilde{\boldsymbol{v}}_h^{n+1}) \tag{4.4.19}$$

$$\frac{\alpha_m^{\mathrm{f}}}{\Delta t\,\gamma^{\mathrm{f}}}(\boldsymbol{v}_h^{n+1}-\tilde{\boldsymbol{v}}_h^{n+1},\boldsymbol{w}_h)-b(p_h^{n+1}-p_h^n,\boldsymbol{w}_h)=\mathbf{0} \tag{4.4.20}$$

As mention before, these equations have the advantage that no matrices need to be built to later be multiplied by a vector, which results in a more optimal code.

4.4.2 Predictor-Corrector Method

Here the predictor multicorrector scheme emerging from Eqs. (4.4.9)-(4.4.11) proposed by Codina and Soto (2004) is used. The goal of this method is to converge to the monolithic problem.

The linearized algebraic system for this method using the θ^{f}-family for integration in time is taken directly from Codina and Badia (2006), yielding

$$\mathbf{M}\frac{1}{\Delta t}(\mathbf{v}_{n+1,i}-\mathbf{v}_n)+\mathbf{K}(\mathbf{v}_{n+\theta^{\mathrm{f}},i-1})\mathbf{v}_{n+\theta^{\mathrm{f}},i}-\mathbf{G}\mathbf{p}_{n+\theta^{\mathrm{f}},i-1}=\mathbf{f}_{n+\theta^{\mathrm{f}}}^{\mathrm{ext}} \tag{4.4.21}$$

$$-\Delta t\,\mathbf{L}(\mathbf{p}_{n+\theta^{\mathrm{f}},i}-\mathbf{p}_{n+\theta^{\mathrm{f}},i-1})=\mathbf{G}^T\mathbf{v}_{n+\theta^{\mathrm{f}},i} \tag{4.4.22}$$

which is an iterative algebraic system where the pressure is uncoupled from the velocity field. If the BDF2 time integration method is used, then Eqs. (4.4.21)-(4.4.22) are written as

$$\mathbf{M}\frac{1}{2\Delta t}(3\mathbf{v}_{n+1,i}-4\mathbf{v}_n+\mathbf{v}_{n-1})+\mathbf{K}(\mathbf{v}_{n+1,i-1})\mathbf{v}_{n+1,i}-\mathbf{G}\mathbf{p}_{n+1,i-1}=\mathbf{f}_{n+1}^{\mathrm{ext}} \tag{4.4.23}$$

$$-\frac{2}{3}\Delta t\,\mathbf{L}(\mathbf{p}_{n+1,i}-\mathbf{p}_{n+1,i-1})=\mathbf{G}^T\mathbf{v}_{n+1,i} \tag{4.4.24}$$

Note that for the first iteration, $i=1$, a predictor for the pressure and the velocity is required. The first order predictor for the pressure and velocity are taken as

$$\mathbf{p}_{n+1,0}=\mathbf{p}_n,\qquad \mathbf{v}_{n+1,0}=\mathbf{v}_n \tag{4.4.25}$$

while the second order predictor yields

$$\mathbf{p}_{n+1,0} = 2\mathbf{p}_n - \mathbf{p}_{n-1}, \qquad \mathbf{v}_{n+1,0} = 2\mathbf{v}_n - \mathbf{v}_{n-1} \tag{4.4.26}$$

Again in this work we use a different time integration scheme that those find in the literature for the predictor-corrector method. This scheme is the generalized-α method, that for the predictor-corrector algorithm take the form of

$$\mathbf{M}\frac{\alpha_m^{\mathrm{f}}}{\Delta t\,\gamma^{\mathrm{f}}}(\mathbf{v}_{n+1,i} - \mathbf{v}_n) + \mathbf{K}(\mathbf{v}_{n+\alpha_f^{\mathrm{f}},i-1})\mathbf{v}_{n+\alpha_f^{\mathrm{f}},i} - \mathbf{G}\mathbf{p}_{n+\alpha_f^{\mathrm{f}},i-1} = \mathbf{f}_{n+\alpha_f^{\mathrm{f}}}^{\mathrm{ext}} - \mathbf{M}\left(1 - \frac{\alpha_m^{\mathrm{f}}}{\gamma^{\mathrm{f}}}\right)\dot{\mathbf{v}}_n \tag{4.4.27}$$

$$-\frac{\Delta t\,\gamma^{\mathrm{f}}}{\alpha_m^{\mathrm{f}}}\,\mathbf{L}(\mathbf{p}_{n+\alpha_f^{\mathrm{f}},i} - \mathbf{p}_{n+\alpha_f^{\mathrm{f}},i-1}) = \mathbf{G}^T\mathbf{v}_{n+\alpha_f^{\mathrm{f}},i} \tag{4.4.28}$$

The compact form for these equations is given by

$$\frac{\alpha_m^{\mathrm{f}}}{\Delta t\,\gamma^{\mathrm{f}}}(\boldsymbol{v}_h^{n+1,i} - \boldsymbol{v}_h^n, \boldsymbol{w}_h) + c(\boldsymbol{v}_h^{n+\alpha_f^{\mathrm{f}},i-1}, \boldsymbol{v}_h^{n+\alpha_f^{\mathrm{f}},i}, \boldsymbol{w}_h) - b(p_h^{n+\alpha_f^{\mathrm{f}},i-1}, \boldsymbol{w}_h) + a(\boldsymbol{v}_h^{n+\alpha_f^{\mathrm{f}},i}, \boldsymbol{w}_h) = (\boldsymbol{b}_h^{n+\alpha_f^{\mathrm{f}}}, \boldsymbol{w}_h) - \left(1 - \frac{\alpha_m^{\mathrm{f}}}{\gamma^{\mathrm{f}}}\right)(\dot{\boldsymbol{v}}_h^n, \boldsymbol{w}_h) \tag{4.4.29}$$

$$-\frac{\Delta t\,\gamma^{\mathrm{f}}}{\alpha_m^{\mathrm{f}}}(\nabla(p_h^{n+\alpha_f^{\mathrm{f}},i} - p_h^{n+\alpha_f^{\mathrm{f}},i-1}), \nabla q_h) = b(q_h, \boldsymbol{v}_h^{n+\alpha_f^{\mathrm{f}},i}) \tag{4.4.30}$$

This mathematical form is the one that is used in the code implemented for solving the computational fluid dynamics equations. We note that for $\rho_\infty^{\mathrm{f}} = 1$ the method is identical to the Crank-Nicolson method given by Eqs. (4.4.21)-(4.4.22) when $\theta^{\mathrm{f}} = \frac{1}{2}$.

4.5 Stabilization Methods

It is well known that two sources of potential numerical instabilities emerge for incompressible flow problems. The first is presented when the Reynolds number for the flow is high, and the convective term tend to dominate the flow equations which yield oscillations in the velocity field. These oscillations can be avoided with a refinement of the finite element mesh for the problem. Unfortunately this is not a solution to the problem due to the high computational cost for very fine meshes.

The other source of instabilities is due to the incompressibility constraint which has several inconveniences due to the zero divergence condition for the velocity field. When the standard Galerkin formulation is used, compatible spaces for the pressure and the velocity field have to be used and must satisfy the Babuška-Brezzi (BB) stability condition, see i.e. Babuska (1973), Brezzi (1974).

To circumvent these problems, several stabilization techniques have been proposed. Essentially, the stabilizing terms added to the original Galerkin formulation

involve the residual of the momentum equation as a factor. The stabilization techniques are consistent in the sense that when an exact solution is substituted into the stabilized formulation, these added terms vanish and the exact solution is satisfied.

One of the stabilization techniques that has been extensively used in convention dominated problems is the *streamline-upwind/Petrov-Galerkin* method, which acronym is SUPG. The original SUPG method was designed for the steady state version of the advection-diffusion equation to avoid the numerical oscillations found using the standard Galerkin formulation. This misbehavior could be avoided by introducing numerical diffusion only along the streamlines as explained in the work of Hughes and Brooks (1979). The final step was the use of the streamline diffusion in the context of weighted residual methods, as given in Hughes and Brooks (1982), that satisfy the BB stability condition.

As demonstrated in Hughes et al. (1986), elements that do not satisfy the BB condition still can achieve a proper stabilization for the Petrov-Galerkin method with equal-order interpolations. Another kind of stabilization is the *pressure-stabilizing/Petrov-Galerkin* method, which acronym is PSPG. The PSPG proposed by Tezduyar et al. (1990) and Tezduyar et al. (1992) consists of a generalization of the Petrov-Galerkin stabilization term proposed in Hughes et al. (1986) for Stokes flows. Coefficients of the PSPG stabilization terms vary with the Reynolds number just as the SUPG terms do. In the zero Reynolds number limit, the PSPG stabilization term reduces to the one proposed in Hughes et al. (1986). In Tezduyar et al. (1990), the SUPG and PSPG stabilization methods are used together with equal-order interpolations. Because the PSPG stabilizing terms involve the residual of the momentum equation as a factor, the stabilized formulation is consistent.

A more general stabilization approach that includes in essence the SUPG and PSPG methods for stabilization was found by Hughes et al. (1989). This idea leads to the well known formulation of the *Galerkin least-square* method, which acronym is GLS. For time-dependent problems, the GLS stabilization needs finite element discretization in both space and time, and therefore leads to a space-time finite element formulation of the problem. Since the stabilizing terms added to the GLS method are obtained by minimizing the sum of the square residual of the momentum equation as a factor, the stabilized formulation is consistent.

With the idea to better understand the origins of stabilized methods, which can be derived from a firm theoretical foundation and a precise definition of the intrinsic time scale parameter, Hughes (1995) developed the *subgrid scale* method. This technique is known as the SGS method and consists in splitting the unknown into a part which can be represented by the finite element mesh and another part that accounts for the unresolvable scales that cannot be reproduced because of the mesh size. In fact the SGS is a family of stabilization techniques where various methods can be recovered as a particular case. In the context of these methods, the *orthogonal sub-scales* method was introduced by Codina (2000). The acronym used for this method is OSS. The main idea here is to assume that the subgrid components are orthogonal to the finite element space. The stabilization of both, convection dominated flows and pressure with transient problems can be found in Codina (2002).

So far all the stabilization methods described require the addition of some ar-

tificial diffusion terms. However another technique where the stabilization terms emerge from the governing equations of the problem is the *finite calculus* method given by Oñate (1998), which acronym is FIC. In this method the concept of flow equilibrium is taken over a finite domain that allows to reinterpret the stabilization terms as an intrinsic and natural contribution to the original differential equations, instead of a correction term introduced at the discrete level. With this natural stabilization concept, the standard forms of the balancing terms appearing in many well known stabilized schemes are easily recognized and can be reinterpreted in a more physical manner. An application for incompressible viscous flows can be found in Oñate (2000).

Other well known stabilization methods are the *characteristic Galerkin* method (CG) developed by Douglas and Russell (1982), and the *Taylor-Galerkin* method (TG) introduced by Donea (1984). A detailed comparison of the most popular stabilization techniques is given by Codina (1998). An interesting comparison between the GLS and the SUPG/PSPG methods can be found in Tezduyar (1992). These stabilization techniques are also explained in Donea and Huerta (2003). In this work the stabilizations used are the SUPG/PSPG, OSS and FIC techniques. They are only implemented in our code to be used for fluid-structure interaction problems.

4.5.1 SUPG/PSPG Stabilization

The stabilization procedure introduced in this section can be found in Tezduyar (1992). In order to account for the linear finite element interpolation chosen for this kind of stabilization, we refer to the work of Dettmer and Peric (2003), where the final outcome consists of adding the discretized term

$$(\dot{\tilde{\boldsymbol{v}}}_h^{n+\alpha_m^{\mathrm{f}}} + \tilde{\boldsymbol{v}}_h^{n+\alpha_f^{\mathrm{f}}} \cdot \nabla \tilde{\boldsymbol{v}}_h^{n+\alpha_f^{\mathrm{f}}} + \nabla p_h^{n+1}, \tau_v \tilde{\boldsymbol{v}}_h^{n+\alpha_f^{\mathrm{f}}} \cdot \nabla \boldsymbol{w}_h + \tau_p \nabla q_h) \tag{4.5.1}$$

to the compact form of the Galerkin method for the fractional step with the generalized-α time discretization. The contribution to the momentum equation is obtained when the pressure test function $q_h = 0$, whereas the contribution to the continuity equation is found when $\boldsymbol{w}_h = \boldsymbol{0}$. The final result for the fractional step method are the stabilized equations

$$\begin{aligned}
&(\dot{\tilde{\boldsymbol{v}}}_h^{n+\alpha_m^{\mathrm{f}}}, \boldsymbol{w}_h) + c(\tilde{\boldsymbol{v}}_h^{n+\alpha_f^{\mathrm{f}}}, \tilde{\boldsymbol{v}}_h^{n+\alpha_f^{\mathrm{f}}}, \boldsymbol{w}_h) - b(p_h^n, \boldsymbol{w}_h) + a(\tilde{\boldsymbol{v}}_h^{n+\alpha_f^{\mathrm{f}}}, \boldsymbol{w}_h) + \\
&\qquad \tau_v(\dot{\tilde{\boldsymbol{v}}}_h^{n+\alpha_m^{\mathrm{f}}} + \tilde{\boldsymbol{v}}_h^{n+\alpha_f^{\mathrm{f}}} \cdot \nabla \tilde{\boldsymbol{v}}_h^{n+\alpha_f^{\mathrm{f}}} + \nabla p_h^n, \tilde{\boldsymbol{v}}_h^{n+\alpha_f^{\mathrm{f}}} \cdot \nabla \boldsymbol{w}_h) = (\boldsymbol{b}_h^{n+1}, \boldsymbol{w}_h) \quad (4.5.2) \\
&-\frac{\Delta t\, \gamma^{\mathrm{f}}}{\alpha_m^{\mathrm{f}}}(\nabla(p_h^{n+1} - p_h^n), \nabla q_h) - \tau_p(\dot{\tilde{\boldsymbol{v}}}_h^{n+\alpha_m^{\mathrm{f}}} + \tilde{\boldsymbol{v}}_h^{n+\alpha_f^{\mathrm{f}}} \cdot \nabla \tilde{\boldsymbol{v}}_h^{n+\alpha_f^{\mathrm{f}}} + \nabla p_h^{n+1}, \nabla q_h) \\
&\qquad = b(q_h, \tilde{\boldsymbol{v}}_h^{n+1}) \quad (4.5.3) \\
&\qquad \frac{\alpha_m^{\mathrm{f}}}{\Delta t\, \gamma^{\mathrm{f}}}(\boldsymbol{v}_h^{n+1} - \tilde{\boldsymbol{v}}_h^{n+1}, \boldsymbol{w}_h) - b(p_h^{n+1} - p_h^n, \boldsymbol{w}_h) = \boldsymbol{0} \quad (4.5.4)
\end{aligned}$$

where τ_v and τ_p are the intrinsic time parameters which multiply the advection term and the pressure term respectively. In this work, the stabilization parameters are the ones chosen by Dettmer and Peric (2003), which are

$$\tau_v = \frac{h_e}{2\,\|\boldsymbol{v}_h\|\,\rho}\,\frac{1}{\sqrt{1+\left(\frac{3}{Re_h}\right)^2}} \tag{4.5.5}$$

$$\tau_p = \frac{h_e}{2\,\|\boldsymbol{v}_h\|\,\rho}\,\frac{\zeta_1}{\sqrt{1+\left(\frac{3\zeta_2}{Re_h}\right)^2}} \tag{4.5.6}$$

where Re_h is the element Reynold number given by

$$Re_h = \frac{\|\boldsymbol{v}_h\|\,h_e\rho}{2\mu} \tag{4.5.7}$$

Here the characteristic element size h_e is defined as the diameter of the circle, the area of which correspond to the finite element e in two dimensions. For 3D problems, h_e is taken as given by Codina (2000). All numerical examples with this stabilization take $\zeta_1 = 30$ and $\zeta_2 = 100$ in this work.

Observe that the pressure in the first equation is treated explicitly, in order to keep the uncoupling of the velocity and pressure calculations. Only the first equation is a nonlinear system, while the second is a linear system. The third equation is simply an update of the velocity.

4.5.2 OSS Stabilization

The orthogonal sub-scales stabilization procedure described in this section is given by Codina (2000). In order to account for the stabilized fractional step method, we refer to the work of Codina (2001), where the final outcome consists in adding

$$\tau(\tilde{\boldsymbol{v}}_h^{\,n+\alpha_f^{\mathrm{f}}}\cdot\nabla\tilde{\boldsymbol{v}}_h^{\,n+\alpha_f^{\mathrm{f}}} + \nabla p_h^{n+1} - \boldsymbol{\pi}_h^n, \tilde{\boldsymbol{v}}_h^{\,n+\alpha_f^{\mathrm{f}}}\cdot\nabla\boldsymbol{w}_h + \nabla q_h) \tag{4.5.8}$$

to the compact form of the Galerkin method for the fractional step with the generalized-α time discretization, where $\boldsymbol{\pi}_h$ is a projection explained ahead. The contribution to the momentum equation is obtained when the pressure test function $q_h = 0$, whereas the contribution to the continuity equation is found when $\boldsymbol{w}_h = \boldsymbol{0}$. The final result for the fractional step method are the stabilized equations

$$(\dot{\tilde{\boldsymbol{v}}}_h^{n+\alpha_m^f}, \boldsymbol{w}_h) + c(\tilde{\boldsymbol{v}}_h^{n+\alpha_f^f}, \tilde{\boldsymbol{v}}_h^{n+\alpha_f^f}, \boldsymbol{w}_h) - b(p_h^n, \boldsymbol{w}_h) + a(\tilde{\boldsymbol{v}}_h^{n+\alpha_f^f}, \boldsymbol{w}_h) + \tau(\tilde{\boldsymbol{v}}_h^{n+\alpha_f^f} \cdot \nabla \tilde{\boldsymbol{v}}_h^{n+\alpha_f^f} + \nabla p_h^n - \boldsymbol{\pi}_h^n, \tilde{\boldsymbol{v}}_h^{n+\alpha_f^f} \cdot \nabla \boldsymbol{w}_h) = (\boldsymbol{b}_h^{n+1}, \boldsymbol{w}_h) \quad (4.5.9)$$

$$-\frac{\Delta t\, \gamma^f}{\alpha_m^f}(\nabla(p_h^{n+1} - p_h^n), \nabla q_h) - \tau(\tilde{\boldsymbol{v}}_h^{n+\alpha_f^f} \cdot \nabla \tilde{\boldsymbol{v}}_h^{n+\alpha_f^f} + \nabla p_h^{n+1} - \boldsymbol{\pi}_h^n, \nabla q_h) = b(q_h, \tilde{\boldsymbol{v}}_h^{n+1}) \quad (4.5.10)$$

$$\frac{\alpha_m^f}{\Delta t\, \gamma^f}(\boldsymbol{v}_h^{n+1} - \tilde{\boldsymbol{v}}_h^{n+1}, \boldsymbol{w}_h) - b(p_h^{n+1} - p_h^n, \boldsymbol{w}_h) = \mathbf{0} \quad (4.5.11)$$

$$(\boldsymbol{\pi}_h^{n+1}, \boldsymbol{\eta}_h) - (\tilde{\boldsymbol{v}}_h^{n+\alpha_f^f} \cdot \nabla \tilde{\boldsymbol{v}}_h^{n+\alpha_f^f} + \nabla p_h^{n+1}, \boldsymbol{\eta}_h) = \mathbf{0} \quad (4.5.12)$$

Observe that in the last equation, $\boldsymbol{\pi}_h$ has the meaning of being the projection of $\tilde{\boldsymbol{v}}_h \cdot \nabla \tilde{\boldsymbol{v}}_h + \nabla p_h$ onto the finite element space. This last equation is just an update of the orthogonal projection, just as the third equation is simply an update of the velocity. The stabilization parameter τ is given in Codina (2001), which is

$$\tau = \left(\frac{4\nu}{h_e^2} + \frac{2\,\|\boldsymbol{v}_h\|}{h_e}\right)^{-1} \quad (4.5.13)$$

This equation is also used to estimate the critical time step size for explicit schemes, where Δt_{crit} is substituted instead of τ in Eq. (4.5.13).

4.5.3 FIC Stabilization

The FIC stabilization introduced by Oñate (2000) for incompressible flow equations is described in this section. The idea behind the method consists in applying the standard conservation laws expressing balance of momentum and mass over a control domain. Assuming that control domain has finite dimensions and representing the variation of mass and momentum over the domain using Taylor series expansions of one order higher than those used in standard infinitesimal theory, the following expressions for the momentum and mass balance respectively are found

$$r_{m_i} - \frac{1}{2} h_j \frac{\partial r_{m_i}}{\partial x_j} = 0 \quad (4.5.14)$$

$$r_d - \frac{1}{2} h_j \frac{\partial r_d}{\partial x_j} = 0 \quad (4.5.15)$$

where r_{m_i} is the residual of the momentum equation obtained from Eq. (4.2.35) and r_d is the residual of the divergence of the velocity given by Eq. (4.2.40). In Oñate et al. (2006), the following assumption is obtained

$$\frac{\partial r_d}{\partial x_j} \approx \frac{h_j}{2a_i} \frac{\partial r_{m_i}}{\partial x_i} \quad (4.5.16)$$

where

$$a_i = \frac{2\nu}{3} + \frac{v_i h_i}{2} \tag{4.5.17}$$

and the following alternative expression for the stabilized mass balance equation is found

$$r_d - \tau_i \frac{\partial r_{m_i}}{\partial x_i} = 0 \tag{4.5.18}$$

with

$$\tau_i = \left(\frac{8\nu}{3h_i^2} + \frac{2v_i}{h_i} \right)^{-1} \tag{4.5.19}$$

τ_i are the intrinsic time parameters. After integrating by parts the resulting momentum and mass balance equations is weak form are

$$\begin{aligned} \int_\Omega \delta v_i \left(\frac{\partial v_i}{\partial t} + v_j \frac{\partial v_i}{\partial x_j} \right) d\Omega - \int_\Omega p \frac{\partial \delta v_i}{\partial x_i} d\Omega + \int_\Omega \nu \frac{\partial v_i}{\partial x_j} \frac{\partial \delta v_i}{\partial x_j} d\Omega \\ - \int_\Omega \delta v_i b_i d\Omega = \int_\Omega \frac{h_j}{2} \frac{\partial \delta u_i}{\partial x_j} r_{m_i} d\Omega \end{aligned} \tag{4.5.20}$$

$$\int_\Omega \delta p \frac{\partial v_i}{\partial x_i} d\Omega = \int_\Omega \tau_i \frac{\partial \delta p}{\partial x_i} r_{m_i} d\Omega \tag{4.5.21}$$

where the only new terms involving the residual r_{m_i} appear on the right hand side of both equations. The computation of the residual terms can be simplified if we introduce the convective projection $\hat{c}_i$ and the pressure gradient projection π_i defined respectively as

$$r_{m_i} = \hat{c}_i - v_j \frac{\partial v_i}{\partial x_j} = 0 \tag{4.5.22}$$

$$r_{m_i} = \pi_i - \frac{\partial p}{\partial x_i} = 0 \tag{4.5.23}$$

Now r_{m_i} can be expressed in Eqs. (4.5.20) and (4.5.21) in terms of $\hat{c}_i$ and π_i respectively which then become additional variables. The system of integral equations is now augmented in the necessary number of additional equations by imposing that the residual vanished for both forms given by Eqs. (4.5.22) and (4.5.23). This gives the final system of governing equations as

$$\begin{aligned} \int_\Omega \delta v_i \left(\frac{\partial v_i}{\partial t} + v_j \frac{\partial v_i}{\partial x_j} \right) d\Omega - \int_\Omega p \frac{\partial \delta v_i}{\partial x_i} d\Omega + \int_\Omega \nu \frac{\partial v_i}{\partial x_j} \frac{\partial \delta v_i}{\partial x_j} d\Omega \\ + \int_\Omega \frac{h_j}{2} \frac{\partial \delta u_i}{\partial x_j} \left(v_j \frac{\partial v_i}{\partial x_j} - \hat{c}_i \right) d\Omega = \int_\Omega \delta v_i b_i d\Omega \end{aligned} \tag{4.5.24}$$

$$\int_\Omega \delta p \frac{\partial v_i}{\partial x_i} d\Omega + \int_\Omega \tau_i \frac{\partial \delta p}{\partial x_i} \left(\frac{\partial p}{\partial x_i} - \pi_i \right) d\Omega = 0 \tag{4.5.25}$$

$$\int_\Omega \delta \hat{c}_i \left(\hat{c}_i - v_j \frac{\partial v_i}{\partial x_j} \right) d\Omega = 0 \tag{4.5.26}$$

$$\int_\Omega \delta \pi_i \left(\pi_i - \frac{\partial p}{\partial x_i} \right) d\Omega = 0 \tag{4.5.27}$$

If the fractional step method is applied to Eqs. (4.5.24)-(4.5.27) together with the generalized-α method, the final result for the stabilized equations in compact form yields

$$(\dot{\tilde{\boldsymbol{v}}}_h^{n+\alpha_m^{\mathrm{f}}}, \boldsymbol{w}_h) + c(\tilde{\boldsymbol{v}}_h^{n+\alpha_f^{\mathrm{f}}}, \tilde{\boldsymbol{v}}_h^{n+\alpha_f^{\mathrm{f}}}, \boldsymbol{w}_h) - b(p_h^n, \boldsymbol{w}_h) + a(\tilde{\boldsymbol{v}}_h^{n+\alpha_f^{\mathrm{f}}}, \boldsymbol{w}_h) + \frac{1}{2}(\tilde{\boldsymbol{v}}_h^{n+\alpha_f^{\mathrm{f}}} \cdot \nabla \tilde{\boldsymbol{v}}_h^{n+\alpha_f^{\mathrm{f}}} - \hat{\mathbf{c}}_h^n, \boldsymbol{h} \cdot \nabla \boldsymbol{w}_h) = (\boldsymbol{b}_h^{n+1}, \boldsymbol{w}_h) \tag{4.5.28}$$

$$-\frac{\Delta t\, \gamma^{\mathrm{f}}}{\alpha_m^{\mathrm{f}}}(\nabla(p_h^{n+1} - p_h^n), \nabla q_h) - \boldsymbol{\tau}(\nabla p_h^{n+1} - \boldsymbol{\pi}_h^n, \nabla q_h) = b(q_h, \tilde{\boldsymbol{v}}_h^{n+1}) \tag{4.5.29}$$

$$\frac{\alpha_m^{\mathrm{f}}}{\Delta t\, \gamma^{\mathrm{f}}}(\boldsymbol{v}_h^{n+1} - \tilde{\boldsymbol{v}}_h^{n+1}, \boldsymbol{w}_h) - b(p_h^{n+1} - p_h^n, \boldsymbol{w}_h) = \mathbf{0} \tag{4.5.30}$$

$$(\hat{\mathbf{c}}_h^{n+1}, \boldsymbol{\zeta}_h) - (\tilde{\boldsymbol{v}}_h^{n+\alpha_f^{\mathrm{f}}} \cdot \nabla \tilde{\boldsymbol{v}}_h^{n+\alpha_f^{\mathrm{f}}}, \boldsymbol{\zeta}_h) = \mathbf{0} \tag{4.5.31}$$

$$(\boldsymbol{\pi}_h^{n+1}, \boldsymbol{\eta}_h) - (\nabla p_h^{n+1}, \boldsymbol{\eta}_h) = \mathbf{0} \tag{4.5.32}$$

Observe that the third equation is simply an update of the velocity, just as the fourth and fifth equations are the updates for the convective projection and pressure projections terms respectively. Advances of the FIC formulation with applications to fluid-structure interaction is been developed by Lynga (2005).

4.6 Solution Strategies

The numerical procedures used to solve nonlinear algebraic equations are iterative, given i.e. by Eqs. (4.5.2), (4.5.9) or (4.5.28), for the only nonlinear terms in fractional steps or predictor corrector schemes. Among the many different procedures available to solve nonlinear problems, in this work only the *Picard iteration* method, see i.e. Reddy (2004), is outlined for computational fluid dynamic problems.

4.6.1 Picard Iteration Method

The Picard iteration method of successive substitution, also known as the direct iteration technique, is the simplest method used in nonlinear problems. In the Picard method, the solution at the i^{th} iteration is obtained from

$$\mathbf{K}(\mathbf{v}^{i-1})\ \mathbf{v}^i = \mathbf{f} \tag{4.6.1}$$

where the nonlinear matrix $\mathbf{K}(\mathbf{v})$ is evaluated using the known solution from the $i-1$ iteration. It is assumed that the initial or guess vector $\mathbf{v}^0$ satisfies the specified boundary conditions of the problem and the nonlinear matrix is invertible.

The Picard iteration method converges when the nonlinearity is mild, and it diverges if the nonlinearity is severe. In this last case, other initial conditions should be taken or a different iterative procedure can be used. The linearized algebraic system for the fractional step method using the generalized-α method for integration in time, applied to Eqs. (4.5.2), (4.5.9) and (4.5.28) yields

$$(\dot{\tilde{\boldsymbol{v}}}_h^{n+\alpha_m^f,i}, \boldsymbol{w}_h) + c(\tilde{\boldsymbol{v}}_h^{n+\alpha_f^f,i-1}, \tilde{\boldsymbol{v}}_h^{n+\alpha_f^f,i}, \boldsymbol{w}_h) - b(p_h^n, \boldsymbol{w}_h) + a(\tilde{\boldsymbol{v}}_h^{n+\alpha_f^f,i}, \boldsymbol{w}_h) + \tau_v(\dot{\tilde{\boldsymbol{v}}}_h^{n+\alpha_m^f,i} + \tilde{\boldsymbol{v}}_h^{n+\alpha_f^f,i-1} \cdot \nabla \tilde{\boldsymbol{v}}_h^{n+\alpha_f^f,i} + \nabla p_h^n, \tilde{\boldsymbol{v}}_h^{n+\alpha_f^f,i-1} \cdot \nabla \boldsymbol{w}_h) = (\boldsymbol{b}_h^{n+1}, \boldsymbol{w}_h) \tag{4.6.2}$$

$$(\dot{\tilde{\boldsymbol{v}}}_h^{n+\alpha_m^f,i}, \boldsymbol{w}_h) + c(\tilde{\boldsymbol{v}}_h^{n+\alpha_f^f,i-1}, \tilde{\boldsymbol{v}}_h^{n+\alpha_f^f,i}, \boldsymbol{w}_h) - b(p_h^n, \boldsymbol{w}_h) + a(\tilde{\boldsymbol{v}}_h^{n+\alpha_f^f,i}, \boldsymbol{w}_h) + \tau(\tilde{\boldsymbol{v}}_h^{n+\alpha_f^f,i-1} \cdot \nabla \tilde{\boldsymbol{v}}_h^{n+\alpha_f^f,i} + \nabla p_h^n - \boldsymbol{\pi}_h^n, \tilde{\boldsymbol{v}}_h^{n+\alpha_f^f,i-1} \cdot \nabla \boldsymbol{w}_h) = (\boldsymbol{b}_h^{n+1}, \boldsymbol{w}_h) \tag{4.6.3}$$

$$(\dot{\tilde{\boldsymbol{v}}}_h^{n+\alpha_m^f,i}, \boldsymbol{w}_h) + c(\tilde{\boldsymbol{v}}_h^{n+\alpha_f^f,i-1}, \tilde{\boldsymbol{v}}_h^{n+\alpha_f^f,i}, \boldsymbol{w}_h) - b(p_h^n, \boldsymbol{w}_h) + a(\tilde{\boldsymbol{v}}_h^{n+\alpha_f^f,i}, \boldsymbol{w}_h) + \frac{1}{2}(\tilde{\boldsymbol{v}}_h^{n+\alpha_f^f,i-1} \cdot \nabla \tilde{\boldsymbol{v}}_h^{n+\alpha_f^f,i} - \hat{\mathbf{c}}_h^n, \boldsymbol{h} \cdot \nabla \boldsymbol{w}_h) = (\boldsymbol{b}_h^{n+1}, \boldsymbol{w}_h) \tag{4.6.4}$$

which are the nonlinear terms of the SUPG/PSPG, OSS and FIC stabilization techniques respectively.

4.7 Code Development

In this work the fluid problem with the presented stabilizations have been implemented in the finite element program COMET (2007). The dynamic analysis with the θ-family method, backward differencing method and Generalized-α method for fluids have also been added to the code. This software is developed at the International Center for Numerical Methods in Engineering (CIMNE) and is used for coupled contact, mechanical and thermal analysis using the finite element method.

4.8 Example Problems

4.8.1 Wall-Driven Cavity Flow

The wall-driven cavity flow problem is often used as a benchmark problem since it has been extensively studied by analytical, numerical and experimental methods.

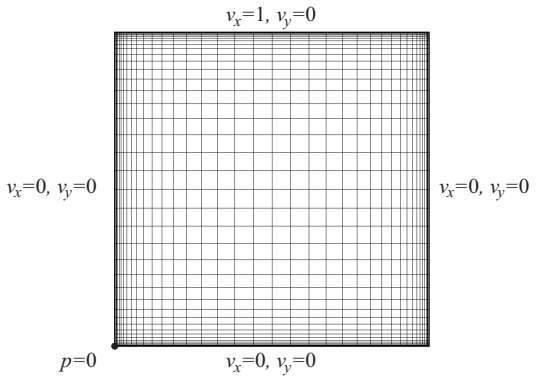

Figure 4.1 *Cavity four-node finite element mesh*

Assuming a unit square and that the velocity of the top wall is unity, the problem is solved with a 40×40 quadrilateral mesh which has been refined near the boundaries, as shown in Fig. 4.1.

In the literature this problem is solved for various Reynolds numbers, which are given by $\mathrm{Re} = \rho v_c l_c / \mu$. In this problem the characteristic velocity $v_c = 1$ and characteristic length $l_c = 1$. If the viscosity is kept constant as $\mu = 1$, then the Reynolds number is given by $\mathrm{Re} = \rho$. In this example the wall-driven cavity flow for a Reynold number of 400 is studied. Consequently, the density for the problem is taken as $\rho = 400$. The generalized-α time integration method has been used with $\rho_\infty^{\mathrm{f}} = 0.9$.

Singularities for this problem exists at each corner where the moving lid of the top meets the side fixed walls. Here it is assumed that $v_x = 1, v_y = 0$ at singularity points. In this example, the FIC stabilization technique has been used with a mesh of 1600 elements, 1681 nodes and a time step size $\Delta t = 0.05$. The pressure contours reached at the steady state for the problem are shown in Fig. 4.2.

The accuracy of the numerical results have been compared to those presented

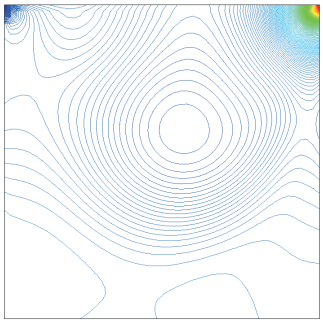

Figure 4.2 *Pressure contours for Re=400*

by Ghia et al. (1982), which were obtained with finite difference solutions and using a very fine grid that made them become a standard reference. The comparison of the x-velocity profile along the cavity mid-section for $x = 0.5$ versus the vertical distance is given in Fig. 4.3.

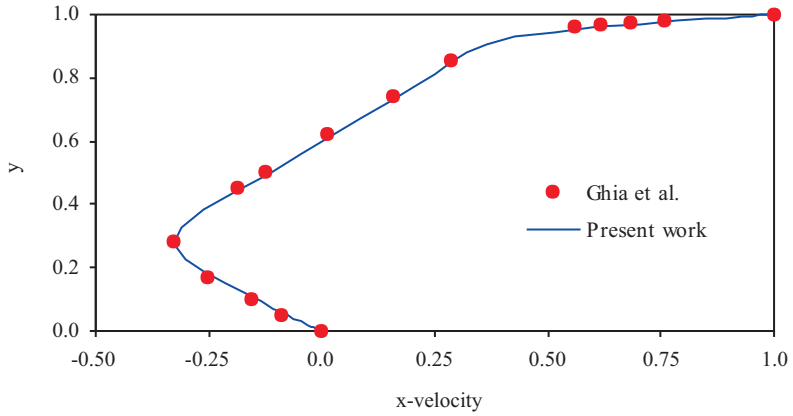

Figure 4.3 *Velocity* $v_x(0.5, y)$ *vs.* y

Again the solution of this work is compared to the numerical results presented by Ghia et al. (1982) for the y-velocity profile along the cavity mid-section for $y = 0.5$ versus the horizontal distance, as shown in Fig. 4.4.

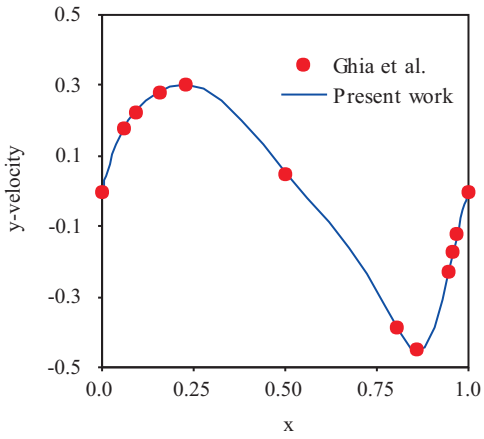

Figure 4.4 *Velocity* $v_y(x, 0.5)$ *vs.* x

Figs. 4.3-4.4 show that the implementation of the computational fluid dynamics methods used in this work together with the FIC stabilization described in section **4.5** lead to the expected solution for this problem.

4.8.2 Flow Past a Circular Cylinder in 2D

The transient flow past a circular cylinder is another widely solved benchmark problem. The interest of this problem is the periodic flow patterns that develops for values of the Reynolds number Re $>$ 40. In this case vortex shedding are generated periodically and alternately from each side of the cylinder, leading to the well known von Karman vortex street.

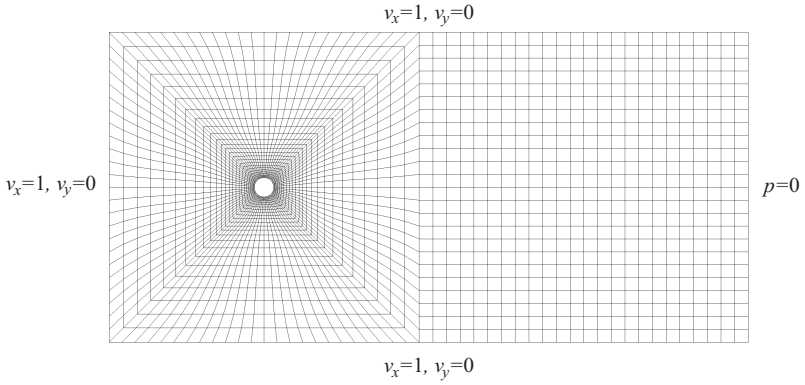

Figure 4.5 *Finite element mesh and boundary conditions*

To describe the geometry of the problem, a circular cylinder of unit diameter is placed inside the domain $\Omega = \{-8 \leq x \leq 25, -8 \leq y \leq 8\}$. The center of the cylinder is placed at the point (0,0). The boundary conditions are given by a value of 1.0 for the x-velocity at the inflow, top and bottom boundaries. At these boundaries, the y-velocity is set to zero. Additionally, the pressure is set to zero at the outflow boundary, as shown in Fig. 4.5.

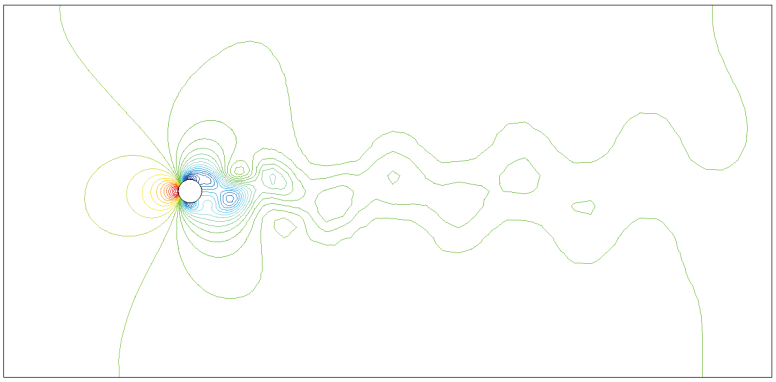

Figure 4.6 *Pressure contours*

The material properties are density $\rho = 0.01$ and viscosity $\mu = 0.0001$, yielding a Reynolds number Re $= 100$. The finite element mesh used for this problem is

shown in Fig. 4.5 and consists of 2880 four-node quadrilateral elements and 3000 nodes. Second order time integration is employed with the Generalized-α scheme with $\rho_\infty^{\mathrm{f}} = 0.9$. The number of time steps studied are 1500 with a time step size $\Delta t = 0.20$. In this problem, the FIC, OSS and SUPG/PSPG stabilization techniques have been employed and compared. Fig. 4.6 shows pressure contours for a time $t = 154.2$.

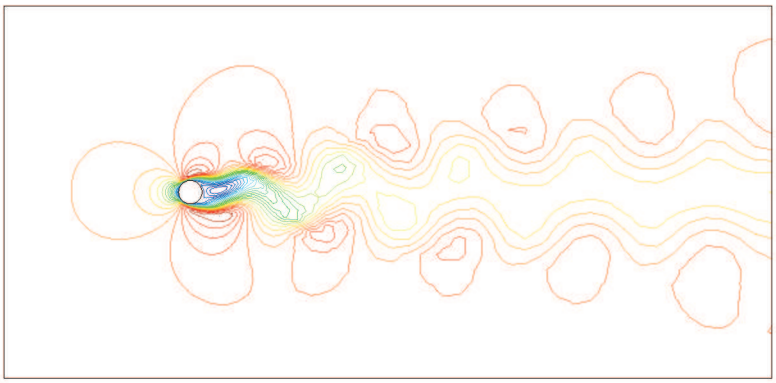

Figure 4.7 *x-velocity contours*

Fig. 4.7 shows x-velocity contours for a time $t = 154.2$, while Fig. 4.8 shows y-velocity contours at the same time.

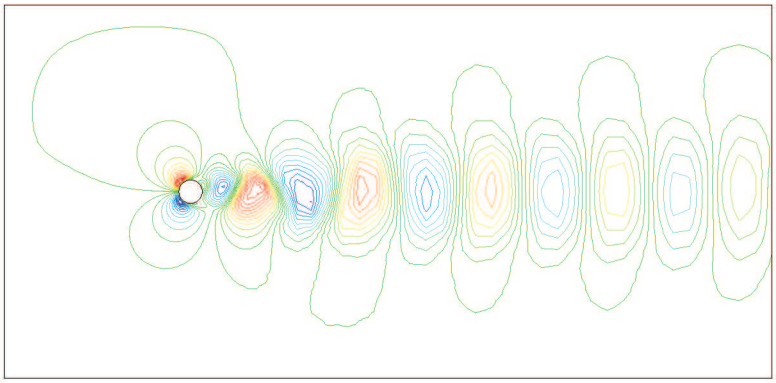

Figure 4.8 *y-velocity contours*

Fig. 4.9 shows a typical plot of the time history of the velocity component v_y at the point $(x, y) = (2, 0)$ given by the SUPG/PSPG stabilization technique.

The forces around the cylinder are used to compute the evolution of the drag C_D and lift C_L coefficients given respectively by

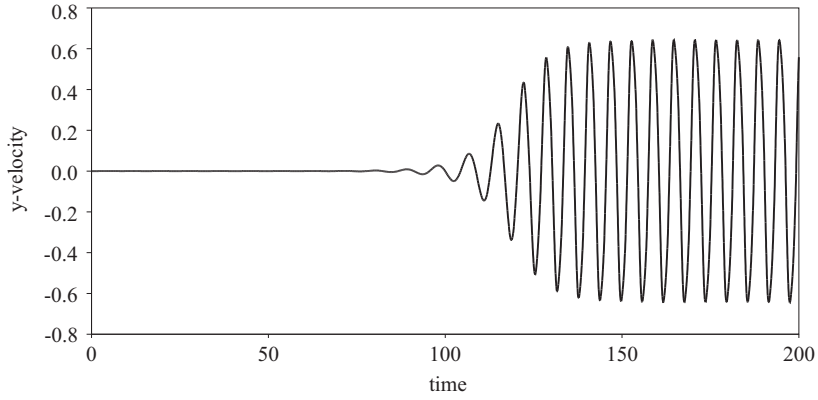

Figure 4.9 *Time history of y-velocity component*

$$C_D = \frac{f_D}{\frac{1}{2}\rho v^2 A} \tag{4.8.1}$$

$$C_L = \frac{f_L}{\frac{1}{2}\rho v^2 A} \tag{4.8.2}$$

where f_D is the drag force measured in the direction of the flow while f_L is the lift force perpendicular to the direction of flow. The solution using the three methods in this example is plotted in the temporal evolution of the drag coefficient C_D, as well as the evolution of the lift coefficient C_L as shown in Figs. 4.10 and 4.11.

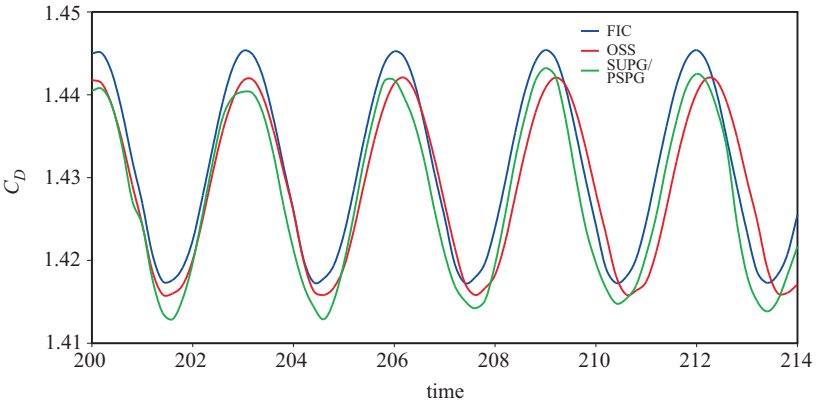

Figure 4.10 *C_D for a flow around a cylinder at Re=100*

For this example, the lift coefficient is almost the same for the three different methods, while in the case of the drag coefficient, the FIC stabilization technique shows a little bit more diffusive behavior than the OSS and SUPG/PSPG stabilization

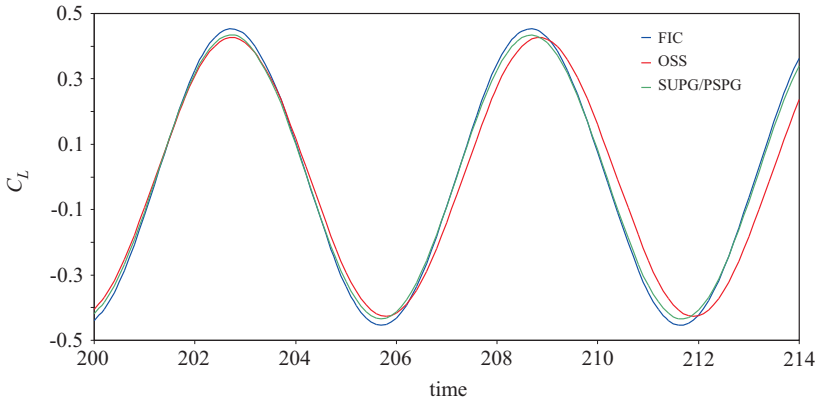

Figure 4.11 *C_L for a flow around a cylinder at Re=100*

techniques. However the amplitude between the three methods is practically the same. For the drag coefficient, the amplitude is about 0.027, while a value of 0.865 is obtained for the lift coefficient. These values are in good agreement with those presented in the numerical comparison of CBS and SGS stabilization techniques presented by Codina et al. (2006).

The Strouhal number or adimensional frequency of the solution is one of the most studied quantities and describes the oscillating flow mechanisms, which is given by

$$St = \frac{freq \cdot l_c}{v_c} \tag{4.8.3}$$

where St is the dimensionless Strouhal number, $freq$ is the frequency of vortex shedding, l_c is the characteristic length (in this example taken as the cylinder diameter) and v_c is the characteristic velocity of the fluid.

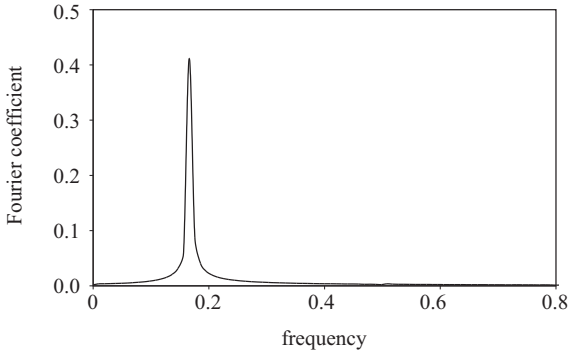

Figure 4.12 *Fourier spectrum of the lift coefficient*

A Fourier analysis of the lift coefficient C_L is performed within the time range [120,300] in order to find the dominant frequency of the solution. In Fig. 4.12, the Fourier spectrum obtained is shown, leading to a frequency $freq = 0.16602\ Hz$, equivalently to a period of 6.02 s. This value gives a dimensionless Strouhal number $St = 0.16602$ which is in good agreement with the experimental result $St = 0.166$ reported by Hammache and Gharib (1991).

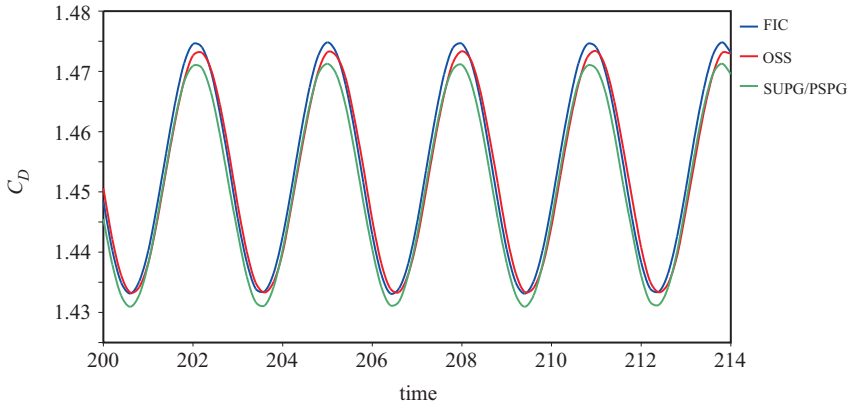

Figure 4.13 *C_D for a flow around a cylinder at Re=100*

This problem is solved again using a finer mesh, consisting of 32000 four-node quadrilateral elements and 32400 nodes. The same second order time integration is employed. The number of time steps studied are 1500 with a time step size $\Delta t = 0.20$. Again, the FIC, OSS and SUPG/PSPG stabilization techniques have been used. Drag and lift coefficients for this mesh are given in Figs. 4.13 and 4.14 respectively.

For the finer mesh, the lift coefficient is practically the same for the three

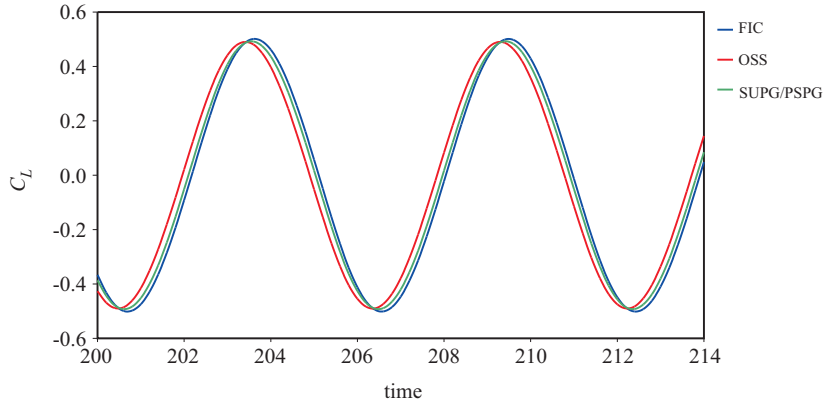

Figure 4.14 *C_L for a flow around a cylinder at Re=100*

different methods, while in the case of the drag coefficient some little differences are presented. The amplitude between the three methods for the drag coefficient is about 0.04, while a value of 1.0 is obtained for the lift coefficient. It can be seen that when the mesh is refined, all methods lead to the same solution. Very small frequency discrepancies between these methods are found, but all of them give a period about 6.0 s.

In this problem, it is shown that the stabilization techniques of these three methods are in fact very similar. The numerical comparison yields no conclusive remarks, but shows that a finer mesh leads to close numerical solutions.

4.8.3 Flow Past a Circular Cylinder in 3D

Here the transient flow past a circular cylinder in 3D is solved using a high quality mesh constructed by Rainald Löhner. The objective of the example is to verify the behavior of the formulations implemented in this work, using a large example and comparing it with a code specialized for fluids.

To describe the geometry of the problem, a circular cylinder of unit diameter is placed inside the domain $\Omega = \{-4 \leq x \leq 15, -4 \leq y \leq 4, 0 \leq z \leq 0.2\}$. The center of the cylinder is placed at the point (0,0,0). The boundary conditions are given by a value of 1.0 for the x-velocity at the inflow, and free x- and z-velocity at top and bottom boundaries. At these boundaries, the y-velocity is set to zero. The right and left boundaries have the z-velocity component set to zero while the x- and y-velocity components are free. Additionally, the pressure is set to zero at the outflow boundary, as shown in Fig. 4.15.

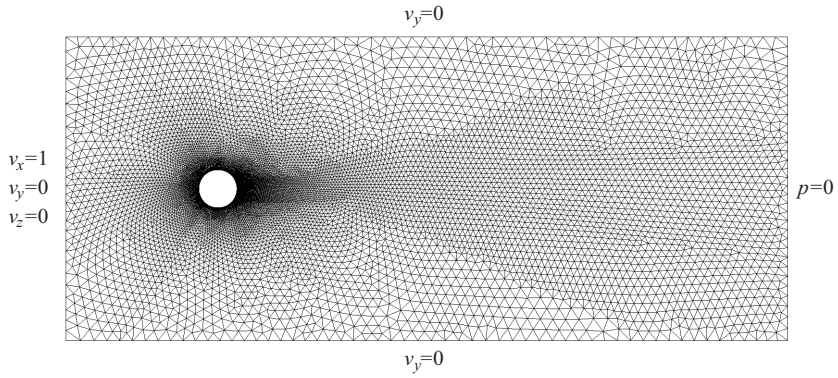

Figure 4.15 *Finite element mesh and boundary conditions*

The material properties are density $\rho = 1.0$ and viscosity $\mu = 0.005263$, yielding a Reynolds number Re = 190. The finite element mesh used for this problem is shown in Fig. 4.15 and consists of 108,147 four-node tetrahedral elements and 30,000 nodes. A detail of the mesh around the cylinder is shown in Fig. 4.16.

Second order time integration is employed with the Generalized-α scheme and $\rho_\infty^{\mathrm{f}} = 0.9$. The number of time steps studied are 2000 with a time step size

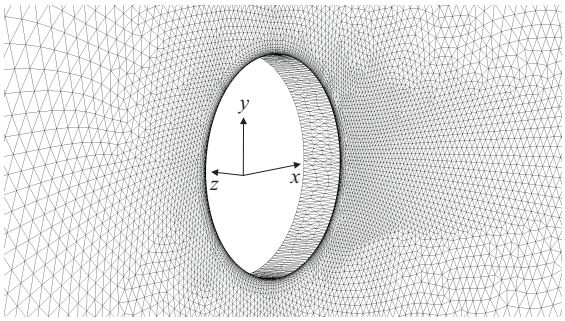

Figure 4.16 *Detail of the mesh around the cylinder*

$\Delta t = 0.05$, beginning from an initially stable configuration. In this problem, the OSS stabilization techniques is been employed and the solution is compared with the one obtained by Coppola-Owen (2006) using the same stabilization and the BDF2 time integration scheme. Fig. 4.17 shows pressure contours for time $t = 100$.

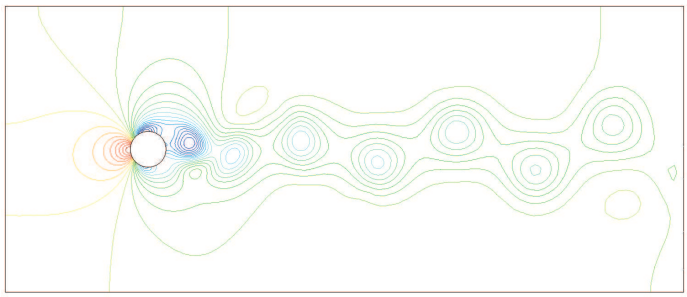

Figure 4.17 *Pressure contours*

Fig. 4.18 shows x-velocity contours for a time $t = 100$, while Fig. 4.19 shows y-velocity contours at the same time.

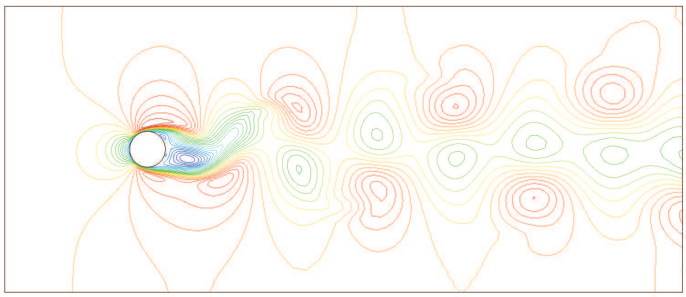

Figure 4.18 *x-velocity contours*

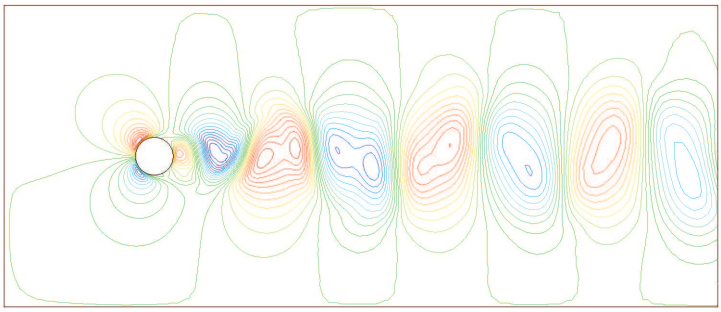

Figure 4.19 *y-velocity contours*

The forces around the cylinder are used to compute the evolution of the drag C_D and lift C_L coefficients given respectively by Figs. 4.20 and 4.21.

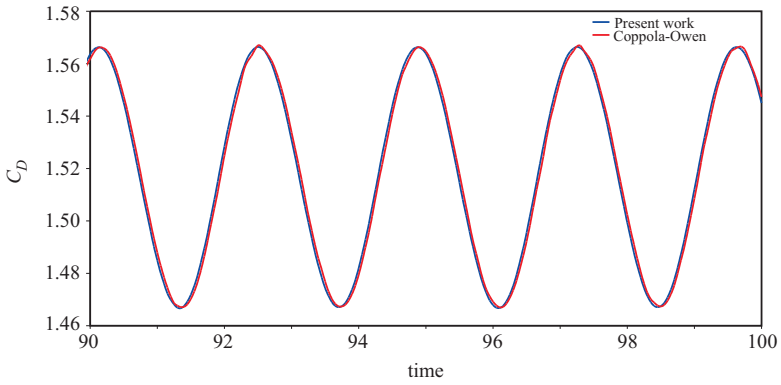

Figure 4.20 *C_D for a flow around a cylinder at Re=190*

In this case, the drag coefficient has an amplitude of 0.10, while a value of 1.45 is obtained for the lift coefficient.

A Fourier analysis of the lift coefficient C_L is performed within the range [65,100] in order to find the dominant frequency of the solution. In Fig. 4.22, the Fourier spectrum obtained is shown, leading to a frequency $freq = 0.19531\ Hz$. The Strouhal number for this example yields a dimensionless value of 0.19531 and a period of 5.12 s.

The solution found by Coppola-Owen (2006) for this example is the same as the one presented in this work.

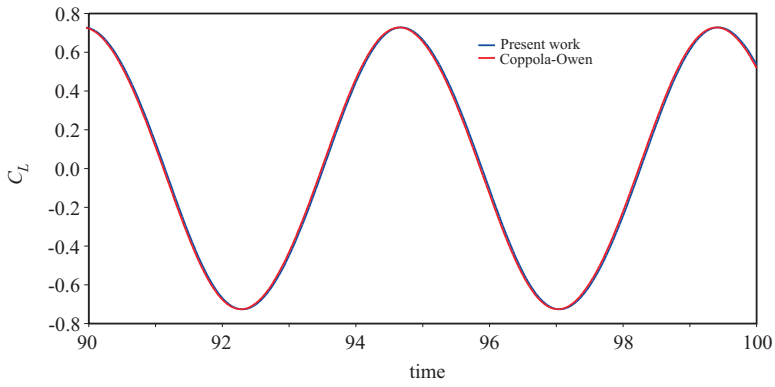

Figure 4.21 *C_L for a flow around a cylinder at Re=190*

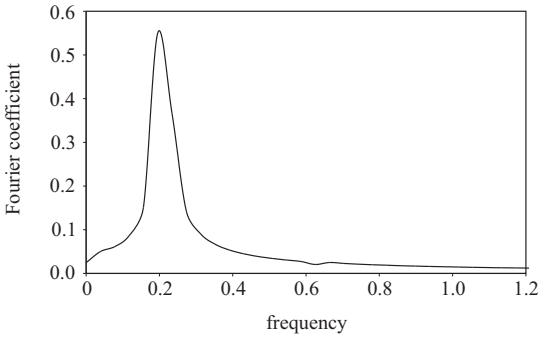

Figure 4.22 *Fourier spectrum of the lift coefficient*

Chapter 5

Fluid-Structure Interaction

Many physical problems of different fields in engineering and applied sciences belong to multiphysic problems. Recently numerical simulation of Fluid-Structure Interaction (FSI) problems have gained great interest from the computational mechanics community in order to reduce development time and cost in coupled systems.

In case of civil engineering applications, the interaction of wind flow and structural motion may lead to *aeroelastic* instabilities which may cause the collapse of the structure. This problem can occur on constructions such as long-span bridges, high-rise buildings and light weight roof structures.

Maybe the most analyzed FSI problem is found in aerospace applications, which are concerned with aeroelastic instabilities for the study of wind flow around flexible wings of aircrafts. Recently, on the other hand, biomechanical applications are interested in the study of hemodynamics, i.e. blood flow through large arteries, which are simulated using numerical FSI of large structural membrane deformations interacting with viscous flows.

FSI problems are complex because they consist of structural nonlinear boundary conditions imposed on fluid moving boundaries where the position is part of the solution. Because the moving position of the structure prescribes part of the fluid boundary, it becomes necessary to perform the integration of the Eulerian fluid equations on a moving mesh. Among the several methods proposed for this problem, in this work it is used the *Arbitrary Lagrangian-Eulerian* (ALE) formulation.

This kind of FSI problems usually are viewed as a two-field coupled problem, however the moving mesh can be viewed as another structural problem, and therefore the complete coupled problem can be formulated as a three-field system: the structure, the fluid and the moving mesh.

5.1 Coupling Strategies

The implementation of a coupled problem can be done using two different global strategies, which are the *monolithic* methods and the *partitioned* methods. In

monolithic methods, the discretized fluid-structure system is solved together with the mesh movement system in a single iteration loop, leading to a very large system of nonlinear equations to be solved simultaneously. Some advantages of this method are that it ensures stability and convergence of the whole coupled problem. On the contrary, in simultaneous solution procedures the time step has to be equal for all subsystems, which may be inefficient if different time scales are presented for the problem. An important disadvantage is the considerably high computing time effort required to solve each algebraic system and sometimes the necessity to develop new software and solution methods for the coupling method. A monolithic approach to FSI is presented by Hübner et al. (2004).

In partitioned methods application of existing appropriate and sophisticated solvers for either structural or fluid subsystems will continue to be used. These methods enjoy great popularity due to the simplified coupling procedure in many cases. Partitioned methods are divided into *weak* or *loose* coupling algorithms and *strong* or *implicit* coupling schemes. Weak algorithms are also known as *staggered* or *explicit* schemes. The major drawbacks of partitioned methods are lack of accuracy and stability problems, which sometimes may diverge from the solution.

Partitioned methods were introduced by Park and Felippa (1983). The key idea for these methods is clearly described in Felippa et al. (1998). Partitioned solutions with staggered coupling algorithms are developed by Farhat et al. (1997) to be used in aeroelastic wing problems. Strong coupling of partitioned algorithms are applied to large displacements 2D structural problems coupled to viscous incompressible fluids by Wall and Ramm (1998) and Wall (1999). They also applied the same method for a coupled fluid structure environment with an initially flat three-dimensional shell model as given in Wall and Ramm (2000). Other large displacements structural problems interacting with incompressible fluids are detailed in Mok (2001), Mok and Wall (2001) and Tallec and Mouro (2001). FSI with large displacements applied to wind problems is developed by Rossi (2005), Wüchner and Bletzinger (2005), Badia (2006) and Wüchner (2006).

More sophisticated developments on strong partitioned method for FSI problems can be found in Steindorf (2002), Matthies and Steindorf (2004), Matthies and Steindorf (2005), Matthies and Steindorf (2006) and Tezduyar et al. (2006). A study on strong coupling partitioned methods for FSI applied to hemodynamic problems can be found in Nobile (2001), Causin et al. (2005), and Fernández and Moubachir (2005). Strong coupling of fluid-structure interaction including free surfaces is studied in Dettmer (2004) and Wall et al. (2007). Recently, a new approach based on Robin transmissions conditions for fluid-structure interaction problems is given in Badia et al. (2007).

These concepts are better explained next. A simple example for a two-field x and y scalar problem, as given in Felippa (2004), is assumed to be governed by the differential equations

$$\begin{aligned} 2x(t) + 4y(t) &= f(t) \\ \dot{y}(t) - 3y(t) + 5x(t) &= g(t) \end{aligned} \tag{5.1.1}$$

in which $f(t)$ and $g(t)$ are the external forces. Using the backward Euler time integration leads to

$$\dot{y}_{n+1} = \frac{y_{n+1} - y_n}{\Delta t} \tag{5.1.2}$$

where Δt is the time step size. Assuming known all values at time step n, and substituting Eq. (5.1.2) into Eq. (5.1.1) yields the following algebraic system

$$\begin{bmatrix} 2 & 4 \\ 5\Delta t & 1 - 3\Delta t \end{bmatrix} \begin{bmatrix} x_{n+1} \\ y_{n+1} \end{bmatrix} = \begin{bmatrix} f_{n+1} \\ \Delta t\, g_{n+1} + y_n \end{bmatrix} \tag{5.1.3}$$

which can be solved simultaneously for x_{n+1} and y_{n+1} as a *monolithic* approach, where a general *multi-field* solver has to be used or developed. However if we want to use our existing codes that solve independently x_{n+1} with the **F** field solver, and y_{n+1} with the **S** field solver, then a *partitioned* approach has to be used. It is assumed that the solvers **F** and **S** are two separate but communicating programs. A simple partitioned solution procedure is obtained with the following steps for a *staggered* partition.

1) Make a prediction for y_{n+1},

$$y_{n+1} = y^p \tag{5.1.4}$$

where the usual choices for the prediction are $y^p = y_n$ or $y^p = y_n + \Delta t\, \dot{y}_n$. Send this information to the **F** field solver as an external force.

2) With the **F** field solver, find x_{n+1} from the partitioned system extracting the first equation from the algebraic system in Eq. (5.1.3) yielding

$$x_{n+1} = \frac{1}{2}\left(f_{n+1} - 4y^p\right) \tag{5.1.5}$$

3) Send x_{n+1} to the **S** field solver.

4) Perform a correction with the **S** field solver for y_{n+1} from the partitioned system extracting the second equation from the algebraic system in Eq. (5.1.3) giving

$$y_{n+1} = \frac{1}{1 - 3\Delta t}\left(\Delta t\, g_{n+1} + y_n - 5\Delta t\, x_{n+1}\right) \tag{5.1.6}$$

5) Now the time step is advanced and the process is repeated for the next time step.

This coupling procedure is known as the *staggered partitioned* scheme or *weak coupling* scheme. It is common to use this kind of coupling method for explicit field solvers where little time steps are used and no convergence of the coupling is checked.

For implicit field solvers, the time step is usually 10 to 100 times larger than the critical time step used for explicit field solvers. In this case, convergence of the coupling after step 4) is required. If the convergence is not reached, step 5) is not performed and the procedure is repeated within each time step, i.e. steps 2 to 4, where y^p of step 2) is substituted by y_{n+1} of step 4). These iterations turn

the staggered approach over a *strong coupling* partitioned procedure which tends to the solution of the monolithic problem.

For fluid-structure interaction problems, the system to solve is nonlinear and adds difficulty to the problem being studied, which sometimes diverge. However the basic idea for solving the problem keeps.

5.2 ALE Framework

Solid and structural formulations are commonly based on Lagrangian descriptions since they deform with the material. On the contrary, fluids are usually formulated on Eulerian descriptions since they involve fixed spatial domains where interest is focused on a particular part of the fixed mesh, i.e. the flow around a solid. In FSI problems, the Eulerian mesh of the fluid is not fixed in space anymore since the motion of the structural mesh moves the fluid mesh and consequently the Eulerian fluid equations must be formulated using a mesh movement technique.

Hybrid techniques such as the ALE descriptions combine the advantages of Lagrangian and Eulerian methods while minimizing the disadvantages. Since ALE descriptions are an arbitrary combination of the Lagrangian and Eulerian descriptions, the user must select an adequate mesh motion as a result of the combination of both descriptions. Equations describing the ALE methods are very similar to those used for the Eulerian formulations. In fact, Eulerian methods can be considered as a special case of ALE methods. A complete description and state of the art for ALE methods can be found in Belytschko et al. (2000) and Donea and Huerta (2003).

Until now for Lagrangian and Eulerian descriptions two configurations have been used: the reference configuration and the deformed configuration. In ALE description, another configuration is needed which is the *ALE configuration*. The domain for an ALE configuration is denoted by $\hat{\Omega}$, which coordinates $\boldsymbol{\mathcal{X}}$ are called ALE coordinates. Two different motions are described in ALE methods: *material motion* and *mesh motion*. Material motion is described just as Eq. (2.1.2) yielding

$$\mathbf{x} = \boldsymbol{\phi}(\mathbf{X}, t) \tag{5.2.1}$$

The corresponding velocity and acceleration is given in Eq. (2.1.7) and Eq. (2.1.8) respectively. The mesh motion is described by

$$\mathbf{x} = \hat{\boldsymbol{\phi}}(\boldsymbol{\mathcal{X}}, t) \tag{5.2.2}$$

where $\mathbf{x}$ represents the deformed or spatial configuration. ALE coordinates can be obtained from Eq. (5.2.2) leading to

$$\boldsymbol{\mathcal{X}} = \hat{\boldsymbol{\phi}}^{-1}(\mathbf{x}, t) \tag{5.2.3}$$

Substituting Eq. (5.2.1) into Eq. (5.2.3) gives the relation between material and ALE coordinates yielding

$$\boldsymbol{\mathcal{X}} = \hat{\boldsymbol{\phi}}^{-1}(\boldsymbol{\phi}(\mathbf{X}, t), t) = \boldsymbol{\psi}(\mathbf{X}, t) \tag{5.2.4}$$

where $\boldsymbol{\psi}$ represents the composition of functions $\hat{\boldsymbol{\phi}}^{-1} \circ \boldsymbol{\phi}$. With all these equations, the material motion can also be expressed as a composition of functions given by

$$\mathbf{x} = \hat{\boldsymbol{\phi}}(\boldsymbol{\psi}(\mathbf{X}, t), t) \tag{5.2.5}$$

and it is concluded that $\boldsymbol{\phi} = \hat{\boldsymbol{\phi}} \circ \boldsymbol{\psi}$. The *mesh displacement* is defined by

$$\hat{\mathbf{u}} = \mathbf{x} - \boldsymbol{\mathcal{X}} = \hat{\boldsymbol{\phi}}(\boldsymbol{\mathcal{X}}, t) - \boldsymbol{\mathcal{X}} \tag{5.2.6}$$

The corresponding *mesh velocity* and *mesh acceleration* is given respectively by

$$\hat{\mathbf{v}} = \frac{\partial \hat{\mathbf{u}}(\boldsymbol{\mathcal{X}}, t)}{\partial t} = \frac{\partial \hat{\boldsymbol{\phi}}(\boldsymbol{\mathcal{X}}, t)}{\partial t} \tag{5.2.7}$$

$$\hat{\mathbf{a}} = \frac{\partial \hat{\mathbf{v}}(\boldsymbol{\mathcal{X}}, t)}{\partial t} \tag{5.2.8}$$

The material time derivative can be obtained similar to the Eulerian description. Therefore, the material time derivative of a function $f(\boldsymbol{\mathcal{X}}, t)$ yields

$$\frac{Df(\boldsymbol{\mathcal{X}}, t)}{Dt} = \frac{\partial f}{\partial t} + \frac{\partial f}{\partial x_j}\frac{\partial x_j}{\partial \mathcal{X}_i}\frac{\partial \mathcal{X}_i}{\partial t} = \frac{\partial f}{\partial t} + \frac{\partial f}{\partial x_j}c_j \tag{5.2.9}$$

where c_j is the *convective velocity* given by the difference between the material and mesh velocities $\mathbf{c} = \mathbf{v} - \hat{\mathbf{v}} = \mathbf{v} - \mathbf{v}_{\text{mesh}}$. In general the material time derivative of any function, vector or tensor given in ALE variables $\boldsymbol{\mathcal{X}}$ and time t can be obtained with

$$\frac{D(\bullet)}{Dt} = \frac{\partial(\bullet)}{\partial t} + \mathbf{c} \cdot \nabla(\bullet) \tag{5.2.10}$$

It is obvious to think that the conservation equations, expressed before in Lagrangian and Eulerian coordinates, must now be expressed in ALE coordinates. Since we are dealing with incompressible fluid equations, the only equation that we need to describe is the momentum equation, yielding

$$\rho\left(\frac{\partial \mathbf{v}}{\partial t} + \mathbf{c} \cdot \nabla \mathbf{v}\right) = \nabla \cdot \boldsymbol{\sigma} + \rho \mathbf{b} \quad \text{or} \quad \rho\left(\frac{\partial v_i}{\partial t} + c_j \partial_j v_i\right) = \frac{\partial \sigma_{ij}}{\partial x_j} + \rho b_i \tag{5.2.11}$$

where the material time derivative of the velocity has been employed. The resulting equations for the fractional step method using the OSS stabilization in ALE configuration yields

$$
\begin{aligned}
(\dot{\tilde{\boldsymbol{v}}}_h^{n+\alpha_m^{\mathrm{f}}}, \boldsymbol{w}_h) + c(\tilde{\boldsymbol{c}}_h^{n+\alpha_f^{\mathrm{f}}}, \tilde{\boldsymbol{v}}_h^{n+\alpha_f^{\mathrm{f}}}, \boldsymbol{w}_h) - b(p_h^n, \boldsymbol{w}_h) + a(\tilde{\boldsymbol{v}}_h^{n+\alpha_f^{\mathrm{f}}}, \boldsymbol{w}_h) + \\
\tau(\tilde{\boldsymbol{c}}_h^{n+\alpha_f^{\mathrm{f}}} \cdot \nabla \tilde{\boldsymbol{v}}_h^{n+\alpha_f^{\mathrm{f}}} + \nabla p_h^n - \boldsymbol{\pi}_h^n, \tilde{\boldsymbol{c}}_h^{n+\alpha_f^{\mathrm{f}}} \cdot \nabla \boldsymbol{w}_h) = (\boldsymbol{b}_h^{n+1}, \boldsymbol{w}_h) \\
-\frac{\Delta t\, \gamma^{\mathrm{f}}}{\alpha_m^{\mathrm{f}}}(\nabla(p_h^{n+1} - p_h^n), \nabla q_h) - \tau(\tilde{\boldsymbol{c}}_h^{n+\alpha_f^{\mathrm{f}}} \cdot \nabla \tilde{\boldsymbol{v}}_h^{n+\alpha_f^{\mathrm{f}}} + \nabla p_h^{n+1} - \boldsymbol{\pi}_h^n, \nabla q_h) \\
= b(q_h, \tilde{\boldsymbol{v}}_h^{n+1}) \\
\frac{\alpha_m^{\mathrm{f}}}{\Delta t\, \gamma^{\mathrm{f}}}(\boldsymbol{v}_h^{n+1} - \tilde{\boldsymbol{v}}_h^{n+1}, \boldsymbol{w}_h) - b(p_h^{n+1} - p_h^n, \boldsymbol{w}_h) = \boldsymbol{0} \\
(\boldsymbol{\pi}_h^{n+1}, \boldsymbol{\eta}_h) - (\tilde{\boldsymbol{c}}_h^{n+\alpha_f^{\mathrm{f}}} \cdot \nabla \tilde{\boldsymbol{v}}_h^{n+\alpha_f^{\mathrm{f}}} + \nabla p_h^{n+1}, \boldsymbol{\eta}_h) = \boldsymbol{0}
\end{aligned}
\tag{5.2.12}
$$

The final equations for the fractional step method using the FIC stabilization in ALE configuration are expressed by

$$
\begin{aligned}
(\dot{\tilde{\boldsymbol{v}}}_h^{n+\alpha_m^{\mathrm{f}}}, \boldsymbol{w}_h) + c(\tilde{\boldsymbol{c}}_h^{n+\alpha_f^{\mathrm{f}}}, \tilde{\boldsymbol{v}}_h^{n+\alpha_f^{\mathrm{f}}}, \boldsymbol{w}_h) - b(p_h^n, \boldsymbol{w}_h) + a(\tilde{\boldsymbol{v}}_h^{n+\alpha_f^{\mathrm{f}}}, \boldsymbol{w}_h) + \\
\frac{1}{2}(\tilde{\boldsymbol{c}}_h^{n+\alpha_f^{\mathrm{f}}} \cdot \nabla \tilde{\boldsymbol{v}}_h^{n+\alpha_f^{\mathrm{f}}} - \hat{\mathbf{c}}_h^n, \boldsymbol{h} \cdot \nabla \boldsymbol{w}_h) = (\boldsymbol{b}_h^{n+1}, \boldsymbol{w}_h) \\
-\frac{\Delta t\, \gamma^{\mathrm{f}}}{\alpha_m^{\mathrm{f}}}(\nabla(p_h^{n+1} - p_h^n), \nabla q_h) - \boldsymbol{\tau}(\nabla p_h^{n+1} - \boldsymbol{\pi}_h^n, \nabla q_h) = b(q_h, \tilde{\boldsymbol{v}}_h^{n+1}) \\
\frac{\alpha_m^{\mathrm{f}}}{\Delta t\, \gamma^{\mathrm{f}}}(\boldsymbol{v}_h^{n+1} - \tilde{\boldsymbol{v}}_h^{n+1}, \boldsymbol{w}_h) - b(p_h^{n+1} - p_h^n, \boldsymbol{w}_h) = \boldsymbol{0} \\
(\hat{\mathbf{c}}_h^{n+1}, \boldsymbol{\zeta}_h) - (\tilde{\boldsymbol{c}}_h^{n+\alpha_f^{\mathrm{f}}} \cdot \nabla \tilde{\boldsymbol{v}}_h^{n+\alpha_f^{\mathrm{f}}}, \boldsymbol{\zeta}_h) = \boldsymbol{0} \\
(\boldsymbol{\pi}_h^{n+1}, \boldsymbol{\eta}_h) - (\nabla p_h^{n+1}, \boldsymbol{\eta}_h) = \boldsymbol{0}
\end{aligned}
\tag{5.2.13}
$$

From the OSS and FIC stabilizations described in ALE coordinates, it can be shown that when the mesh velocity $\mathbf{v}_{\mathrm{mesh}} = 0$, the convective velocity $\mathbf{c} = \mathbf{v}$ and the Eulerian methods described in chapter **4** are recovered.

5.3 Governing Equations

The governing equations for the couple incompressible fluid-structure problem consist of the momentum equations together with the continuity equation. However the fluid and the structural parts of the domain must be treated differently. Then the problem is split into the fluid test functions over the fluid domain and the solid test function operating over the structural part.

For convenience, the boundary of the coupled problem is divided into the Dirichlet boundary for the fluid Γ_{f}^D and the solid Γ_{s}^D, the Neumann boundary for the fluid Γ_{f}^N and the solid Γ_{s}^N, and a common interface boundary Γ^I between the fluid and the solid. Then the boundary of the couple problem is $\Gamma = \Gamma^D \cup \Gamma^N \cup \Gamma^I$, where $\Gamma^D = \Gamma_{\mathrm{f}}^D \cup \Gamma_{\mathrm{s}}^D$ and $\Gamma^N = \Gamma_{\mathrm{f}}^N \cup \Gamma_{\mathrm{s}}^N$.

Also the coupled problem domain is divided into a solid part Ω^{s} and a fluid part Ω^{f}, where $\Omega = \Omega^{\mathrm{s}} \cup \Omega^{\mathrm{f}}$. In particular, the solid motion $\mathbf{x}^{\mathrm{s}}$ sets the solid displacements $\mathbf{u}^{\mathrm{s}}$ yielding

$$\mathbf{u}^{\mathrm{s}}(\mathbf{X}, t) = \mathbf{x}^{\mathrm{s}} - \mathbf{X} \tag{5.3.1}$$

where $\mathbf{X} \in \Omega_0^{\mathrm{s}}$. The fluid mesh motion $\mathbf{x}^{\mathrm{f}}$ is defined as a function of the solid interface displacements $\mathbf{x}^{\mathrm{s}} \in \Gamma^I$ as an extension over the fluid domain Ω^{f}, where the fluid (mesh) displacements are given by

$$\hat{\mathbf{u}} = \mathbf{u}^{\mathrm{f}} = \mathrm{Ext}(\mathbf{u}^{\mathrm{s}}_{\Gamma^I}) \tag{5.3.2}$$

where different forms to make this extension are presented ahead in section **5.5**. Since our fluid domain is moving, the ALE formulation is needed. The corresponding mesh velocity is found substituting Eq. (5.3.2) into Eq. (5.2.7) yielding $\mathbf{v}_{\mathrm{mesh}} = \hat{\mathbf{v}}(\mathbf{u}^{\mathrm{f}})$.

Before writing the continuous formulation of the couple fluid-structure interaction problem, the subspace test functions for the fluid, with a homogeneous Dirichlet boundary condition, are defined by

$$\delta w_i \in \mathcal{W}_0, \quad \mathcal{W}_0 = \left\{ \delta w_i \in H^1(\Omega^{\mathrm{f}}),\ \ \delta w_i = 0 \ \text{ on } \ \Gamma^D_{\mathrm{f}} \cup \Gamma^I,\ \ \delta w_i = 0 \ \text{ on } \ \Omega^{\mathrm{s}} \right\} \tag{5.3.3}$$

and the subspace test functions for the structure are expressed as

$$\delta w_i \in \mathcal{W}_0, \quad \mathcal{W}_0 = \left\{ \delta w_i \in H^1(\Omega^{\mathrm{s}}),\ \ \delta w_i = 0 \ \text{ on } \ \Gamma^D_{\mathrm{s}},\ \ \delta w_i = \mathrm{Ext}(\delta w_{i|\Gamma^I}) \ \text{ on } \ \Omega^{\mathrm{f}} \right\} \tag{5.3.4}$$

Note that the test functions for the fluid vanish at the interface and inside the solid subdomain, while the solid test functions are nonzero on the interface and extend inside the fluid subdomain. In this way, the *kinematic* continuity for the displacement and velocity field is imposed as Dirichlet boundary conditions on the fluid by the interface, and *kinetic* continuity for the traction is given as Neumann boundary conditions on the structure at the interface.

Since the continuity equation is the same that for CFD problems, then the fluid problem is obtained by substituting into the momentum equation the corresponding test functions, which vanish in the solid part, yielding after integrating by parts

$$\int_{\Omega^{\mathrm{f}}} \delta w_i \left(\rho \frac{\partial v_i}{\partial t} + \rho c_j \frac{\partial v_i}{\partial x_j} \right) d\Omega + \int_{\Omega^{\mathrm{f}}} \sigma_{ij} \frac{\partial \delta w_i}{\partial x_i} d\Omega = \int_{\Omega^{\mathrm{f}}} \delta w_i \rho b_i d\Omega \tag{5.3.5}$$

This equation must be complemented by adequate boundary conditions dictated by the fluid space test functions. Since fluid the test functions vanish at the interface, then the displacement and velocity field can only be governed by imposing the kinematic compatibility given by the Dirichlet condition

$$\mathbf{u}^{\mathrm{f}}_{\Gamma^I} = \mathbf{u}^{\mathrm{s}}_{\Gamma^I} \tag{5.3.6}$$

$$\mathbf{v}^{\mathrm{f}}_{\Gamma^I} = \mathbf{v}^{\mathrm{s}}_{\Gamma^I} \tag{5.3.7}$$

Similarly, the structural problem is obtained by considering the space of the solid test functions on the momentum equations, yielding

$$\int_{\Omega^{\mathrm{s}}_0} \delta w_i \rho_0 \ddot{u}_i d\Omega_0 + \int_{\Omega^{\mathrm{s}}_0} \delta E_{ij} S_{ij} d\Omega_0 = \int_{\Omega^{\mathrm{s}}_0} \delta w_i \rho_0 b_i d\Omega_0 + \int_{\Gamma^N_{0;\mathrm{s}}} \delta w_i \bar{t}^0_i d\Gamma_0 + \mathbf{L}(\delta w_{i|\Gamma^I}) \tag{5.3.8}$$

where $\mathbf{L}$ is the interface load corresponding to the part of the momentum equation which is integrated on the fluid domain, and is given by the choice of the solid test functions in Eq. (5.3.4). Then $\mathbf{L}$ can be written as

$$\begin{aligned}\mathbf{L}(\delta w_{i|\Gamma^I}) = &\int_{\Omega^{\mathrm{f}}} \mathrm{Ext}(\delta w_{i|\Gamma^I}) \rho b_i d\Omega - \int_{\Omega^{\mathrm{f}}} \mathrm{Ext}(\delta w_{i|\Gamma^I}) \left(\rho \frac{\partial v_i}{\partial t} + \rho c_j \frac{\partial v_i}{\partial x_j} \right) d\Omega \\ &- \int_{\Omega^{\mathrm{f}}} \sigma_{ij} \frac{\partial \mathrm{Ext}(\delta w_{i|\Gamma^I})}{\partial x_i} d\Omega\end{aligned} \tag{5.3.9}$$

which is the residual of the fluid equations evaluated with the extension of the interface test functions $\mathrm{Ext}(\delta w_{i|\Gamma^I})$, as given in Tallec and Mouro (2001). Remembering that the fluid is considered with a homogeneous Dirichlet boundary condition, the last term in Eq. (5.3.9) is integrated by parts yielding

$$\int_{\Omega^{\mathrm{f}}} \sigma_{ij} \frac{\partial \mathrm{Ext}(\delta w_{i|\Gamma^I})}{\partial x_i} d\Omega = \int_{\Gamma^I} \delta w_i n^{\mathrm{f}}_j \sigma_{ij} d\Gamma - \int_{\Omega^{\mathrm{f}}} \mathrm{Ext}(\delta w_{i|\Gamma^I}) \frac{\partial \sigma_{ij}}{\partial x_j} d\Omega \tag{5.3.10}$$

Substituting Eq. (5.3.10) into Eq. (5.3.9) leads to

$$\begin{aligned}\mathbf{L}(\delta w_{i|\Gamma^I}) = &\int_{\Omega^{\mathrm{f}}} \mathrm{Ext}(\delta w_{i|\Gamma^I}) \rho b_i d\Omega - \int_{\Omega^{\mathrm{f}}} \mathrm{Ext}(\delta w_{i|\Gamma^I}) \left(\rho \frac{\partial v_i}{\partial t} + \rho c_j \frac{\partial v_i}{\partial x_j} \right) d\Omega \\ &+ \int_{\Omega^{\mathrm{f}}} \mathrm{Ext}(\delta w_{i|\Gamma^I}) \frac{\partial \sigma_{ij}}{\partial x_j} d\Omega - \int_{\Gamma^I} \delta w_i n^{\mathrm{f}}_j \sigma_{ij} d\Gamma\end{aligned} \tag{5.3.11}$$

Since the first three terms in the above equation are the solution of the fluid part, Eq. (5.3.11) is finally expressed as

$$\mathbf{L}(\delta w_{i|\Gamma^I}) = -\int_{\Gamma^I} \delta w_i n^{\mathrm{f}}_j \sigma^{\mathrm{f}}_{ij} d\Gamma = \int_{\Gamma^I} \delta w_i n^{\mathrm{s}}_j \sigma^{\mathrm{f}}_{ij} d\Gamma \tag{5.3.12}$$

which shows the interface traction obtained directly from the momentum conservation equation and not considered as an additional independent equation.

The continuity equation for the fluid part remains the same that for the CFD problem, which is given by Eq. (4.2.10). The stabilization terms involve are expressed by Eq. (5.2.12) or Eq. (5.2.13).

The fluid solver **F** for the couple problem is given by the following weak formulation

$$\begin{aligned}
&\int_{\Omega^{\mathrm{f}}} \delta w_i \left(\rho \frac{\partial v_i}{\partial t} + \rho c_j \frac{\partial v_i}{\partial x_j} \right) d\Omega - \int_{\Omega^{\mathrm{f}}} p \frac{\partial \delta w_i}{\partial x_i} d\Omega + \int_{\Omega^{\mathrm{f}}} \mu \frac{\partial v_i}{\partial x_j} \frac{\partial \delta w_i}{\partial x_j} d\Omega \\
&\quad - \int_{\Omega^{\mathrm{f}}} \delta w_i \rho b_i d\Omega - \int_{\Omega^{\mathrm{f}}} \delta p \frac{\partial v_j}{\partial x_j} d\Omega + \int_{\Omega^{\mathrm{f}}} \delta w_i^m \left(\mathbf{u}^{\mathrm{f}} - \mathrm{Ext}(\mathbf{u}^{\mathrm{s}}_{\Gamma^I}) \right) d\Omega \\
&\quad + \int_{\Gamma^I} \delta w_i^u \left(\mathbf{u}^{\mathrm{f}} - \mathbf{u}^{\mathrm{s}} \right) d\Gamma + \int_{\Gamma^I} \delta w_i^v \left(\mathbf{v}^{\mathrm{f}} - \mathbf{v}^{\mathrm{s}} \right) d\Gamma + \mathsf{Stabilization} = 0
\end{aligned} \tag{5.3.13}$$

where the ALE framework for the momentum equation, with its corresponding stabilization technique, has been considered together with the incompressibility constraint. Besides the mesh movement in the fluid subdomain and the kinematic compatibility at the interface are included in the formulation.

The corresponding solid solver **S** for the couple problem is given by the weak formulation shown next

$$\begin{aligned}
&\int_{\Omega^{\mathrm{s}}_0} \delta w_i \rho_0 \ddot{u}_i d\Omega_0 + \int_{\Omega^{\mathrm{s}}_0} \delta E_{ij} S_{ij} d\Omega_0 - \int_{\Omega^{\mathrm{s}}_0} \delta w_i \rho_0 b_i d\Omega_0 \\
&\quad - \int_{\Gamma^N_{\mathrm{s}}} \delta w_i \bar{t}_i d\Gamma - \int_{\Gamma^I} \delta w_i n^{\mathrm{s}}_j \sigma^{\mathrm{f}}_{ij} d\Gamma = 0
\end{aligned} \tag{5.3.14}$$

where the momentum equation is complemented with the traction fluid forces of the couple problem at the interface.

5.4 Partitioned Methods

With the developed equations for the fluid solver **F** and the solid solver **S** given in the last section, the problem consist in finding the appropriate partitioned method to solve the fluid-structure interaction problem.

Numerical simulation of FSI problems is not only difficult because of the problems associated with the fluid or structure solution, but also because of the coupling interface between these two fields which sometimes represents another challenge. These difficulties depend strongly on the *added mass* effect introduced by the fluid over the structure, as given in Causin et al. (2005). When the structure density ρ^{s} is much larger than the fluid density ρ^{f}, the added mass effect of the fluid is not significant and the problem can be solved with staggered partitioned schemes or strong coupling partitioned techniques as in the case of *aeroelasticity*. However when the structure and fluid densities are of the same order, as in the case of *hemodynamics*, the added mass effect of the fluid over the structure is very important and the coupling algorithm to be used must be a strong coupling partitioned scheme with relaxation, or even better techniques as the exact Newton or inexact Newton method for strong coupling problems, or the recently partitioned procedures based on Robin transmissions conditions given by Badia et al. (2007).

To explain these methods, assume that the fluid unknowns are grouped together in the vector $\mathbf{x}$ and that the nonlinear iterative fluid solver is written as

$$\mathbf{x}^i = \mathbf{F}(\mathbf{x}^{i-1}, \mathbf{y}) \tag{5.4.1}$$

where $\mathbf{y}$ represent the displacements of the structure, which also define the current configuration of the interface. The nonlinear iterative solid solver is given by

$$\mathbf{y}^i = \mathbf{S}(\mathbf{y}^{i-1}, \mathbf{x}) \tag{5.4.2}$$

where $\mathbf{x}$ defines the nodal fluid velocities and pressure including the traction fluid forces at the interface for the structure. With these equations, the following strong coupling schemes are described within a time step.

5.4.1 Block Jacobi Method

The easiest method to perform an iterative strong coupling scheme between different field solvers is the *Block Jacobi* method. This method consist in iterating the fluid and solid solvers independently as shown next

$$\mathbf{x}^i = \mathbf{F}^p(\mathbf{x}^{i-1}, \mathbf{y}^{i-1}) \tag{5.4.3}$$

$$\mathbf{y}^i = \mathbf{S}^q(\mathbf{y}^{i-1}, \mathbf{x}^{i-1}) \tag{5.4.4}$$

where p and q are the number of times that the solvers $\mathbf{F}$ and $\mathbf{S}$ are repeated respectively. Also for $i = 1$, $\mathbf{x}^0_{n+1} = \mathbf{x}_n$ and $\mathbf{y}^0_{n+1} = \mathbf{y}_n$. Once the tolerance or maximum number of iterations is reached, the time step is advanced and the process is repeated.

5.4.2 Block Gauss-Seidel Method

With a simple modification to Eqs. (5.4.3)-(5.4.4), the *Block Gauss-Seidel* method is obtained. As before, this method consist in iterating the fluid and solid solvers independently yielding

$$\mathbf{x}^i = \mathbf{F}^p(\mathbf{x}^{i-1}, \mathbf{y}^i) \tag{5.4.5}$$

$$\mathbf{y}^i = \mathbf{S}^q(\mathbf{y}^{i-1}, \mathbf{x}^i) \tag{5.4.6}$$

where in Eq. (5.4.5) a predicted value for $\mathbf{y}^1$ is needed when $i = 1$, as explained in step 1) of section **5.1** for the staggered partition. When the tolerance or maximum number of iterations is reached, the time step is advanced and the process is repeated.

This method is the most common to find in fluid-structure interaction problems with strong coupling schemes, because existing and sophisticated solvers for each field can be used with minor modifications.

Even though the iterations within each time step lead to the monolithic solution, sometimes relaxation techniques are combined with this method when important values for the added mass effect are presented to ensure a convergence of the problem, or simply to accelerate the convergence of the coupling scheme when the added mass effect is negligible. Such technique is described in the works of Mok (2001), Mok and Wall (2001), Tallec and Mouro (2001), Wüchner and Bletzinger (2005), Causin et al. (2005), Wüchner (2006), and Wall et al. (2007). The relaxation technique used in this work is detailed in section **5.6**.

5.4.3 Inexact Block Newton Method

The *inexact Block Newton* method, or *quasi-Newton* method, is derived from the monolithic Newton-Raphson procedure, which for a two-field couple problem can be written as

$$\begin{bmatrix} \partial_{\mathbf{x}}\mathbf{F} - \mathbf{I} & \partial_{\mathbf{y}}\mathbf{F} \\ \partial_{\mathbf{x}}\mathbf{S} & \partial_{\mathbf{y}}\mathbf{S} - \mathbf{I} \end{bmatrix}_{\mathbf{x}^{i-1},\mathbf{y}^{i-1}} \begin{bmatrix} \mathbf{x}^i - \mathbf{x}^{i-1} \\ \mathbf{y}^i - \mathbf{y}^{i-1} \end{bmatrix} = \begin{bmatrix} \mathbf{x} - \mathbf{F} \\ \mathbf{y} - \mathbf{S} \end{bmatrix}_{\mathbf{x}^{i-1},\mathbf{y}^{i-1}} \tag{5.4.7}$$

where $\partial_{\mathbf{x}}$ and $\partial_{\mathbf{y}}$ are the partial derivatives with respect $\mathbf{x}$ and $\mathbf{y}$ respectively. Since a strong coupling partitioned procedure is being developed, then Eq. (5.4.7) is split into two separate equations.

However the problem emerges when the cross Jacobians $\partial_{\mathbf{y}}\mathbf{F}$ and $\partial_{\mathbf{x}}\mathbf{S}$, which represents the sensitivity of the fluid state with respect to the structure and vice versa, need to be evaluated. This is due to the fact that existing solvers are used and we do not have direct access to the cross Jacobians of Eq. (5.4.7).

Approximation of the cross Jacobians is developed in the work of Steindorf (2002) and Matthies and Steindorf (2004) where finite differences are used with an auxiliary vector $\mathbf{z}$ and a small time step-size h yielding

$$\partial_{\mathbf{y}}\mathbf{F}(\mathbf{x},\mathbf{y})\mathbf{z} = \frac{1}{h}\Big(\mathbf{F}(\mathbf{x},\mathbf{y}+h\mathbf{z}) - \mathbf{F}(\mathbf{x},\mathbf{y})\Big) \tag{5.4.8}$$

More details can also be found in Matthies and Steindorf (2005) and Matthies and Steindorf (2006). Another method that evaluate approximately the cross Jacobians is given by Tezduyar et al. (2006), where a mixed analytical/numerical element-vector based technique is introduced.

5.4.4 Exact Block Newton Method

The *exact Block Newton* method, or simply *Newton* method, is derived from the monolithic Newton-Raphson procedure, just as the inexact block Newton method does, where the Eq. (5.4.7) is used again.

In the exact block Newton method, the cross Jacobians are derived exactly using the existing solvers with some more advanced ideas, as given in Dettmer (2004), Fernández and Moubachir (2005) and Dettmer and Peric (2006).

The exact block Newton method shows superior convergence properties that any of the above methods mentioned with just a few iterations. While sometimes the Gauss-Seidel method with relaxation or the quasi-Newton fail to converge, it is

demonstrated in Fernández and Moubachir (2005) that the Newton method does converge. However the cost of each Newton and quasi-Newton iteration is much higher that the Gauss-Seidel method. Consequently, Newton based methods do not imply an overall reduction of computational cost. Besides the computational implementation is harder than the Gauss-Seidel method. These reasons make the block Gauss-Seidel partitioned method still be an attractive method in the fluid-structure interaction community.

5.5 Mesh Movement Techniques

Since the interface of the fluid-structure interaction problem follows the solid displacements, it is necessary to use *mesh movement techniques*, also known as *mesh update equations*, to update the internal nodes of the finite element mesh inside the fluid subdomain. The mesh moving algorithm updates the nodal coordinates of the fluid mesh in response to the deforming boundaries at the interface, and maintaining freeze the rest of the boundary.

Among the wide possibilities to update meshes in this field, the most common are mentioned next. The simplest one is the Laplacian method which can be found in Belytschko et al. (2000). Other methods are based on the pseudo-structural system, which can be done through the elastic spring analogy, i.e. see Farhat (1997) and Degand and Farhat (2002), or by solving the elasticity equation as a pseudo-elastic system, i.e. see Johnson and Tezduyar (1994), Belytschko et al. (2000) and Chiandussi et al. (2000). In this way, the mesh is considered as another system. Therefore the fluid-structure interaction problem yields a couple three-field system.

The Laplacian method, used in this work, updates the position of the nodes by solving the Laplace equation, where the contours solution are approximately orthogonal. This method in strong form consists in finding the mesh displacements such that

$$\begin{aligned} \nabla^2 \hat{\mathbf{u}} &= \mathbf{0} \quad \text{in} \quad \Omega^{\mathrm{f}} \\ \hat{\mathbf{u}} &= \mathbf{u} \quad \text{on} \quad \Gamma^{I} \\ \hat{\mathbf{u}} &= \mathbf{0} \quad \text{on} \quad \Gamma^{D}_{\mathrm{f}} \end{aligned} \tag{5.5.1}$$

where ∇^2 is the Laplacian of the mesh displacements $\hat{\mathbf{u}}$, and $\mathbf{u}$ are the displacements on the interface given by the structural deformation.

This method has the advantage that it can be uncoupled for the displacements and find independently $\hat{u}_x$, $\hat{u}_y$ and $\hat{u}_z$, which represents a faster solution of the mesh displacements. Since it is desirable to retain the original shape of the elements in the refined areas, this method can be improved by assigning different element *stiffness* to small and large elements by simply dividing (instead of multiplying) the Jacobian determinant during element integration.

On the other hand, in the pseudo-elastic structural technique, the mesh is assumed to be an elastic body, and a standard linear problem is solved. This method in strong form consists in finding the mesh displacements such that

$$\begin{aligned} \mathbf{K}\hat{\mathbf{u}} &= \mathbf{0} \quad \text{in} \quad \Omega^{\mathrm{f}} \\ \hat{\mathbf{u}} &= \mathbf{u} \quad \text{on} \quad \Gamma^{I} \\ \hat{\mathbf{u}} &= \mathbf{0} \quad \text{on} \quad \Gamma^{D}_{\mathrm{f}} \end{aligned} \tag{5.5.2}$$

where $\mathbf{K}$ is the stiffness matrix for the elastostatic system, $\hat{\mathbf{u}}$ are the unknown mesh displacements, and $\mathbf{u}$ are the displacements on the interface given by the structural problem. For small displacements on the interface, the linear elastic system is sufficient, however in the presence of large deformations at the interface, a nonlinear model for the mesh may be more accurate. For example, Dettmer and Peric (2006) use a nonlinear hyperelastic Neo-Hookean model, which after a few iterations yield a mesh with a uniform element distortion.

In this work the pseudo-structural system of Chiandussi et al. (2000) is used, which is simple to implement and instead of solving an iterative nonlinear structural problem, a linear-elastic problem is solved twice. Of course this method is more expensive than the Laplacian method, but for large displacements of the interface this method yields a better mesh distributions of the internal fluid nodes. The method is described next.

First, assign an isotropic homogeneous material with constant Young properties, i.e. $E = 1$ and $\upsilon = 0$, to each element. Then solved the pseudo-structural problem with the appropriate boundary conditions at the interface.

After the solution of the first analysis pseudo-structural problem is found, the strain field is computed together with its principal strains ε_i. Then the new Young modulus for each element is found with

$$E = \frac{1}{\bar{\varepsilon}^{\,2}\ n_{\mathrm{dime}}} \sum_{i=1}^{n_{\mathrm{dime}}} \varepsilon_i^2 \tag{5.5.3}$$

where $\bar{\varepsilon}$ is the uniform strain. Now the second pseudo-structural problem is solved with the appropriate boundary conditions at the interface. In this second analysis, a uniform mesh distortion is obtained. Further details on this method including other alternatives for evaluating the Young modulus and measurements of the mesh quality using a mesh quality indicator are given in Chiandussi et al. (2000). Since this method is more expensive than the Laplacian method, applying only a few iterations when using iterative solvers, instead of iterating until convergence, gives a good alternative to move nodes inside the fluid subdomain.

5.6 Strong Coupling with Relaxation

In this work, the strong coupling block Gauss-Seidel partitioned method with relaxation has been implemented. The structural solver S given by Eq. (5.3.14) is now referred to as the computational solid dynamic (CSD) solver. The fluid solver F given by Eq. (5.3.13) solves the fluid equations plus the movement of the mesh, yielding in a high-cost task from the computational point of view. Therefore the

fluid solver **F** is split into the computational mesh dynamic (CMD) solver that moves the interior nodes of the finite element mesh of the fluid subdomain with the methods given in section **5.5**, and the computational fluid dynamic (CFD) solver that uses the fractional step method described in chapter **4** and the ALE technique incorporated in the momentum equation as given in section **5.2**. All solvers of each field use an implicit scheme.

There are several methods in the literature to accelerate the solution of the problem by means of relaxation, i.e. Mok (2001). In this work the Aitken method is implemented, i.e. Irons and Tuck (1969), which yields excellent solutions with simple modifications to the code.

In order to compute the coupled fluid-structure interaction problem, a unified algorithmic framework for the whole procedure is presented next. Considering known all values of solid, fluid and mesh at time step t_n, the new step t_{n+1} is found following the simple steps given ahead:

1. Advance time step: $t_{n+1} = t_n + \Delta t$
2. Set iteration $i = 1$
3. Compute interface predictor displacement with one of the following methods
   (a) Structural predictor: Solve the CSD problem to find $\hat{\mathbf{u}}^{n+1}_{|\Gamma^I,i}$ at the interface from $\mathbf{u}^{n+1}_{|\Omega^s,i}$ with a predicted external force given by:
      i. Pressure:
         · Order 1: $\mathbf{p}_{n+1} = \mathbf{p}_n$
         · Order 2: $\mathbf{p}_{n+1} = 2\mathbf{p}_n - \mathbf{p}_{n-1}$, (for $n \geq 2$)
      ii. Force $\mathbf{t}^f = \mathbf{n}^s \boldsymbol{\sigma}^f_{|\Gamma^I}$: (where $\boldsymbol{\sigma}^f_{|\Gamma^I,0} = 0$)
         · Order 1: $\mathbf{t}^f_{n+1} = \mathbf{t}^f_n$
         · Order 2: $\mathbf{t}^f_{n+1} = 2\mathbf{t}^f_n - \mathbf{t}^f_{n-1}$, (for $n \geq 2$)
   (b) Interface displacement predictor: Set $\mathbf{u}^1_{|\Gamma^I,1} = 0$ and find directly $\hat{\mathbf{u}}^{n+1}_{|\Gamma^I,i}$ at the interface with a prediction of the form
      i. Order 0: $\hat{\mathbf{u}}^{n+1}_{|\Gamma^I,i} = \hat{\mathbf{u}}^n_{|\Gamma^I}$
      ii. Order 1: $\hat{\mathbf{u}}^{n+1}_{|\Gamma^I,i} = \hat{\mathbf{u}}^n_{|\Gamma^I} + \Delta t\, \hat{\mathbf{v}}^n_{|\Gamma^I}$
      iii. Order 2: $\hat{\mathbf{u}}^{n+1}_{|\Gamma^I,i} = \hat{\mathbf{u}}^n_{|\Gamma^I} + \Delta t \left(\frac{3}{2}\hat{\mathbf{v}}^n_{|\Gamma^I} - \frac{1}{2}\hat{\mathbf{v}}^{n-1}_{|\Gamma^I} \right)$, (for $n \geq 2$)
4. Iterate the coupled FSI problem
   (a) CMD solver: Move Mesh with Eq. (5.5.1) or Eq. (5.5.2)
      i. Transfer $\hat{\mathbf{u}}^{n+1}_{|\Gamma^I,i}$ to the mesh solver
      ii. Solve the CMD problem and find $\hat{\mathbf{u}}^{n+1}_i = \hat{\mathbf{u}}^{n+1}_{|\Omega^f,i}$
      iii. Compute mesh velocities $\hat{\mathbf{v}}^{n+1}_i$
   (b) CFD solver: Solve fluid with Eq. (5.2.12) or Eq. (5.2.13)
      i. Transfer $\hat{\mathbf{v}}^{n+1}_i$ to the fluid solver
      ii. Solve the CFD problem and find $\mathbf{v}^{n+1}_i$, $\mathbf{p}^{n+1}_i$
      iii. Compute fluid stress tensor at interface $\boldsymbol{\sigma}^f_{|\Gamma^I}$

(c) CSD solver: Solve structure with Eq. (5.3.14)
   i. Transfer $\boldsymbol{\sigma}^{\mathrm{f}}_{|\Gamma^I}$ to the solid solver and compute structure forces $\mathbf{t}^{\mathrm{f}}$
   ii. Solve the CSD problem and find $\mathbf{u}^{n+1}_{i+1}$

(d) Relaxation phase
   i. Compute optimal relaxation parameter $\bar{w}_i$ via Aitken method
   ii. Relaxation of predicted interface position with
   $\hat{\mathbf{u}}^{n+1}_{|\Gamma^I,i+1} = (1-\bar{w}_i)\hat{\mathbf{u}}^{n+1}_{|\Gamma^I,i} + \bar{w}_i \mathbf{u}^{n+1}_{|\Gamma^I,i+1}$

(e) Advance iteration: $i = i+1$

(f) Check convergence. If reached, go to 5, else go to 4

5. Check time step. If end of time not reached, go to 1, else end of calculation

The Aitken method of relaxation is based on Aitken's acceleration method for vectors. The method can be easily implemented in any code which then ensures converge of the coupled problem for adequate time step parameters. The Aitken relaxation parameter is computed with the following algorithm, as given in Wall et al. (2007).

1. For the first time step and $i = 1$, $\bar{\mu}^{n+1}_1 = 0$ and $\bar{w}_1 = 1$
2. For $i = 1$, $\bar{\mu}^{n+1}_0 = \bar{\mu}^{n}_{i_{max}}$ and $\hat{\mathbf{u}}^{n+1}_{|\Gamma^I,0} = \hat{\mathbf{u}}^{n}_{|\Gamma^I,i_{max}}$
3. Compute Aitken optimal relaxation parameter $\bar{w}_i$

(a) Compute the difference between previous and actual interface solution
$\Delta\hat{\mathbf{u}}^{n+1}_{i} = \hat{\mathbf{u}}^{n+1}_{|\Gamma^I,i-1} - \mathbf{u}^{n+1}_{|\Gamma^I,i}$
$\Delta\hat{\mathbf{u}}^{n+1}_{i+1} = \hat{\mathbf{u}}^{n+1}_{|\Gamma^I,i} - \mathbf{u}^{n+1}_{|\Gamma^I,i+1}$

(b) Compute Aitken factor
$\bar{\mu}^{n+1}_i = \bar{\mu}^{n+1}_{i-1} + (\bar{\mu}^{n+1}_{i-1} - 1)\frac{\left(\Delta\hat{\mathbf{u}}^{n+1}_{i} - \Delta\hat{\mathbf{u}}^{n+1}_{i+1}\right)\cdot\Delta\hat{\mathbf{u}}^{n+1}_{i+1}}{\left(\Delta\hat{\mathbf{u}}^{n+1}_{i} - \Delta\hat{\mathbf{u}}^{n+1}_{i+1}\right)^2}$

(c) Compute Aitken optimal relaxation parameter
$\bar{w}_i = 1 - \bar{\mu}^{n+1}_i$

More sophisticated and computationally expensive methods, such as the gradient method, lead to solutions as good as the Aitken method for fluid-structure interaction problems. Additional computational cost for this technique is insignificant since only vector operations over the interface nodes are performed.

5.7 Code Development

In this work the fluid-structure interaction problem has been implemented in the finite element program COMET (2007) following the algorithm given in section 5.6. The dynamic analysis with the θ-family method, backward differencing method and Generalized-α method for fluids have also been added to the code. This software is developed at the International Center for Numerical Methods in Engineering (CIMNE) and is used for coupled contact, mechanical and thermal analysis using the finite element method.

5.8 Example Problems

5.8.1 Nonlinear Shell Vibration Excited by Fluid Vortex

This model problem was originally proposed by Wall and Ramm (1998) to demonstrate the ability of their FSI formulation to deal with complex flow-flexible structure interactions exhibiting large deformations. Later Steindorf (2002) and recently Dettmer (2004) test their numerical simulations with this problem. Also, with a modification at the inflow velocity, Hübner et al. (2004) have used this problem to test their FSI monolithic code.

The problem consists of a thin elastic nonlinear shell attached to a fixed square rigid body, which are submerged in an incompressible fluid flow. Vortices separating from the corners of the rigid body generate oscillating forces on the shell. Geometry and boundary conditions are given in Fig. 5.1.

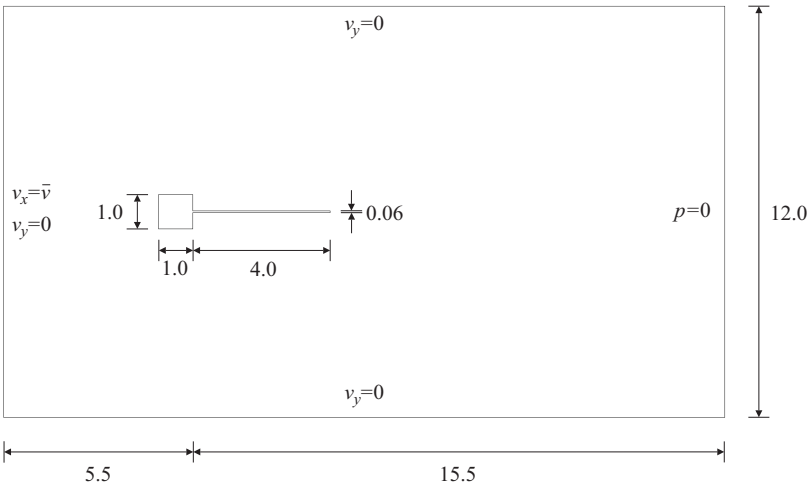

Figure 5.1 *Geometry and boundary conditions [cm]*

5.8.1.1 Hübner's problem

The easiest couple problem involving fluid and structural large deformations was proposed by Hübner et al. (2004), where the material properties are given for the structure with a density $\rho^{\mathrm{s}} = 2.0\ g/cm^3$, Young's modulus $E = 2.0 \times 10^6\ g/(cm\ s^2)$ and Poisson's ratio $\upsilon = 0.35$. The fluid material properties are density $\rho^{\mathrm{f}} = 1.18 \times 10^{-3}\ g/cm^3$ and viscosity $\mu = 1.82 \times 10^{-4}\ g/(cm\ s)$. The inflow velocity is taken as $\bar{v} = 31.5\ cm/s$, leading to a Reynolds number $\mathrm{Re} = 204$ if the length of the square rigid body is taken as the characteristic length.

The finite element mesh used for this problem is shown in Fig. 5.2 and consists of 14218 three-node triangular elements and 7278 nodes for the fluid part, and 20 nine-node quadrilateral elements in one layer over the thickness with 123 nodes for

the structural part using plane stress conditions. The fluid part uses the second order backward differencing BDF2 time integration scheme, while the generalized-α time integration method with $\rho^{\mathrm{s}}_{\infty} = 0.8$ is used for the structural part. The time interval studied is of 25 s using a time step size $\Delta t = 0.005$. Since the density $\rho^{\mathrm{s}} >> \rho^{\mathrm{f}}$, a staggered coupling technique is used together with a structural predictor of 1^{st} order.

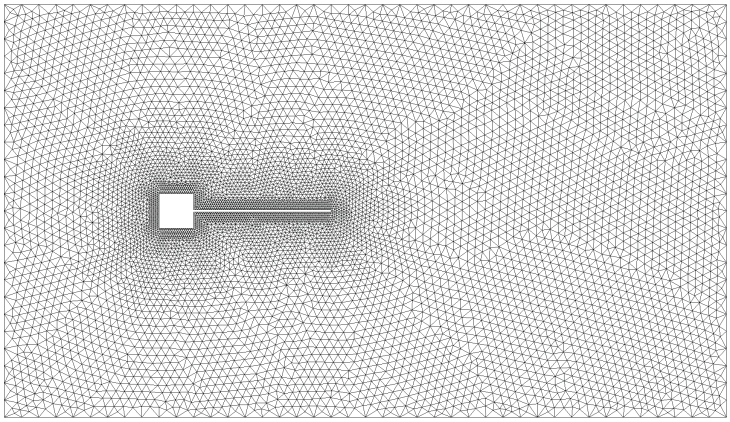

Figure 5.2 *Reference finite element mesh*

For this example, the FIC stabilization technique has been employed. Mesh movement is obtained by employing the pseudo-elastic structural technique presented in section **5.5**. Initially the fluid and the structure are at rest, and at $t = 0$ the inflow velocity is applied instantaneously. Fig. 5.3 shows the maximum vertical tip displacement of the structure, that oscillates mainly in the second mode and it is compared with the work of Hübner et al. (2004).

The first two natural frequencies of the structural part in its initial configuration become $freq^{\mathrm{s}}_1 = 0.607\ Hz$ and $freq^{\mathrm{s}}_2 = 4.087\ Hz$. The dominant frequency of the fluid field yields $freq^{\mathrm{f}} = 3.71\ Hz$.

A Fourier analysis of the coupled problem for lift forces f_L is performed in order to find the dominant frequency of the solution. Fig. 5.4 shows the Fourier spectrum obtained, leading to a frequency for the couple problem $freq^{\mathrm{c}} = 3.22\ Hz$. This value is in good agreement with the result reported by Hübner et al. (2004) with a frequency of the couple problem of 3.10 Hz. It can be seen that even the dominant frequency of the fluid field and the second natural frequency of the structural part are similar, the coupled problem dominant frequency is lower that both of them. This may be though as a consequence of the influence of the first frequency of the structure over the couple problem.

A close-up of the fluid mesh around the shell is given in Fig. 5.5 for a time instant when the structure has a maximum tip displacement. There can also be observed that the structure displacements oscillates in its second mode of vibration. Figs. 5.6-5.7 show different time instants of the pressure field and its corresponding structural displacements.

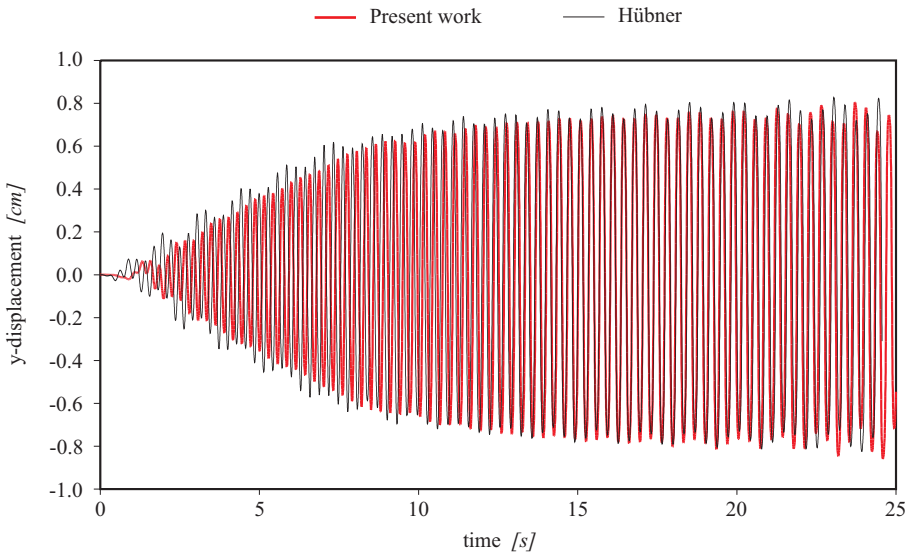

Figure 5.3 *History of maximum vertical tip displacement*

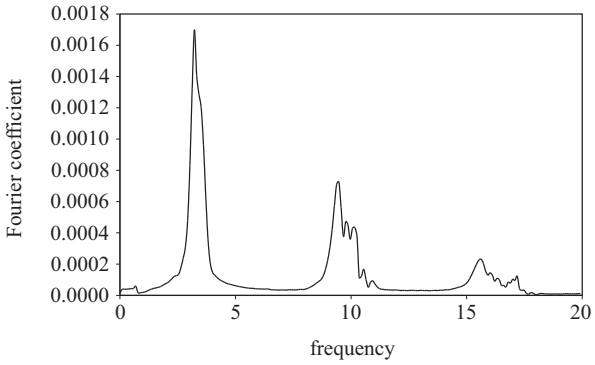

Figure 5.4 *Fourier spectrum of the lift forces*

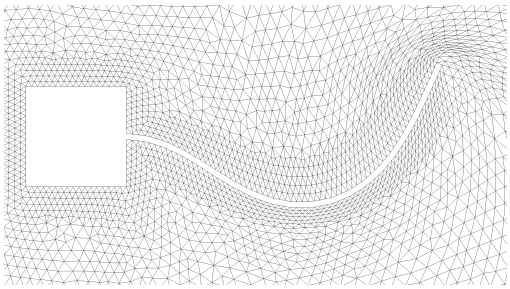

Figure 5.5 *Detail of the fluid mesh around the shell*

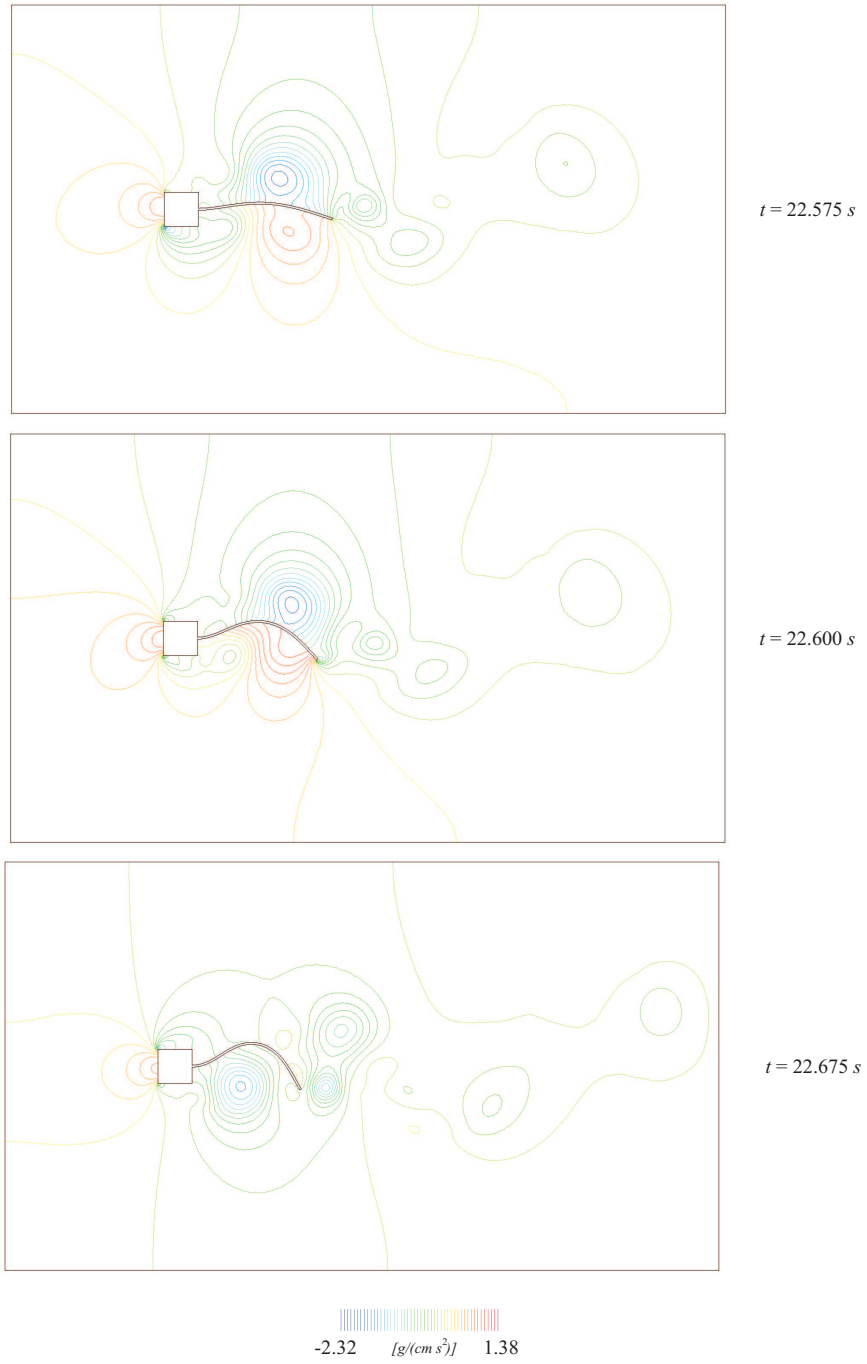

Figure 5.6 *Pressure fields for different time steps*

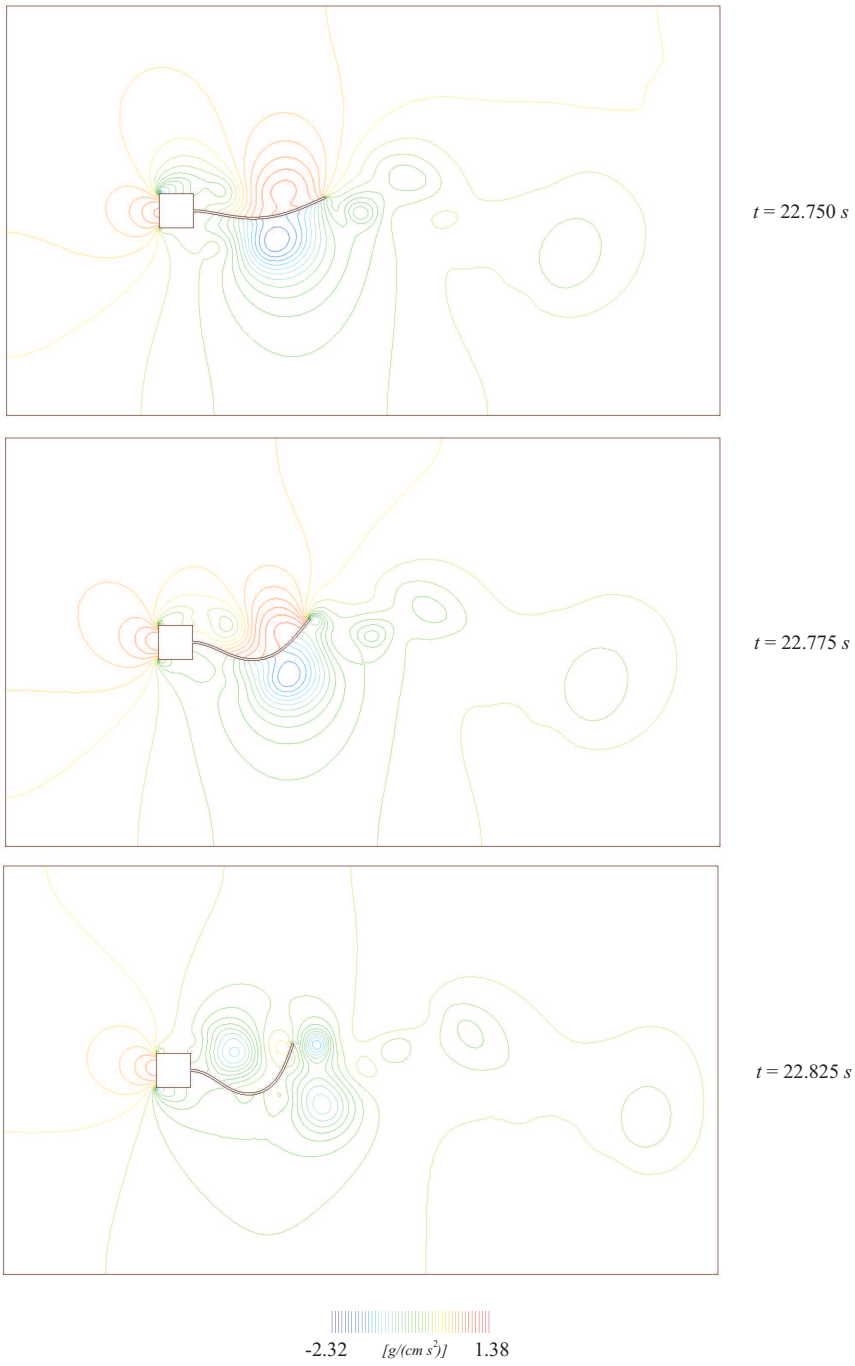

Figure 5.7 *Pressure fields for different time steps (cont.)*

5.8.1.2 Wall's problem

Hübner's problem is solved again, but with the material properties and boundary conditions proposed by Wall and Ramm (1998). This problem is more complicated to solve that the one proposed by Hübner et al. (2004). The material properties are given for the structure with a density $\rho^{\mathrm{s}} = 0.1\ g/cm^3$, Young's modulus $E = 2.5 \times 10^6\ g/(cm\ s^2)$ and Poisson's ratio $\upsilon = 0.35$. The fluid material properties are density $\rho^{\mathrm{f}} = 1.18 \times 10^{-3}\ g/cm^3$ and viscosity $\mu = 1.82 \times 10^{-4}\ g/(cm\ s)$. The inflow velocity is taken as $\bar{v} = 51.3\ cm/s$, leading to a Reynolds number Re = 333 if the length of the square rigid body is taken as the characteristic length.

The finite element mesh used for the coupled problem is the same that the one used for the former problem and it is shown in Fig. 5.2. The fluid part uses the generalized-α time integration scheme with $\rho^{\mathrm{f}}_{\infty} = 0.8$ while the generalized-α time integration method with $\rho^{\mathrm{s}}_{\infty} = 0.5$ is used for the structural part. The time interval studied is of 10 s using a time step size $\Delta t = 0.005$. In this example, the OSS stabilization technique has been employed. After 100 initial steps for the fluid with the inflow velocity applied instantaneously, the coupling between the fluid and the structure is performed. For this problem, a strongly coupling procedure is used with a structural predictor of 1$^{\mathrm{st}}$ order and without relaxation. Fig. 5.8 shows the maximum vertical tip displacement of the structure, that oscillates mainly in the first mode and it is compared with the work of Steindorf (2002).

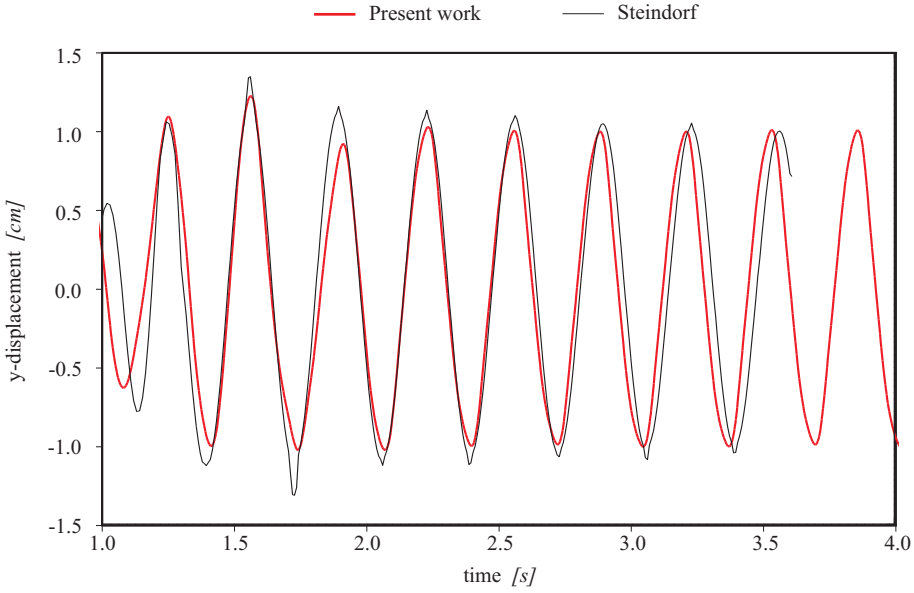

Figure 5.8 *History of maximum vertical tip displacement*

The first two natural frequencies of the structural part in its initial configuration become $freq^{\mathrm{s}}_1 = 3.033\ Hz$ and $freq^{\mathrm{s}}_2 = 19.023\ Hz$. The dominant frequency of the fluid field yields $freq^{\mathrm{f}} = 5.761\ Hz$. A Fourier analysis of the coupled problem for

lift forces f_L is performed in order to find the dominant frequency of the solution yielding a frequency for the couple problem $freq^c = 3.125\ Hz$. In this case, there are no similarities between the dominant frequency of the fluid and the structural part. However the couple dominant frequency is higher than the first frequency of the structure, maybe because of the little influence of the fluid dominant frequency over the couple interaction problem.

Figs. 5.9-5.10 show different time instants of the pressure field and its corresponding structural displacements, corresponding mainly to the oscillation of the first structural mode.

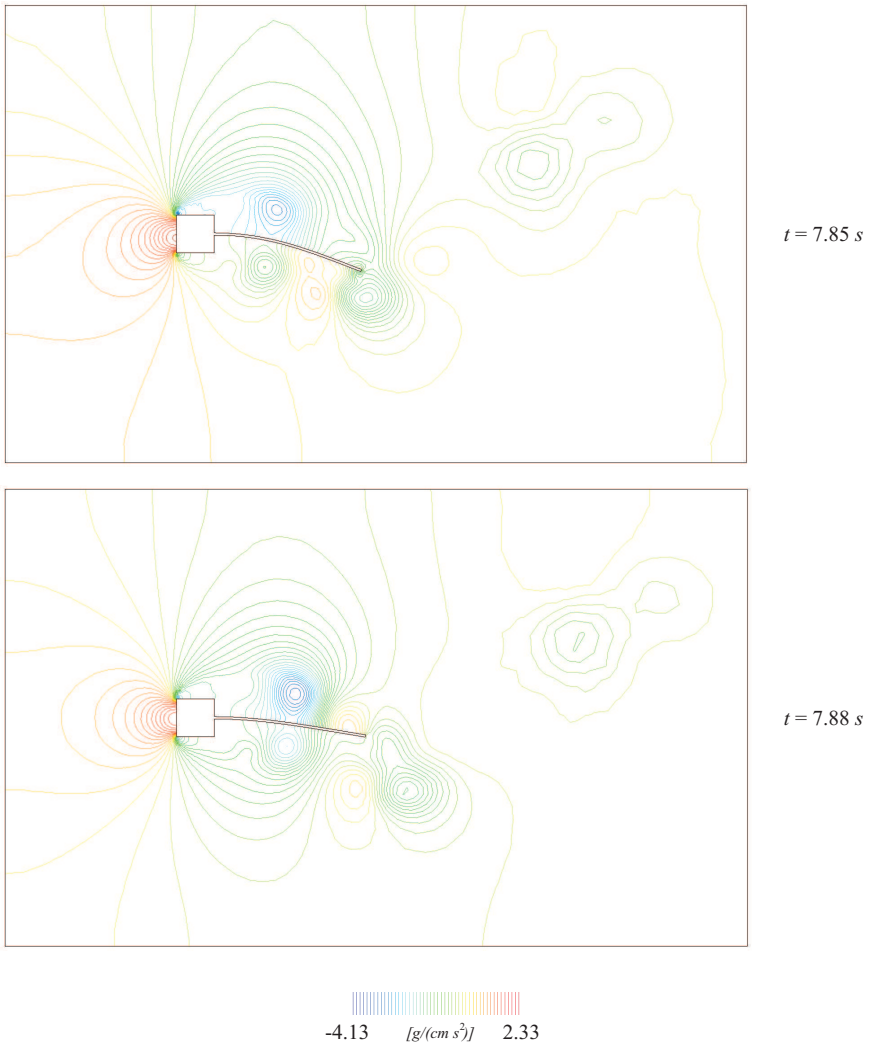

Figure 5.9 *Pressure fields for different time steps*

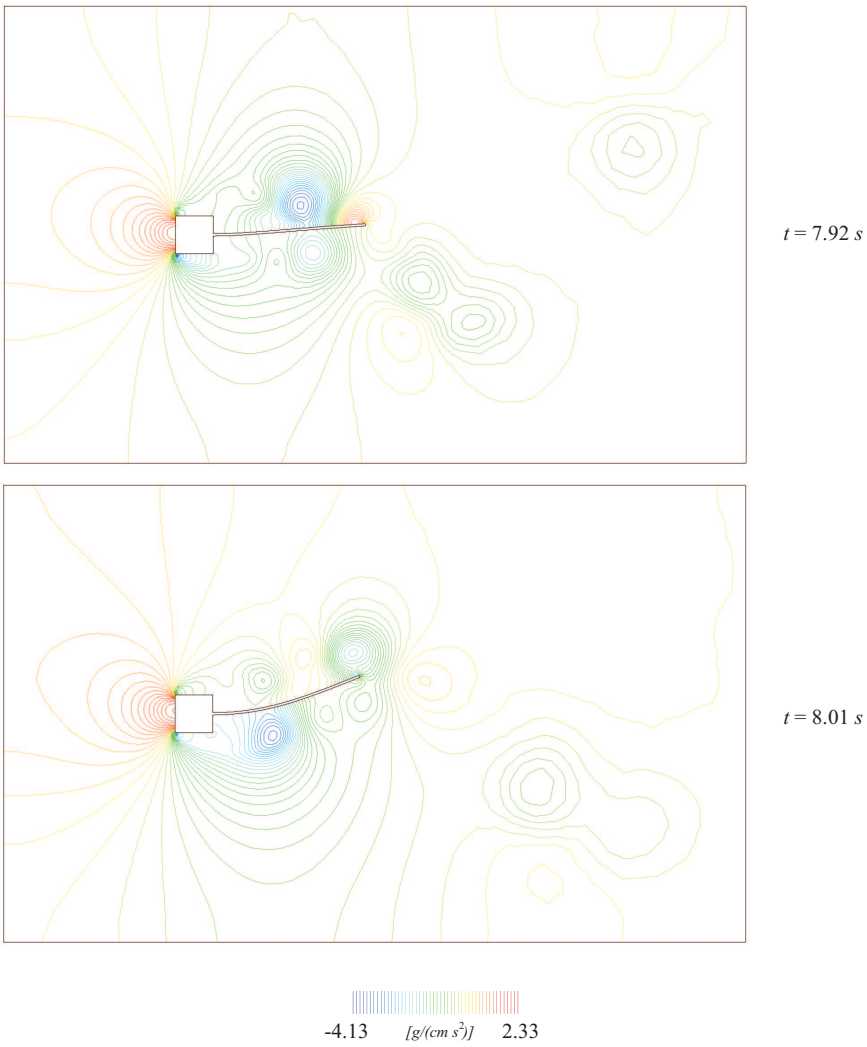

Figure 5.10 *Pressure fields for different time steps (cont.)*

5.8.2 Cavity with Flexible Bottom Membrane in 2D

This example is taken from the work of Mok (2001) which consists of a modification of the well known wall-driven cavity flow problem used in fluid dynamics. In this problem the originally constant top velocity is change for an oscillatory top velocity, including the corner nodes, given by

$$\bar{v} = 1 - cos\left(\frac{2\pi t}{5}\right) \tag{5.8.1}$$

yielding a velocity interval between $v_x = 0\ m/s$ and $v_x = 2\ m/s$. The cavity bottom originally fixed is changed for a flexible bottom membrane. Also the fluid inflow and outflow is allowed near the top face which allow the volume to change in time. Geometry and boundary conditions for this problem are shown in Fig. 5.11.

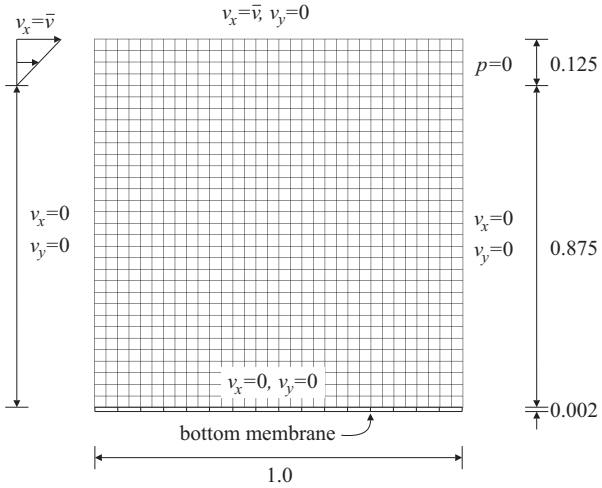

Figure 5.11 *Geometry and boundary conditions [m]*

The fluid mesh consists of a four-node quadrilateral mesh of 32×32 divisions and the structural part is constructed with 16 nine-node quadrilateral plane-stress elements. The fluid properties are taken with a density $\rho^{\mathrm{f}} = 1.0\ Kg/m^3$ and a viscosity $\nu = 0.01\ m^2/s$. For the structure, the density is taken as $\rho^{\mathrm{s}} = 500\ Kg/m^3$, Young's modulus $E = 250.0\ N/m^2$ and a Poisson ratio of $\upsilon = 0.0$. The time interval analyzed is $t \in [0.0, 70.0]$, using a time-step size of $\Delta t = 0.01\ s$. Time integration for the fluid is made with the generalized-α method with $\rho^{\mathrm{f}}_{\infty} = 0.9$ and the structural time integration uses the generalized-α technique with $\rho^{\mathrm{s}}_{\infty} = 0.8$.

As shown in Mok (2001), this example can be solved without any relaxation method. In this case, the number of Gauss-Seidel coupling iterations needed to reach a tolerance of 10^{-6} varies between 12 and 20 iterations. If the relaxation method is used with a fixed value $w = 0.825$, the range of iterations to reach the tolerance is reduced between the interval 8 to 10 iterations. Finally if the Aitken optimal relaxation parameter is computed automatically, the number of

iterations to reach the tolerance is reduced to an interval between 6 and 8 iterations. Consequently, the Aitken relaxation method shows an excellent behavior that is preferable to use instead of the standard block Gauss-Seidel coupling technique.

Fig. 5.12 shows the vertical displacement of the membrane midpoint. It can be noted that the present solution is indeed different from the solution presented by Mok. The reason is that not all the boundary conditions used by Mok to solve the problem are available in the reference cited. The amplitude obtained by Mok is of 7.3 *cm* while the amplitude obtained in this work is of 7.4 *cm*. The period of both solutions is the same with a value of 5.12 *s*. The main difference between both works is that while Mok yield a mean vertical displacement of 18.1 *cm*, the present solution has a mean vertical displacement of 23.5 *cm*. However the general tendency of the coupled problem is the same. Also Rossi (2005) find this general tendency using cable elements in the bottom of the cavity instead of nonlinear plane-stress elements as used in this work.

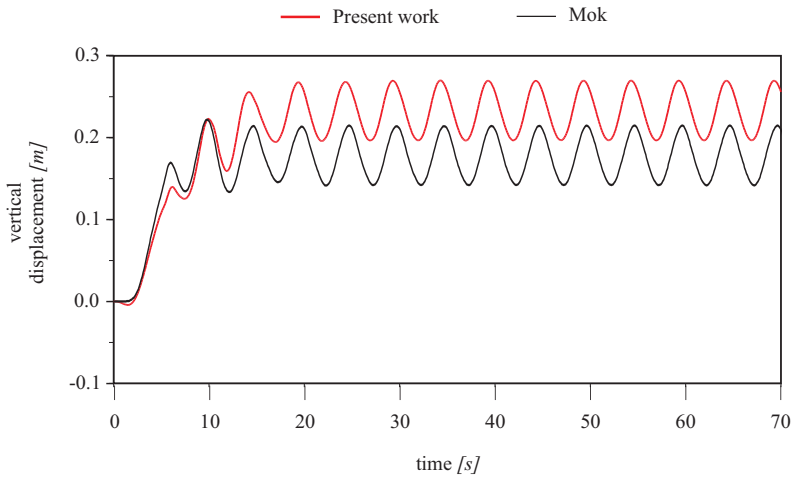

Figure 5.12 *Bottom midpoint vertical displacement*

In this example the structural density is two orders of magnitude greater than the fluid density and it can be thought that also the faster staggered coupling technique can be employed in the problem solution. However Mok (2001) showed that staggered schemes failed to obtain the problem solution even if any predictor is used and only strong coupling iterative methods yield a stable long-time solution.

Fig. 5.13 shows different time instants of the pressure field together with their deformation associated to the bottom membrane displacements. In this figure, when time $t = 2.54$ *s* the vertical displacement is just beginning. After time $t = 17.04$ *s*, the deformation cycle is repeated with a period of 5.12 *s*. From Fig. 5.12, it can be seen that for time $t = 17.04$ *s*, the minimum displacement is presented and has a value of 19.8 *cm*. Graphically this deformation is shown in Fig. 5.13. This value is repeated every 5.12 *s*. For time $t = 19.54$ *s*, the maximum displacement is given with a value of 27.2 *cm*, and it is repeated every 5.12 *s*.

Figure 5.13 *Pressure fields for different time instants*

5.8.3 Cavity with a Thin Bottom Shell in 3D

This example is also taken from the work of Mok (2001) which consists of an extension to 3D of the well known wall-driven cavity flow problem used in fluid dynamics. In this problem the originally constant top velocity is change for an oscillatory top velocity, including the corner edges, given by

$$\bar{v} = 1 - cos\left(\frac{2\pi t}{5}\right) \tag{5.8.2}$$

yielding a velocity interval between $v_x = 0\ m/s$ and $v_x = 2\ m/s$. The cavity bottom originally fixed is changed for a thin bottom shell. Also the fluid inflow and outflow is allowed near the top face which allow the volume to change in time, everywhere else the velocity is fixed to zero in all directions. Geometry and boundary conditions for this problem are shown in Fig. 5.14.

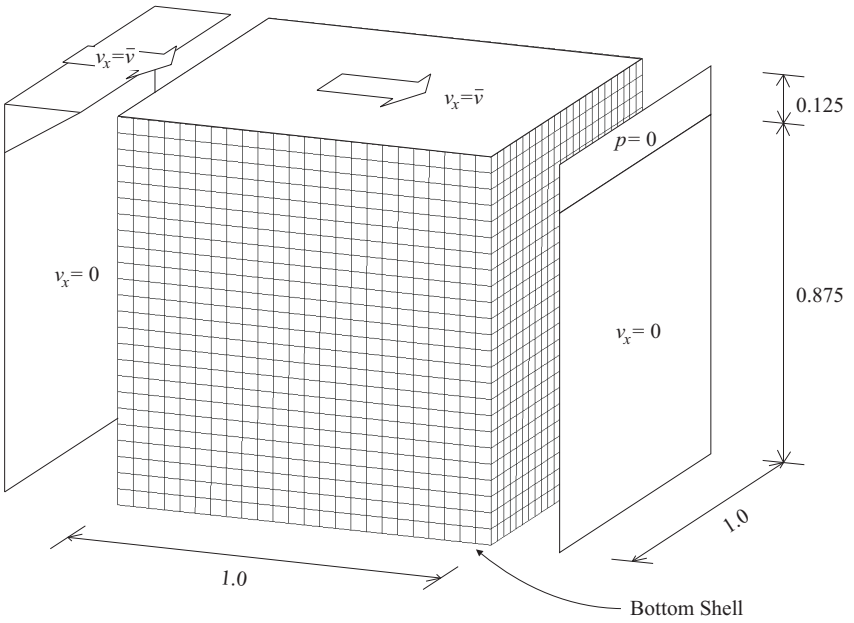

Figure 5.14 *Geometry and boundary conditions [m]*

The fluid mesh consists of an eight-node hexahedral mesh of $24\times24\times24$ divisions and the structural part is constructed with 1152 three-node triangular rotation-free shell elements with 625 nodes. The fluid properties are taken with a density $\rho^{\mathrm{f}} = 1.0$ Kg/m^3 and a viscosity $\nu = 0.01\ m^2/s$. For the structure, the density is taken as $\rho^{\mathrm{s}} = 500\ Kg/m^3$, Young's modulus $E = 250.0\ N/m^2$, Poisson ratio of $\upsilon = 0.0$ and the thickness is $0.002\ m$. The time interval analyzed is $t \in [0.0, 70.0]$, using a time-step size of $\Delta t = 0.1\ s$. Time integration for the fluid is made with the generalized-α method with $\rho^{\mathrm{f}}_{\infty} = 0.9$ and the structural time integration uses the generalized-α technique with $\rho^{\mathrm{s}}_{\infty} = 0.9$.

As shown by Mok (2001), this problem can be solved with the staggered coupling scheme using a displacement predictor of order zero. If a displacement predictor of order 1^{st} or 2^{nd} is used, the coupling scheme fails. If the Gauss-Seidel coupling technique is used, the method converges yielding a stable long-time solutions. In this example the iterative coupling scheme is used together with the automatic Aitken relaxation method for faster convergence. The number of iteration needed to reach a tolerance of 10^{-6} lies between 3 and 4 per time step with the Aitken method.

Fig.5.15 shows the vertical displacement of the shell middle point. As in the previous problem, the solution obtained is different from the solution presented by Mok. Again the reason is that not all boundary conditions used by Mok to solve this problem are available in the reference cited. The amplitude obtained by Mok is of 6.0 *cm* while the amplitude obtained in this work is of 8.8 *cm*. The period of both solutions is the same with a value of 5.12 *s*. Another difference between both works is that while Mok yield a mean vertical displacement of 11.0 *cm*, the present solution has a mean vertical displacement of 20.1 *cm*. However the general tendency of the coupled problem is the same.

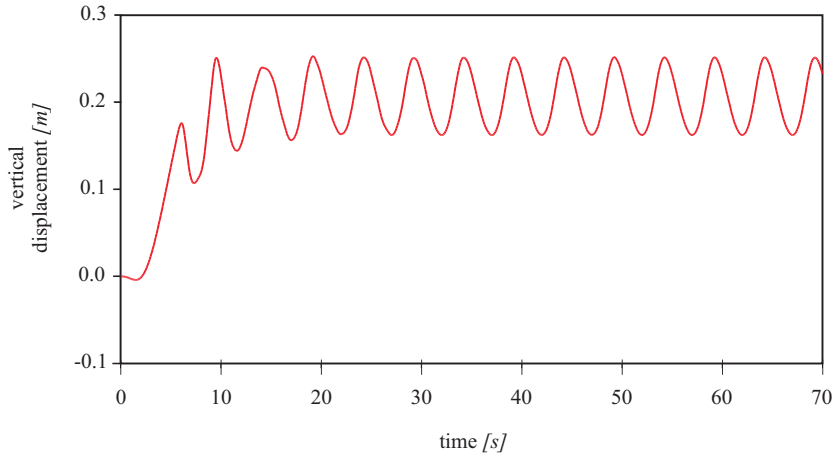

Figure 5.15 *Shell midpoint vertical displacement*

Figs. 5.16-5.17 show different time instants of the bottom shell deformation together with their displacement field. Fig. 5.16 shows the vertical displacement for time $t = 4.0$ *s* and $t = 6.0$ *s* where the deformation process has just began. After time $t = 21.8$ *s* the deformation process become cyclical with a period of 5.12 *s*. From Fig. 5.15, it can be seen that for time $t = 21.8$ *s*, the minimum vertical displacement of the cycle is 16.3 *cm*, which is plotted in Fig. 5.17 and is repeated each 5.12 *s*. For time $t = 24.3$ *s*, the maximum vertical displacement is given with a value of 25.3 *cm*, which is repeated every 5.12 *s*.

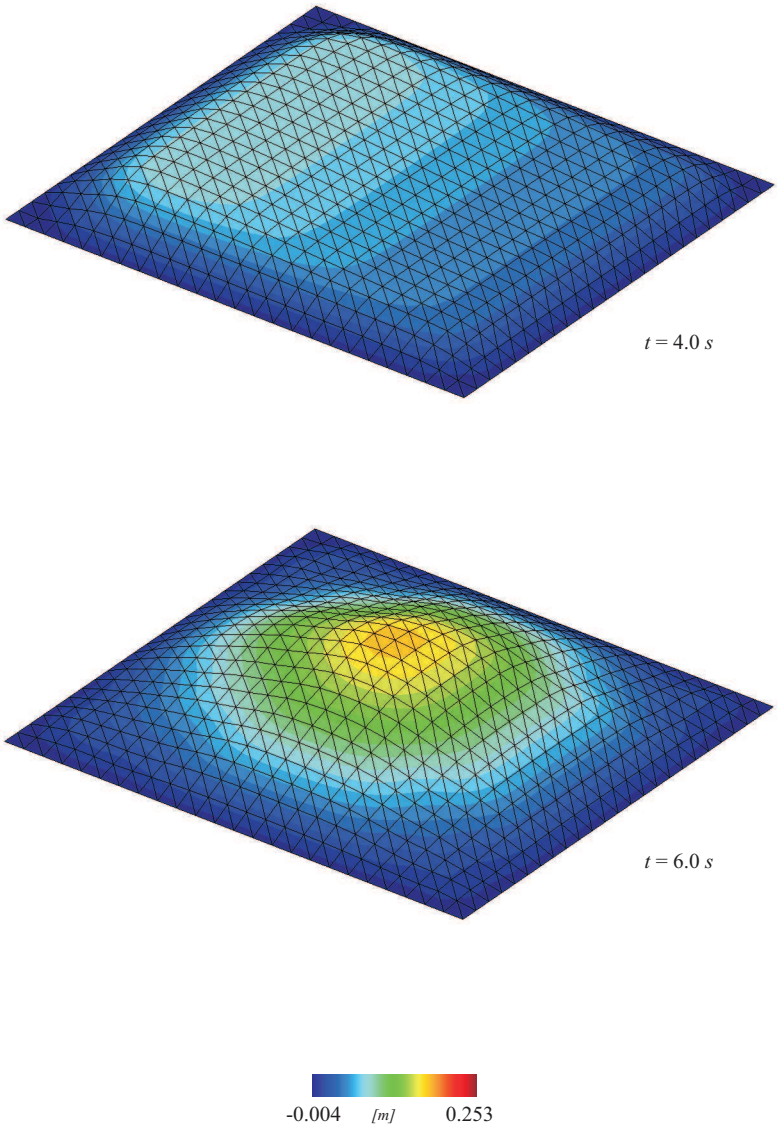

Figure 5.16 *Shell vertical displacement field*

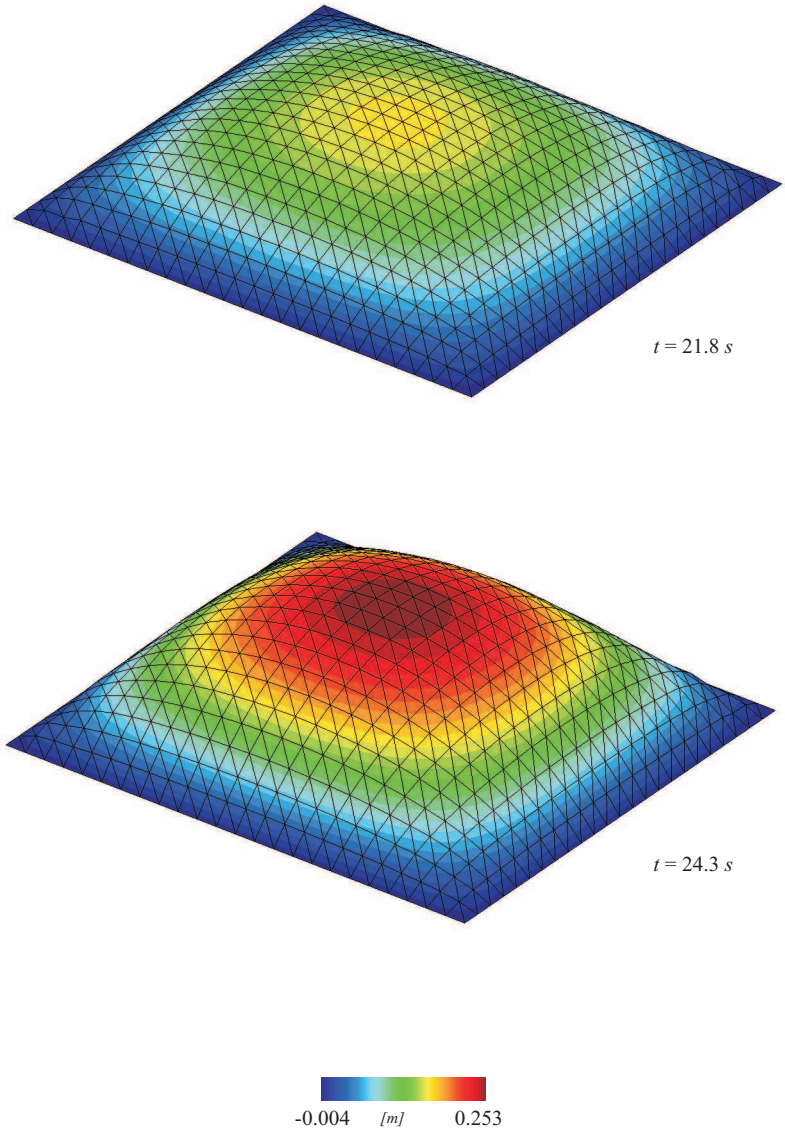

Figure 5.17 *Shell vertical displacement field (cont.)*

5.8.4 Channel with Flexible Wall

This model problem was originally proposed by Mok (2001) and Wall and Mok (2001) as a challenging test for coupled problems involving similar densities between the fluid and the structure. Obviously, if the Gauss-Seidel strong coupling method is used, this kind of problems can only be solved if a relaxation technique is employed. Standard Gauss-Seidel methods fail to solve problems with similar densities. Geometry and boundary conditions of the problem are given in Fig. 5.18.

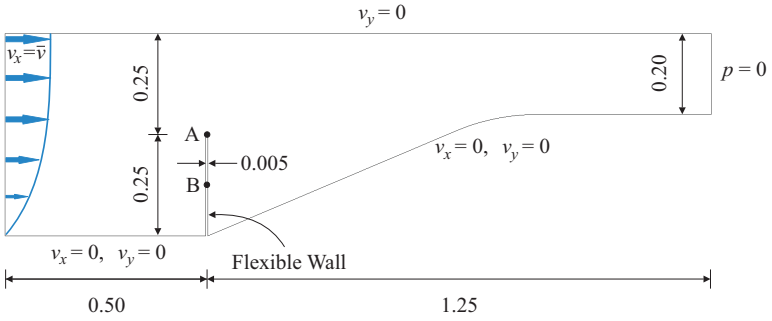

Figure 5.18 *Channel geometry and boundary conditions [m]*

The material properties are taken for the structure with a density $\rho^{\mathrm{s}} = 1500.0$ kg/m^3, Young's modulus $E = 2.3 \times 10^6$ N/m^2 and Poisson's ratio $\upsilon = 0.45$. The fluid material properties are density $\rho^{\mathrm{f}} = 956.0$ Kg/m^3 and viscosity $\mu = 0.145$ $kg/(m\ s)$. The inflow velocity is parabolic and is applied slowly with the function shown in Fig. 5.19, where after 10 s the x-velocity component is kept constant with a value of 0.06067 m/s.

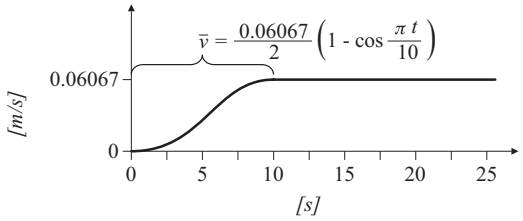

Figure 5.19 *Channel inflow x-velocity component*

The finite element mesh used for this problem has 6008 three-node triangular elements and 3218 nodes for the fluid part, and 6 nine-node quadrilateral elements in one layer over the thickness with 39 nodes for the structural part using geometrically nonlinear plane stress conditions. The fluid part uses the generalized-α time integration method with $\rho^{\mathrm{f}}_{\infty} = 0.9$, while the generalized-$\alpha$ time integration method for second-order equations with $\rho^{\mathrm{s}}_{\infty} = 0.6$ is used for the structural part. The time interval studied is 25 s using a time step size $\Delta t = 0.1$. The FIC stabi-

lization technique has been employed in this example. Mesh movement is obtained by using the pseudo-elastic structural technique.

Fig. 5.20 shows a comparison between the pressure history solution obtained by Mok (2001) and the present work. At point B, the solution of both works is practically the same, while point A present little variations. However the solution of point A is the same that the solution given by Rossi (2005).

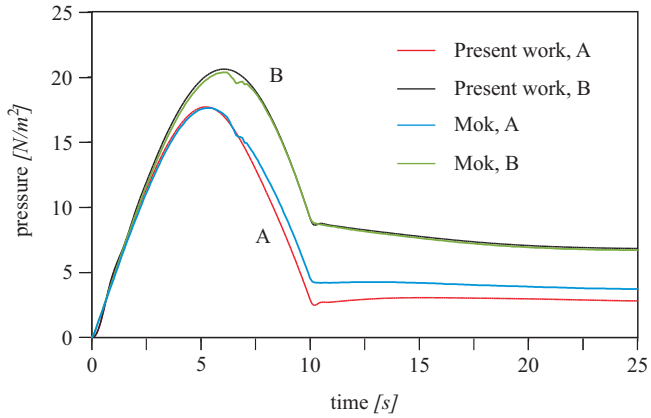

Figure 5.20 *Time history for pressure*

Fig. 5.21 shows a comparison between the x-velocity component time history solution. The tendency between both works is the same, presenting little changes probably because of the mesh and geometry studied.

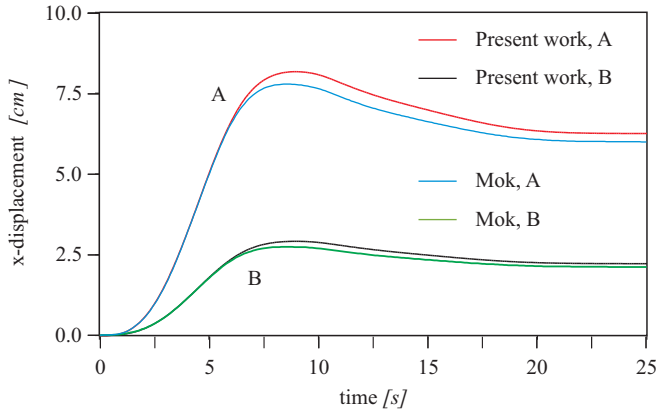

Figure 5.21 *Time history for x-displacement component*

Figs. 5.22-5.23 show different time instant of fluid-structure interaction for the x-velocity component together with its associated deformation. This solution is in accordance with the solution presented by Mok (2001) and Wall and Mok (2001).

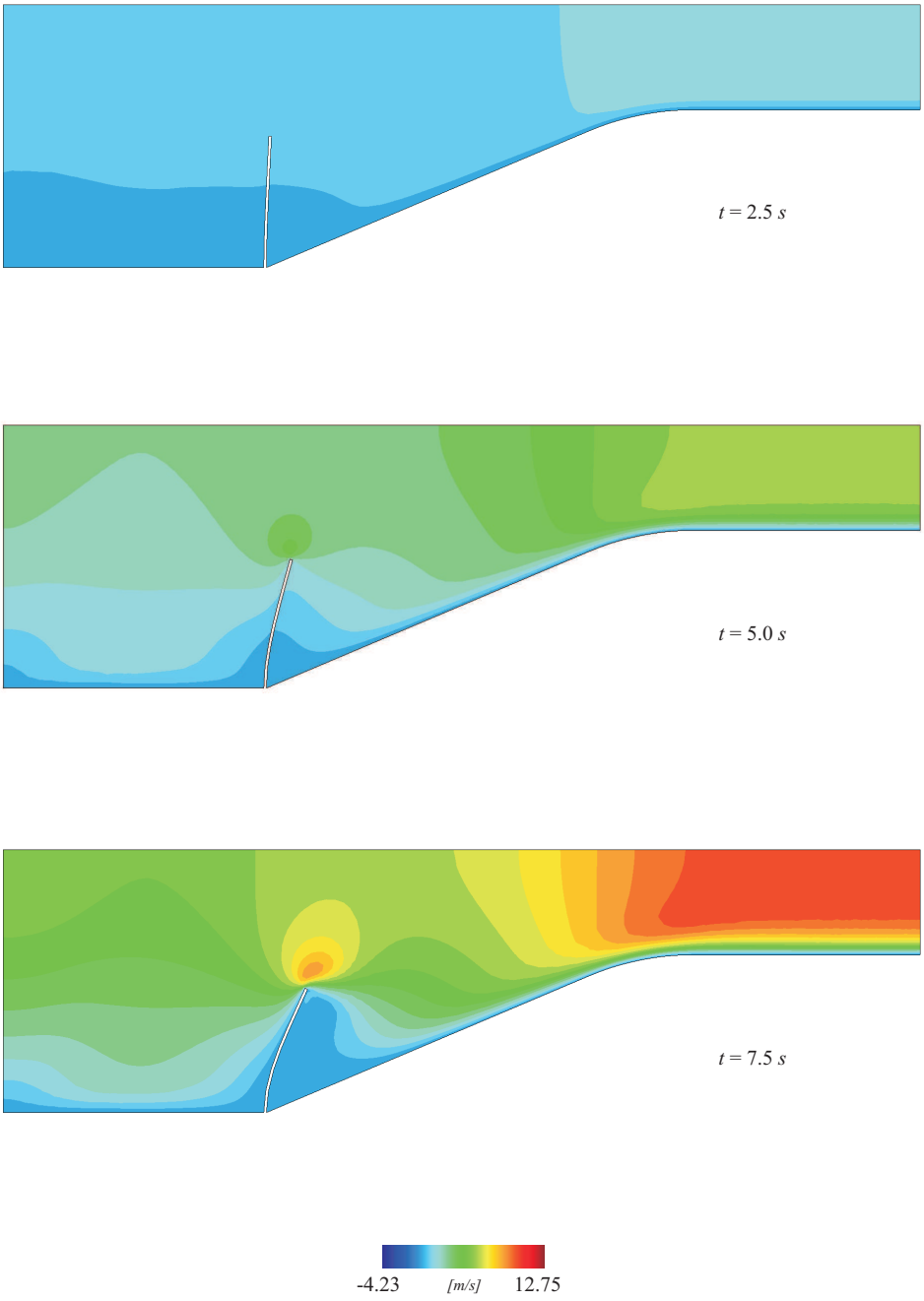

Figure 5.22 *Contour field for x-velocity component and deformed geometry*

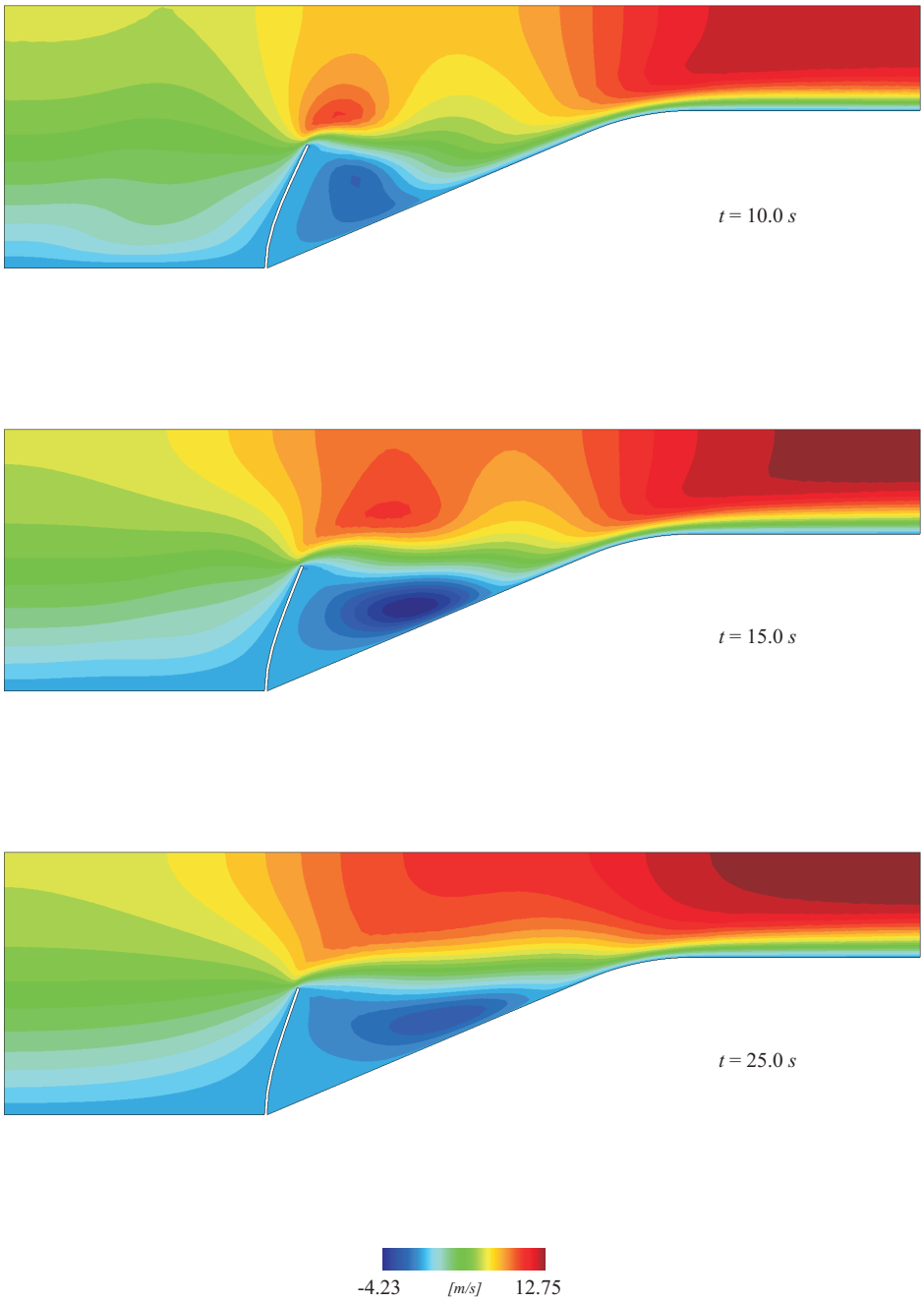

Figure 5.23 *Contour field for x-velocity component and deformed geometry (cont.)*

5.8.5 Pressure Pulse in a Compliant Vessel

This model problem was originally proposed by Nobile (2001) and Formaggia et al. (2001) to consider the fluid-structure interaction arising in the modelling of blood flow in large arteries. Recently Fernández and Moubachir (2005) has made a variation at the inlet data using the same geometry and physical parameters to demonstrate the quadratic convergence of their FSI formulation.

The problem consists of a thin elastic vessel, that here is modelled with rotation-free shell elements, conveying the blood flow modelled by an incompressible fluid using the Navier-Stokes equations .

The geometry used for the computation has been made with a straight cylinder of radius $r_0 = 0.5\ cm$ and length $L = 5\ cm$. The fluid physical parameters are taken as those given by Formaggia et al. (2001) with a density $\rho^{\mathrm{f}} = 1\ g/cm^3$ and viscosity $\mu = 0.03\ g/(cm\ s)$. The surrounding solid parameters are density $\rho^{\mathrm{s}} = 1.2\ g/cm^3$, Young's modulus $E = 3.0 \times 10^6\ g/(cm\ s^2)$, Poisson ratio $\upsilon = 0.3$ and a thickness of $0.1\ cm$. The structure is clamped at the inlet and outlet. The fluid is initially at rest and an overpressure of $1.3332 \times 10^4\ g/(cm\ s^2)$ (10 mmHg) has been imposed at the inlet boundary for $0.003\ s$. To introduce this Neumann boundary condition, Eq. (4.2.6) has to be added to the momentum equation.

The fluid mesh consists of 1600 hexahedral eight-node elements and 1869 nodes, while the structure mesh has 1280 three-node triangular rotation-free shell elements and 656 nodes. The structure has also been modelled with 640 hexahedral eight-node elements with two layers over the thickness and 1008 nodes for comparison purposes. The fluid solver uses the generalized-α time integration method with $\rho^{\mathrm{f}}_{\infty} = 0.9$, while the solid solver uses the generalized-α time integration method with $\rho^{\mathrm{s}}_{\infty} = 0.8$. The time interval studied is of $0.01\ s$ using a time step size of $\Delta t = 0.0001\ s$. The FIC stabilization technique has been employed in this example. Mesh movement is obtained by using the Laplacian method. The Gauss-Seidel strong coupling technique is used together with the automatic Aitken relaxation method. The number of iterations needed to reach a tolerance of 10^{-6} lies between 12 and 15 per time step.

Figs. 5.24-5.25 shows a pressure wave propagation together with the fluid deformed configuration for different time steps. A reflection wave is expected due to the numerical side-effect of the outlet boundary condition. As can be seen, these results are similar to those given by Formaggia et al. (2001) and Fernández and Moubachir (2005). Fig. 5.26-5.27 shows the half solid deformed configuration of the rotational free shell structure compared with the solid deformed configuration of the hexahedral structure. It can be observed that the solution obtained with the rotation-free shell elements is practically the same that the solution found with the 3D solid elements. But the advantage of using the shell elements is the faster solution in the CSD solver. It is not the purpose of this example to study realistic physiological simulation of blood-arteries interaction, but to show the capabilities of the coupling formulation implemented to deal with this kind of problems. Displacements of all the figures in this example have been magnified by a factor of 20 for clarity.

Fig. 5.28 shows the time history analysis for radial displacements at different

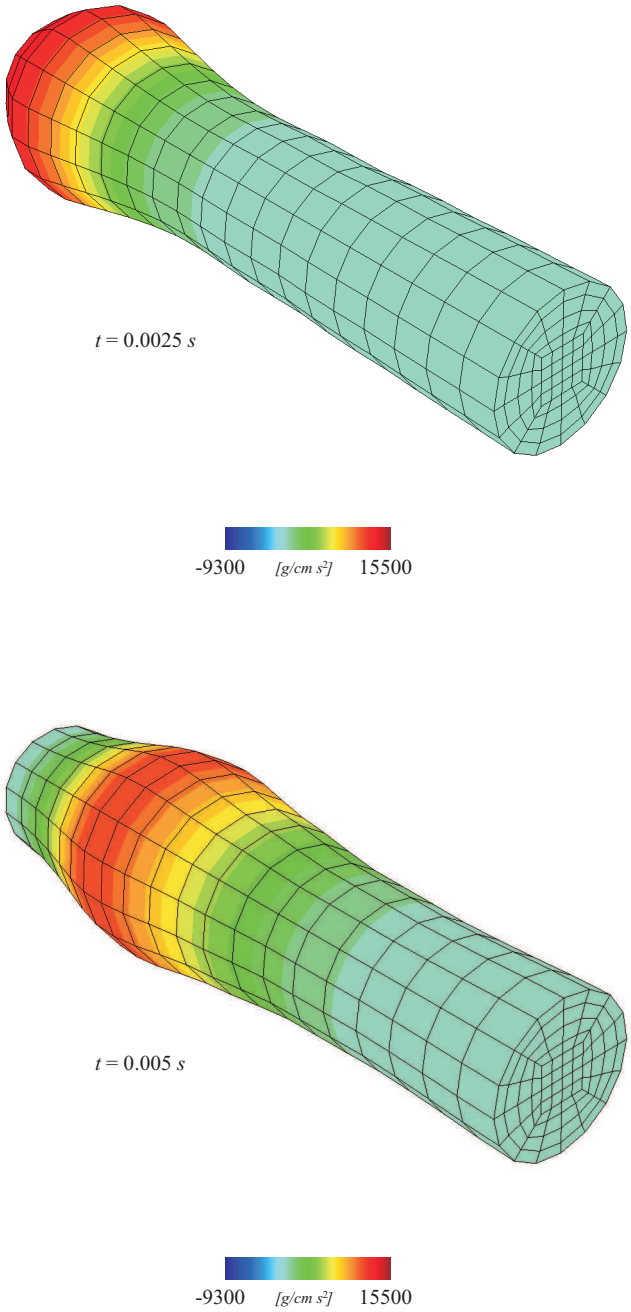

Figure 5.24 *Wave propagation generated by pressure pulse at the inflow*

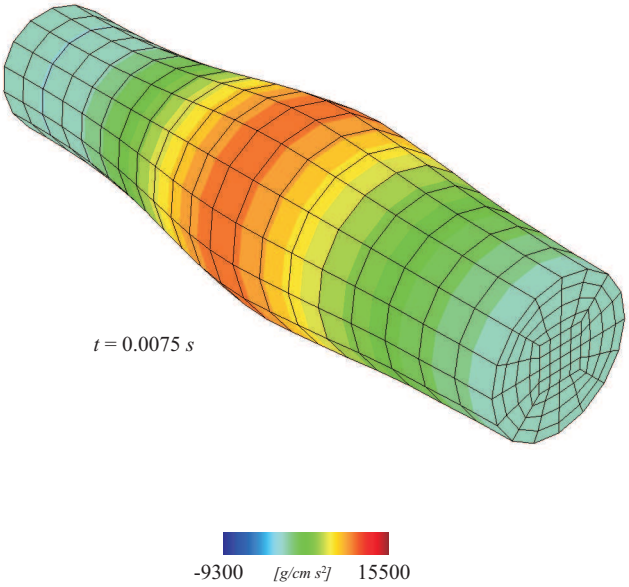

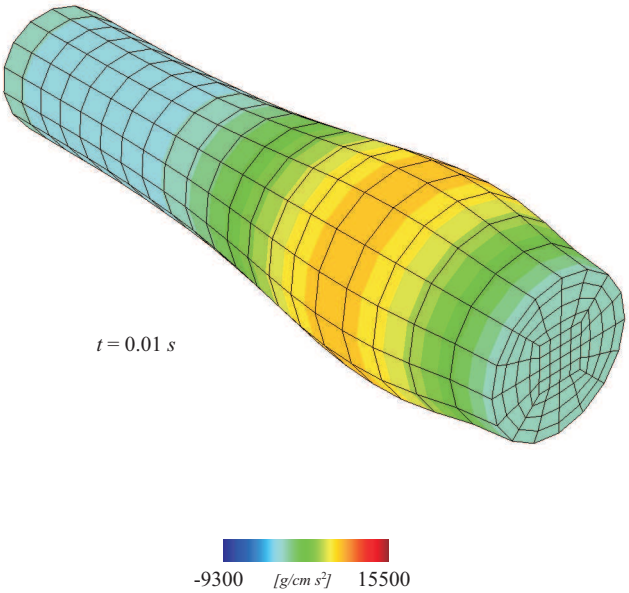

Figure 5.25 *Wave propagation generated by pressure pulse at the inflow (cont.)*

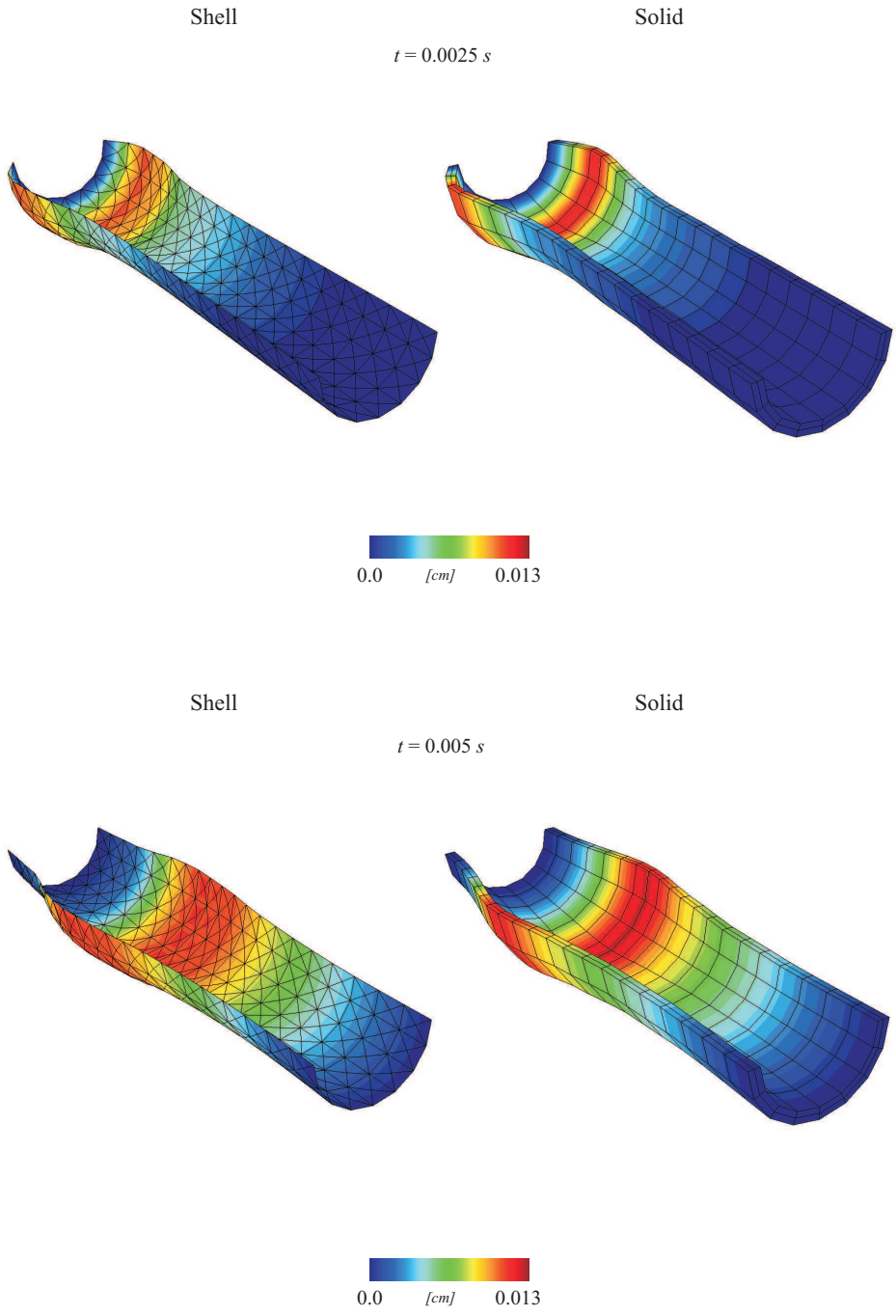

Figure 5.26 *Structure deformed configuration. Displacements norm*

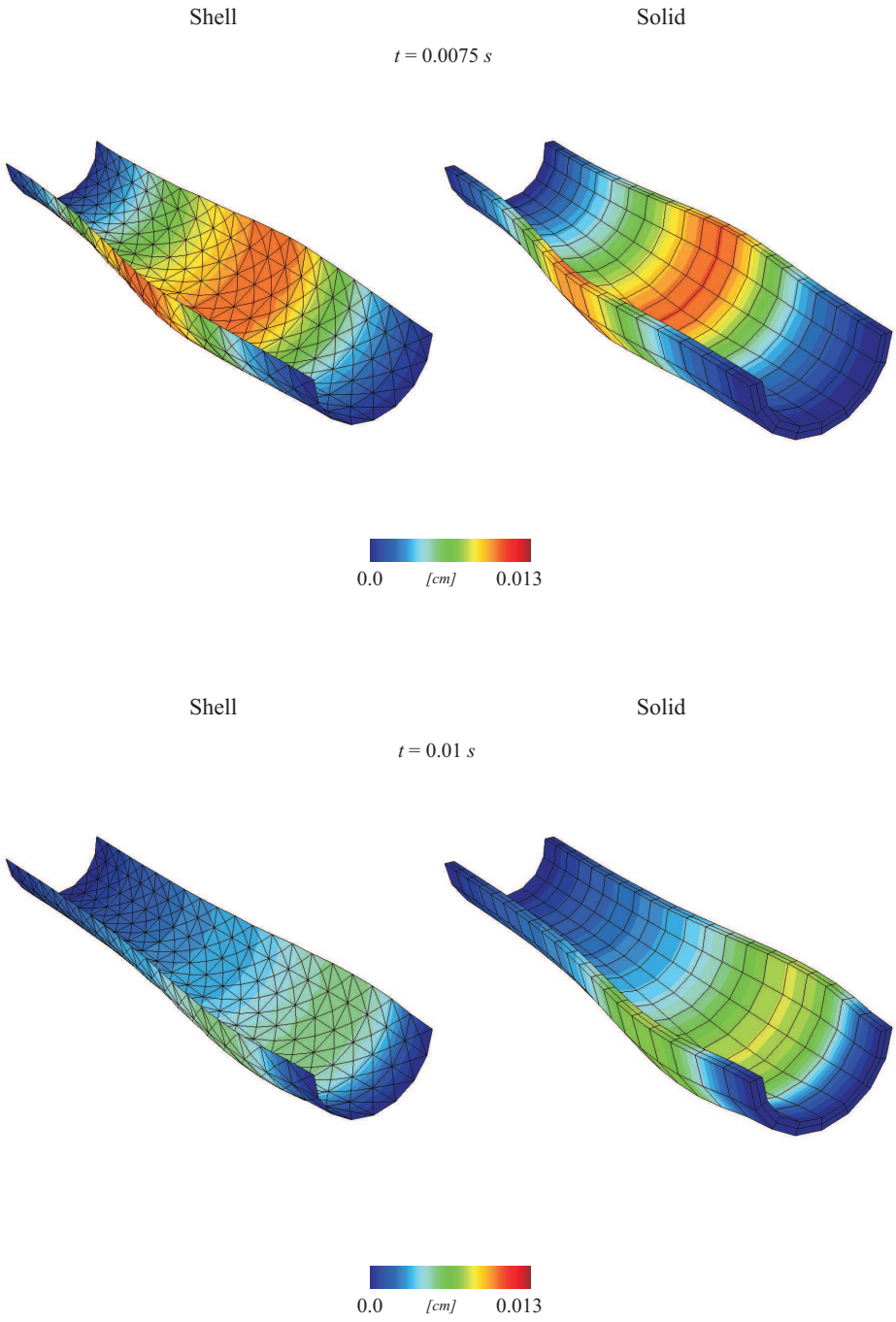

Figure 5.27 *Structure deformed configuration. Displacements norm (cont.)*

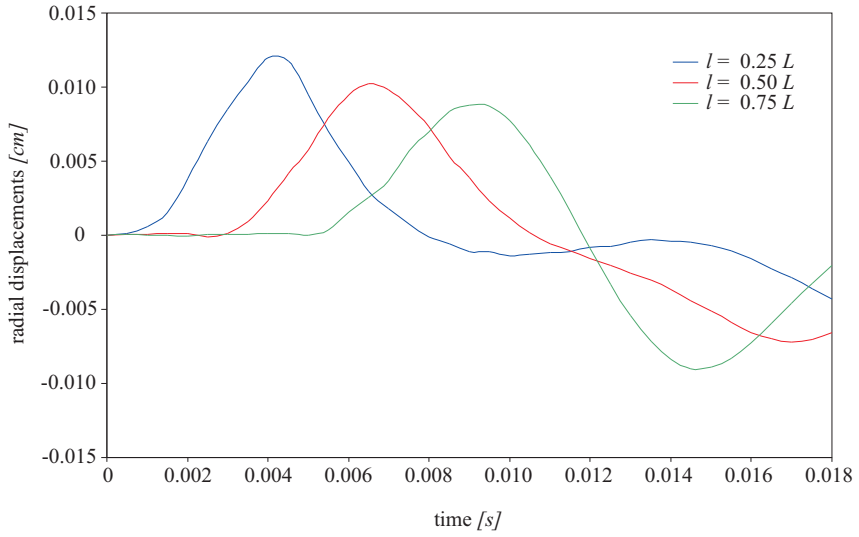

Figure 5.28 *Time history for radial displacements*

lengths from the inlet pressure: $l = 0.25L\ cm$, $l = 0.50L\ cm$ and $l = 0.75L\ cm$. Since the outlet pressure is set to zero, it is expected that the maximum radial displacements become smaller when the distance to the outflow is closer.

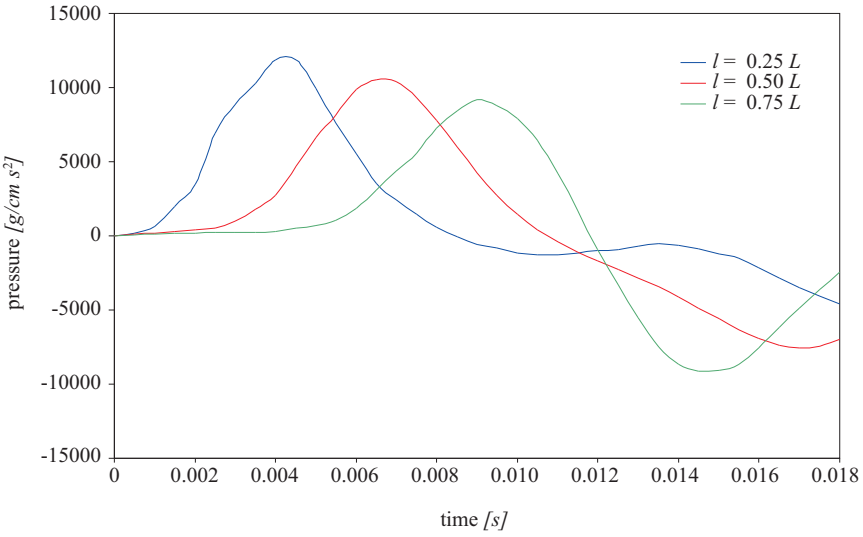

Figure 5.29 *Time history for pressure*

Fig. 5.29 shows the time history analysis for the pressure at different lengths

from the inlet pressure. Also the effect of the reflection wave can be observed in Figs. 5.28-5.29 due to the numerical side-effect of the outlet boundary condition that develop negative pressures near this boundary.

It is important to remark that the fluid part of this example was solved using the predictor-corrector scheme because the fractional step method lead to some oscillations in the solution. A way to avoid these oscillations is the use of the fractional step method twice per time step. In this form, oscillations are drastically reduced, but still the predictor-corrector method gives a smoother solution.

Chapter 6

Conclusions

This monograph deals with the analysis of structures with large deformations, incompressible fluid flows and fluid-structure interaction problems, which objectives pursued were introduced in section **1.3** and have been fulfilled satisfactorily. An algorithm to solve these three field problems has been developed and implemented in the context of the finite element method.

Structures. The structural part of this work is concerned with the geometrically nonlinear analysis of membrane and rotation-free shell structures. Improvement to the formulations already existing is began with the continuum expression of the virtual internal work in curvilinear coordinates. Then a new formulation based on the principal fiber orientation is performed. The idea to use the fiber orientation of the material for our analysis comes from the manufacturing process where a direction for the principal fiber of the material is needed to build the structure. The fiber orientation is mesh dependent and has great advantages, which can be stated as follow:

- It is based on an idea which is very simple to understand.
- A suitable implementation as a preprocess in a finite element code makes it a true alternative to take into account for structural analysis, since a wider range of problems can be solved.
- Allows adequate postprocess of the problem being analyzed since any number of patches that conform the structure can be postprocessed with different local orientations.
- It allows to perform analysis with orthotropic and composite materials including structures having an initially out-of-plane configuration.

Following a detailed explanation of the classical membrane theory, the inclusion of the fiber orientation allows to improve the membrane formulation, where the classical membrane theory is considered as a particular case of this new and general formulation.

Even though the new finite element discretization for the membrane formulation is expressed in a general context, in particular the triangular three-node finite

element is implemented. This particularity is done with the intention to be used as a part of the rotation-free shell formulation considered in this work.

An important aspect of the new formulation is the possibility to add prestressed forces to the membrane structure in a simple and almost direct way. This is possible because the new formulation of the three dimensional membrane structure has its manufacturing fibers already oriented and then the prestressed forces can be added directly to the internal forces.

Since conventional membrane theory allows compression stresses, a wrinkling algorithm based on modifying the constitutive equation has been developed. Without this wrinkling algorithm, finite element analysis of membranes would lead to inexistent compression stresses that would yield a final configuration of the membrane structure completely different to the real one.

On the other hand, conventional shell formulations require a lot of memory and computing time for their analysis. Therefore shell formulations with displacements as the only degrees of freedom have been investigated by several authors. In this work, the Kirchhoff-Love theory of thin shells is studied. Since the virtual internal work for this kind of shells is built with a membrane and a bending part, the new membrane formulation is used to form the membrane part of these elements. For the bending part, the new formulation presented is based on the fiber orientation technique. The choice to use triangular three-node finite elements for the rotation-free shell discretization is due to the higher approximation of the solution compared to other type of finite elements used in these kind of shell formulations.

The basic shell triangle formulation of Flores and Oñate (2001) has been reformulated using the fiber orientation technique. The resulting new formulation has improved its range of applications for engineering problems. As in the case of membranes, the new rotation-free shell formulation can be used to analyze orthotropic and prestressed shells.

Usually the Newmark time integration scheme is used in structural dynamic problems. However geometrically nonlinear analysis for long periods of time introduce spurious high frequencies that spoil the solution. In order to minimize unwanted low frequency dissipation while achieving high frequency dissipation without regarding the order of accuracy, other time integration schemes are studied. The easiest method to implement in a finite element code is the Bossak method. Another widely used method is the Hilber-Hughes-Taylor time integration technique. These last two methods produce very similar solutions for large deformation structural problems. However the generalized-α strategy is the best choice for this kind of problems, since it can reproduce the solution of the last two methods mentioned before, and provide a third option for better results.

The structural problems solved with the improved membrane and shell formulations have demonstrated their robustness and accuracy for the different variety of applications presented.

Fluids. The fluid part of this work is concerned with the solution of the Navier-Stokes and continuity equation for incompressible flow problems. The monolithic solution of these equations take great computer effort to solve the nonlinear system of equations, specially for 3D problems. Instead of using a monolithic solu-

tion for incompressible flow problems, pressure segregation methods have earned a widespread popularity because of the computational efficiency given by the uncoupling of the pressure from the velocity field. In this work, the fractional step and predictor-corrector methods are explained.

Three well known stabilization techniques have been implemented in the finite element code used in this work. They are the SUPG/PSPG, OSS and FIC stabilization methods with equal-order interpolation finite elements. Until now, the SUPG/PSPG stabilization method have been used with monolithic solvers for incompressible flow problems. In this work, the SUPG/PSPG scheme is developed to be used with fractional step and predictor-corrector methods following the ideas that solve the OSS and FIC techniques with pressure-segregation methods.

Additionally, the generalized-α time integration scheme for fluids is adapted to these three stabilization techniques with pressure segregation methods, which has only been used for monolithic solutions. As in the case of structural problems, the generalized-α technique for fluids seeks to minimize unwanted low frequency dissipation while achieving high frequency dissipation without regarding the order of accuracy.

Fluid problems extensively studied by analytical, numerical and experimental methods are often used as benchmark problems to validate numerical simulations. In this work, some well-known example problems have validated and demonstrated the good performance of the fluid formulations implemented.

Coupling. From the available types for coupling fluid and structural problems, the strong coupling block Gauss-Seidel partitioned technique is implemented in this work. The fluid-structure interaction problem is built with the structure and fluid contributions of this work.

A very important aspect to take into account for fluid-structure interaction problems with large structural deformations is the time integration scheme used for the simulation. Usually this kind of problem are studied for long periods of time, which introduced spurious high frequencies that spoil the solution. One way to avoid this problem is to reduce the time step size used for the analysis that sometimes is unacceptable. The best way to solve this problem is to used time integration schemes that minimize unwanted low frequency dissipation while achieving high frequency dissipation without regarding the order of accuracy. In this work, the method suggested to use is the generalized-α technique for both, the structural and the fluid parts.

Many fluid-structure interaction problems are solved with staggered coupling techniques, which are only acceptable for problems where the added mass effect do not have influence in the structure. However this kind of problem may become unstable for long time periods of study. To avoid this problem, strong coupling partitioned schemes are advised.

However when the added mass effect plays an important role in the structure, partitioned methods with block Newton schemes are an excellent choice. Another option is the block Jacobi or block Gauss-Seidel method with relaxation techniques. These last two methods are useless if they do not include the relaxation technique. In this work, the strong coupling block Gauss-Seidel partitioned method with a re-

laxation technique based on Aitken's method is implemented, yielding an excellent solution to all the examples presented.

Finally, a detailed algorithm for the fluid-structure interaction problem using the strong coupling block Gauss-Seidel partitioned method is presented. In there, a relaxation technique with Aitken's method is explained. However, other relaxation techniques can be added with minor modifications.

6.1 Achievements

The achievements made in this work are summarized as follows:

- A methodology for the fiber orientation of materials used for the construction of light-weight structures is developed based on the finite element mesh of the discretized problem.
- Development of an improved membrane formulation based on the fiber orientation, where the classical membrane formulation can be considered as a particular case of this new formulation.
- The new membrane formulation allows the analysis of orthotropic membrane structures. The initial configuration of the membrane can be flat or curved.
- The inclusion of prestressed forces is accounted for in the new membrane formulation, since usually membranes have a prestressed field that give the design shape to the structure.
- Development of an improved rotation-free shell formulation based on the fiber orientation.
- The new rotation-free shell formulation allows to analyze orthotropic and prestressed structured.
- Local postprocess for membrane and shell structures with different principal fiber orientations.
- Development of the incompressible flow formulation with the SUPG/PSPG stabilization technique in the context of pressure segregation methods. Specially for fractional step and predictor-corrector methods.
- Adaptation of the generalized-α time integration scheme for fluids to fractional step and predictor-corrector methods, using the SUPG/PSPG, OSS and FIC stabilization techniques.
- Coupling of large deformation membrane and shell structures with incompressible fluid flow formulations. Membrane and shell new formulation developed in this work are used in the structural part. Fluid improvements with the generalized-α technique for pressure segregation methods are used in the fluid part.

6.2 Possible Future Research Lines

The following research lines to continue the development of the structure, fluid and fluid-structure interaction problems of this work are suggested:

- To develop a constitutive equation for membrane and shell finite elements capable of dealing with composite materials for the study of recent structural applications.
- Improving the computational fluid dynamic solver to account for turbulence models and wall-functions will allow the solution of high mean flow Reynolds numbers problems.
- When excessive large displacements of the structure are transferred to the moving mesh algorithm, it may fail. Then it is necessary to remesh the fluid domain. Therefore the implementation of an internal remesh solver in the actual code will be needed.
- Implementation of strong coupling block Newton partitioned methods for fluid-structure interaction problems.
- Parallelization of the code to save computer time for complex analysis.
- Develop a form-finding algorithm.

References

Adams, D. D. and Wood, W. L. (1983). Comparison of hilber-hughes-taylor and bossak α-methods for the numerical integration of vibration equations. *International Journal for Numerical Methods in Engineering*, 19:765–771.

Babuska, I. (1973). Finite-element method with lagrangian multipliers. *Numerische Mathematik*, 20:179–192.

Badia, S., Nobile, F., and Vergara, C. (2007). Fluid-structure partitioned procedures based on robin transmissions conditions. *Journal of Computational Physics*, submitted.

Badia, S. I. (2006). *Stabilized Pressure Segregation Methods and Their Application to Fluid-Structure Interaction Problems*. PhD thesis, Technical University of Cataluña.

Barbat, A. H. and Canet, J. M. (1994). *Estructuras sometidas a acciones sismicas. Cálculo por ordenador*. CIMNE, Barcelona, 2nd edition.

Barnes, M. R. (1977). *Form Finding and Analysis of Tension Space Structures by Dynamic Relaxation*. PhD thesis, Department of Civil Engineering, The City University, London.

Batchelor, G. K. (2000). *An introduction to fluid dynamics*. Cambridge University Press, Cambridge, 1st cambridge mathematical library edition.

Bathe, K.-J. (1996). *Finite Elements Procedures*. Prentice-Hall, New Jersey.

Bathe, K.-J. and Dvorkin, E. N. (1985). A four node plate bending element based on mindlin/reissner plate theory and mixed interpolation. *International Journal for Numerical Methods in Engineering*, 21:367–383.

Belytschko, T., Liu, W. K., and Moran, B. (2000). *Nonlinear Finite Elements for Continua and Structures*. Wiley, Chichester.

Blasco, J., Codina, R., and Huerta, A. (1998). A fractional-step method for the incompressible navier-stokes equations related to a predictor-multicorrector algorithm. *International Journal for Numerical Methods in Fluids*, 28:1391–1419.

Bletzinger, K.-U. and Wüchner, R. (2001). Form finding of anisotropic prestressed membrane structures. In Wall, W. A., Bletzinger, K.-U., and Schweizerhof, K., editors, *Trends in Computational Structural Mechanics*, pages 595–603, Barcelona. CIMNE.

Bonet, J. and Wood, R. D. (1997). *Nonlinear Continuum Mechanics for Finite Element Analysis*. University Press, Cambridge.

Bonet, J., Wood, R. D., Mahaney, J., and Heywood, P. (2000). Finite element analysis of air supported membrane structures. *Computer Methods in Applied Mechanics and Engineering*, 190:579–595.

Braun, M., Bischoff, M., and Ramm, E. (1994). Nonlinear shell formulations for complete three-dimensional constitutive laws include composites and laminates. *Computational Mechanics*, 15:1–18.

Brezzi, F. (1974). On the existence, uniqueness and approximation of saddle point problems araising from lagrange multipliers. *Revue Française d'Automatique Informatique et Recherche Opérationalle*, 8:129–151.

Brooks, A. N. and Hughes, T. (1982). Streamline upwind petrov-galerkin formulations for convection dominated flows with particular emphasis on the incompressible navier-stokes equations. *Computer Methods in Applied Mechanics and Engineering*, 32:199–259.

Brunet, M. and Sabourin, F. (1994). Prediction of necking and wrinkles with a simplified shell element in sheet forming. In Kröplin, B., editor, *Proceedings of the International Conference of Metal Forming Simulation in Industry II*, pages 27–48.

Bütchter, N., Ramm, E., and Roehl, D. (1992). Three-dimensional extension of non-linear shell formulations based on the enhanced assumed strain concept. *International Journal for Numerical Methods in Engineering*, 37:2551–2568.

Causin, P., Gerbeau, J. F., and Nobile, F. (2005). Added-mass effect in the design of partitioned algorithms for fluid-structure problems. *Computer Methods in Applied Mechanics and Engineering*, 194:4506–4527.

Cendoya, P. (1996). *Nuevos elementos finitos para el análisis dinámico elastoplástico no lineal de estructuras laminares*. PhD thesis, Technical University of Cataluña.

Chiandussi, G., Bugeda, G., and Oñate, E. (2000). A simple method for automatic update of finite element meshes. *Communications un Numerical Methods in Engineering*, 16:1–19.

Chorin, A. J. (1967). A numerical method for solving incompressible viscous problems. *Journal of Computational Physics*, 2:12–26.

Chung, J. and Hulbert, G. M. (1993). A time integration algorithm for structural dynamics with improved numerical dissipation: the generalized-α method. *Journal of Applied Mechanics*, 60:371–375.

Cirak, F. and Ortiz, M. (2001). Fully c^1-conforming subdivision elements for finite deformation thin-shell analysis. *International Journal for Numerical Methods in Engineering*, 51:813–833.

Cirak, F., Ortiz, M., and Schröeder, P. (2000). Subdivision surfaces: a new paradigm for thin-shell finite element analysis. *International Journal for Numerical Methods in Engineering*, 47:2039–2072.

Clemente, R. (2007). *Análisis Estructural de Edificios Historicos Mediante Modelos Localizados de Fisuración*. PhD thesis, Technical University of Cataluña.

Clough, R. W. and Tocher, J. L. (1965). Finite element stiffness matrices for analysis of plates in bending. *Proc. Conf. Matrix Methods In Structural Mechanics, AFIT*, Air Force Base, Ohio:515–545.

Codina, R. (1998). Comparison of some finite element methods for solving the diffusion-convection-reaction equation. *Computer Methods in Applied Mechanics and Engineering*, 156:185–210.

Codina, R. (2000). Stabilization of incompressibility and convection through orthogonal sub-scales in finite element methods. *Computer Methods in Applied Mechanics and Engineering*, 190:1579–1599.

Codina, R. (2001). Pressure stability in fractional step finite element methods for incompressible flows. *Journal of Computational Physics*, 170:112–140.

Codina, R. (2002). Stabilized finite element approximation of transient incompressible flows using orthogonal subscales. *Computer Methods in Applied Mechanics and Engineering*, 191:4295–4321.

Codina, R. and Badia, S. (2006). On some pressure segregation methods of fractional-step type for the finite element approximation of incompressible flow problems. *Computer Methods in Applied Mechanics and Engineering*, 195:2900–2918.

Codina, R., Coppola-Owen, H., Nithiarasu, P., and Liu, C.-B. (2006). Numerical comparison of cbs and sgs stabilization techniques for the incompressible navier-stokes equations. *International Journal for Numerical Methods in Engineering*, 66:1672–1689.

Codina, R. and Soto, O. (2004). Approximation of the navier-stokes equations using orthogonal subscale stabilization and pressure segregation on anisotropic finite element meshes. *Computer Methods in Applied Mechanics and Engineering*, 193:1403–1419.

COMET (2007). *Software for Coupled Contact, Mechanical and Thermal Analysis*. Miguel Cervera, Carlos Agelet de Saracibar and Miquelle Chiumenti. CIMNE, Barcelona.

Contri, P. and Schrefler, B. A. (1988). A geometrically nonlinear finite element analysis of wrinkled membrane surfaces by a no-compression model. *Communications in Applied Numerical Methods*, 4:5–15.

Cook, R. D., Malkus, D. S., and Plesha, M. E. (1989). *Concepts and Applications of Finite Element Analysis*. Wiley, New York, 3rd edition.

Coppola-Owen, H. (2006). Flow past a circular cylinder in 3d. *Private Communication*, CIMNE, Barcelona.

Crisfield, M. A. (1991). *Non-linear Finite Element Analysis of Solids and Structures*, volume 1 and 2. Wiley, Chichester.

Decolon, C. (2000). *Analysis of Composite Structures*. Hermes Science Publications, Paris.

Degand, C. and Farhat, C. (2002). A three-dimensional torsional spring analogy method for unstructured dynamic meshes. *Computer and Structures*, 80:305–316.

Dettmer, W. and Peric, D. (2003). An analysis of the time integration algorithms for the finite element solutions of incompressible navier-stokes equations based on a stabilised formulation. *Computer Methods in Applied Mechanics and Engineering*, 192:1177–1226.

Dettmer, W. and Peric, D. (2006). A computational framework for fluid-structure interaction: Finite element formulation and applications. *Computer Methods in Applied Mechanics and Engineering*, 195:5754–5779.

Dettmer, W. G. (2004). *Finite Element Modelling of Fluid Flow with Moving Free Surfaces and Interfaces Including Fluid-Solid Interaction*. PhD thesis, School of Engineering, University of Wales, Swansea.

Donea, J. (1984). A taylor-galerkin method for convection transport problems. *International Journal for Numerical Methods in Engineering*, 20:101–119.

Donea, J. and Huerta, A. (2003). *Finite Element Methods for Flow Problems*. John Wiley and Sons, Chichester.

Douglas, J. and Russell, T. F. (1982). Numerical methods for convection dominated diffusion problems based on combining the method of characteristics with finite element or finite difference procedures. *SIAM Jour. Numer. Anal.*, 19:871–885.

Farhat, C. (1997). Parallel and distribuited solution of coupled nonlinear dynamic aeroelastic response problems. In Papadrakakis, M., editor, *Parallel Solution Methods in Computational Mechanics*, pages 243–301. J. Wiley and Sons.

Farhat, C., Lesoinne, M., Stern, P., and Lantéri, S. (1997). High performance solution of three-dimensional nonlinear aeroelastic problems via parallel partitioned algorithms. *Advances in Engineering Software*, 28:43–61.

Farrashkhalvat, M. and Miles, J. P. (2003). *Basic Structures Grid Generation*. Butterworth-Heinemann, Oxford.

Felippa, C. A. (2004). *Course on Fluid-Struture Interaction: Chapters 1-11*. Internet. Department of Aerospace Engineering Sciences, University of Colorado at Boulder.

Felippa, C. A., Park, K. C., and Farhat, C. (1998). Partitioned analysis of coupled systems. In Oñate, E. and Idelsohn, S., editors, *IV World Congress on Computational Mechanics*, Barcelona. CIMNE.

Fernández, M. A. and Moubachir, M. (2005). A newton method using exact jacobians for solving fluid-structure coupling. *Computers and Structures*, 83:127–142.

Flores, F. G. and Oñate, E. (2001). A basic thin shell triangle with only translational dofs for large strain plasticity. *International Journal for Numerical Methods in Engineering*, 51:57–83.

Flores, F. G. and Oñate, E. (2005). Improvements in the membrane behaviour of the three node rotational-free bst shell triangle using an assumed strain approach. *Computer Methods in Applied Mechanics and Engineering*, 194:907–932.

Formaggia, L., Gerbeau, J. F., Nobile, F., and Quarteroni, A. (2001). On the coupling of 3d and 1d navier-stokes equations for flow problems in compliant vessels. *Computer Methods in Applied Mechanics and Engineering*, 191:561–582.

Ghia, U., Ghia, K. N., and Shin, C. T. (1982). High-re solution for incompressible flow using the navier-stokes equations and the multigrid method. *Journal of Computational Physics*, 48:387–411.

GiD (2007). *Software for preprocess and postprocess of the finite element method*. R, Ribó, M Pasenau, E. Escolano, J. Suit and A. Coll. CIMNE, Barcelona.

Gil, A. J. (2003). Finite element analysis of prestressed hyperelastic saint venant-kirchhoff membranes under large deformations. In Oñate, E. and Kröpling, B., editors, *Textile Composites and Inflatable Structures*, pages 206–211, Barcelona. CIMNE.

Gunzburger, M. D. (1989). *Finite Element Methods for Viscous Incompressible Flow*. Academic Press, San Diego.

Gurtin, M. E. (1981). *An Introduction to Continuum Mechanics*. Academic Press, Florida.

Hammache, M. and Gharib, M. (1991). An experimental study of the parallel and oblique vortex shedding from circular cylinders. *Journal of Fluid Mechanics*, 232:567–590.

Hampshire, J. K., Topping, B. H. V., and Chan, H. C. (1992). Three node triangular elements with one degree of freedom per node. *Engineering Computations*, 9:49–62.

Hübner, B., Walhorn, E., and Dinkler, D. (2004). A monolithic approach to fluid-structure interaction using space-time finite elements. *Computer Methods in Applied Mechanics and Engineering*, 193:2087–2104.

Hilber, H. M., Hughes, T. J. R., and Taylor, R. L. (1977). Improved numerical dissipation for time integration algoriths in structural dynamics. *Earthquake Engineering and Structural Dynamics*, 5:283–292.

Holzapfel, G. A. (2000). *Nonlinear Solid Mechanics*. Wiley, Chichester.

Hughes, T. J. R. (1987). *The Finite Element Method*. Prentice-Hall, New Jersey.

Hughes, T. J. R. (1995). Multiscale phnomena: Green's functions, the dirichlet-to-neumann formulation, subgrid scale models, bubbles and the origins of stabilized methods. *Computer Methods in Applied Mechanics and Engineering*, 127:387–401.

Hughes, T. J. R. and Brooks, A. N. (1979). A multi-dimensional upwind scheme with no crosswind diffusion. In Hughes, T. J. R., editor, *FEM for Convection Dominated Flows*, New York. ASME.

Hughes, T. J. R. and Brooks, A. N. (1982). A theoretical framework for petrov-galerkin methods with discontinuous weighting functions: applications to the streamline upwind procedure. In Gallagher, R. H., Norrie, D. M., Oden, J. T., and Zienkiewicz, O. C., editors, *Finite Element in Fluids*, volume IV, pages 46–65, London. Wiley.

Hughes, T. J. R., Franca, L. P., and Balestra, M. (1986). A new finite element formulation for computational fluid dynamics: V. circumventing ths babuska-brezzi condition: A stable petrov-galerkin formulation of the stokes problem accommodating equal-order interpolations. *Computer Methods in Applied Mechanics and Engineering*, 59:85–99.

Hughes, T. J. R., Franca, L. P., and Hulbert, G. M. (1989). A new finite element formulation for computational fluid dynamics: Viii.the galerkin/least-squares method for advective-diffusive equations. *Computer Methods in Applied Mechanics and Engineering*, 73:173–189.

Hughes, T. J. R., Taylor, R. L., and Kanoknukulchai, W. (1977). A simple and efficient element for plate bending. *International Journal for Numerical Methods in Engineering*, 11:1529–1543.

Irons, B. and Tuck, R. C. (1969). A version of the aitken accelerator for computer implementation. *International Journal for Numerical Methods in Engineering*, 1:275–277.

Jansen, K. E., Whiting, C. H., and Hulbert, G. M. (2000). A generalized-α method for integrating the filtered navier-stokes equations with a stabilized finite element method. *Computer Methods in Applied Mechanics and Engineering*, 190:305–319.

Jarasjarungkiat, A., Wüchner, R., and Bletzinger, K.-U. (2007). A wrinkling model based on material modification for isotropic and orthotropic membranes. In *Computer Methods in Applied Mechanics and Engineering*. doi:10.1016/j.cma.2007.09.005.

Jetteur, P. (2005). Material with small resistance in compression, dual formulation. In Oñate, E. and Kröpling, B., editors, *Textile Composites and Inflatable Structures*, pages 317–323, Stutgart. CIMNE.

Johnson, A. A. and Tezduyar, T. E. (1994). Mesh update strategies in parallel finite element computations of flow problems with moving boundaries and interfaces. *Computer Methods in Applied Mechanics and Engineering*, 119:73–94.

Kirchhoff, G. (1876). *Vorlesungen über Mathematische Physik*. Mechanik, Leipzig.

Kondo, K., Iai, T., Moriguri, T., and Murasaki, T. (1955). In *Memoirs of the Unifying Study of the Basic Problems in Engineering by Means of Geometry*, pages 417–441.

Kundu, P. K. and Cohen, I. M. (2002). *Fluid Mechanics*. Academis Press, San Diego.

Levy, R. and Spillers, W. (1995). *Analysis of Geometrically Nonlinear Structures*. Chapman and Hall.

Löhner, R. (2001). *Applied CFD Techniques. An Introduction Based on Finite Element Methods*. Wiley.

Löhnert, S., Tegeler, K., and Wriggers, P. (2003). A simple wrinkling algorithm for orthotropic membranes at finite deformations. In Oñate, E. and Kröpling, B., editors, *Textile Composites and Inflatable Structures*, pages 119–122, Barcelona. CIMNE.

Libai, A. and Simmonds, J. G. (1998). *The Nonlinear Theory of Elastic Shells*. Cambridge University Press, New York, 2nd edition.

Liu, X., Jenkins, C. H., and Schur, W. (2001). Large deflection analysisof pneumatic envelopes using a penalty parameter modified material model. *Finite Elements in Analysis and Design*, 37:233–251.

Love, A. E. H. (1934). *The Mathematical Theory of Elasticity*. Cambridge University Press, New York.

Lu, K., Accorsi, M., and Leonard, J. (2001). Finite element analysis of membrane wrinkling. *International Journal for Numerical Methods in Engineering*, 50:1017–1038.

Lynga, H. (2005). *A finite element method for solving the Navier-Stokes equations using finite calculus and its application in fluid-structure interaction*. PhD. Thesis Project, CIMNE, Barcelona.

Malvern, L. E. (1969). *Introduction to the Mechanics of a Continuous Medium*. Prentice-Hall, New Jersey.

Mansfiled, E. H. (1970). Load transfer via a wrinkled membrane. In *Proceedings of the Royal Society of London*, pages 269–289, London. Series A(316).

Mansfiled, E. H. (1977). Analysis of wrinkled membranes with anisotropic and nonlinear elastic properties. In *Proceedings of the Royal Society of London*, pages 477–498, London. Series A(353).

Matthies, H. G. and Steindorf, J. (2004). *Partitioned Strong Coupling Algorithms for Fluid-Structure-Interaction*. Institute of Scientific Computing, Technical University Braunschweig, Brunswick, Germany.

Matthies, H. G. and Steindorf, J. (2005). *Partitioned but Strongly Coupled Iteration Schemes for Nonlinear Fluid-Structure Interaction*. Institute of Scientific Computing, Technical University Braunschweig, Brunswick, Germany.

Matthies, H. G. and Steindorf, J. (2006). *Strong Coupling Methods*. Institute of Scientific Computing, Technical University Braunschweig, Brunswick, Germany.

Melosh, R. J. (1961). A stiffness matrix for the analysis of thin plates in bending. *Journal of Aerospace Science*, 28:34–42.

Mindlin, R. D. (1951). Influence of rotatory inertia and shear in flexural motions of isotropic elastic plates. *Journal of Applied Mechanics*, 18:31–38.

Mok, D. P. (2001). *Partitionierte Lösungsansätze in der Strukturdynamik und der Fluid-Struktur-Interaktion*. PhD thesis, Institut für Baustatik, Universität Stuttgart.

Mok, D. P. and Wall, W. A. (2001). Partitioned analysis schemes for the transient interaction of incompressible flows and nonlinear flexible structures. In Wall, W. A., Bletzinger, K. U., and Schweizerhof, K., editors, *Trends in Computational Structural Mechanics*, pages 689–698, Barcelona. CIMNE.

Muttin, F. (1996). Finite element for wrinkled curved elastic membranes and its applications to sails. *Communications in Numerical Methods in Engineering*, 12(11):775–785.

Nay, R. A. and Utku, S. (1972). An alternative to the finite element method. *Variational Methods in Engineering*, 1.

Newmark, N. (1959). A method of computation for structural dynamics. *Journal of the Engineering Mechanics Division*, 85:67–94.

Nobile, F. (2001). *Numerical Approximation of Fluid-Structure Interaction Problems with Application to Haemo-dynamics*. PhD thesis, Département de Mathématiques, École Polytechnique Fédérale de Laussane.

Oñate, E. (1992). *El Metodo de los Elementos Finitos*. CIMNE, Barcelona.

Oñate, E. (1998). Derivation of stabilized equations for numerical solution of advective-diffusive transport and fluid flow problems. *Computer Methods in Applied Mechanics and Engineering*, 151:233–265.

Oñate, E. (2000). A stabilized finite element method for incompressible viscous flows using a finite increment calculus formulation. *Computer Methods in Applied Mechanics and Engineering*, 182:355–370.

Oñate, E. and Cervera, M. (1993). Derivation of thin plate elements with one degree of freedom per node. *Engineering Computations*, 10:543–561.

Oñate, E., Garcia, J., Idelsohn, S. R., and del Pin, F. (2006). Finite calculus formuations for finite element analysis of incompressible flows. eulerian, ale and lagrangian approaches. *Computer Methods in Applied Mechanics and Engineering*, 195:3001–3037.

Oñate, E., Hinton, E., and Glover, N. (1979). Techniques for improving the performance of isoparametric shell elements. In Brebbia, C. and E.Alarcón, editors, *Applied Numerical Modelling*. Pentch Press.

Oller, S. (2001). *Dinamica no-lineal*. CIMNE, Barcelona.

Park, K. C. and Felippa, C. A. (1983). Partitioned analysis of coupled systems. In Belytschko, T. and Hughes, T. J. R., editors, *Computational Methods for Transient Analysis*, pages 157–219. Elsevier Science Publishers.

Raible, T. A. (2003). *Concepts for Nonlinear Orthotropic Material Modeling with Applications to Membrane Structures*. PhD thesis, Universität Hannover. Institut für Baumechanik und Numerische Mechanik.

Reddy, J. N. (2004). *An Introduction to Nonlinear Finite Element Analysis*. University Press, Oxford.

Reissner, E. (1938). On tension field theory. In *Procedures of the 5th International Congress of Applied Mechanics*, pages 88–92.

Reissner, E. (1945). The effect of transverse shear deformation on the bending of elastic plates. *Journal of Applied Mechanics*, 12:69–76.

Roddeman, D. G. (1991). Finite element analysis of wrinkling membranes. *Communications in Applied Numerical Methods*, 7:299–307.

Roddeman, D. G., Drukker, J., Oomens, C. W. J., and Janssen, J. D. (1987a). The wrinkling of thin membranes: Part i-theory. *ASME Journal of Applied Mechanics*, 54:884–887.

Roddeman, D. G., Drukker, J., Oomens, C. W. J., and Janssen, J. D. (1987b). The wrinkling of thin membranes: Part ii-numerical analysis. *ASME Journal of Applied Mechanics*, 54:888–892.

Rojek, J., Oñate, E., and Postek, E. (1998). Application of explicit codes to simulation of sheet and bulk metal forming processes. *Journal of Materials Processing Technology*, 80-81:620–627.

Rossi, R. (2005). *Light-weight Structures. Numerical Analysis and Coupling Issues.* PhD thesis, University of Bologna, Italy.

Rossi, R., Lazzari, M., Vitaliani, R., and Oñate, E. (2003). Convergence of the modified material model for wrinkling simulation of light-weight membrane structures. In Oñate, E. and Kröpling, B., editors, *Textile Composites and Inflatable Structures*, pages 148–153, Barcelona. CIMNE.

Rossi, R., Lazzari, M., Vitaliani, R., and Oñate, E. (2005). Simulation of light-weight membrane structures by wrinkling model. *International Journal for Numerical Methods in Engineering*, 62:2127–2153.

Schoop, H., Taenzer, L., and Hornig, J. (2002). Wrinkling of nonlinear membranes. *Computational Mechanics*, 29:68–74.

Simo, J. C. and Fox, D. D. (1989). On a stress resultant geometrically exact shell model. part i: Formulation and optimal parametrization. *Computer Methods in Applied Mechanics and Engineering*, 72:267–304.

Simo, J. C., Fox, D. D., and Rifai, M. S. (1990a). On a stress resultant geometrically exact shell model. part iii: Computational aspects of the nonlinear theory. *Computer Methods in Applied Mechanics and Engineering*, 79:21–70.

Simo, J. C. and Kennedy, J. G. (1992). On a stress resultant geometrically exact shell model. part v: Nonlinear plasticity: Formulation and integration algorithms. *Computer Methods in Applied Mechanics and Engineering*, 96:133–171.

Simo, J. C., Rifai, M. S., and Fox, D. D. (1990b). On a stress resultant geometrically exact shell model. part iv: Variable thickness shells with through-the-time-thickness stretching. *Computer Methods in Applied Mechanics and Engineering*, 81:91–126.

Spencer, A. J. M. (1980). *Continuum Mechanics.* Longman mathematical texts, London.

Steindorf, J. (2002). *Partitionerte Verfahren für Probleme der Fluid-Struktur Wechselwirkung.* PhD thesis, Technischen Universität Braunschweig.

Tallec, P. L. and Mouro, J. (2001). Fluid structure interaction with large structural displacements. *Computer Methods in Applied Mechanics and Engineering*, 190:3039–3067.

Taylor, R. L. (2001). *Finite Element Analysis of Membrane Structures*. Internal CIMNE report, Barcelona.

Temam, R. (1969). Sur l'approximation de la solution des équations de navier-stokes par la méthode des pas fractionaires (i). *Archives for Rational Mechanics and Analysis*, 32:135–153.

Tessler, A., Sleight, D. W., and Wang, J. T. (2003). Effective modeling strategies for nonlinear shell analysis of thin membranes exhibiting structural wrinkling. *submited to: Journal of Spacecraft and Rockets, AIAA*.

Tezduyar, T. E. (1992). Stabilized finite element formulations for incompressible flow computations. *Advances in Applied Mechanics*, 28:1–44.

Tezduyar, T. E., Mittal, S., Ray, S. E., and Shih, R. (1992). Incompressible flow computations with stabilized bilinear and linear equal-order-interpolation velocity-pressure elements. *Computer Methods in Applied Mechanics and Engineering*, 95:221–242.

Tezduyar, T. E., Sathe, S., and Stein, K. (2006). Solution techniques for the fully discretized equations in computation of fluid-structure interactions with space-time formulations. *Computer Methods in Applied Mechanics and Engineering*, 195:5743–5753.

Tezduyar, T. E., Shih, R., and Mittal, S. (1990). Time-accurate incompressible flow computations with quadrilateral velocity-pressure elements. *University of Minnesota. Supercomputer Institute Research Report UMSI 90/143*, August.

Ugural, A. C. (1981). *Stresses in plates and shells*. McGraw Hill, New York.

Valdés, J. G. (2002). *Análisis de Membranas*. Internal CIMNE report, Barcelona.

Valdés, J. G., Oñate, E., and Canet, J. M. (2004). Assignment of principal fibers direction to analyze orthotropic membranes. In Mora, J., Escolano, E., Pasenau, M., Ribó, R., and Pérez, J. S., editors, *Conference on Advances and Applications of GiD*, pages 105–108, Barcelona. CIMNE.

Valdés, J. G., Oñate, E., and Canet, J. M. (2005). A modified material model to simulate wrinkling of orthotropic membranes at finite deformations. In Oñate, E. and Kröpling, B., editors, *Textile Composites and Inflatable Structures*, pages 113–122, Stutgart. CIMNE.

Wagner, H. (1929). Flat sheet metal girders with very thin metal web. *Zeitschrift für Flugtechnik Motorluftschiffahrt*, 20:200–207.

Wall, W. A. (1999). *Fluid-Struktur-Interaktion mit stabilisierten Finiten Elementen*. PhD thesis, Institut für Baustatik, Universität Stuttgart.

Wall, W. A., Genkinger, S., and Ramm, E. (2007). A strong coupling partitioned approach for fluid-structure interaction with free surfaces. *Computers and Fluids*, 36:169–183.

Wall, W. A. and Mok, D. P. (2001). Partitioned analysis schemes for the transient interaction of incompressible flows and nonlinear flexible structures. In *Trends in computational structural mechanics*, Barcelona. CIMNE.

Wall, W. A. and Ramm, E. (1998). Fluid-structure interaction based upon a stabilized (ale) finite element method. In Oñate, E. and Idelsohn, S., editors, *IV World Congress on Computational Mechanics*, Barcelona. CIMNE.

Wall, W. A. and Ramm, E. (2000). A coupled fluid structure environment with a three-dimensional shell model. In *ECCOMAS 2000*, Barcelona. CIMNE.

Wüchner, R. (2006). *Mechanik und Numerik der Formfindung und Fluid-Struktur-Interaktion von Membrantragwerken.* PhD thesis, Technischen Universität München.

Wüchner, R. and Bletzinger, K.-U. (2005). Stress-adapted numerical form finding of pre-stressed surfaces by the updated reference strategy. *International Journal for Numerical Methods in Engineering*, 64:143–166.

Wood, W. L., Bossak, M., and Zienkiewics, O. C. (1980). An alpha modification of newmark's method. *International Journal for Numerical Methods in Engineering*, 15:1562–1566.

Wu, C. H. and Canfield, T. R. (1981). Wrinkling in finite plane-stress theory. *Quarterly of Applied Mathematics*, 39:179–199.

Ziegler, R. (2001). *Theorie und Numerik für den Entwurf von Vorgespannten Membrantragwerken.* PhD thesis, Universität Karlsruhe.

Ziegler, R., Wagner, W., and Bletzinger, K.-U. (2003). A finite element model for the analysis of wrinkled membrane structures. *International Journal of Space Structures*, 18(1):1–14.

Zienkiewics, O. C. and Cheung, Y. K. (1964). The finite element method for analysis of elastic isotropic and isotropic slabs. *Proc. Inst. Civil Engineering*, 28:471–488.

Zienkiewics, O. C., Taylor, R. L., Papadopoulus, P., and Oñate, E. (1990). Plate bending elements with discrete constraints: new triangular elements. *Computers and Structures*, 35:505–512.

Zienkiewicz, O. C. and Taylor, R. L. (1989). *The Finite Element Method*, volume 1 and 2. McGraw-Hill, London, 4th edition.

Zárate, F. (1996). *Nuevos Elementos Finitos para Placas y Láminas.* PhD thesis, Technical University of Cataluña.

Index